SCANNING TUNNELING MICROSCOPY STUDIES OF METAL CLUSTERS SUPPORTED ON GRAPHENE AND SILICA THIN FILM

A Dissertation

by

ZIHAO ZHOU

Submitted to the Office of Graduate Studies of
Texas A&M University
in partial fulfillment of the requirements for the degree of

DOCTOR OF PHILOSOPHY

August 2012

Major Subject: Chemistry

SCANNING TUNNELING MICROSCOPY STUDIES OF METAL CLUSTERS SUPPORTED ON GRAPHENE AND SILICA THIN FILM

A Dissertation

by

ZIHAO ZHOU

Submitted to the Office of Graduate Studies of
Texas A&M University
in partial fulfillment of the requirements for the degree of

DOCTOR OF PHILOSOPHY

Approved by:

Co-Chairs of Committee,	D. Wayne Goodman
	James D. Batteas
Committee Members,	Glenn Agnolet
	Robert R. Lucchese
Head of Department,	David H. Russell

August 2012

Major Subject: Chemistry

ABSTRACT

Scanning Tunneling Microscopy Studies of Metal Clusters Supported on Graphene and Silica Thin Film. (August 2012)

Zihao Zhou, B.S., University of Science and Technology of China (P. R. China)

Co-Chairs of Advisory Committee: Dr. D. Wayne Goodman
Dr. James D. Batteas

The understanding of nucleation and growth of metals on a planar support at the atomic level is critical for both surface science research and heterogeneous catalysis studies. In this dissertation, two planar substrates, including graphene and ultra-thin silica film were employed for supported model catalysts studies. The structure and stability of several catalytically important metals supported on these two substrates were thoroughly investigated using scanning tunneling microscopy (STM) coupled with other traditional surface science techniques.

In the study of the graphene/Ru(0001) system, the key factors that govern the growth and distribution of metals on the graphene have been studied based on different behaviors of five transition metals, namely Pt, Rh, Pd, Co, and Au supported on the template of a graphene moiré pattern formed on Ru(0001). Both metal-carbon (M-C) bond strength and metal cohesive energies play significant roles in the cluster formation process and the M-C bond strength is the most important factor that affects the morphology of clusters at the initial stages of growth. Interestingly, Au exhibits two-dimensional (2-D) structures that span several moiré unit cells. Preliminary data

obtained by dosing molecular oxygen onto CO pre-covered Au islands suggest that the 2-D Au islands catalyze the oxidation of CO. Moreover, graphene/Ru(0001) system was modified by introducing transition metals, oxygen or carbon at the interface between the graphene and Ru(0001). Our STM results reveal that the geometric and/or electronic structure of graphene can be adjusted correspondingly.

In the study of the silica thin film system, the structure of silica was carefully investigated and our STM images favor for the [SiO_4] cluster model rather than the network structure. The nucleation and adsorption of three metals, namely Rh, Pt and Pd show that the bond strength between the metal atom and Si is the key factor that determines the nucleation sites at the initial stages of metal deposition. The annealing effect studies reveal that Rh and Pt atoms diffuse beneath the silica film and form the 2-D islands that are covered with a silica thin film. In contrast, the formation of Pd silicide was observed upon annealing to high temperatures.

DEDICATION

To my mother Wei and my father Jinghui

ACKNOWLEDGEMENTS

I would like to thank my advisor, Dr. D. Wayne Goodman, for providing me the opportunities and environment for performing research at the cutting edge of science, and in particular for his guidance, trust and support throughout the period of my studies. And I would like to thank my committee member Dr. Glenn Agnolet and the co-chair of my advisory committee Dr. James D. Batteas for helping me proofread and revise this dissertation. Special thanks also go to my committee member Dr. Robert R. Lucchese for his guidance and support throughout the course of my research.

My deepest gratitude also goes to Dr. Fan Yang, Dr. Zhen Yan, Dr. Li Liu, Dr. Feng Gao, Dr. Mingshu Chen and other members of Dr. Goodman's research group for their help and support. Thanks also go to Amy Liu for her secretarial assistance and warm support. And I would like to thank my friends, the department faculty and staff for making my time at Texas A&M University a great experience. I also want to extend my gratitude to the Department of Energy and the Robert A. Welch Foundation for the research funding they provided for this research.

Finally, I want to thank my family for their love and support. I am grateful to my mother who has always been supporting me and proud of what I do. I would also like to thank my father for always supporting my decision to pursue my interest.

TABLE OF CONTENTS

Page

LIST OF FIGURES

FIGURE Page

FIGURE Page

FIGURE Page

FIGURE Page

FIGURE Page

FIGURE Page

FIGURE Page

FIGURE Page

LIST OF TABLES

1. INTRODUCTION

1.1 Heterogeneous Catalysis Studies Using Surface Science Techniques

The study of heterogeneous catalysts is of great importance because of its wide applications in many areas, including chemical production, material synthesis, energy storage and conversion, pollution control, etc. For instance, heterogeneous catalysis is fundamental to the production of plastics and fuels, which is the basis of the chemical and materials industries. Another widespread application is the catalytic converter equipped on automobiles to reduce pollutants such as NO and CO. Owing to its importance in practically every aspect of our modern living, substantial efforts have been devoted to understanding this subject. In the history of study and development of heterogeneous catalysis, scientist noticed that the nature of the top layers of the catalysts mostly determines the reaction rate and small amounts of additives can poison or promote the reaction. In other words, the surfaces are crucial for heterogeneous catalysis. It is not only the amount of the surface area, but also the composition and structure that is important for the activity and selectivity of a reaction. Therefore, surface science has been a fundamental approach to study and understand heterogeneous catalysis since the early twentieth century [1].

One of the major tasks of surface science research in heterogeneous catalysis is to understand the correlation of the elemental composition and atomic-scale structure of catalysts with their catalytic reactivity and selectivity toward specific chemical reactions.

This dissertation follows the style and format of *Surface Science*.

With the development of surface science techniques in the past thirty years, scientists are capable of characterizing the elemental composition of catalyst surfaces as well as providing structural information at the atomic level. Moreover, the combination of these modern surface science techniques with a traditional experimental approach enables us to understand the mechanism of various surface catalytic reactions.

Surface science techniques can be divided into three groups based on their operating principles and working conditions. The first group includes techniques such as low energy ion scattering (LEIS), X-ray photoelectron spectroscopy (XPS), Auger electron spectroscopy (AES), low energy electron diffraction (LEED), etc. All of them involve detecting charged particles such as electrons and ions or molecules. These techniques are required to work under high vacuum conditions ($< 10^{-6}$ Torr) because the mean free path of these particles is too short to reach the detector under high pressures. The second group of techniques involves detecting light with optical probes which can be operated under either ambient pressures or high vacuum conditions. These surface sensitive approaches, such as polarization-modulation infrared reflection absorption spectroscopy (PM-IRAS) and sum frequency generation spectroscopy (SFG) can provide valuable information regarding the composition, orientation, and structure of molecules adsorbed on the surface at atmospheric pressures [2-8]. The last group is the family of scanning probe microscope (SPM) using a physical probe that scans the sample line by line and an image of the surface is created by recording the information obtained from the probe as a function of surface position. Such techniques include STM, atomic force microscope (AFM), near-field scanning optical microscopy (NSOM), etc. STM has

greatly advanced the development of surface science since its invention because of its ability to provide structural information of the surface at the atomic level in both vacuum and atmosphere. In this dissertation, STM is the most important technique employed to investigate the structure and stability of the supported model catalysts.

Although the modern surface science techniques have significantly facilitated the understanding of heterogeneous catalysis, we encounter two limitations when applying the knowledge obtained from surface science to the real world catalysts, that are often referred to the materials gap [9] and the pressure gap [10]. The materials gap originates from the discrepancy between the well-ordered single crystals employed as model catalysts in surface science studies and the real world catalysts with more complex surface structures, which are highly dispersed metal clusters supported on an inert porous carrier with a high surface area. Obviously, the well-defined single crystal metal surfaces cannot represent the metal clusters in the sense that these metal clusters with a certain size have special structures and also interact with the support material to some extent. On the other hand, the pressure gap arises from the difference between the ultrahigh vaccum (UHV) conditions ($< 10^{-9}$ Torr) under which most surface science techniques work and atmospheric or higher pressures at which chemical reactions occur in the industrial process. Therefore, the facts obtained in UHV might not hold at high pressures.

Bridging the Materials Gap

Even with the advanced modern surface techniques, it is still difficult to obtain

the detailed picture of real world catalysts for the following reasons. First, the electronic, structural and chemical information of real catalysts supported on porous oxide cannot be obtained by most surface spectrometers because charging of the insulated oxide bulk usually leads to poor sensitivity [9]. Second, the structure of metal clusters supported on a porous oxide are usually non-uniform because of the wide range of particle sizes and various local morphologies, thus making it impossible to draw any general conclusion based on the local information. Third, undesired impurities and contamination from real catalysts also hinder our understanding of the nature of heterogeneous catalysts. It appears to be impossible for surface scientists to directly study the real world catalysts in practice.

To solve the above problems, model catalyst systems were developed, including single crystal model catalysts [11] and supported model catalysts [12]. Single crystal model catalysts are catalytic metals with an extended well-ordered surface, as shown in Fig. 1(a). Many single crystal facets with low-index have been investigated and their structural and chemisorptive properties are well understood [13]. The uniform structure can be directly related to the information obtained during a catalytic process, such as the kinetics of a reaction and the favorite binding site of surface adsorbate species. In addition, with the uniform and clean surface, it is relatively straightforward to identify the reaction intermediates, promoters or inhibitors during a catalytic reaction [13,14].

However, as mentioned earlier, the studies of single crystal model catalysts often oversimplify the catalytic process. The real catalysts are metal clusters with the size in a range from a few nanometers to hundreds of nanometers which are extremely dispersed

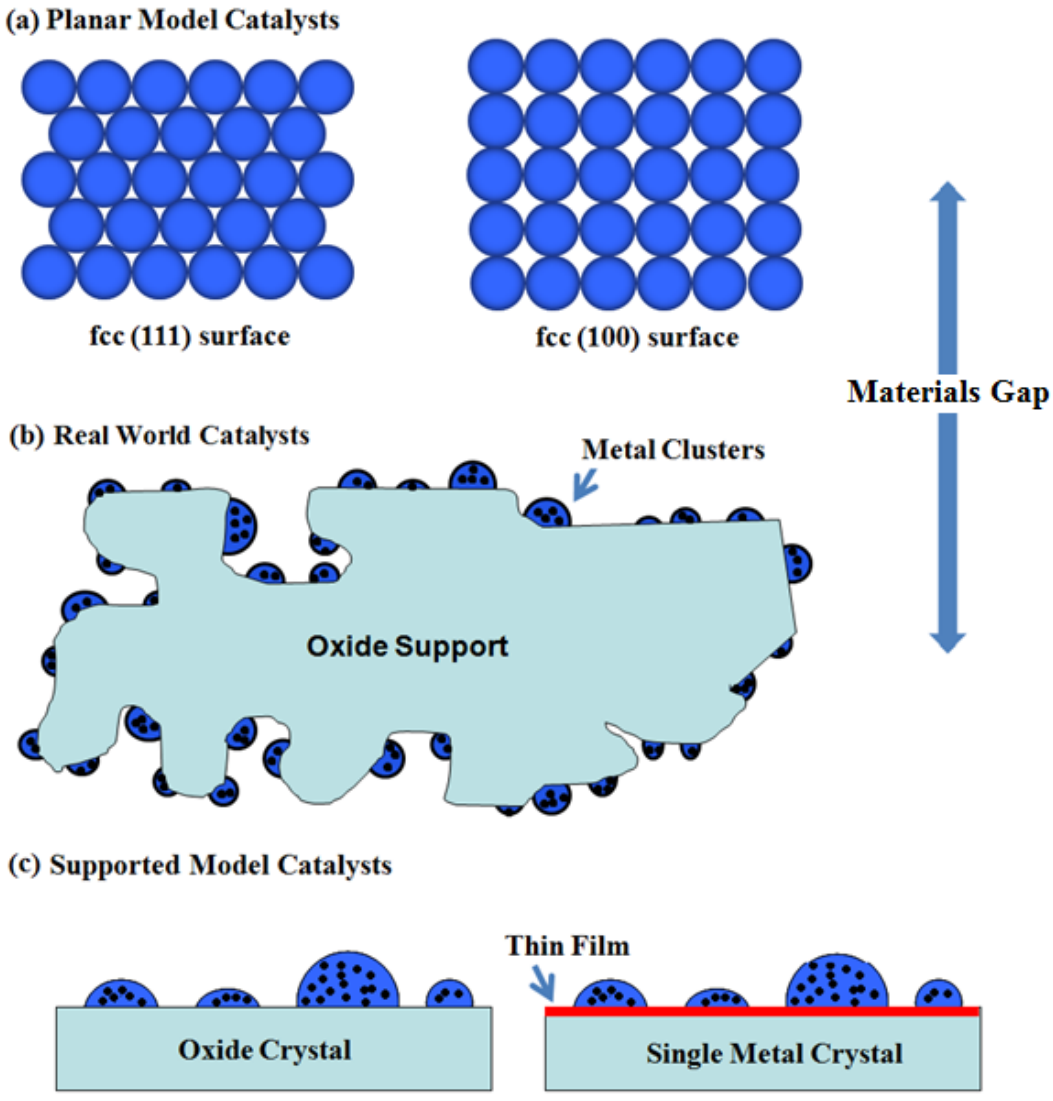

Fig. 1 Schematic drawing of three types of catalysts and the materials gap.

on a high-surface-area oxide support, as shown in Fig. 1(b). It has been reported that the reactivity and selectivity of catalysts are often dependent on the cluster size [15]. Also, the oxide carrier may play an important role in a catalytic process since the oxide does not only provide the mechanical support for the metal clusters but also interacts with metal clusters to modify their geometric and electronic structures. For example, migration of oxide over metal clusters can happen in the case of strong metal-support interaction (SMSI) effect, which can dramatically change the selectivity and reactivity of a catalyst [16]. Obviously, studies of planar model catalysts cannot address either the particle size effect or the metal-support interaction.

In order to bridge the materials gap between the planer model catalysts and the real catalysts, supported model catalysts have been synthesized and employed in heterogeneous catalysis studies. This type of model catalysts consist of small metal clusters supported on a planar surface, as shown in Fig. 1(c). Extensive efforts have been made to fabricate various planar surfaces and design different supported catalysts [17-25]. The planer support can either be a conductive single crystal of oxide or a thin film grown on a metal single crystal. Metals of interest can be prepared on the planer support mainly via the following ways: vapor deposition of metals in UHV, nanolithography, or deposition of metal-organic precursors. Vapor deposition of metals in UHV is the most frequently used method to prepare supported model catalysts because of its convenience. Various methodologies for preparation of supported model catalysts provide us opportunities either to modify the support or to control the size and structure of metal clusters. Since the supports are conductive, typical surface science techniques can be

applied to such systems without charging problems. In addition, SPM methods such as STM and AFM are also suitable to study the morphologies of the supported catalysts because the surface is relatively flat [26]. To sum up, metal-support interactions and cluster size effects can be addressed in the investigation of supported model catalysts.

Bridging the Pressure Gap

As mentioned earlier, the pressure gap is the discrepancy between the UHV conditions (< 10^{-9} Torr) under which most surface science studies are performed and high pressures (> 750 Torr) at which real catalysts work. Such inconsistency arises for two reasons. First, increase in the pressure of reactant gases often leads to a dramatic change in chemisorption on the catalyst surface because the chemical potential of reactants is increased by more than 20 kJ/mol as the pressure is increased from 10^{-9} Torr to 750 Torr at room temperature. As a result, the binding sites of reactants on the surface may also alter, and the catalytic process may be totally different from that occurring under UHV conditions. Second, changes in the surface structure of catalysts can also be induced in the presence of high pressures via reconstruction of their surfaces [27-29]. As the structure of surfaces changes, catalytic processes can also be different. For example, the reconstruction of noble metals surfaces, such as Pt, leads to an oscillation in CO oxidation [30-32]. As such, it may not be correct to apply the knowledge obtained under UHV conditions to real catalysts at high pressures directly.

Over the past few decades, significant efforts have been devoted to bridging the pressure gap. One method commonly used is to integrate elevated-pressure cells or

micro-reactors in UHV chambers, thus allowing for the transfer of the sample from a UHV chamber to a high pressure cell for real catalytic reactions. The model catalysts can be examined in UHV before and after reactions and the structural as well as chemical information can be related to the catalytic performance at high pressures. In our studies, an elevated-pressure cell is equipped to the UHV chamber, and a series of differential pumping systems are employed to separate them [33-35]. The detailed setup of this system can be found in the experimental section (Section #2.1).

However, the drawback of the above method is that the structural and chemical information of catalysts during the working phase of the reactions is still missing. To obtain a thorough picture of catalysts during a reaction, we can either use techniques such as STM and PM-IRRAS that can work at ambient pressures or modify the conventional surface techniques that are restricted to UHV conditions to allow them to operate at higher pressures. For instance, STM, which can work either under UHV or at ambient pressures, was demonstrated to be capable of imaging the catalyst surfaces *in situ* at high pressures and high temperatures by Somorjai and coworkers in 1990s [36-43]. Since then, a serious of *in situ* STM studies on both adsorbate surface structures and reconstruction of metal surfaces in the presence of high pressure reactant gases have been conducted, which provided valuable structural information of catalysts in the working phase [44-62]. On the other hand, high pressure surface science techniques such as high pressure XPS and high pressure LEIS, that can work under the pressures up to several Torr, have also been developed in recent years [63,64]. The working principle of the high pressure techniques is to separate the sample which is exposed to high pressures

from the detector that is still in vacuum by differential pumping systems. The charged particles generated from the sample are immediately transferred to vacuum chamber, thus allowing them to move through their trajectory without scattering by gas-phase molecules. Considering high pressure XPS for example, the application started in 1970s with the work by K. Siegbahn and coworkers [65-69], in which they demonstrated the compounds in the gas phase, liquid phase and surfaces at high pressures could be measured and characterized by XPS. In 2002, Salmeron *et al.* [64] designed a high pressure XPS with a differentially pumped electrostatic lens system, which allows the working pressure to extend up to 10 Torr. In this design, the differential pumping system near the sample region was also an electrostatic lens, which could focus the photoelectrons from the sample onto the intermediate aperture, and the following electron lens elements could refocus the electrons into the detector. With this approach, most of the electrons ejected from the sample could pass through the aperture and then be collected. Consequently, the signal was increased dramatically compared to a passive differential pumping system.

To summarize, scientists should carefully deal with the materials gap and the pressure gap in the studies of heterogeneous catalysis. Apparently, the supported model catalysts that lay in the intersection of the heterogeneous catalysis field and surface science are the key to fully understand the real world catalysts using surface science techniques. Therefore, it is the foremost focus in our research.

1.2 Nucleation and Growth of Metals

One of the most fundamental issues in the studies of supported model catalysts is to investigate the morphology of metals on the planar support, which is the key to understand the role that surface structure plays in a reaction process because it is closely related to the catalytic performance of model catalysts. The nucleation sites and morphologies in the initial stage of metal growth highly depend on the interface chemistry and physics between the metals and substrate [16,24,70,71].

At the onset of metal deposition on a planar support, a series of consecutive steps determine the morphologies of the metals, including adsorption of metals, diffusion of metal atoms, as well as nucleation and growth of metals. All these steps are determined by kinetic and thermodynamic parameters of the surface and deposited metals. It was reported that the growth of metals on an oxide at low temperatures is usually controlled by kinetics, which leads to quasi 2-D islands. On the other hand, metal growth at high temperatures is controlled by thermodynamics leading to three-dimensional (3-D) clusters in order to minimize the surface energy by reducing the surface area and increasing average surface coordination [24].

Three primary modes by which metals grow on the planer supports have been observed: Volmer-Weber (VM) growth mode, Stranski-Krastanov (SK) growth mode, and Frank-van der Merwe (FM) growth mode. In VM growth mode, the interaction between metal adatoms is stronger than the metal-support interaction, which leads to the formation of 3-D metal clusters and islands. In FM growth mode, the metal-support interaction is stronger and thus metal atoms prefer to form flat and smooth 2-D islands

for the coverages lower than 1 ML. And the further deposition leads to a layer-by-layer growth mode, in which complete films form prior to the growth of subsequent layers. SK growth mode is an intermediary process, in which the coexistence of 2-D layer and 3-D islands is observed, and thus this mode is also called layer plus island growth. Transition from layer-by-layer to 3-D island growth occurs at a critical layer thickness which is determined by the chemical and physical properties of the substrate and deposited metals. Fig. 2 schematically illustrates the three growth modes at different coverages.

The driving force for metal growth on the substrate is to minimize the total energy of the system; therefore, the growth mode of metals on the substrate is determined by several thermodynamic parameters, including the surface free energy of the deposited metal, the surface free energy of the planer support and the interfacial energy between the metal and support [72]. If the free energy of the support is lower than the free energy of the metal plus the interfacial energy, the metal follows the VM mode, in which formation of 3-D clusters and islands is observed. On the contrary, if the free energy of the substrate is larger than the sum of the other two, either FM mode or SK mode occurs, depending on whether the lattice spacings match between the metal and substrate or not. The metal follows FM growth mode when the metal lattice spacing matches that of the substrate, whereas lattice mismatch often leads to SK growth mode. For example, transition metals have free surface energies of a few J/m^2 [72], while the free surface energy of metal oxide surface are substantially smaller, often one-tenth of that, e.g. TiO_2 of 0.35 J/m^2 [73]. Thus, the VM mode usually dominates metals growth on various oxide supports. LEIS and STM are usually employed to study the growth

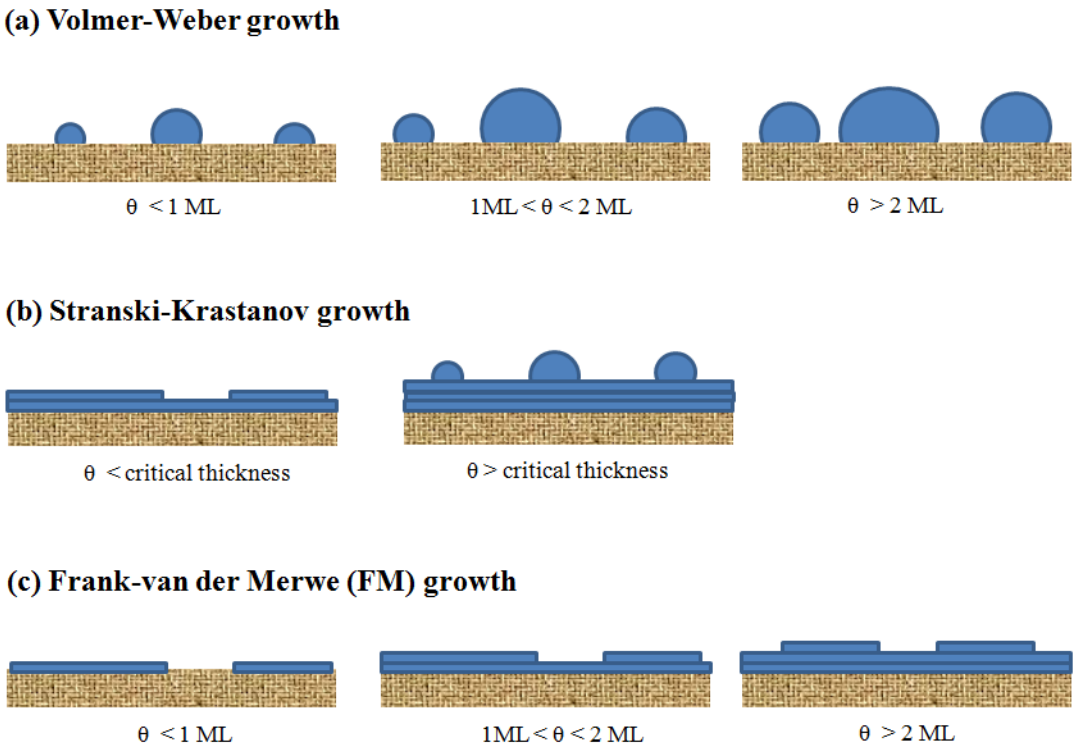

Fig. 2 Cross-section views of three primary modes of metal growth on a planar support. (a) Volmer-Weber growth mode, (b) Stranski-Krastanov growth mode, and (c) Frank-van der Merwe growth mode. Each mode is shown for several different coverages Θ.

mode of metals on oxide supports due to their high sensitivity to the atomic composition and structure of the topmost surface [74-84].

In addition, a wide variety of defects on the surface frequently influence the nucleation sites and morphologies of metals. The most common defects are the one-dimensional ones in the form of atomic steps. Point defects such as kink sites at the step are also often observed. For the metal atoms with large diffusion lengths on the surface, they prefer to adsorb at the step sites due to difficulty of migration over these steps. Terraces often exhibit point defects such as vacancies and adatoms. For example, two types of oxygen vacancies were observed on TiO_2 surface due to either missing bridging oxygen atoms or losing in-plane oxygen atoms [85]. Generally speaking, the absence of oxygen or other anions results in lower coordination and lower oxidation state of cations, thus making them more active toward binding adsorbates [86]. As such, it is often observed that metal atoms or gases prefer to adsorb on the point defects on the terrace.

In this dissertation, the nucleation and growth of several catalytically important metals on graphene and ultra-thin silica film were carefully studied using STM and other surface science techniques.

1.3 Thermal Stability of Metal Clusters

Thermal stability has been central in supported model catalysts studies because it is intimately related to the activity and selectivity of catalysts at working temperatures. Two changes in supported model catalysts are usually observed when increasing the annealing temperatures: sintering and encapsulation. Both of them are of primary

concern in heterogeneous catalysis studies, especially for the structure sensitive reactions because they may cause a decrease in the efficiency of catalysts.

Sintering of supported metal catalysts is one of the most important issues in catalysis research because this phenomenon often causes catalysts deactivating during its life time in an industrial plant. The main reason for sintering is that the catalyst system tends to lower the total surface energy by merging separated smaller clusters into fewer larger particles. Under most cases, the higher the annealing temperatures, the faster this process occurs. During sintering, the total surface area is reduced while the average surface coordination is increased, thus leading to the deactivation of catalysts [87]. There are mainly two modes by which sintering of supported metal clusters can occur, either by migration of whole clusters or by diffusion of single metal atoms or metal complexes. Fig. 3 schematically illustrates the two modes. In the first mode, metal atoms diffuse on the surface of the cluster and accumulate on one side by random fluctuations, leading to the migration of the whole cluster. As the events of diffusion and accumulation repeat over time, clusters appear to move on the substrate following Brownian motion and they may coalesce with neighboring clusters. The second mode, known as Ostwald ripening, is a process where metal atoms or metal complexes dissociate from the cluster and then diffuse and coalesce with larger clusters. Both the detachment of atoms from the edge of metal clusters and diffusion of atoms on the substrate determine the sintering rate.

To avoid sintering of catalysts, better understanding of the mechanism is required. To this end, the mass transport mode and kinetics of sintering were studied by relating the averaged cluster size with theoretically established kinetic models [87,88]. The rate

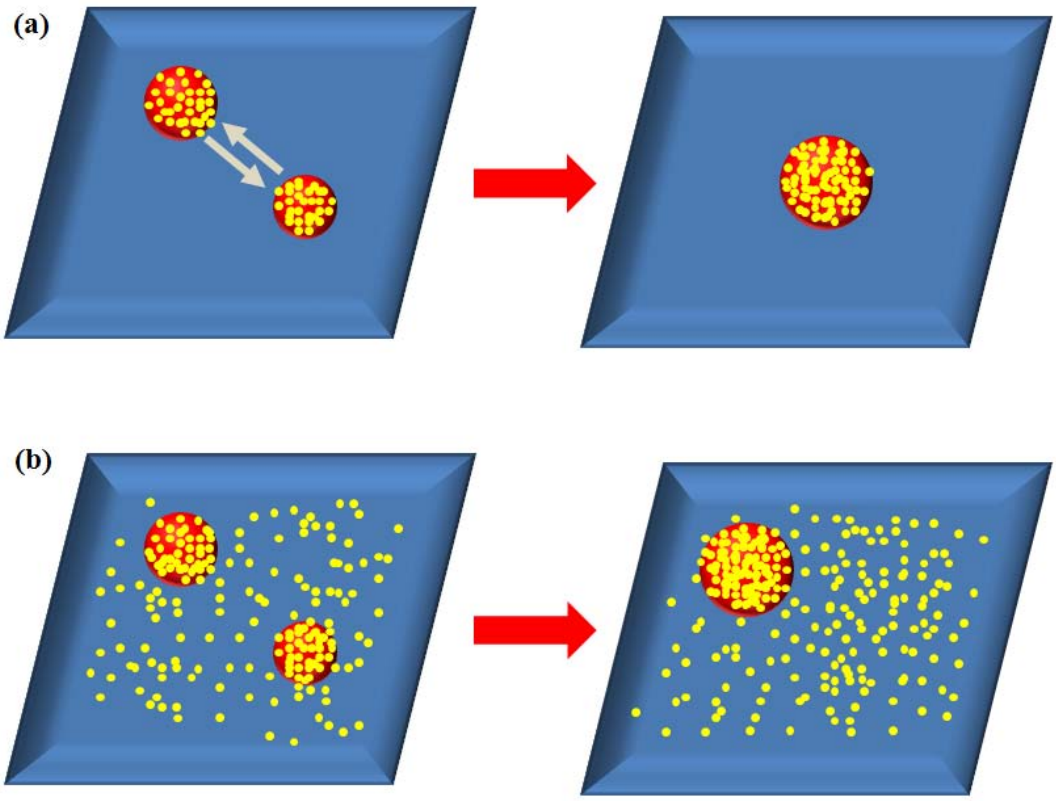

Fig. 3 Schematic drawing of two sintering modes: (a) cluster migration, and (b) Ostwald ripening.

equation for the averaged cluster could be obtained, which was then applied to all the clusters on the surface. Apparently, this method ignores the behavior of the individual clusters but only focuses on the whole cluster ensemble, such as average cluster dispersion and size. On the contrary, *in situ* STM provides a great opportunity to monitor individual clusters at certain annealing temperatures [47,49]. Continuous STM images of a single cluster during the sintering process cannot only reveal which mode dominates the sintering process but also help us determine the kinetics and activation energy of sintering by monitoring the volume change of a single cluster.

Encapsulation or decoration of catalysts is also of importance in catalysis studies because this process also has a great influence on the activity and selectivity of catalysts. During the process of encapsulation, the metal particles are covered by either a thin layer or a reduced oxide support; as a result, the active sites on the metal surfaces are blocked. Encapsulation usually occurs at high annealing temperatures in the systems with SMSI effect, e.g. group VIII metals (e.g. Fe, Ni, Rh, Ir) supported on reducible oxides (e.g. TiO_2, CeO_2, V_2O_5). For instance, encapsulation of metal clusters by an oxide layer was observed by LEIS, AES and XPS in systems such as Rh/TiO_2, Pt/TiO_2, and Pd/TiO_2 [89-95].

A variety of experiments have been performed to understand the reaction mechanisms of the encapsulation phenomena. It is believed that the encapsulation involves the mass transport from the oxide support onto the surface of metal particles, which leads to SMSI state and partial reduction of the oxide support. The driving force for the encapsulation is to minimize the total surface energy [92,96,97]. Thus the metals

with high surface energies supported on the oxides with low surface energies more easily undergo encapsulation [96]. For example, Pt and Pd are more likely to be covered by the oxide support than metals with relatively low surface energies, such as Au and Cu. TiO_2 and V_2O_5 more easily form the SMSI state than surfaces with relatively high surface energies, such as Al_2O_3 and SiO_2. In addition, it was observed that the existence of oxygen vacancies on the oxide support also plays an important role in the encapsulation process under UHV conditions [92]. Experimental results show that encapsulation of Pd clusters only occurs on the reduced or Ar^+ sputtered TiO_2 crystals but does not on the untreated TiO_2 surface [95]. Another important factor for encapsulation is the balance between the metal-metal bonding and metal-oxide bonding, which has been ascribed to the thermodynamic driving force of the decoration of metal clusters [90,91].

In our studies, the annealing effect of various metal clusters supported on graphene and ultra thin silica film was carefully studied using STM in conjunction with other surface science techniques.

2. EXPERIMENTAL

This chapter contains general descriptions of our experimental setup, summaries of related theories and discussions of some experimental preparation procedures.

2.1 Instrumentation

Most of our experiments were performed under UHV conditions for the following two reasons. First, UHV conditions can keep the sample clean for extended time, thus allowing us to characterize the sample without the interference of contamination. At the pressure of 1.0×10^{-6} Torr, one monolayer of gas molecules can stick on the surface in a second, assuming all of the molecules which strike the surface stick [98]. Therefore, to maintain a clean surface for extended period of time, most surface analysis techniques routinely require pressures of 10^{-9} Torr or lower. Second, the probes that most surface techniques use are often charged particles, which interact strongly with gas-phase molecules. Such techniques must be performed in vacuum in order to enable charged particles to move through their trajectory without scattering by gas phase molecules. Therefore, to eliminate the effects of collisions with the gas molecules, these techniques should be operated at least under pressures of 1.0×10^{-6} Torr, under which condition charged particles have a mean free path of 10^{2} meters [99].

Our UHV surface analysis system mainly consists of four parts: a STM chamber, a sample preparation chamber, a surface analysis chamber and an elevated-pressure cell. Additional parts include a pumping system, leak valves connected to a main gas

manifold and a sample manipulator. The detailed setup of the system is shown in Fig. 4. The STM chamber contains an Omicron room temperature STM (STM-1) for surface structure characterization. The sample preparation chamber contains an array of metal and semiconductor evaporators (e.g. Au, Pd, Pt, Rh, Si, etc.) for metal deposition and thin film preparation by resistive heating. A tip heating apparatus is also mounted in this chamber for degassing and annealing newly-made tips. The surface analysis chamber is equipped with a double-pass cylindrical mirror analyzer (PHI model 25-255) for AES measurements and a set of low energy electron diffraction (LEED) optics (Perkin-Elmer) for surface structure characterization, as well as an ion gun for Ar^+ sputtering. The elevated-pressure cell is a small chamber located at one end of the chamber. The sample can be linearly transferred into the cell by sample manipulator for high pressure exposures and catalysis studies. As the sample is moved into the high pressure cell, the cell is separated from the UHV system by a double stage differentially pumping system, where a vacuum tight seal is formed by the outer wall of the sample probe and the inner walls of 3 spring-loaded Teflon seals. More details can be found in [33-35]. The seals can hold the UHV condition of the main chamber even when the cell is exposed to atmosphere. In addition to conducting high-pressure experiments, the high pressure cell allows us to change the tip and mount the sample without baking out the whole UHV system.

During the procedure of sample preparation, the sample resides in a Ta made sample holder, which is located at the end of the sample manipulator, thus allowing us to transfer the sample in the sample preparation chamber, the surface analysis chamber or

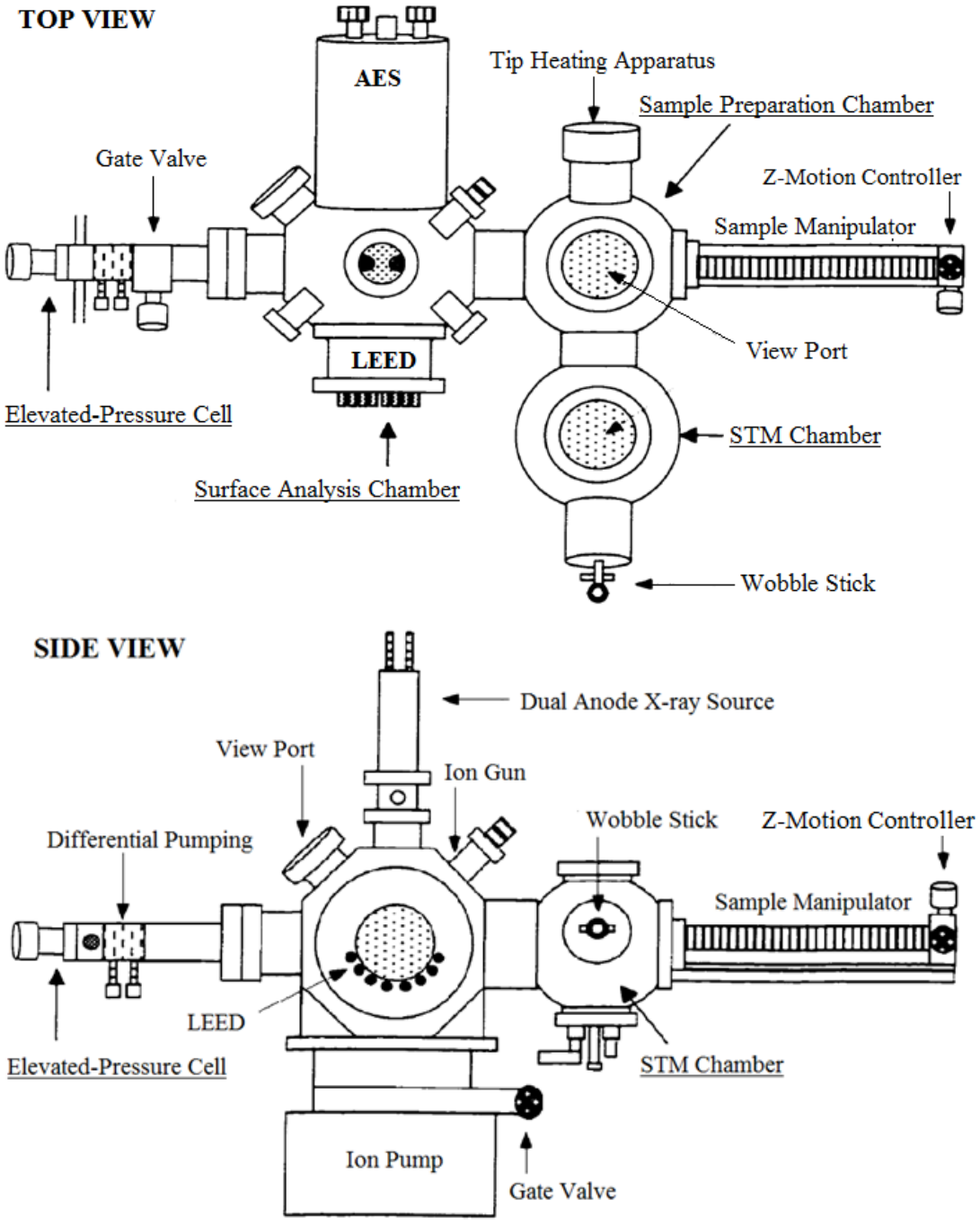

Fig. 4 Schematic diagram of the UHV surface analysis system.

the elevated-pressure cell. In order to heat the sample to desired temperatures, an electron beam heater consisting of a W filament is mounted at the back of the Ta sample holder that can heat the sample up to 3000 K with a voltage of 400 volts applied to the sample. If necessary, the sample can be exposed to the desired gas such as O_2, CH_4, or C_3H_6 by leaking the gas into the preparation chamber through the leak valves. A nude ionization gauge is mounted inside the main chamber for pressure monitoring. After sample preparation, the sample can be transferred to the STM chamber for structure characterization with a wobble stick which is located in the STM chamber.

The base pressure of the main chamber is typically on the order of 1.0×10^{-10} Torr, which is achieved and maintained by a series of pumping systems: two mechanical roughing pumps (Alcatel and Adixen), a 170 l/s turbomolecular pump (Balzers-Pfeiffer), two ion pumps (PE model, 500 l/s and 60 l/s), and a titanium sublimation pump (TSP). The first pumping stage is the mechanical roughing pumps that pump down the chamber from atmosphere to the millitorr pressure range. The second stage is the turbomolecular pump that is backed up by the Adixen mechanical pump, operating in the pressure range from 10^{-3} to 10^{-9} Torr. Higher vacuum of 10^{-10} Torr is achieved by 500 l/s ion getter pump and TSP. The ion pump does not require any backing pumps once its operating pressure regime ($< 10^{-6}$ Torr) is reached. A TSP provides additional efficiency by capturing most molecules striking on the reactive titanium film. In particular, the TSP is capable of trapping hydrogen molecules, which are not easily removed by the turbomolecular pumps and ion pumps [13,98]. The 60 l/s ion pump is used to pump down the sliding seals area in the sample manipulator as well as the bellows. Compared

to turbomolecular pumps, the ion pump and TSP do not only enhance the vacuum and cleanliness of the system, but also provide a vibration free environment, which is critical for STM measurement.

2.2 Surface Analysis Techniques

In this chapter, we discuss the working principles of the major surface analysis techniques employed in our study, including STM, AES and LEED. STM and LEED experiments are performed for characterizing the structure of sample surfaces, while AES is employed for measuring the composition of surfaces. STM and AES are capable of identifying trace irregularities (< 1% of one monolayer) in the surface structure and composition. In contrast, LEED is used for detecting structures with long range order on the surface.

Scanning Tunneling Microscopy

Invented in 1982 by Binnig and Rohrer [100,101], STM has been developed into a powerful surface and interface analysis technique for surface structure characterization with atomic resolution. Unlike other microscopes, STM does not require lenses, special light or electron sources. The fundamental working principle of STM is based on the quantum electron tunneling between a tip and a conducting sample. With a small bias voltage applied between the tip and the sample, the tunneling current flows between them when the tip-sample separation is only a few Å. The tunneling current is exponentially dependent on the tip-sample separation:

$$I = c\,V\,e^{-s\sqrt{\emptyset}}$$

where c is a constant, V is the bias, s is the tip-sample separation, $\emptyset$ is the mean barrier height between the tip and the sample [102]. From the above equation, assuming the barrier height $\emptyset = 4$ eV, I changes by an order of magnitude with a change of 1 Å in s. Thus the gap between the sample and tip can be controlled with great precision by the tunneling current. When imaging the surface, the piezoelectric tripod controls the position of the tip in the z-direction, as well as scans the tip across the surface in the x-direction and y-direction. Fig. 5(a) shows the schematic diagram of a typical STM, where the scanning unit maintains the tip position with respect to the sample. The data are acquired and processed by a computer to produce an image, the quality of which can be enhanced by the image processing software.

STM can be operated in two modes for image acquisition: constant current mode and constant height mode, as shown in Fig. 5(b). In the constant current mode, the tip scans the surface at constant tunneling current, which is maintained at a preset value by a feedback circuit. Using a feedback loop, the piezo adjusts the vertical position of the tip to keep the tunneling current stable, while the z displacement is read and processed as a function of xy coordinates by a computer, which creates a corresponding STM image. Constant current mode is more common in practice because it is capable of tracking surface morphology that is not atomically flat. However, the slow response time of both feedback circuit and piezo drivers limits the scanning speed.

On the contrary, constant height mode allows a tip to scan across the surface quickly at constant height and voltage, where the feedback system is fully turned off or

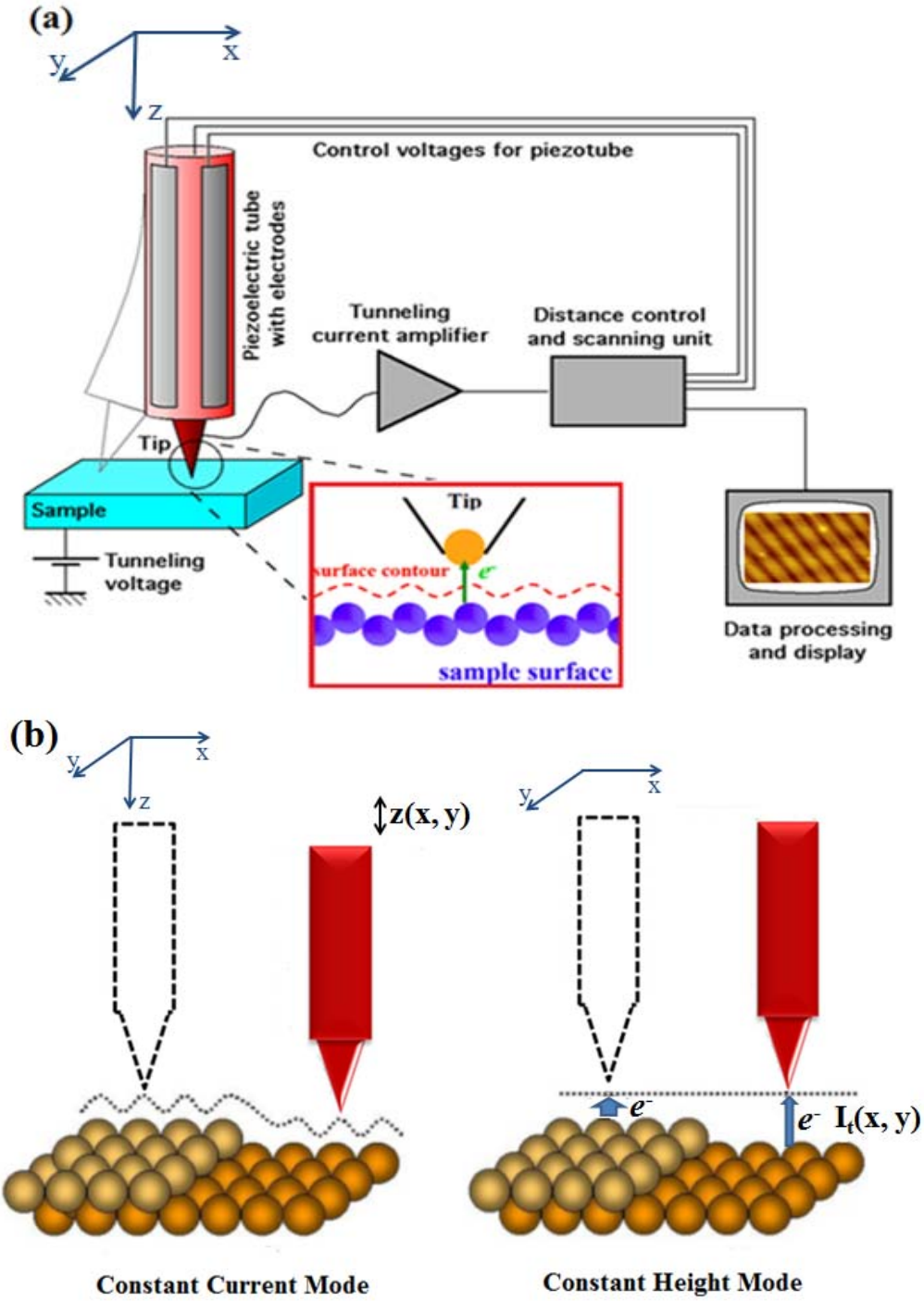

Fig. 5 Schematic view of (a) operating principle of STM, and (b) constant current mode and constant height mode. z(x, y) and I_t(x, y) are tip height and tunneling current as a function of xy coordinates, respectively.

slowed down. The change in tunneling current due to the tip passing over the surface features is measured as a function of the scanning position, and the topographic height can be derived and plotted by a computer. Since the real-time response of the feedback loop and piezo drivers to the surface features is not required, the STM can image the surface much faster, thereby allowing us to study dynamic processes occurring on the surface *in situ*. In addition, fast scanning also reduces the chance of image distortion caused by piezoelectric creep, hysteresis and thermal drifts. However, the main disadvantage of this mode is a significantly higher risk of tip crashing on surfaces due to irregular protrusions or large steps.

The most critical advancement of STM is its ability to resolve the real space surface structure at the atomic level, which means that scientists can study non-periodic features such as vacancies, defects and dislocations on surfaces. Moreover, unlike other electron microscopes and surface analytical techniques that require UHV conditions, STM can also operate in air or in liquid. Therefore, the applications of STM are not only limited to surface science, but also extended to other disciplines such as *in situ* studies of electrochemical reactions and *in vivo* investigations of biological materials. Since its invention, STM has been applied to many disciplines in physics, chemistry, biology, metrology, and material science.

However, STM also encounters some limitations. First, STM lacks chemical sensitivity, which means compositional information cannot be obtained from STM measurements. A combination with other surface techniques such as AES and XPS is often essential to extract chemical information of surfaces. Second, what an STM

measures is the electronic states near the Fermi level that are overlapping with the tip wave function rather than the physical position of atoms on the surface. In other words, STM images represent the electronic structure instead of the physical structure. Third, the size, shape and chemical identity of the tip have an influence on the resolution and the measured electronic structure due to its involvement in the tunneling current. For example, a blunt tip cannot precisely probe the shape and depth of narrow grooves on the surface. Worse still, tip geometry is not available if made by the convenient tip preparation methods such as electrochemical etching and mechanical cutting. Another problem is that the tip may not be mechanically or chemically stable under the STM scanning process due to the interaction with surface atoms or reaction with gas molecules adsorbed on the surface. Fourth, the area that STM measures is typically quite small, only about 1 μm^2 or less. It may not be possible to draw any general conclusions for the whole surface from the local information obtained from such a small area. This problem can be partially solved by randomly choosing multiple scanning areas.

Nevertheless, STM has been successful in resolving the structures of supported model catalysts in many studies. In this dissertation, all STM images were obtained using a room temperature Omicron UHV STM-1 system in constant current mode with an electrochemically etched W tip. The bias voltages are reported with reference to the sample.

Auger Electron Spectroscopy

Since the observation of Auger electron excitation by P. Auger [103] in 1925,

Auger electron has been the subject of extensive theoretical and experimental investigations. In 1953, Lander [104] observed small characteristic peaks when studying the energy distribution of secondary electrons emitted from solid samples irradiated with electrons. He was the first to point out that Auger electrons could be used as a tool for surface analysis. With the development of an analyzer and detector system and using electronically differentiated energy distribution d$N(E)$/dE, the resolution, sensitivity and signal to noise ratio was enhanced to the extent that detection of surface impurities with the concentration as low as 1% of one monolayer became possible [105,106]. AES has become one of the most widely used surface analysis techniques to study the identification of surface elements.

As is usual for other spectroscopic techniques, the major components of an AES system include a source of primary excitation, the sample, an analyzer and a detector. The source of primary excitation can be photons, electrons, or high energy ions, all of which are able to ionize the inner shells of atoms to excite Auger electrons. The commonly used source is an electron beam with a kinetic energy between 1 keV to 10 keV (3 keV and 5 keV are frequently used). As for the sample, any solid can be used as a sample in principle. Different types of analyzer and detector have been implemented in the AES system, including the 127° energy analyzer, retarding field grid system, and cylindrical mirror analyzer. The last one shows the best performance, which provides an ultimate sensitivity of 0.1% of a monolayer [98].

The mechanism of the Auger process is illustrated in Fig. 6. The incident electron ionizes the atom and creates a core hole in the electron orbital of the atom. The core hole

is then filled by an outer electron and the energy released is transmitted in a non-radiation process to a second electron, which leaves the atom with a characteristic kinetic energy. The ejecting electron is called the Auger electron. Taking $KL_1L_{2,3}$ Auger process as an example, the incident electron creates a core hole in the K shell, and an electron from L_1 fills the hole in the K shell. The energy released ($E_K - E_{L_1}$) is transmitted to an electron in the $L_{2,3}$ shell, which is ejected from the atom, leaving the atom in a doubly ionized state. The kinetic energy of the ejected Auger electron is given by:

$$E_{KL_1L_{2,3}} = E_K - E_{L_1} - E_{L_{2,3}} - \emptyset$$

where E_K, E_{L_1}, $E_{L_{2,3}}$ are the binding energies of electrons in the K, L_1, and $L_{2,3}$ shells, respectively, and $\emptyset$ is the work function. From the equation, an Auger transition is characterized primarily by the locations of the initial hole and final two holes. Therefore, the Auger transition varies with different elements, which can be used to identify the chemical elements. Note that three electrons are involved in the Auger process, so hydrogen and helium cannot be detected by AES.

In AES spectra, an intense background from bombardments of secondary electrons coexists with the AES peaks, making the analysis of AES signal difficult. To emphasize the AES signal, Auger spectra are commonly collected in the derivative mode, in which d*N(E)*/d*E* is recorded as a function of kinetic energy. The relative amount of an element on the surface is proportional to the height of the differentiated Auger peak.

AES is one of the most widely used surface techniques to determine the chemical composition of solid surfaces because of its high surface sensitivity. As mentioned above,

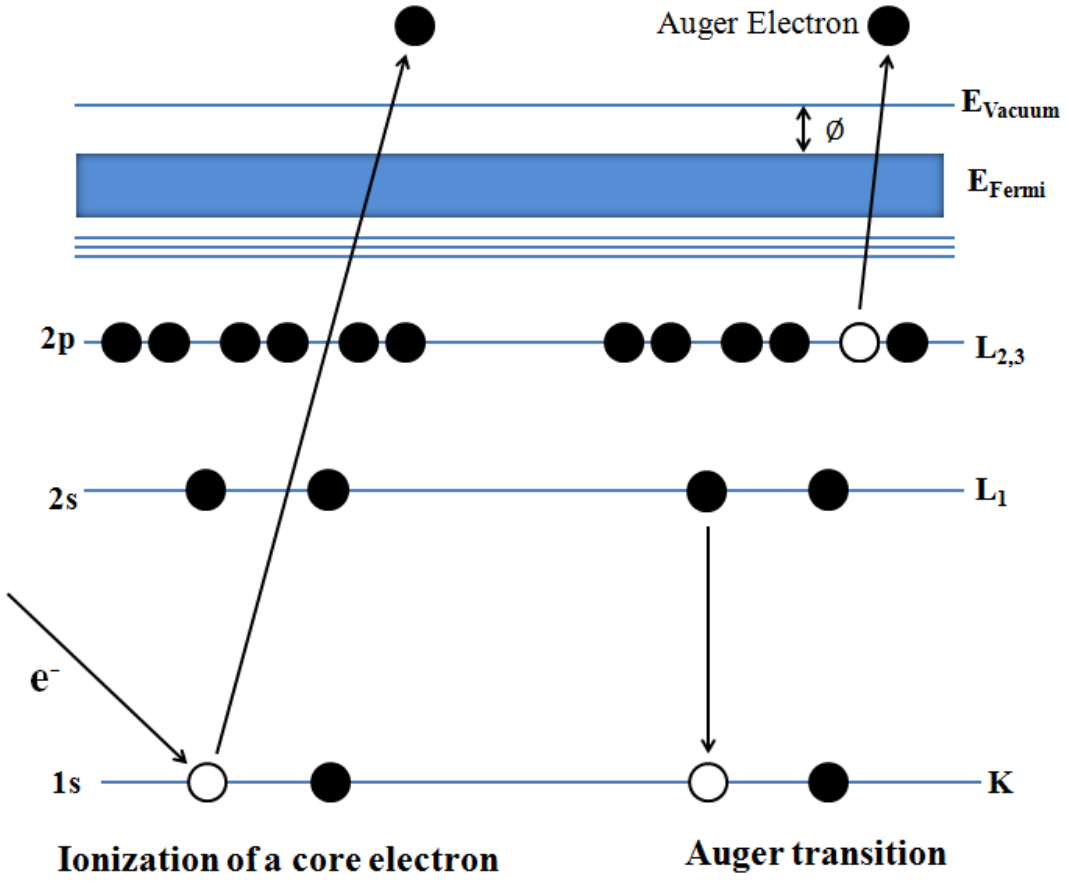

Fig. 6 Schematic drawing of $KL_1L_{2,3}$ Auger process. The incident electron first ionizes the atom and creates a core hole in the K shell, as shown on the left. Then the core hole is filled by an electron in L_1 and the energy released is transmitted to a second electron in the $L_{2,3}$ shell, which leaves the atom with a characteristic kinetic energy, as shown on the right.

the ultimate sensitivity of 0.1% of one monolayer can be achieved. The reason lies in the fact that the typical kinetic energy of an ejected Auger electron used for analysis is in the range of 25 ~ 1000 eV, which has a relatively short inelastic mean free path in solids, usually less than 10 Å. Therefore, Auger electrons originating from the first few atomic layers can leave the surface, while those from deeper layers cannot reach the surface due to scattering by top layer atoms. The surface sensitivity can be further enhanced by collecting ejected Auger electrons at a smaller grazing incidence angle with respect to the surface.

In our studies, AES data are acquired using a Perkin-Elmer cylindrical mirror analyzer for both element identification and quantitative information. For example, AES can check surface cleanliness by measuring the peak intensities of contaminations, such as carbon, oxygen, or argon. Also, AES is used for quantitative analysis to determine the surface coverage of a specific element by measuring the relative peak intensity of that element.

Low Energy Electron Diffraction

LEED is another common technique used in surface science to probe the long range order of the periodic surface structures as well as the partially disordered system. The discovery of interference phenomenon of electron diffraction was strongly related to the development of the principles of wave-particle duality postulated by L. de Broglie [107] in 1924. According to de Broglie relation

$$\lambda = h/mv$$

where λ is wavelength, h is Plank's constant, m is mass and v is velocity, the wavelength for electrons with energies in the range of 20 ~ 200 eV is comparable with the atomic spacing. Thus, a beam of electrons can be equally regarded as a succession of electron waves which interfere with periodic crystal lattices if the beam is incident on the crystal. This theory was confirmed experimentally by Davisson and Germer [108] in 1925, who observed the diffraction of electrons by a Ni crystal for the first time. With the development of instruments and improvement of vacuum conditions, it became common to use LEED as a tool to investigate the surface structure in surface science studies.

The essential parts for a LEED system contain an electron gun for producing parallel electron beam with energies typically in the range between 20 and 200 eV and a detection system for monitoring elastically scattered electrons. A typical LEED system is shown in Fig. 7, which has a hemispherical fluorescent screen and an electron gun at the central axis of the screen. The suppressor grid between the sample and fluorescent screen can remove the inelastically scattered electrons by applying a negative potential slightly smaller than the primary electron energy. The elastically scattered electrons can pass the grids and then they are accelerated onto the fluorescent screen by a positive voltage of a few kilovolts. The diffraction spots will display on the screen. It is also possible to observe diffraction spots from the backside of the screen if the screen is transparent. Similar to other surface science techniques, LEED is surface sensitive because the scattered low energy electrons can only penetrate the top few layers of the solid.

The principle of LEED is based on the de Broglie equation, as mentioned above.

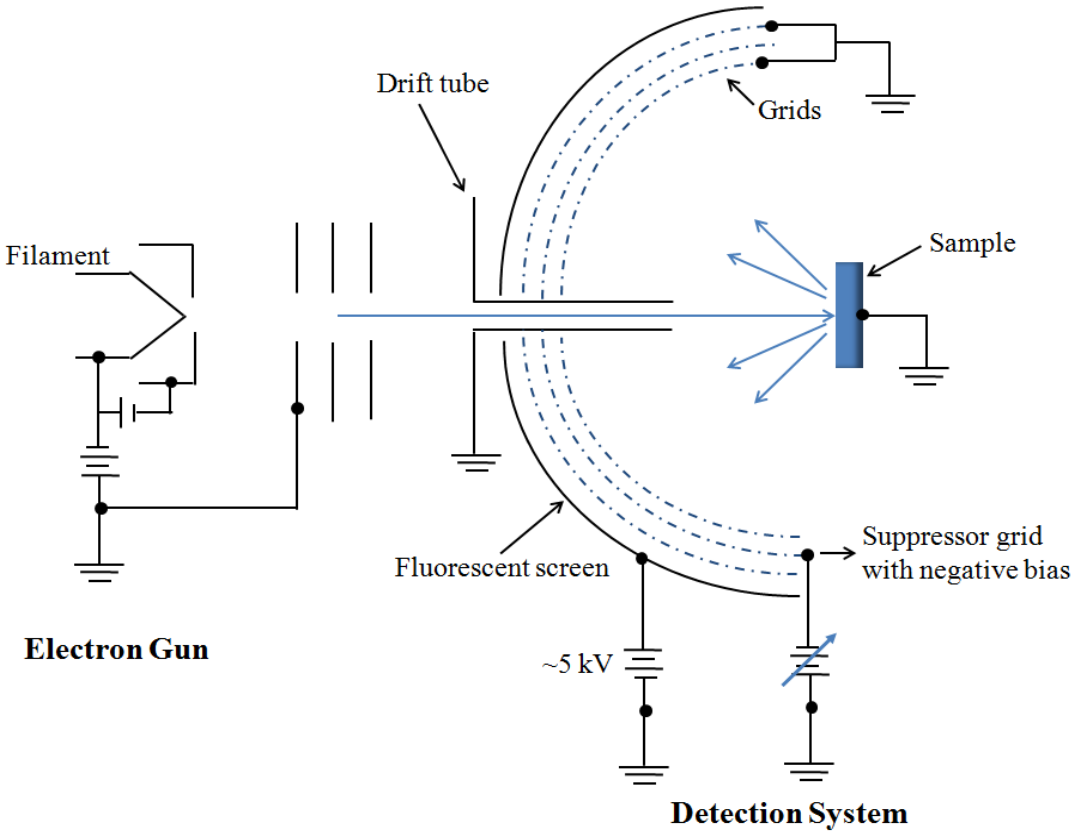

Fig. 7 Scheme of a LEED system

Consider the electron wave scattering in one dimensional, where the primary electron wave strikes with an angle φ_0 onto a chain of atoms which have atomic separation α. The constructive interference takes place only if the scattered waves from neighboring atoms have path difference of $n\lambda$, where n is an integer. In other words, the constructive interference occurs only when the Bragg condition is satisfied [98]:

$$\alpha(sin\,\varphi - sin\,\varphi_0) = n\lambda$$

The practical method for interpreting LEED diffraction patterns involves using the concept based on the construction of the reciprocal lattice since the observed LEED pattern is a scaled representation of the reciprocal lattice of the surface structure. More details regarding analyzing LEED pattern with reciprocal lattice method can be found in [98].

LEED is not only a useful tool for acquiring qualitative information about the size, symmetry and rotational alignment of the adsorbate unit cell with respect to the substrate by analyzing the spot positions, but it is also a powerful technique to obtain quantitative information on atomic positions by studying the I-V curves, which are the intensities of the various diffracted beams as a function of the incident electron beam energy. In our studies, LEED was used to interpret the structures of single crystals and thin films grown on single crystals. All LEED patterns were taken from the backside view using a set of Perkin-Elmer LEED optics.

2.3 Experimental Preparation

Deposition of Metals

Metal deposition was achieved by evaporating the target metal from a heated doser, which is a target metal wire of high purity wrapped around a resistively-heated tantalum or tungsten wire. Extensive outgassing of all dosers was performed prior to use. The pressure during evaporation was lower than 5×10^{-10} Torr. The deposition amount is defined in terms of monolayer equivalents (ML) where 1 ML corresponds to the number density of metal atoms in the substrate surface, which is quantified using the Auger break point method. In this method, a plot of the ratio of the AES peaks of the deposited metal and the substrate is recorded as a function of deposition time. If the deposited metal follows a layer-by-layer growth mode on the substrate, a break occurs in the plot at the onset of the second overlayer. The flux rate of the doser can also be calculated based on the information obtained from the break point plot. The deposition amount is further verified by STM measurements.

Graphene/Ru(0001) Preparation

In the studies of model catalysts and catalytic reactions, graphene/Ru(0001) is an important supporting material for metal clusters. The Ru(0001) substrate was cleaned using a standard approach, which includes cycles of Ar ion sputtering, annealing in 1.0×10^{-7} Torr of O_2 at ~1100 K, and flashing to 1800 K in vacuum. The surface cleanness was confirmed by AES and STM. Single-layer graphene was formed by first dissociating methane (at 700 K) or ethylene (at 300 K) or propylene (at 300 K) on the clean Ru(0001)

with a pressure of 1×10^{-7} Torr, followed by annealing the sample to 1300 K, and then slowly cooling down to room temperature. Due to the chemical inertness of methane, a slightly higher dissociation temperature (at 700 K) and relatively longer exposures are generally required compared to ethylene and propylene [109]. This process can be repeated several times to generate graphene that fully covers the Ru substrate. Graphene formation is generally easy to control due to the self-limitation of the process, however, occasionally large carbon particles form due to the defects of the substrate. The quality of graphene was characterized by AES, LEED, and STM. It is worth pointing out that monolayer graphene on Ru(0001) was first prepared and imaged with STM by our group in 1994 [109].

Graphene/Ru(0001) Modifications

In order to study the substrate effect of graphene, we also modified corrugations as well as electronic structures of the graphene systems. Three modified graphene systems were investigated: 1) graphene/transition metal (TM)/Ru(0001) system, where graphene is prepared on a pseudomorphic single layer of TM, including Co, Pd, Au, and Ni; 2) graphene/O/Ru(0001) system, where oxygen atoms are intercalated between graphene and Ru(0001) substrate; and 3) carbon-rich graphene system, where a layer of amorphous carbon is formed at the interface between graphene and Ru(0001).

Graphene/TM/Ru(0001) was prepared in two steps. First, certain amount of target TM was deposited on Ru(0001) followed by high temperature annealing, where a pseudomorphic single layer was formed on Ru/(0001), as called TM/Ru(0001). Second,

exposing TM/Ru(0001) to propylene or ethylene with a pressure of 1×10^{-7} Torr at room temperature, followed by annealing the sample to 1100 K for 10 min and subsequently cooling it down to room temperature. This process can be repeated several times to generate graphene that fully covers the surface. The quality of graphene was characterized by AES, LEED, and STM.

Graphene/O/Ru(0001) was prepared by making a single layer graphene on Ru(0001) followed by oxidizing the graphene/Ru(0001) surface by heating the sample to ~700 K in 1×10^{-7} Torr of oxygen for 10 min, leading to the formation of Ru-(2 × 1)-O surface structure beneath graphene. The intercalation of O_2 decouples the graphene from the Ru(0001) substrate.

Carbon-rich graphene was prepared by making regular graphene/Ru(0001) first. Then the sample was transferred to the high pressure cell and exposed to atmosphere for about 5 min. Then the sample was transferred back to the main chamber and annealed in vacuum to 500 K for 30 min to remove any adsorbed contaminations. LEED and STM showed the typical structure of graphene, while AES indicated a large accumulation of carbon on the surface.

h-BN Nanomesh Preparation

In addition to the graphene systems, we also investigated the hexagonal boron nitride (h-BN) nanomesh grown on Ru(0001), which is an isoelectronic system to graphene. h-BN nanomesh was prepared on a clean Ru(0001) surface. The sample was first annealed to 800 K in vacuum followed by exposing to 5×10^{-7} Torr borazine for 5

min. Then borazine was pumped out while the sample was still kept at 800 K for another 3 min. In practice, we found a lower pressure and higher temperature would lead to a high quality h-BN film. The annealing temperature should be precisely controlled because the nanomesh film starts to decompose as the temperature exceeds 1200 K. The quality of h-BN film was checked by AES, LEED and STM.

Ultra-thin Silica Film Preparation

The ultra-thin silica film was fabricated on Mo(112). First, the Mo(112) sample was cleaned by repeated cycles of sputtering by Ar^+ and oxidation at 1200 K followed by flashing to 2200 K. AES and LEED were used to check the cleanliness and structure of the sample surface. Then the sample was exposed to 5×10^{-8} Torr O_2 at 850 K for approximately 10 min. The amount of O_2 was checked by AES and a sharp p(2 × 3)-O surface could be observed by LEED. To prepare the ultra-thin silica film, less than 1 ML Si was evaporated onto the Mo(112)-p(2 × 3)-O surface from a Si doser in UHV at room temperature followed by annealing to 800 K in 5×10^{-8} Torr O_2 for 5 min. Then the temperature was increased to 1250 K for an additional 5 min. The above Si deposition/ oxidation/annealing procedure was repeated several times until a constant Si/Mo AES ratio was achieved. The silica film was then annealed in UHV at 1250 K for 5 min to remove the multi-layer silica. The growth of silica film by this method is self-limited and the constant Si/Mo AES ratio indicates approximately 1 ML of silica film, and is therefore called an ultra-thin silica film. Note the annealing temperature is the most critical factor to prepare the high quality silica film. In practice, we found that if the

annealing temperature is lower than 1250 K, SiO_x islands and clusters are formed on the terrace due to the insufficient surface diffusion and desorption. On the other hand, if the annealing temperature is higher than 1250 K, the ultra-thin silica film starts to decompose and forms an amorphous SiO_2 layer on the surface, which completely disappears at annealing temp eratures above 1400 K. The structure of such prepared silica film was examined by LEED and STM.

Tip Preparation

Since the invention of STM, scientists have paid extensive attention to making atomically sharp tips for acquiring high resolution STM images. To prepare an ideal tip, it is necessary to choose the correct tip material and adopt the proper preparation techniques [110-119].

Tip can be made from different metals and alloys, such as W, Au, Ag, Pt, Pt-Ir, Pt-Rh, etc. Usually transition metals are chosen to ensure continuous electron density of states near the Fermi level. W tips are most often used for UHV STM measurements because they are hard and convenient to fabricate. The hardness of W tips makes them highly resistant to accidental tip crashes. However, W tips are not chemically stable under high pressure conditions since they are oxidized by high pressure O_2. Under high pressures, especially in the presence of reactant gases, the chemical and thermal stability of the tip is of great importance. Tips made from inert metals, such as Au and Pt-Ir tips, are widely used for tunneling in such conditions due to their resistance to corrosion.

Methods for preparing atomically sharp STM tips are also of primary importance

in STM studies and the quality of STM images often highly depends on the shape of the tip. Mechanical cutting and electrochemical etching are two common methods adopted by various STM groups. Cutting is a simple and quick way to make tips, especially effective for Pt-Ir tips. A pair of scissors or a wire cutter is sufficient. However, tips prepared by this method suffer from many problems such as poor reproducibility, lack of apex symmetry, large cone angel, and multiple tips [111,120]. In contrast, electrochemical etching method is more complicated and time-consuming but yields more reliable tips [121]. Wires with diameters of 0.05-0.025 mm are frequently used for tip fabrication. The electrochemical solution used for etching tip varies with different tip metals. For example, W tips are frequently etched by 1.0 ~ 2.0 M aqueous KOH or NaOH solution. And Pt-Ir tips are often etched by a mixture of 3.0 M NaCN and 1.0 M NaOH.

In our studies, tips are prepared by a homemade etching device, as schematically shown in Fig. 8, where the positive and negative electrodes are the metal wire to be etched and the Pt loop, respectively. The electrolyte is the electrochemical solution membrane on the Pt loop. Prior to etching, the Pt loop is dipped into the electrolyte and a membrane is formed on the loop due to the solution surface tension. Then the metal wire is inserted into the membrane, where a small electrochemical cell system is constructed. Either a DC voltage (~4 volts) or an AC voltage (~10 volts) can be applied to the system. The etching process proceeds until the metal wire breaks at the etching point or the membrane breaks. If the membrane breaks, dip the Pt wire loop into the etching solution and the above procedure is repeated. If the metal wire breaks, two tips are obtained: one

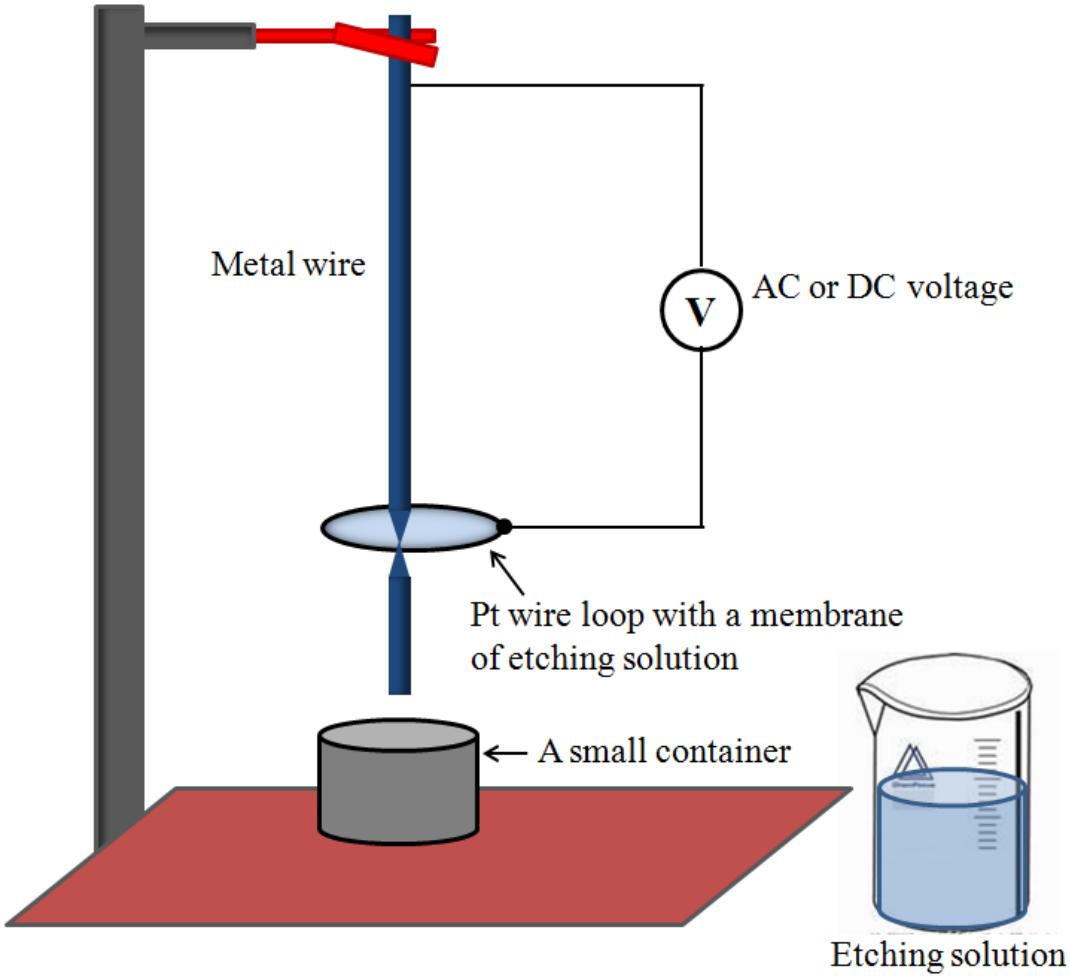

Fig. 8 A drawing of the tip etching setup. The tip is hold by a manipulator which allows for precisely positioning the tip. The small container underneath is used to hold the lower part of the wire after the wire breaks at the etching point.

from the upper part and the other from the lower part. In practice, we found tip from the upper part is better if prepared by AC voltage, whereas tip from the lower part is superior if etched by DC voltage.

Tips prepared by the above etching method usually have thick oxide layers on the top, which should be removed before they are put in the vacuum chamber because such insulating oxide layers prevent tunneling. Otherwise tip easily crashes on the sample during scanning. To eliminate oxide layers, the tip is rinsed by deionized water for several times and then rinsed with acetone. To further remove any contamination, tips are then degassed and annealed to 1000 K in vacuum by the tip heating device in the preparation chamber.

In situ tip regeneration during scanning is also critical to obtain atomically sharp tips. Such *in situ* tip improvement method cannot only treat tips that are not originally well prepared, but it can also rescue tips that have been deteriorated due to picking up poorly conducting materials or reacting with reactant gases. In this method, a voltage pulse from 3 volts to hundreds of volts is applied between the tip and sample when the tip is in the tunneling range. Field emission is induced, which cleans the STM tip. Therefore, *in situ* tip regeneration is especially important when scanning in the presence of high pressure reactant gases.

Temperature Calibration

The temperatures are measured by a pyrometer (OMEGA OS3700) during sample preparation and subsequent annealing studies. The emissivity varies with

different samples. Prior to use, the pyrometer is calibrated by surface temperatures read from a W-5% Re/W-26% Re thermocouple that is attached to the edge of the sample.

3. DEPOSITION OF METALS ON GRAPHENE/RU(0001)

Graphene is a fascinating material with a 2-D structure, which has extremely high hardness, high crystallographic quality, high thermal and chemical stability, and special electronic properties. These properties will undoubtedly lead to its wide applications as new materials and electronic devices in the near future [122,123]. The crystallographic quality as well as thermal and chemical stability makes graphene an attractive supporting material for metal clusters in model catalyst and catalytic reaction studies, where in principle effects caused by the supporting material can be largely eliminated.

Adsorbed graphene on TMs surfaces has been known since 1960s, when single layer graphite was observed during the preparation of Pt and Ru single crystals [124-128]. Upon annealing the crystals to high temperatures, carbon impurities are segregated from bulk to surface, leading to the formation of single layer graphite. However, the importance of graphene in such form was not realized until free-standing version of graphene was obtained in 2004, which initiated extensive research on graphene systems [122,123,129]. Epitaxial growth of graphene on TMs soon became one of the most important preparation methods, with the advantage of achieving large domains with uniform thickness compared to other methods such as mechanical exfoliation from graphite and decomposition of SiC [130-132]. Many studies have been reported regarding the epitaxial growth of graphene on various TMs, namely Ir(111) [133-136], Pt(111) [137-140], Rh(111) [141-143], Ru(0001) [144-149], Ni(111) [150-152], etc. via

methods of either chemical vapor decomposition (CVD) of carbon-containing molecules or segregation of carbon atoms from bulk.

Several studies have been reported regarding the growth of metal clusters on graphene supported on transition metals [153-155]. N'Diaye *et al.* have focused on studying metals on a moiré-patterned graphene/Ir(111) surface and have found that at the lowest coverages, Ir forms uniformly monodispersed clusters when deposited on graphene. The metal clusters so formed grow exclusively in hcp hollow regions and maintain the 2-D structure [153]. At higher coverages these clusters transform to 3-D structures yet remain largely monodispersed. Feibelman performed density functional theory (DFT) calculations to elucidate the patterning and growth of these clusters [156,157] and showed there to be $sp^2 \rightarrow sp^3$ rehybridization of C beneath clusters comprised of more than two Ir atoms. This rehybridization contributes to Ir-C bond formation as well as graphene layer chemisorption onto the Ir(111) substrate. Furthermore, other metals, namely Pt, W, Re, Fe and Au on graphene/Ir(111) have been studied by N'Diaye *et al.* who reported that Pt, W, and Re form epitaxial cluster superlattices while Fe and Au do not. Based on these results, they concluded that the metals which grow epitaxial cluster superlattices have three characteristics: (i) a large cohesive strength to form strong bonds; (ii) a large extension of a localized valence orbital to efficiently interact with graphene and thus to initiate rehydridization of carbon atoms; and (iii) a certain match with the graphene unit cell [158].

In more recent investigations, Pt cluster deposition was studied on graphene/ Ru(0001) surfaces [154,155]. Although some similar properties are observed, such as

high dispersion of metal clusters and no preferential step edge decoration, there are mainly three differences between graphene/Ru(0001) and graphene/Ir(111). For Pt clusters grown on graphene/Ru(0001), (i) the smallest 2-D clusters prefer fcc hollow regions instead of hcp sites; (ii) clusters are less uniform and epitaxial cluster superlattices cannot be fabricated at room temperature; and (iii) conversion from 2-D to 3-D of clusters occurs at much lower coverages. Owing to these differences, it is instructive to carry out studies of other metals deposited on graphene/Ru(0001). In this section, we present results of Pd, Pt, Rh, Co and Au deposition on graphene/Ru(0001) obtained with STM, aiming to elucidate the key factors that govern metal growth on graphene/Ru(0001).

3.1 Graphene/Ru(0001) Structure

A graphene layer was prepared on a Ru(0001) substrate using the method described in the experimental section. The graphene coverage on the Ru(0001) substrate can be monitored using the ratio of the positive to negative portions of the 272 eV Auger feature [159,160]. For the clean Ru(0001) surface, this ratio (*R*) is 0.80, as shown in Fig. 9(a) (black line), whereas for an essentially fully covered graphene surface, this ratio is 0.46, as shown in Fig. 9(a) (red line). STM measurements show that more than 95% of the Ru(0001) substrate is covered by graphene for a surface with an *R* of 0.46.

A typical LEED pattern, shown in the inset of Fig. 9(b), presents evidence for the formation of a coherent, graphene overlayer, noting the sharp, satellite spots surrounding the (1 × 1) spots of the Ru(0001) substrate. The ratio of the distance between Ru(0001)

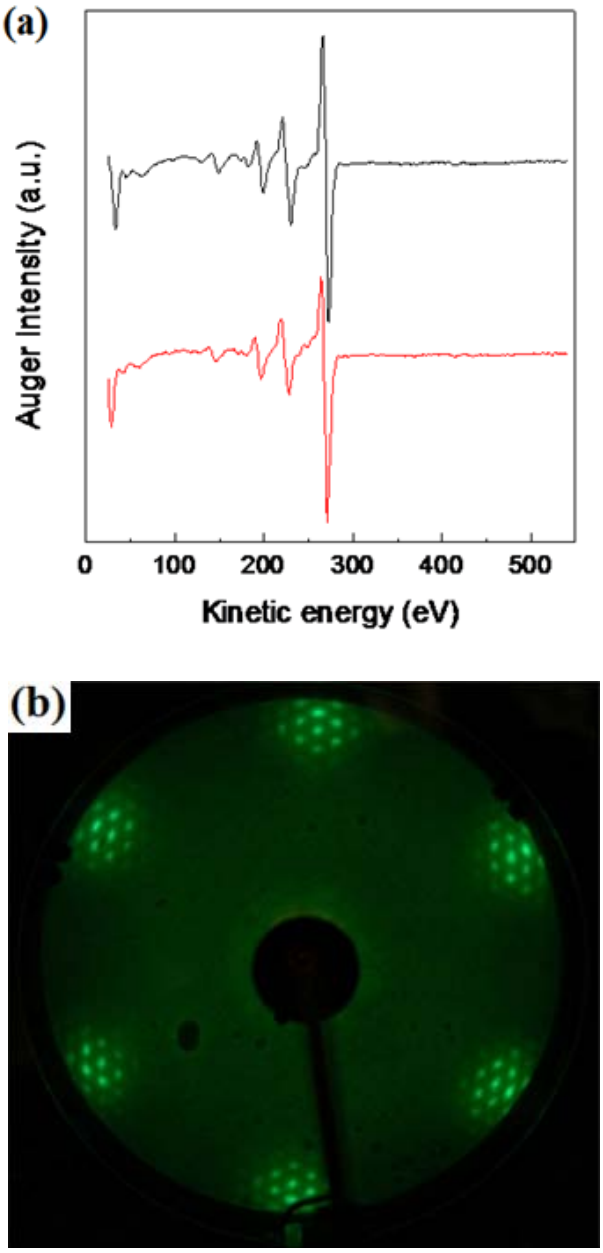

Fig. 9 (a) AES of a clean Ru(0001) surface (black line) and Ru(0001) surface fully covered with single-layer graphene (red line). (b) LEED pattern of graphene/Ru(0001) surface taken at an electron energy of 71 eV.

Note: This figure is reprinted with permission from "The 2-D growth of gold on single-layer graphene/Ru(0001): Enhancement of CO adsorption" by L. Liu, Z. Zhou, Q. Guo, Z. Yan, Y. Yao, D. W. Goodman, Surface Science, 605 (2011) L47–L50. Copyright 2011 Elsevier B.V.

diffraction spots to that between graphene moiré satellite spots is approximately 11, in agreement with previously published data [109,160].

Fig. 10(a) and (b) display typical STM topographic images of the graphene moiré template. As indicated by the marked moiré unit cell, three different sites, i.e., bright, medium dark and dark sites, are observed. An atomic model of the surface structure is displayed in Fig. 11(a) using one graphene layer over two Ru layers. Three different sites with different patterns are found. Fig. 11(b) shows a unit cell of moiré pattern, where a (12 × 12) unit cell of graphene is on top of a (11 × 11) unit cell of two layers of Ru. The bright, medium dark and dark regions are assigned to atop, fcc and hcp sites, respectively [161]. Note that this model is an approximation and the real commensurate superstructure is even more complex [162].

3.2 Nucleation and Growth of Pt, Rh, Pd and Co Metal Clusters

Morphologies of Metal Clusters

Four catalytically important metals, namely Rh, Pt, Pd, and Co were used in this study. As shown in Fig. 12, templated growth of Rh clusters is observed at a coverage of 0.05 ML where the majority of the clusters are found to occupy the fcc sites of the moiré structure. A closer examination of the image reveals that even at such a low coverage, the cluster growth has deviated substantially from monodispersity. The dashed circles mark the selected clusters and the numbers indicate the approximate layers of the clusters. This is verified by the height profiles of each cluster, in which cluster 1, 2, 3, 4 are shown to be of height 0.3, 0.6, 0.9 and 1.2 nm, respectively. Clearly clusters from

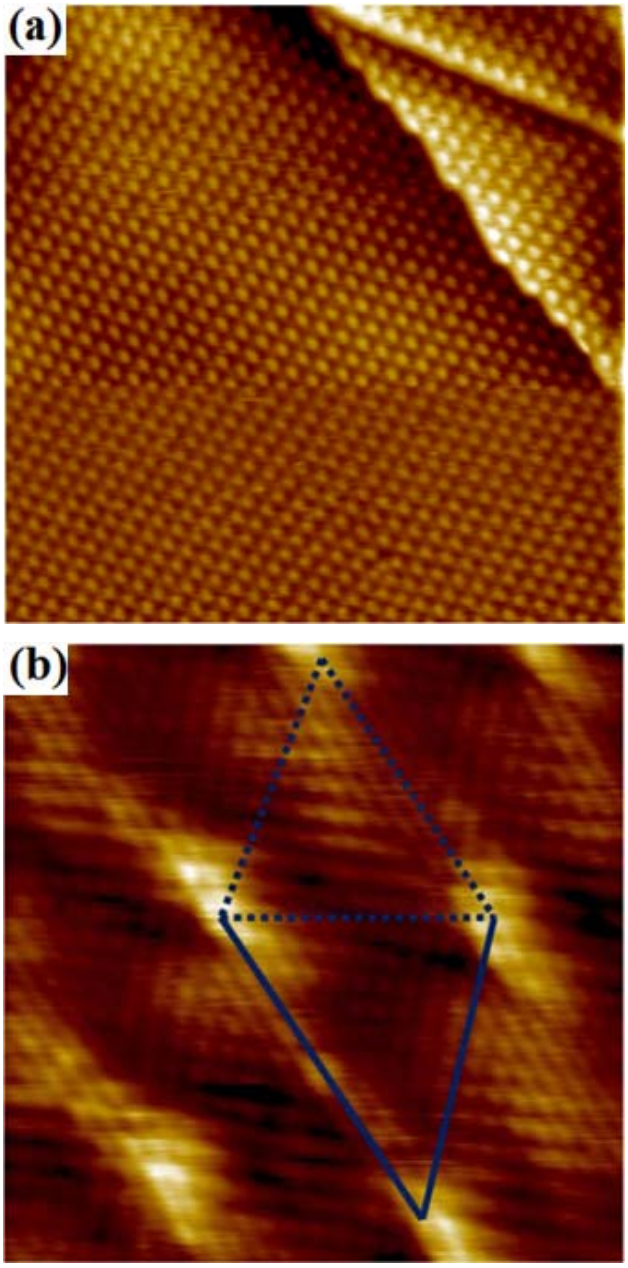

Fig. 10 (a) A typical STM image (100 nm × 100 nm, V_b = 1 V, I_t = 0.2 nA) of the graphene/Ru(0001) moiré structure and a typical LEED pattern (as an inset). (b) A close up STM image (6 nm × 6 nm, V_b = -0.3 V, I_t = 1.0 nA) of the graphene/Ru(0001) moiré structure. The highlighted unit cell is shown, in which the atop sites are the bright spots, and fcc and hcp sites are marked by the dotted and solid lines, respectively.

Note: This figure is reprinted with permission from "Deposition of metal clusters on single-layer graphene/Ru(0001): Factors that govern cluster growth" by Z. Zhou, F. Gao, D. W. Goodman, Surface Science, 604 (2010) L31–L38.

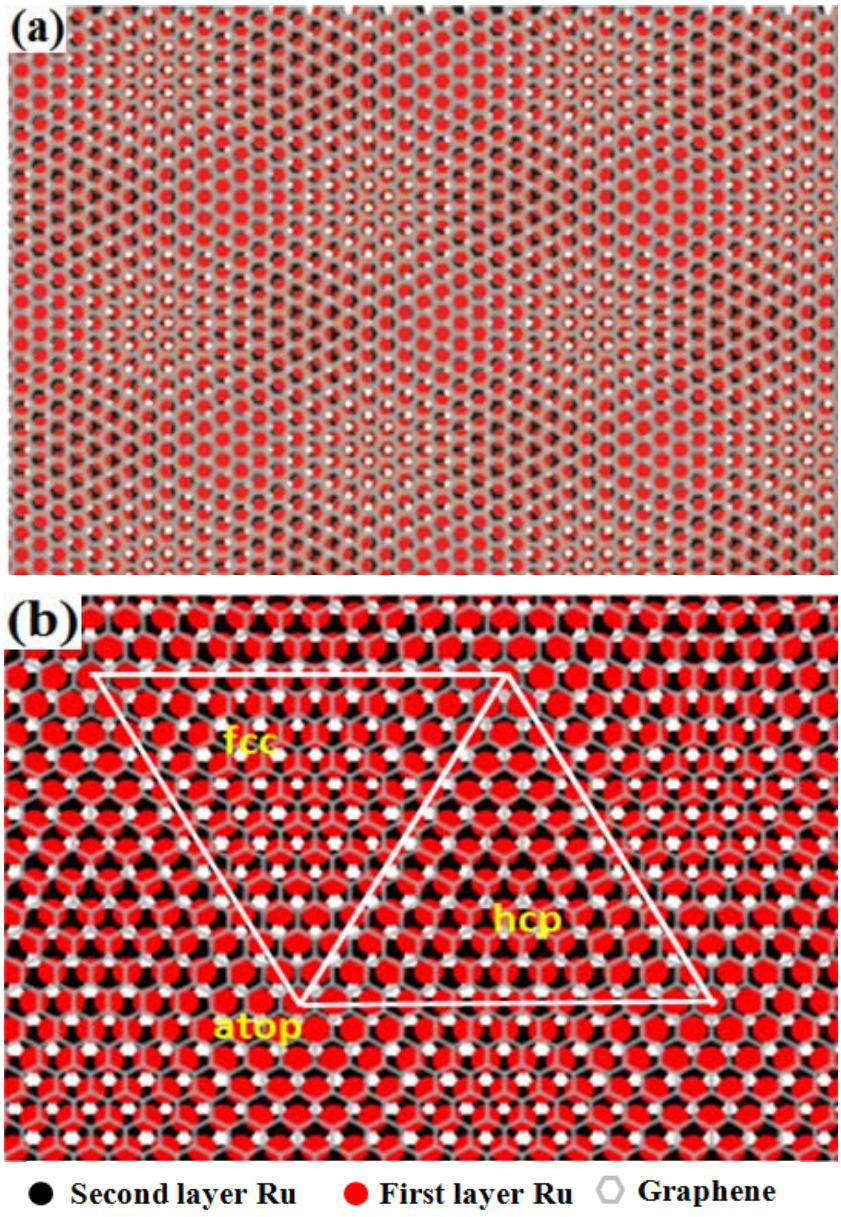

Fig. 11 Atomic models of the graphene moiré structure. (a) Large scale with multiple unit cells. (b) A unit cell where three different sites (atop, fcc hollow, and hcp hollow) are marked.

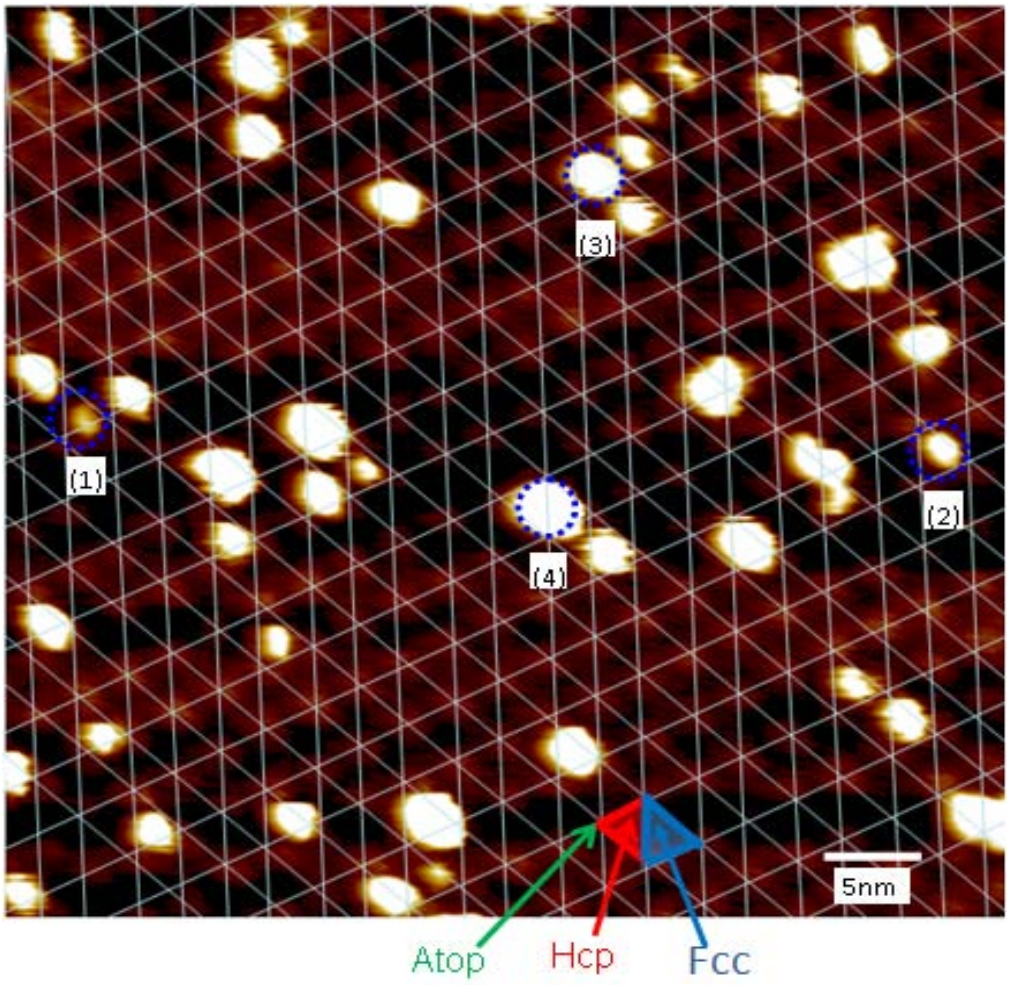

Fig. 12 The STM image (50 nm × 50 nm, V_b = -0.6 V, I_t = 0.1 nA) of 0.05 ML Rh deposited on graphene/Ru(0001) at room temperature. The marked unit cell where three different sites are highlighted with different colors and arrows is also shown. White lines are added to indicate unit cells and help locate the positions of those clusters. Note that certain clusters are marked with dashed circles and numbered (see text).

---

one to four layers coexist and most of the clusters grow in the 3-D mode.

Fig. 13 depicts STM images acquired at various Rh coverages from 0.05 to 0.80 ML, and the size histograms are shown in Fig. 14 based on randomly chosen 100 nm × 100 nm STM images at every coverage, indicating that Rh on graphene/Ru(0001) grows with a narrow size distribution in a self-limiting manner. Fig. 15 is a plot of the density (upper panel) and average dimension (middle and bottom panels) of the Rh clusters as a function of coverage. It is obvious that at later stages of cluster growth, cluster size and height increase steadily, whereas cluster density only increases slightly. Identical experiments were also conducted with Pt. The behavior of Pt is very similar to Rh where highly dispersed Pt clusters with a diameter of ~2 nm prefer fcc sites at low coverages (< 0.1 ML) and clusters (diameter < ~5 nm) with rather narrow size distribution are observed at coverages less than ~1 ML (data not shown). Note that this is fully consistent with recent studies by other groups on this system [154,155].

Figs. 16(a) and (b) are STM images of 0.10 and 0.40 ML Pd deposited on graphene/Ru(0001). Although Pd also prefers fcc sites at extremely low coverages (data not shown), large clusters develop at the very early stages of growth. For example, average cluster diameters of ~8 and ~14 nm are found at Pd coverages of 0.10 and 0.40 ML, respectively. Compared with Rh or Pt clusters at the same coverages, Pd clusters are substantially larger in size with a much lower number density. Figs. 16(c) and (d) display images of 0.20 and 0.40 ML of Co on graphene/Ru(0001). Clearly Co also forms 3-D clusters at the very early stages of growth, and averaged cluster sizes of ~10 and ~12 nm are observed at coverages of 0.20 and 0.40 ML, respectively.

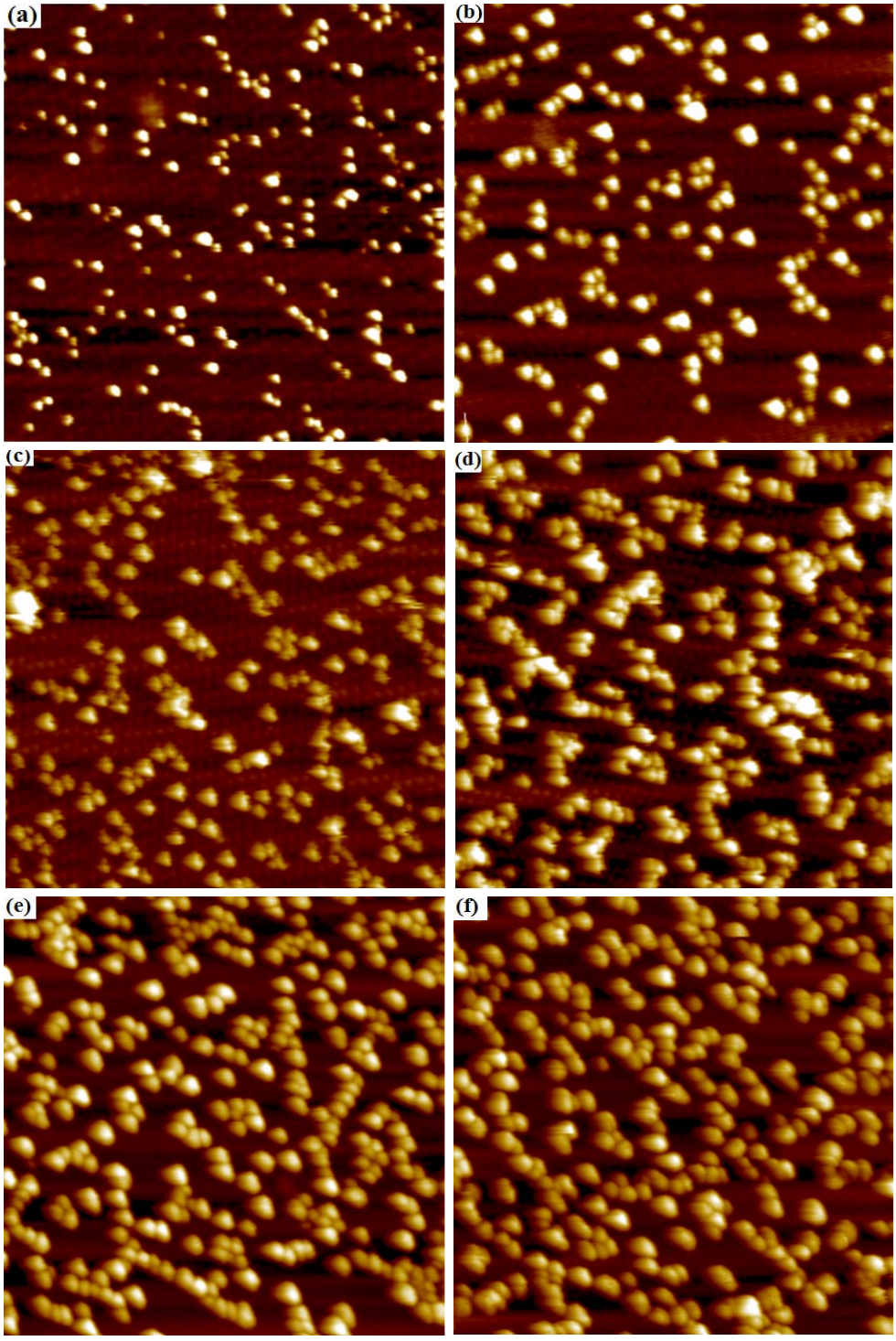

Fig. 13 STM images (100 nm × 100 nm, V_b = 1.0 V, I_t = 0.1 nA) of (a) 0.05 ML, (b) 0.10 ML, (c) 0.20 ML, (d) 0.40 ML, (e) 0.60 ML and (f) 0.80 ML Rh deposited on graphene/ Ru(0001) at room temperature.

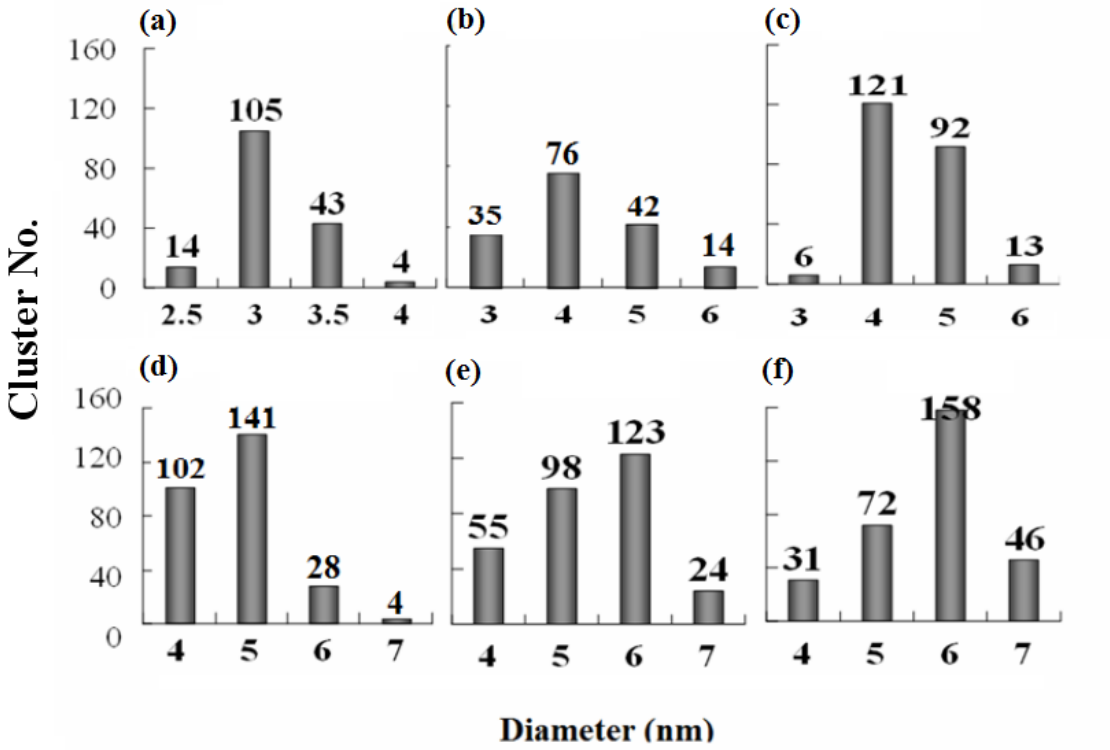

Fig. 14 Histograms of the number of particles as a function of their diameter in a typical 100 × 100 nm STM image randomly chosen at each coverage: (a) 0.05 ML, (b) 0.10 ML, (c) 0.20 ML, (d) 0.40 ML, (e) 0.60 ML and (f) 0.80 ML Rh.

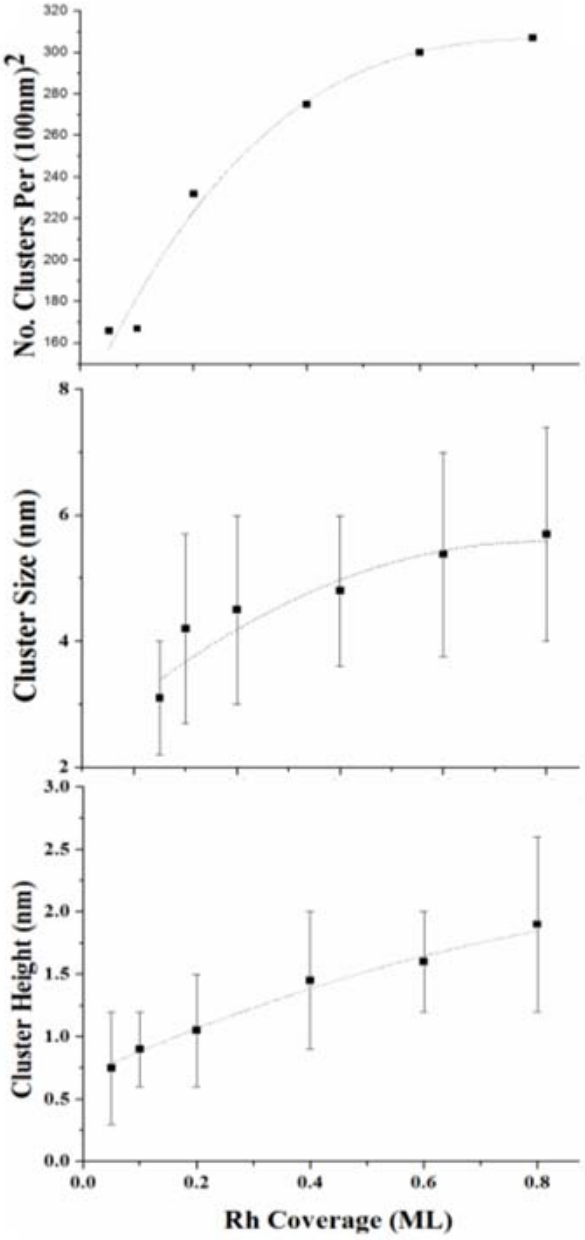

Fig. 15 Rh cluster height (bottom panel), Rh cluster size (middle panel) and number density (upper panel) as a function of coverage. The bars in the middle and bottom panel indicate the size and height of the largest and smallest clusters in the STM images.

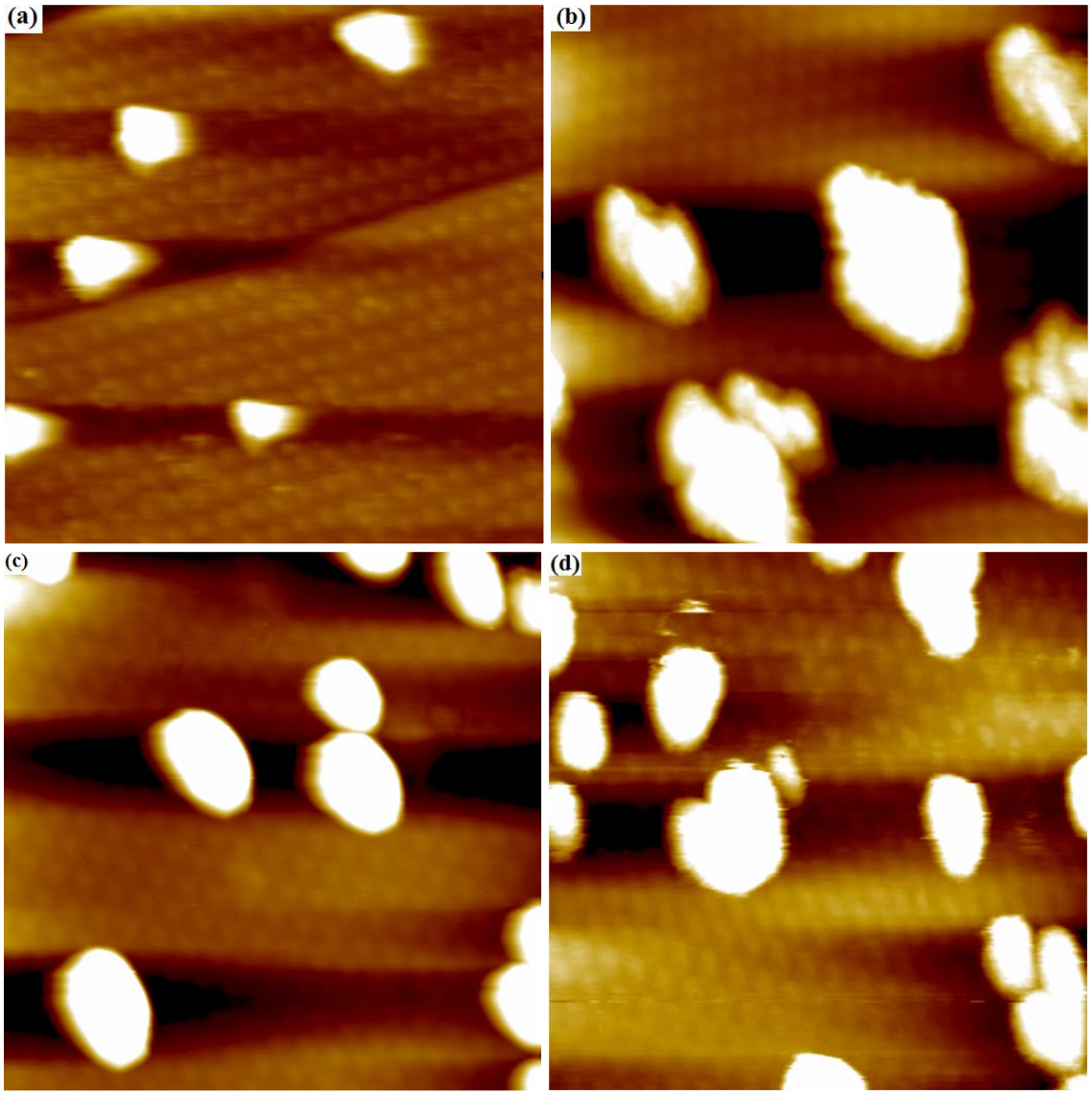

Fig. 16 STM images (50 nm × 50 nm, V_b = 1.0 V, I_t = 0.1 nA) of (a) 0.10 ML Pd, (b) 0.40 ML Pd, (c) 0.20 ML Co, (d) 0.40 ML Co supported on graphene/Ru(0001).

Growth Mechanism of Metal Clusters

The surface free energy of graphene is reported to be 46.7 mJ/m^2 [163], which is significantly smaller than those of deposited metal particles, e.g. 2.05 J/m^2 for Pd [164]. This suggests that all deposited metals should form 3-D clusters at temperatures where metal atoms have sufficient mobility (for example at room temperature), were there not strong interaction between the metal atoms and the graphene substrate. Indeed N'Diaye and coworkers have observed significant 3-D clusters of Ir graphene/Ir(111) at relatively high metal coverage; however, up to an Ir coverage of ~0.2 ML, monodispersed 2-D clusters are stable at room temperature with the clusters located at hollow sites of the moiré unit cell [154]. This extra stabilization has been suggested to be due to $sp^2 \rightarrow sp^3$ rehybridization of C in the graphene layer beneath the overlayer metal and formation of M-C bond [158,165]. Following this mechanism, we can attribute the difference among the metals on graphene/Ru(0001) to the different strengths of the M-C bond, which, in turn, determine the diffusion coefficients. The stronger the M-C bond, the smaller the diffusion coefficient for the metal on graphene at a given flux. In other words, a smaller coefficient means a larger nucleation rate, thus facilitating better dispersion of the 2-D clusters (seeds) at the initial growth stage. Table 1 displays M-C bond dissociation energies that are relevant to the current study. As expected, the metals with higher M-C bond dissociation energies, i.e. Ir, Pt, and Rh, form highly dispersed clusters whereas Pd and Co, with weaker M-C bonds form large 3-D clusters with low number densities. Note the degree of dispersion also follows the order of M-C bond strength.

With increasing coverage, the cluster growth becomes a competitive process

Table 1 Metal-Carbon bond Dissociation Energies [166,167]

Metal	D(M-C), kJ/mol
Ir	631
Pt	610
Rh	580
Pd	436
Co	347

between adsorption on graphene and nucleation on the initial 2-D cluster seeds. The cohesive energy is the key parameter in estimating the strength of the metallic bonds. It is expected that metals with higher cohesive energies will favor nucleation on the 2-D seeds to form 3-D clusters. However, the cohesive energy is difficult to determine since it depends on the size, shape, and structure of the nanoclusters. For nanoclusters that are not embedded in the substrate, the cohesive energy decreases with decreasing cluster size if the nanoclusters maintain a specific shape and structure, as has been shown experimentally [168] and interpreted by various models [169,170]. Therefore one cannot simply compare the cohesive energies of bulk crystals with the M-C bond strength in predicting the growth mode at high metal coverages. Nevertheless, the STM images

observed in our study can be explained by the competitive process mentioned above. In the case of Rh, for example, at the onset of deposition, the strong interaction between Rh and rehybridized carbon leads to a small diffusion coefficient of Rh in the fcc areas, thus allowing for the high dispersion of 2-D Rh seeds located at fcc sites. At an Rh coverage of 0.05 ML, the coexistence of both 2-D and 3-D clusters indicates that the Rh-C bond strength and cohesive energy are essentially equal. As the coverage increases, the increasing cohesive energy (absolute value) surpasses the Rh-C dissociation energy, resulting in the conversion of most of the Rh clusters to 3-D and some unoccupied fcc sites. This also accounts for the fact that the cluster density essentially saturates whereas the cluster size and height increase steadily with deposition at high coverages (See Fig. 15). This explanation is further supported by the fact that the cohesive energy of Rh in a bulk crystal has been estimated to be -742 kJ/mol [171]. Fig. 17(a) shows the cohesive energy of Rh nanocrystal as a function of nanocrystal size under ideal conditions based on the surface-area-difference (SAD) model [170], in which the cohesive energy is computed using

$$E_{coh} = E_b(1 - \frac{3p\alpha d_{hkl}}{D})$$

where E_b is the cohesive energy (absolute value) of the bulk crystal; p is the parameter used in determining the coherence between the nanocrystals and the matrix; α is related to the shape of nanocrystals; dhkl is the interplanar distance of (hkl); and D is the size of the nanocrystal. From STM images, most Rh nanoclusters are found to be spherical. As such, a shape factor of α = 1 for spherical nanoparticles has been chosen in our calculation. It is also well known that nanoparticles tend to adopt low index surface

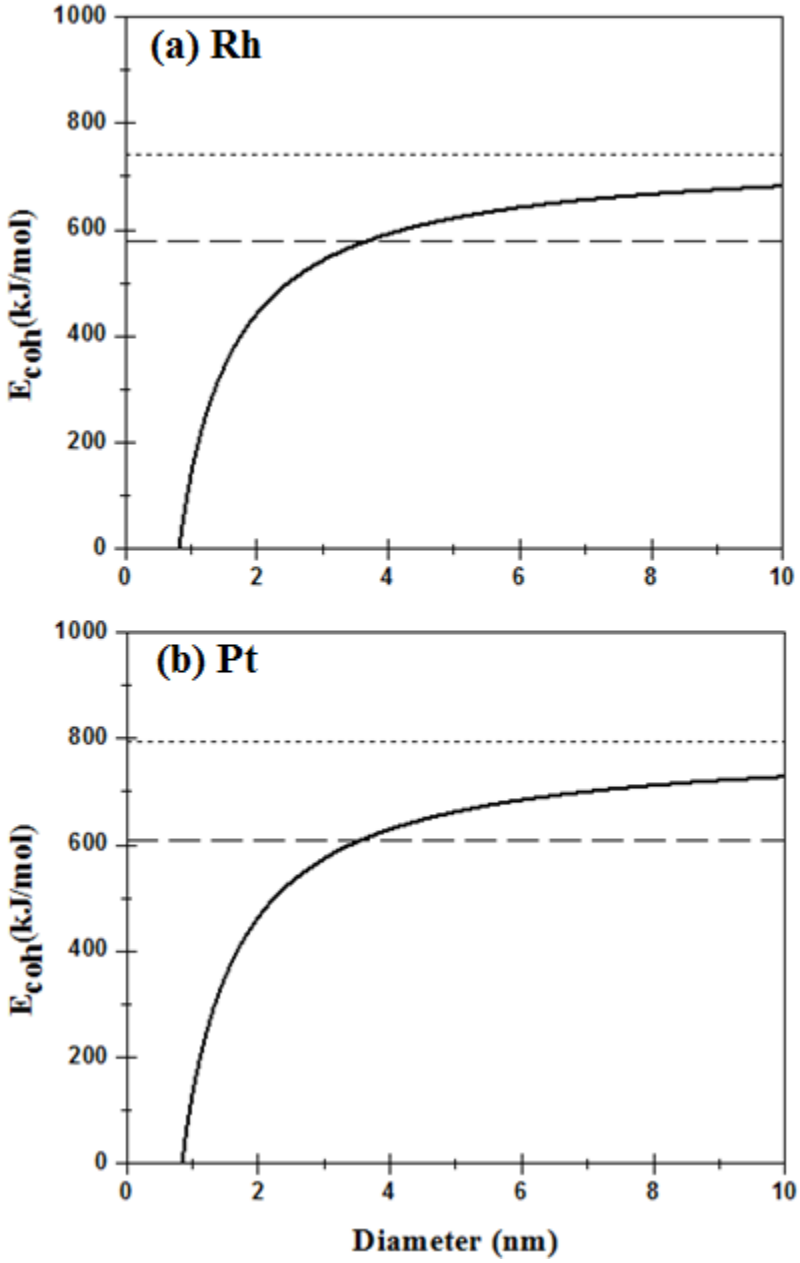

Fig. 17 Cohesive energy of Rh (a) and Pt (b) nanocrystals with free surface. The solid line is calculated by equation (1). In plot (a) p = 1, d_{100}(Rh) = 0.269 nm, E_b (Rh) = 742 kJ/mol and α = 1, and in plot (b) p = 1, d_{100}(Pt) = 0.2775 nm, E_b (Pt) = 795 kJ/mol and α = 1.The cohesive energy and M-C dissociation energy of Rh and Pt have been marked by the dotted and dashed lines, respectively.

planes to lower the total surface energy. Therefore, we assume Rh nanoparticles are surrounded by crystal planes. The results of Fig. 17(a) were obtained assuming that spherical Rh nanoparticles (α = 1) with crystal planes on the surface grow on graphene with a non-coherent interface (p = 1). From Fig. 17(a), the SAD model predicts that the conversion from 2-D to 3-D should occur at a cluster size of 3.6 nm, where the cohesive energy of the Rh nanocrystal is equal to the Rh-C dissociation energy of 580 kJ/mol. In fact, even if a shape factor of α = 1.245 (the mean value for regular polyhedral nanoparticles) is chosen [170], the plot deviates only slightly from the original line and identical trend could be obtained. In this case, crossover point will be 4.5 nm. If we consider some level of coherence interaction between Rh clusters and graphene, p will be slightly lower than 1, and the crossover point will get closer to our experimental observations (2.5 nm). The same analysis also applies to Pt as shown in Fig. 17(b), which predicts the conversion of Pt should occur at 3.5 nm. This result also agrees well with our experimental findings. The trend in Fig. 17 indicates that, for Rh and Pt, a critical point exists where the cohesive energy (absolute value) of the clusters with a certain size and shape is equal to the dissociation energy of the M-C bond. 2-D seeds form before the critical point and conversion to 3-D occurs after this critical point. To sum up, for Ir, Pt and Rh, the strong interaction between metals and rehybridized carbon plays a more important role at the initial growth stage, thus allowing for the formation of more finely dispersed small clusters. On the other hand, the Pd-C and Co-C bonds are too weak to compete with the cohesive energies, resulting in the formation of large 3-D clusters at a very early growth stage.

Effect of Substrate Metals

Based on our experimental findings and recent studies by N'Diaye *et al*. [158], we note that the behavior of the same metal, such as Pt, is not exactly the same on different substrates, e.g. graphene/Ru(0001) and graphene/Ir(111), as pointed out at the beginning of this section. We attribute this difference to different interactions between graphene and the substrate metals. Based on DFT calculations, the distance between graphene and the Ir(111) surface has been predicted to be 0.34 nm [156], which is close to the distance between graphene planes in graphite (0.334 nm), indicative of the weak electronic interaction between graphene and the Ir substrate. Whereas the distance between the graphene and the Ru(0001) surface has been estimated to be 0.145 nm, a result of the strong electronic interaction [147]. It is expected that graphene with a strong electronic interaction with the substrate should have less interaction with a deposited metal, which explains the facts that metal clusters on graphene/Ru(0001) are less ordered and that conversion from 2-D to 3-D of clusters on graphene/Ru(0001) occurs at much lower coverages. The above explanation still cannot answer the question as to why the deposited metal clusters prefer different locations, i.e. hcp sites on graphene/Ir(111) and fcc sites on graphene/Ru(0001). The difference between fcc sites and hcp sites only lies in the fact that either a threefold coordinated fcc hollow site or a threefold coordinated hcp hollow site is centered in the carbon ring (See Fig. 11(b)). Owing to this slight difference, theoretical studies such as DFT calculation should be very informative in addressing this question.

3.3 Thermal Stability of Metal Clusters

Unlike Pd, Co or Au, the metals Ir, Rh, and Pt can be nucleated at certain sites on graphene yielding clusters that are highly dispersed and with a narrow size distribution, thus allowing them to be potential candidates for nanocatalysts. In our studies, the thermal stability of Rh was carefully examined by STM. The thermal evolution of the 0.80 ML Rh clusters deposited on graphene is shown in Fig. 18. Prior to imaging, the sample was first annealed to the target temperature and maintained for 10 min before cooling to room temperature. No detectable change is obvious at an annealing temperature of 900 K or lower. Sintering initiates at ~900 K as indicated by the decreased cluster density and larger dimensions, and becomes more pronounced at 1100 K. It should be noted that these annealing temperatures are not high enough for Rh to desorb from the surface. To further test the stability of Rh under reaction conditions, the effect of cluster annealing in an atmosphere of CO was also studied. STM results (data not shown) indicate that Rh clusters maintain their original morphology even after annealing to 700 K in 1 Torr CO for 10 min.

The high thermal stability of Rh clusters can also be rationalized in terms of strong Rh-C bond formation due to $sp^2 \rightarrow sp^3$ rehybridization of carbon atoms beneath the metal atoms. It is proposed that the sintering mode for Rh on graphene is Ostwald ripening instead of migration of the whole particle for two reasons: (i) Rh clusters are fixed at fcc sites due to the formation of strong Rh-C bonds, making it difficult for a cluster to move; and (ii) from the STM images, some smaller clusters appear at 900 K, which are not observed at lower temperatures, indicating some Rh atoms dissociate from

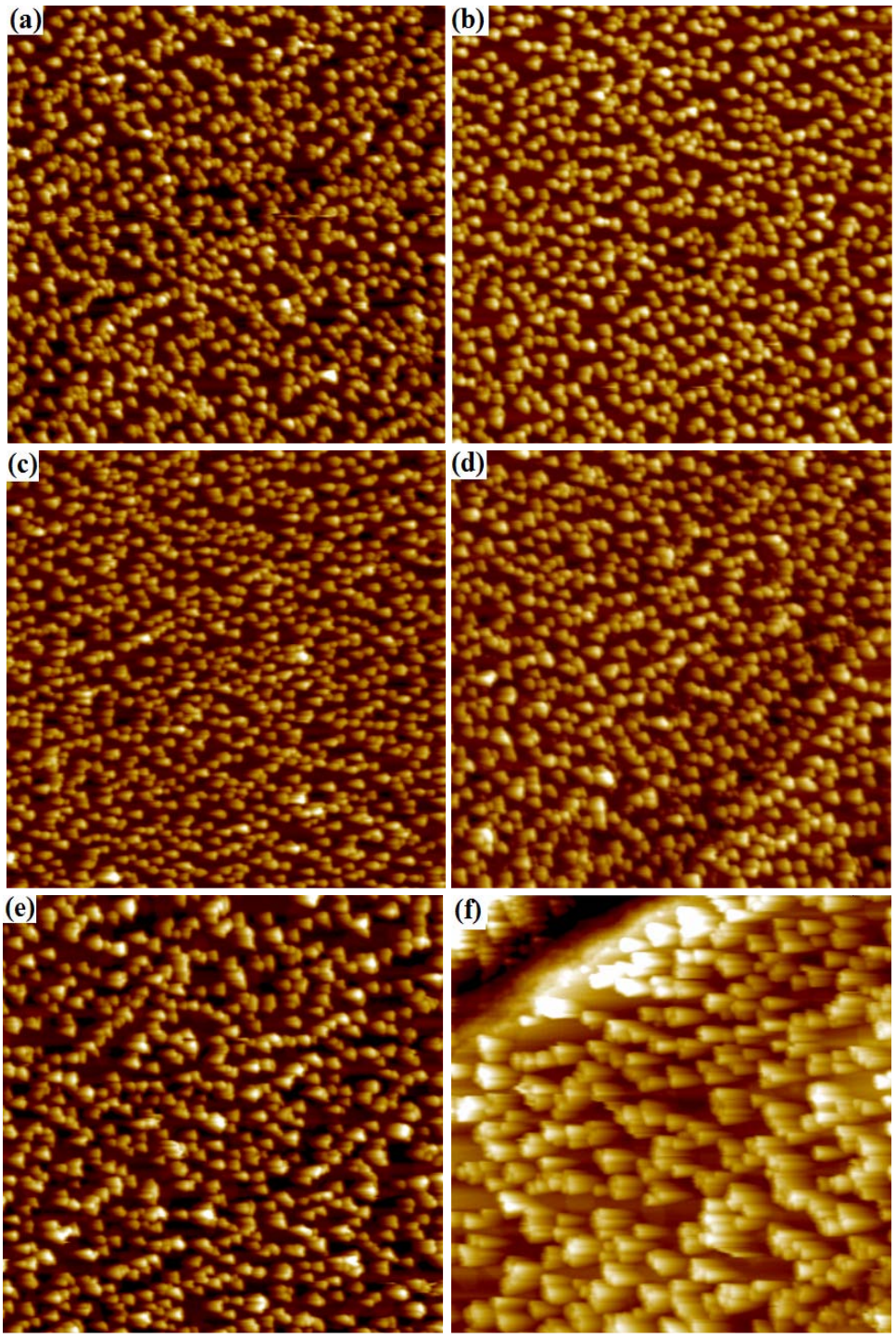

Fig. 18 STM images (200 nm × 200 nm, V_b = 1.0 V, I_t = 0.1 nA) of 0.80 ML Rh on graphene/Ru(0001) annealed to (a) 600 K, (b) 700 K, (c) 800 K, (d) 900 K, (e) 1000 K and (f) 1100 K. All images are acquired after the sample has been cooled to room temperature after a 10 min annealing.

small particles, diffuse to, and then coalesce with larger particles. For more conclusive evidence, *in situ* STM studies are required. Also, it is expected that Ir and Rh should have similar thermal stabilities due to their strong M-C bonds.

3.4 The Structure and Activity of 2-D Au Islands

The Morphology of 2-D Au Islands

Following the growth mechanism mentioned above, Au clusters should also form large 3-D clusters on graphene due to the weak interaction between Au and carbon. As expected, the formation of Au 3-D large clusters was observed by N'Diaye and coworkers on graphene/Ir(111) surface [158]. However, this is not the case for Au grown on graphene/Ru(0001). Formation of 2-D Au islands has been observed by STM, as shown in Fig. 19(a), where 0.25 ML Au was deposited on graphene/Ru(0001). At the onset of deposition, similar to the metals studied above, small 2-D Au cluster seeds are observed to reside at fcc sites (data not shown); however, with an increase in coverage, Au forms a 2-D islands with the lateral sizes on the order of a few nanometers. Interestingly, the graphene moiré structure was also observed on the 2-D Au islands which can be seen as a continuation of the graphene moiré in the lateral directions, suggesting that Au atoms align themselves with the periodicity of the graphene lattice.

The apparent height of the 2-D Au islands is 0.55 ± 0.03 nm, as shown in the red line profile across the graphene substrate and one of the Au 2-D islands (Fig. 19(b)). It was found that the apparent heights of the 2-D Au islands do not change as a function of bias voltages from -1.5 V to 1.5 V. Therefore, the measured apparent height should

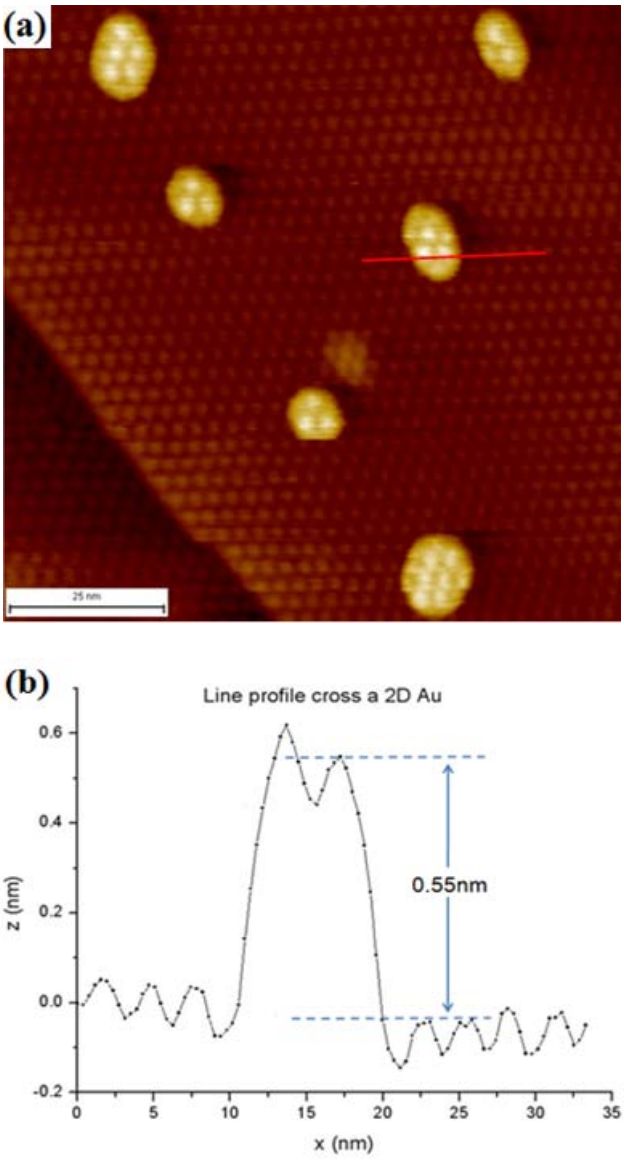

Fig. 19 (a) Room temperature UHV STM image (100 nm × 100 nm) of 2-D Au on graphene/Ru(0001) at a Au dosage of 0.25 ML. Tunneling parameters: V_b = 1.0 V, I_t = 0.1 nA. (b) Line profile along the red line in (a).

Note: This figure is reprinted with permission from "The 2-D growth of gold on single-layer graphene/Ru(0001): Enhancement of CO adsorption" by L. Liu, Z. Zhou, Q. Guo, Z. Yan, Y. Yao, D. W. Goodman, Surface Science, 605 (2011) L47–L50. Copyright 2011 Elsevier B.V.

correspond to the geometric height of the Au 2-D islands. The 2-D morphology of the Au islands is preserved for Au dosages up to 1.0 ML. Fig. 20 shows the STM images of Au 2-D islands for Au dosages of 0.50 ML and 0.75 ML. Even though the image is not as well-resolved as in Fig. 19(a) due to tip contamination by Au, the 2-D morphology of the Au islands and their conformation to graphene moiré patterns are clearly evident.

This is particularly intriguing mainly for two reasons. First, Au nanoparticles exhibit exceptional catalytic activity for a wide range of reactions, including low temperature CO oxidation, water gas shift, selective oxidation, etc [172-181]. The performance of Au catalysts is dependent on many factors [182] and one of the most important ones is the particle size. It has been observed that the size should be within nanometer range for high catalytic performance [173]. Particularly, Au particles with a bilayer structure are the most active due to their unique electronic and chemical properties compared to bulk Au [177]. Second, the catalytic performance of Au particles is intimately related to the interaction of Au with support materials because the support materials have a large influence not only on the size of Au particles, but also on their geometric and electronic structures. Graphene moiré offers a relatively inert support that is both thermally and chemically stable under moderate conditions [183-185]. Moreimportantly, it also serves as an excellent template for nanoparticles [158]. Therefore, graphene substrate may simplify the metal-support interaction and help us understand the active sites and detailed mechanism of Au catalysts.

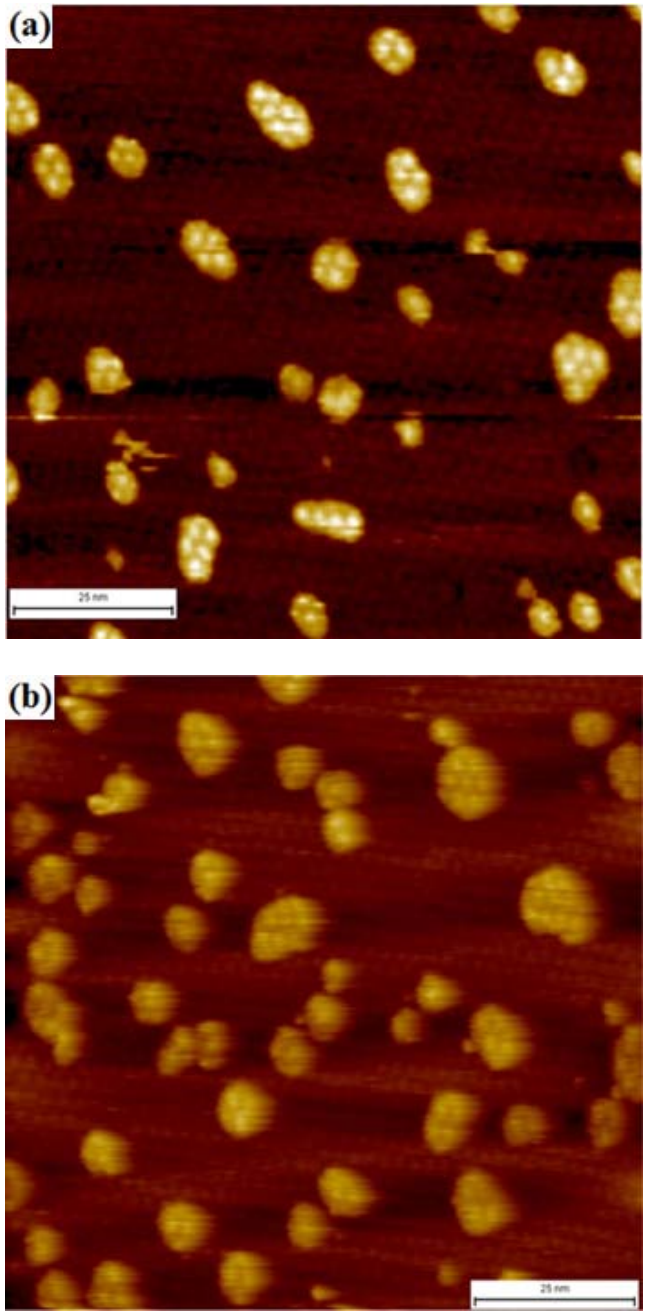

Fig. 20 Room temperature UHV STM images of (a) 0.50 ML and (b) 0.75 ML Au dosage on graphene/Ru(0001) (100nm × 100 nm, V_b = 1.0 V, I_t= 0.1 nA).

Note: Fig.20(b) is reprinted with permission from "The 2-D growth of gold on single-layer graphene/Ru(0001): Enhancement of CO adsorption" by L. Liu, Z. Zhou, Q. Guo, Z. Yan, Y. Yao, D. W. Goodman, Surface Science, 605 (2011) L47–L50. Copyright 2011 Elsevier B.V.

The Structure of 2-D Au Islands

To understand the growth mechanism of 2-D Au film on graphene/Ru(0001), different atomic models were proposed based on STM image. Furthermore, DFT calculations have been performed to assess several different Au overlayer structures. Considering the large difference between the Au-Au cohesive energies even in its low dimensional structures and the Van de Waals energy between the Au and the graphene substrate, a plausible structural model is that Au atoms are closely packed in a double-layer structure and weakly adsorb on the graphene moiré, as shown in Fig. 21, where each moiré unit cell has close-packed (11 × 11) bilayer of Au containing 242 Au atoms. The Au layers prefer to conform to the corrugation of the underlying graphene and possess a moiré pattern with a similar corrugation of 0.16 nm. In a freestanding Au bilayer, the equilibrium in-plane Au-Au distance is calculated to be 0.276 nm. The maximum height of this model is 0.70 nm, which does not agree with the observed height of the Au islands.

Another possible model without a strained Au double layer, but with more under-coordinated Au atoms per unit area, is shown in Fig. 22. Au islands have three layers. Each Au atom in the first layer sits on top of a carbon hexagon, with the neighboring carbon hexagons remaining unoccupied. Therefore, the distance between neighboring Au atoms is 0.42 nm. The Au atoms in the second and third layers sit on the threefold hollow sites formed by the underlying Au layers. The maximum height of this model is 0.59 nm, consistent with our STM measurements. It is noted that the Au-Ru binding through graphene may compensate for part of the energy loss due to the under-

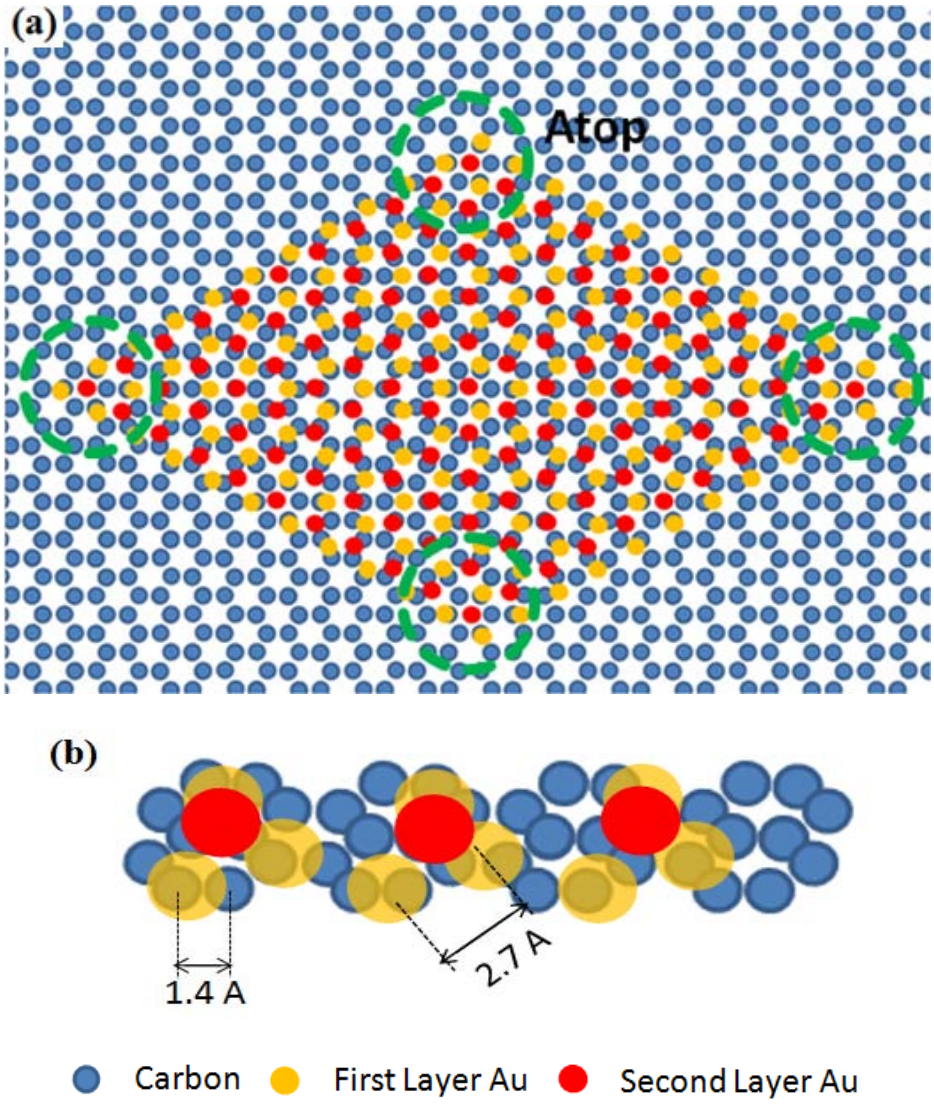

Fig. 21 A structural model for the 2-D Au islands on graphene/Ru(0001) with close-packed (11 × 11) Au bilayer. (a) top view and (b) side view.

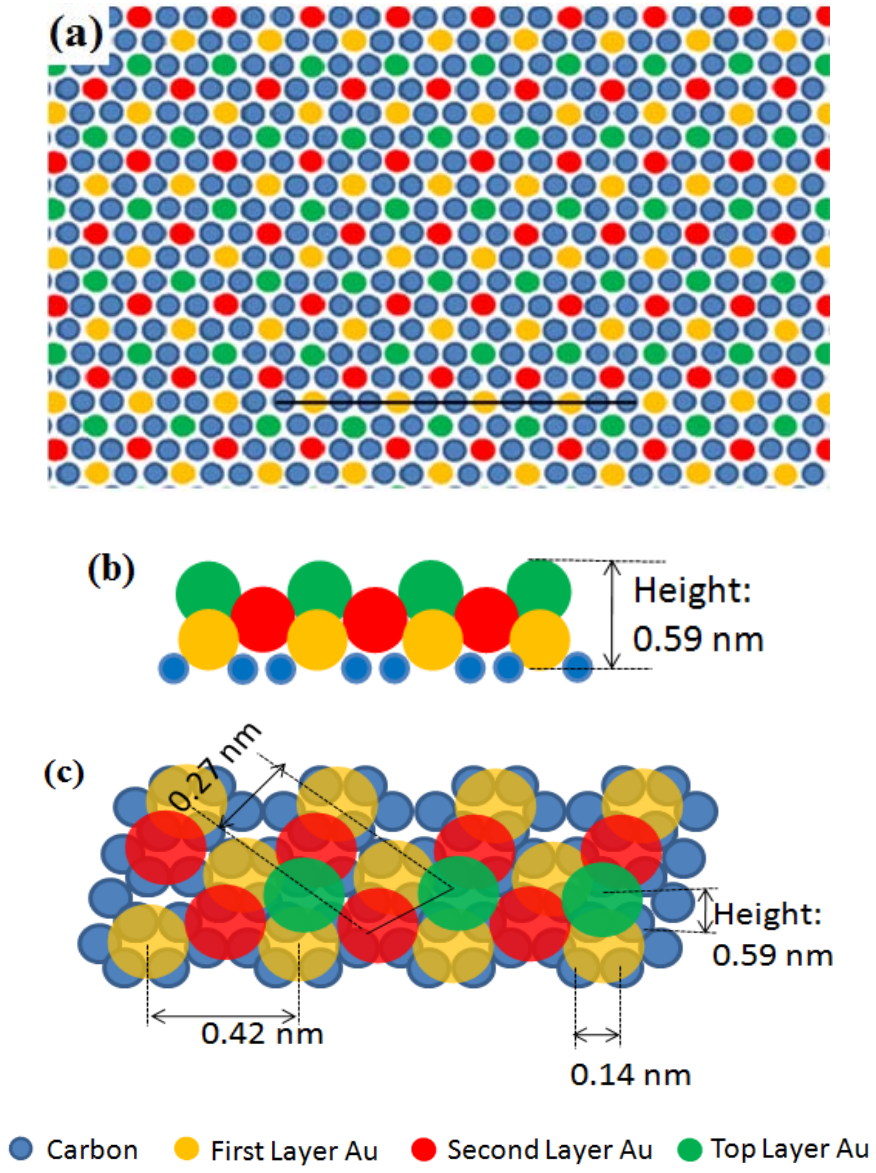

Fig. 22 A triple layers structural model for the 2-D Au islands on graphene/Ru(0001). (a) top view, (b) cross section view corresponding to the black line in (a), and (c) side view.

Note: This figure is reprinted with permission from "The 2-D growth of gold on single-layer graphene/Ru(0001): Enhancement of CO adsorption" by L. Liu, Z. Zhou, Q. Guo, Z. Yan, Y. Yao, D. W. Goodman, Surface Science, 605 (2011) L47–L50. Copyright 2011 Elsevier B.V.

coordinated Au atoms compared with the closely packed model.

DFT calculations were performed on the 2-D Au islands structure. In order to thoroughly study all possible structures, besides the above two models, another two models were also considered: a close-packed (11 × 11) monolayer of Au containing 121 Au atoms per moiré unit cell and a (12 × 12) Au monolayer with the Au atoms above the mound region significantly outward to relieve any compression of Au atoms. Detailed structures can found in [186]. The adsorption energy of each model is calculated by DFT as:

$$E_{ads} = E_{total} - E_{graphene/Ru} - nE_{Au_x}$$

where E_{total} and $E_{graphene/Ru}$ are the total energies of the overall system (including the Au structure) and graphene/Ru(0001), respectively, and E_{Au_x} is the total energy of a single Au atom in the reference state, which could be either the gas phase, bulk fcc phase, or a free monolayer/bilayer, as indicated by g, s and L, respectively. The calculated results are shown in Table 2.

It is instructive to compare the energy of a single Au atom in each model to an isolated Au adatom adsorbed on graphene/Ru(0001). The E_{ads} for the Au adatom has been calculated to be -1.41 eV, consistent with previous results [187]. Note this result is also close to the adsorption energy of an Au adatom on rutile TiO_2 (110) [188] or TiO_x/Mo(112) [189]. The calculated E_{ads} for the Au structures in all four models is noticeably more negative than that of the Au adatom, which is attributed to the formation of strong Au-Au bonds that out-competes bonding with the surface. Among these four models, smooth, the close-packed (11 × 11) Au monolayer and bilayer are more stable

Table 2 E_{ads} (in eV, per Au atom) and maximum height (in nm) of different Au models on graphene/Ru(0001), and total Bader charge of Au structures normalized by unit cell area (in e^{-}/nm^{2})*.

Model	$Au_{(g)}$	$Au_{(s)}$	$Au_{(L)}$	Max. Height	Bader charge
(11 × 11) Au Monolayer	-2.76	+0.23	-0.08	0.40	-0.17
(11 × 11) Au Bilayer	-2.77	+0.22	-0.04	0.70	-0.35
(12 × 12) Au monolayer	-2.68	+0.31	_	0.68	-0.40
Au trilayer	-2.66	+0.33	_	0.59	-0.35
Au adatom	-1.41	+1.58	_	0.22	_

* $Au_{(g)}$, $Au_{(s)}$, and Au_{L} refer to an Au atom in the gas-phase, in the bulk fcc phase, and in a free Au monolayer/bilayer.

Note: Table 2 is reprinted with permission from "Exploring the structure and chemical activity of 2-D gold islands on graphene moiré/Ru(0001)" by Y. Xu, L. Semidey-Flecha,L. Liu, Z. Zhou and D. W. Goodman, Faraday Discuss., 2011, 152, 267–276. Copyright The Royal Society of Chemistry 2011.

but do not agree with the height of the 2-D Au islands observed by STM. The textured triple layers structure does exhibit a maximum height that agrees well with the observed height of the Au islands but is less stable than the close-packed structures. Note that all four models examined are metastable compared with bulk Au structure.

The Activity of 2-D Au Islands

The adsorption of CO was studied with PM-IRAS and high resolution electron energy loss spectroscopy (HREELS) at 85 K; as shown in Fig. 23. In Fig. 23(a), for the graphene/Ru(0001) surface, due to the fact that CO adsorbs on clean Ru(0001) [190], the absence of the CO stretching feature at ~2060 cm^{-1} confirmed that the Ru(0001) substrate was fully covered by graphene. For 0.50 ML Au on graphene, a CO stretching feature at 2095 cm^{-1} was observed. The HREELS data (see Fig. 23(b)) are consistent with the PM-IRAS results, showing a CO peak at ~2097 cm^{-1} for 0.80 ML of Au on graphene.

The thermal stability of CO adsorbed on 2-D Au islands on graphene/Ru(0001) was studied by monitoring the intensity of the CO stretching feature as a function of the sample temperature. HREELS data, as shown in Fig. 24(a), display that the CO peak gradually decreased as the sample temperature was increased stepwise from 80 K to 130 K. Based on the rate of the intensity decrease, the estimated CO adsorption energy on these 2-D Au is 30 ~ 40 kJ/mole [191].

Numerous studies have shown that the effective charge of Au strongly affects the bonding of CO and consequently the C-O vibrational frequency, as shown in Fig. 25.

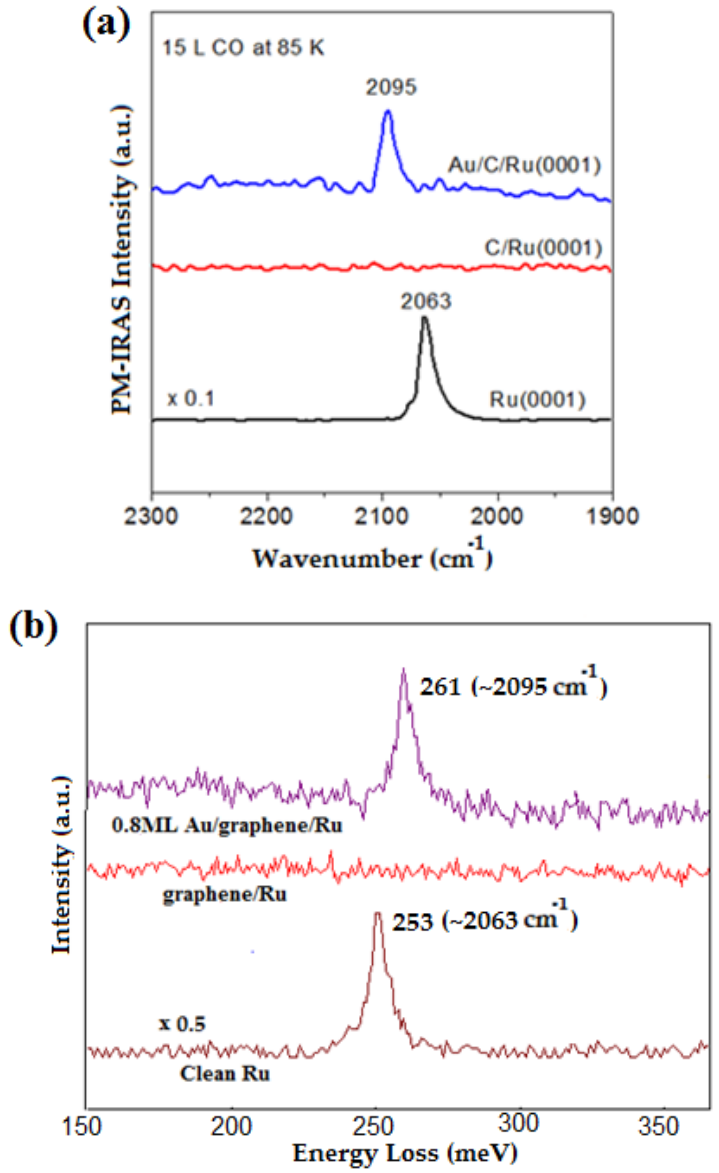

Fig. 23 (a) PM-IRAS spectra acquired at 85 K on Ru(0001), graphene/Ru(0001), and 0.50 ML Au/graphene/Ru(0001) after a CO exposure of 15 L. (b) HREELS spectra acquired on Ru(0001), graphene/Ru(0001), and 0.80 ML Au/graphene/Ru(0001) under the same conditions as (a).

Note: Figures 23(a), 24(b) and 25 are reprinted with permission from "The 2-D growth of gold on single-layer graphene/Ru(0001): Enhancement of CO adsorption" by L. Liu, Z. Zhou, Q. Guo, Z. Yan, Y. Yao, D. W. Goodman, Surface Science, 605 (2011) L47–L50. Copyright 2011 Elsevier B.V.

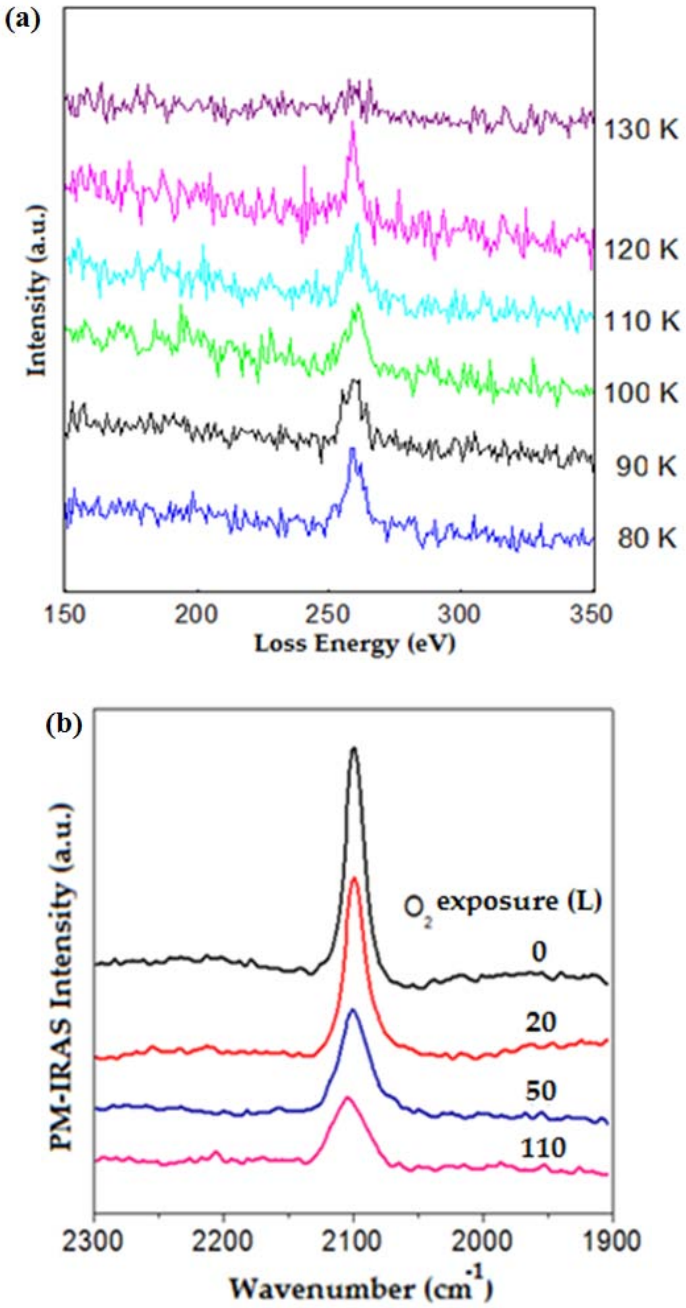

Fig. 24 (a) HREELS spectra acquired on 0.80 ML Au/graphene/Ru(0001) surface pre-covered by CO at indicated temperatures, (b) PM-IRAS spectra acquired after the indicated O_2 exposure at 85 K on 1.0 ML Au/graphene/Ru(0001) surface pre-covered by CO.

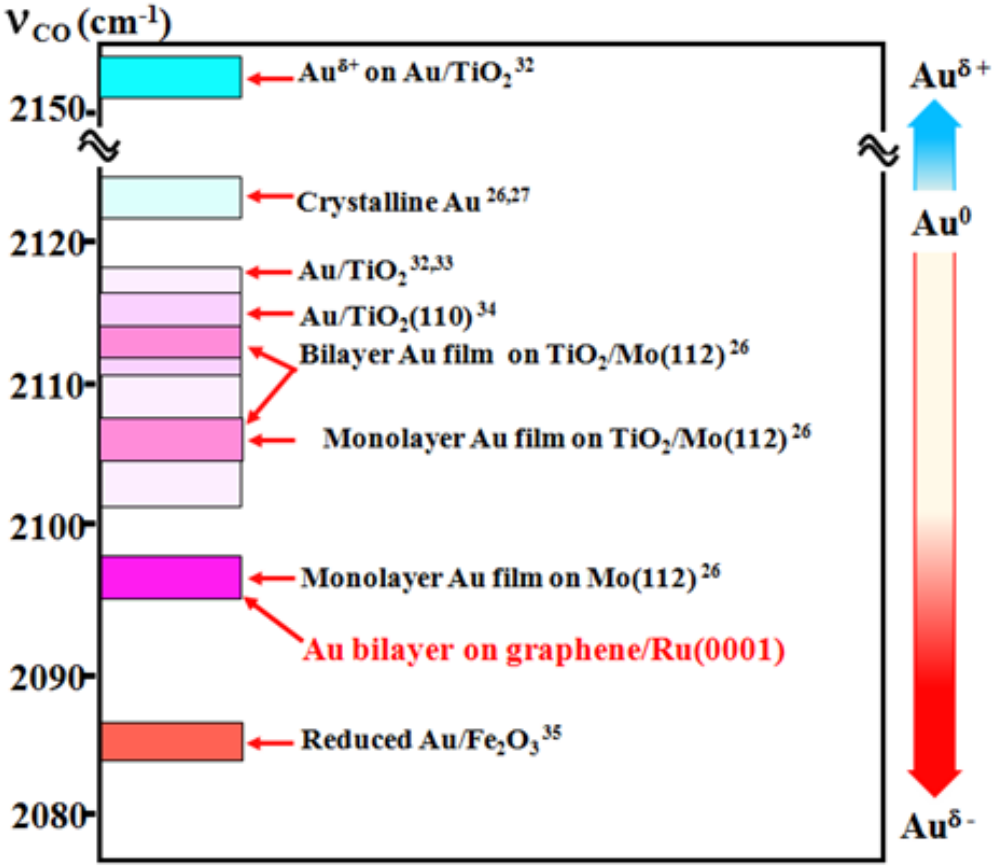

Fig. 25 Comparison of the stretching frequencies for CO adsorption on many supported Au catalysts.

The CO stretching frequency is around 2120 cm^{-1} on charge neutral Au [192,193], shifts red on electron-rich Au, and shifts blue on electron-deficient Au. The magnitude of the shift depends on the effective charge of Au [194]. A CO stretching frequency of 2095 cm^{-1} observed for the 2-D Au on graphene/Ru(0001) suggests that the Au in the 2-D islands is electron rich. This is also supported by recent DFT calculations, which show a weak electron transfer from graphene to Au when graphene is adsorbed on the Au(111) surface [195,196]. Our PM-IRAS and HREELS data indicate that the electron transfer from graphene to Au occurs when the graphene is supported on a Ru(0001) substrate.

It has been reported that electron-rich Au adsorbs molecular oxygen more strongly than neutral Au and can activate the O-O bond via charge transfer from Au by forming a superoxo-like species [197]. The activity of the 2-D Au islands towards CO oxidation was studied by dosing O_2 on CO pre-covered surfaces. Fig. 24(b) shows the CO feature measured with PM-IRAS and HREELS as a function of O_2 exposure. The intensity of the CO peak decreased with increasing O_2 dosage, consistent with reactions between CO and O_2. Thus, the preliminary data suggest that this adsorbed CO is reactive toward molecular oxygen.

4. GRAPHENE/RU(0001) MODIFICATIONS AND H-BN NANOMESH

One key issue in many of the current investigations is how graphene interacts with the underlying TM substrates for the reason that bonding between graphene and TMs may significantly change the electronic properties of graphene as well as complicate separation of graphene from the metal substrate. Preobrajenski *et al.* have shown that the interaction of graphene with TMs varies and the strength of covalent bonding between graphene and substrate grows in the following series: Pt, Ir, Rh, Ru, leading to different geometric corrugations and distinct electronic properties of graphene [198]. The difference is even more evident when metal clusters are deposited on these surfaces, which exhibit distinct morphologies despite similar moiré pattern of graphene. For example, Pt forms epitaxial cluster superlattices on graphene/Ir(111) [165,199,200], while highly dispersed Pt 3-D clusters are observed on graphene/Ru(0001) [201-203]. Au forms 3-D clusters on graphene/Ir(111) [200], whereas 2-D Au islands with diameter of more than 10 nm are found on graphene/Ru(0001) [201,204].

Owing to the above differences, it is particularly important to control and tune the interaction between graphene and its substrate. Efforts to change this interaction have mostly been focused on the intercalation of small molecules or metal atoms into the interface between graphene and substrate. For instance, intercalation of Au atoms into the interface between graphene and Ni(111) recovers the intriguing electronic properties of freestanding graphene on a solid surface [205]. Also, alkali metal atoms of much smaller size were inserted into the graphene/Ni(111) system, where change in the band

structure of graphene was observed due to dilation of the graphene-Ni interlayer distance [206]. However, the intercalation method has two disadvantages: first, strict conditions are required for intercalated object, such as size and electronic structure; second, the quality of graphene is compromised in most cases.

In this chapter, we mainly discuss three ways to modify the coupling between graphene and substrate. The first one is a novel and versatile method, which prepares high quality graphene on a pseudomorphic single layer of TM supported on Ru(0001), thus allowing us to modify the corrugations of graphene systems. Moreover, many metallic ultrathin films, such as Co and Pd thin films, show unique magnetic behavior [207,208], which can be coupled with the special electronic features of graphene, leading to a fascinating material. The second method is to intercalate oxygen at the interface between graphene and Ru(0001), which decouples graphene from the Ru(0001) substrate by selective oxidation of a ruthenium surface beneath graphene, where an ordered (2 × 1)-O structure is formed [209,210]. And the last method is to prepare a carbon-rich graphene by exposing graphene/Ru to atmosphere. All of the three methods can tune the coupling between graphene and the substrate, which in turn change the morphologies of deposited metal clusters.

In addition, hexagonal boron nitride (h-BN) nanomesh grown on Ru(0001), a system isoelectronic to graphene, was studied. To compare with the graphene/Ru(0001) system, morphologies and thermal stability of Au clusters supported on h-BN nanomesh were also investigated.

4.1 Graphene/Transtion Metal/ Ru(0001)

Graphene/Co/Ru(0001)

As mentioned in the experimental section, a pseudomorphic layer of Co was first prepared on Ru(0001) substrate before growing graphene. At room temperature, growth of Co follows SK mode, where one Co wetting layer co-exists with subsequent 3-D Co clusters grown on the Ru surface [211]. After annealing the Ru surface to 500K, single-atomic irregular 2-D Co islands are formed, as shown in Fig. 26(a). With annealing temperature further increased, Co atoms with higher diffusivity coalesce, forming larger and more compact islands [211]. Although it has been reported that at higher coverages (> 1.0 ML), expanded Co lattice relaxes to its bulk spacing after high temperature annealing [207], Co in submonolayer regime still retains the Ru(0001) lattice as shown in Fig. 26(b). The observation of a sharp p(1 × 1) pattern, which is identical to the original LEED pattern of Ru(0001), indicates that the single layer of Co preserves the Ru(0001) lattice despite a ~6% mismatch.

AES data confirm no loss of Co on Ru(0001) upon annealing to 1100 K. Figs. 27(a) and 27(b) show AES of 1.0 ML Co/Ru(0001) before and after annealing at 1100 K, respectively. The coverage amount of Co is monitored using the ratio of the Co peak at 775 eV to the Ru peak at 231 eV, and AES break point (data not shown) suggests Ru(0001) is fully covered by 1.0 ML Co with a ratio of 0.30, consistent with STM measurements. Upon annealing to 1100 K for 10 min, AES maintains the same ratio of 0.30, indicating that Co keeps the 2-D morphology and does not desorb at 1100 K. Thermal stability studies reveal that Co is stable on Ru(0001) up to 1200 K and that a

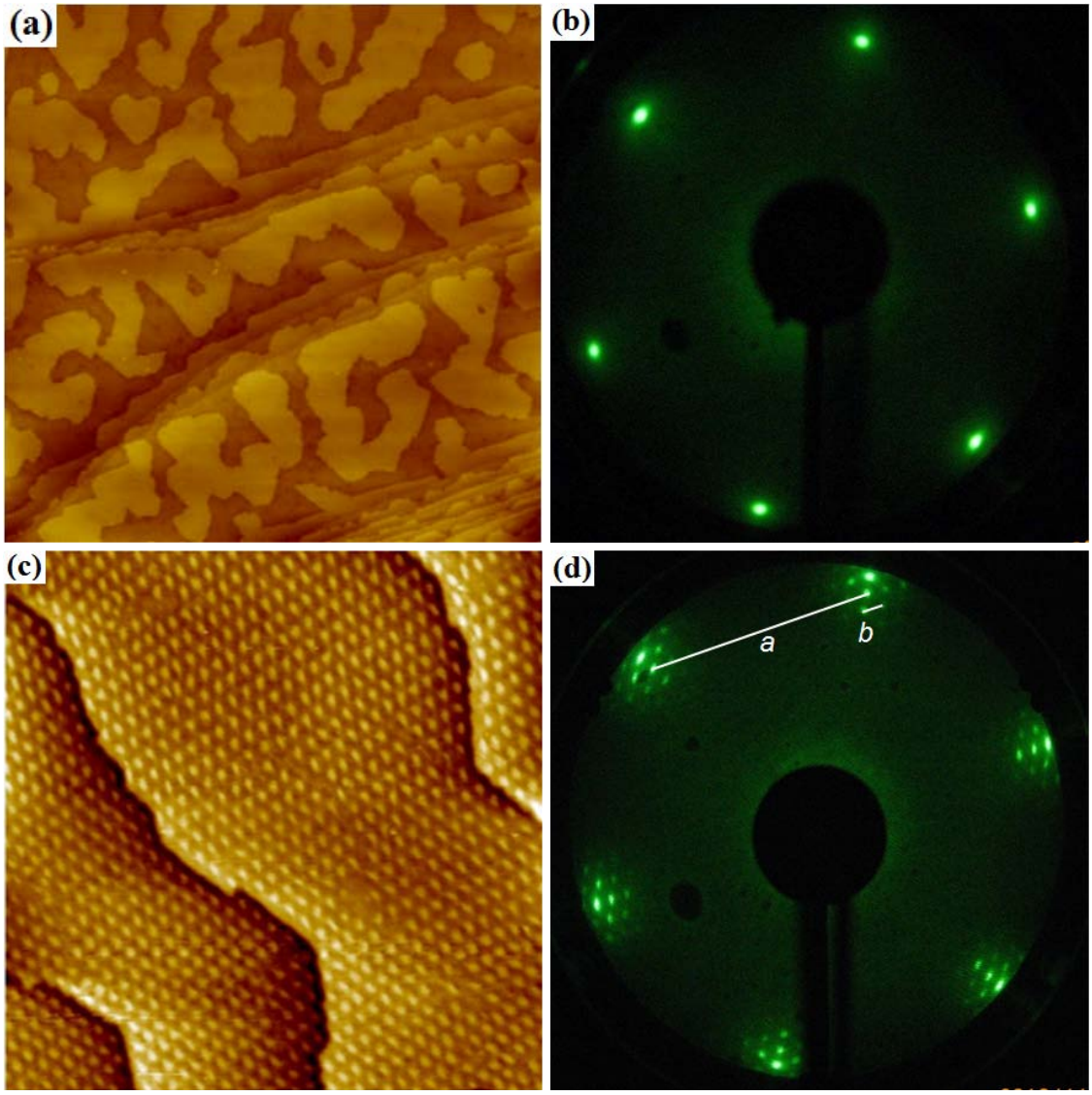

Fig. 26 (a) Room temperature STM image (200 nm × 200 nm, V_b = 1.0 V, I_t = 0.2 nA) of 0.70 ML Co on Ru(0001) after annealing to 500 K for 5 min. (b) LEED pattern of 1.0 ML Co on Ru(0001) with post-annealing at 1100 K for 10 min (beam energy: 70 eV). (c) STM image (200 nm × 200 nm, V_b = 1.0 V, I_t = 0.1 nA) of graphene grown on 1.0 ML Co supported on Ru(0001). (d) LEED pattern of graphene/1.0 ML Co/Ru(0001) taken at 71 eV. The distance between neighboring Ru(0001) substrate spots and graphene satellites spots are marked by *a* and *b*, respectively.

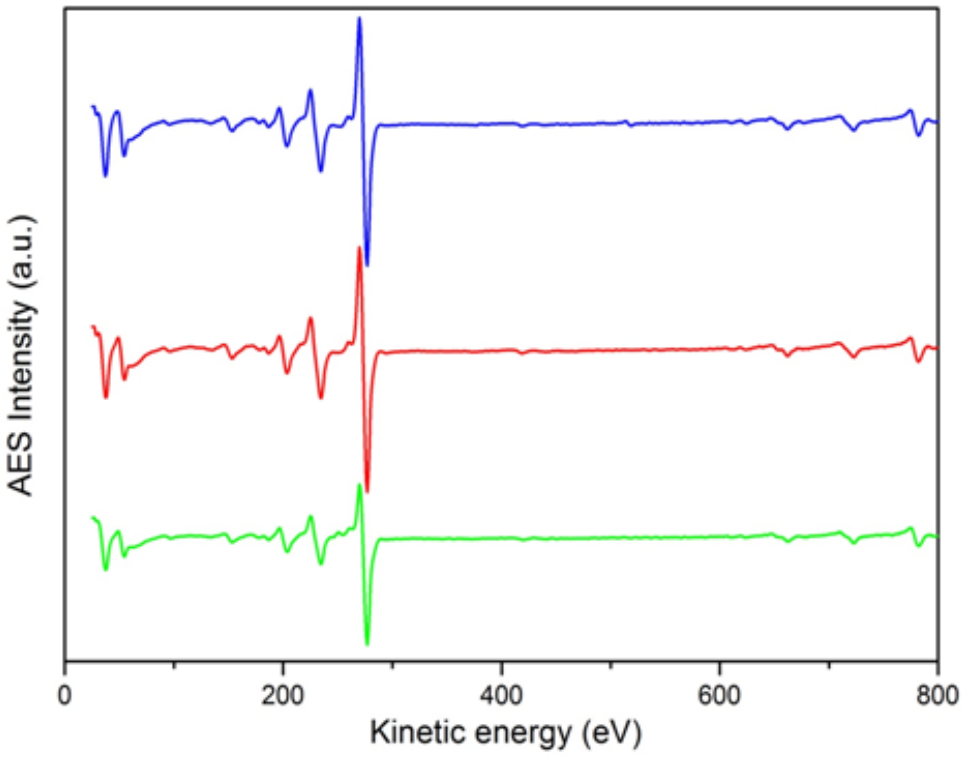

Fig. 27 AES of (a) 1.0 ML Co on Ru(0001), (b) 1.0 ML Co on Ru(0001) after annealing to 1100 K for 10 min and (c) graphene/1.0 ML Co/Ru(0001).

surface alloy does not form at this temperature.

A graphene layer is then prepared by dissociating C_2H_4 or C_3H_6 on Co/Ru(0001) followed by annealing the sample *in vacuo* to ~1100 K. Fig. 26(c) displays a typical STM topographic image of the graphene moiré template on 1.0 ML Co/Ru(0001) surface. Graphene moiré with high quality almost covers the entire surface. The inset of Fig. 28(a) shows that the moiré superstructure lattice constant is ~3.0 nm, the same as graphene/Ru(0001), indicating that the moiré unit cell arises from superposition of 12 graphene unit cells and 11 unit cells of Co/Ru(0001). Clearly, Co atoms still adopt Ru(0001) lattice even with a layer of adsorbed graphene. The measured corrugation is 0.21 nm, as shown in the inset of Fig. 28(a), which is higher than 0.12 nm for graphene/Ru(0001) [146]. Fig. 28(b) shows a high resolution STM image of graphene/ Co/Ru(0001). The highlighted unit cell is shown, in which the bright, medium dark and dark regions are assigned to atop, fcc and hcp sites, respectively, based on previous experimental and theoretical results of graphene/TMs [212]. Similar to graphene/Ru, only every other carbon atoms can be resolved due to the asymmetric interactions with the underlying substrate. It should be noted that, compared to graphene/Ru(0001), the atomic resolution of graphene/Co/Ru(0001) is much more difficult to obtain at room temperature, which might be due to the modification of electronic structure of graphene by the Co interlayer.

LEED confirms that STM results are valid over macroscopic areas on Co/ Ru(0001), as shown in Fig. 26(d). Satellite spots surrounding the bright substrate spots are caused by the graphene overlayer. The overlayer periodicity has shown to be 11.4

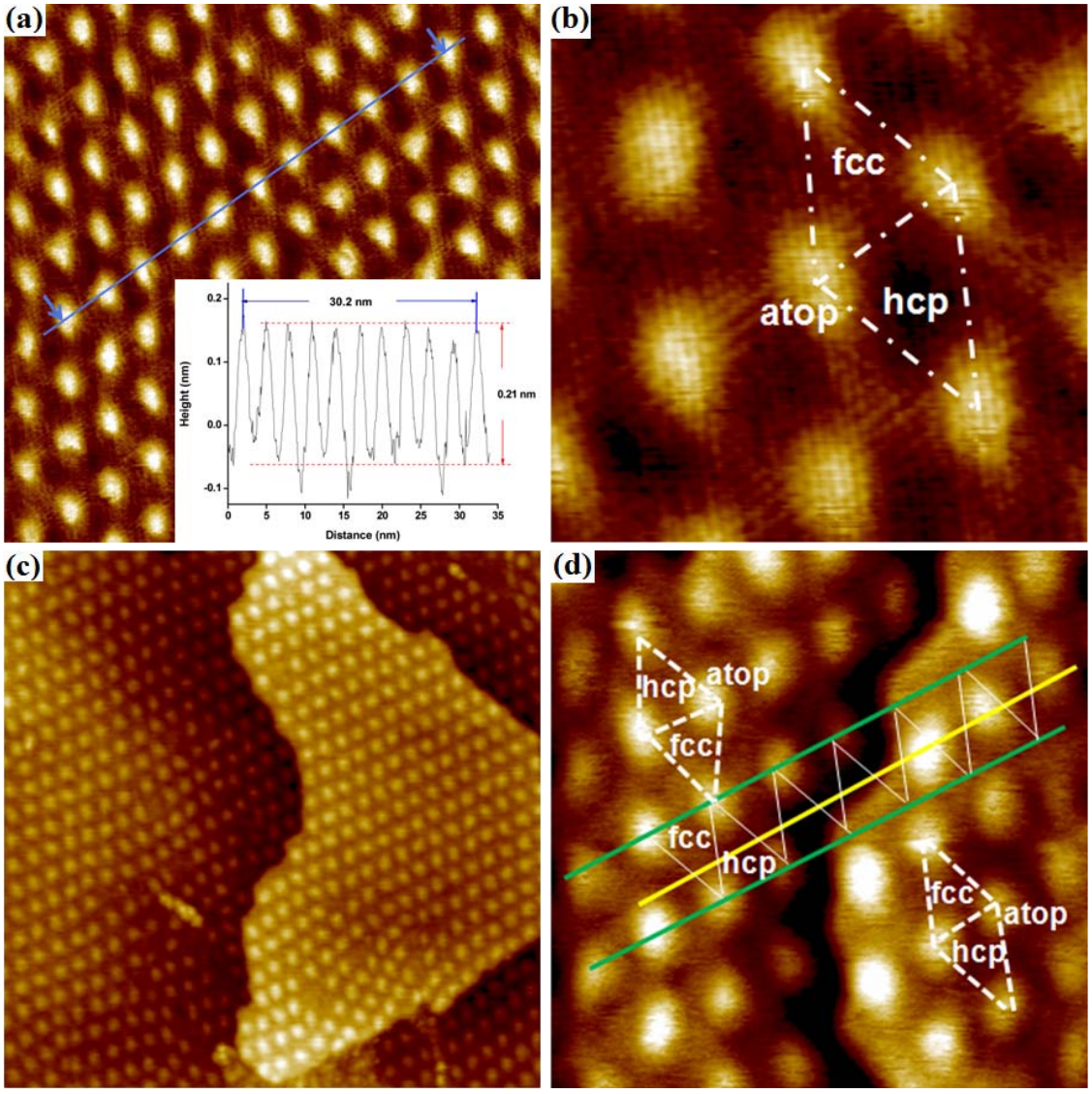

Fig. 28 (a) 40 nm × 40 nm image (V_b = 1.0 V, I_t = 0.1 nA) showing graphene grown on 1.0 ML Co/Ru(0001). The inset shows the line profile of the moiré pattern. (b) High resolution STM image (10 nm × 10 nm, V_b = 0.8 V, I_t = 0.4 nA) of graphene/1.0 ML Co/Ru(0001). The unit cell is highlighted and three different sites are marked. (c) 70 nm × 70 nm image (V_b = 0.7 V, I_t = 0.2 nA) of graphene/0.50 ML Co/Ru(0001) displaying graphene grown on a monolayer Co island with a triangular shape on Ru(0001). (d) 20 nm × 20 nm zoomed-in STM image (V_b = 0.7 V, I_t = 0.2 nA) showing the boundary between graphene/Ru(0001) (left side) and graphene/Co/Ru(0001) (right side). Green and yellow lines highlight the rows of atop sites of graphene/Ru(0001) and graphene/Co/Ru(0001), respectively. White lines are used to aid eyes to distinguish fcc and hcp sites.

times the substrate lattice constant, which is obtained from the ratio of *a* to *b*, where *a* denotes the distance between substrate spots and *b* denotes the distance between neighboring satellites. This number is quite close to graphene/Ru(0001) with a ratio of 11.6 [146], indicating that Co does not relax to its bulking spacing upon growing graphene, which agrees well with the STM results.

Fig. 27(c) shows AES of graphene/1.0 ML Co/Ru(0001). With an overlayer of graphene adsorbed, the ratio of the Co peak at 775 eV to the Ru peak at 231 eV increases from 0.3 to 0.37, which can be understood in terms of a greater attenuation of Ru than Co because Ru has been covered by both graphene and Co. Nevertheless, no evidence of Co loss from the surface has been observed after graphene is prepared. In addition, the information regarding graphene coverage can be obtained using the ratio of the upper to lower portions of the 271 eV Auger transition feature [146,159]. A ratio of 0.50 is observed from Fig.27(c), which is close to a ratio of 0.46 [204] corresponding to fully covered graphene.

To gain a deeper understanding on the structure of graphene/Co/Ru(0001), graphene grown on 0.50 ML Co/Ru(0001) was studied by STM. Fig. 28(c) is a 70 nm × 70 nm STM image, where the graphene moiré pattern covers the whole surface, showing the co-existence of graphene/Ru(0001) and graphene/Co/Ru(0001). The triangular island covered with graphene is denoted as graphene/Co/Ru(0001) and lower terrace is graphene/Ru(0001). Fig. 28(d) is a zoomed-in STM image showing the boundary between graphene/Ru(0001) and graphene/Co/Ru(0001). No evidence of a discontinuity of graphene over the step edge was observed, which is consistent with the established

growth mechanism of graphene on many TMs [140,142,147,148].

Close inspection of Fig. 28(d) illustrates that the moiré patterns are not lined up at the boundary, as marked by the green and yellow lines, highlighting the rows of atop sites on graphene/Ru and graphene/Co/Ru, respectively. In addition, the positions of hcp and fcc sites on graphene/Ru(0001) and graphene/Co/Ru(0001) are swapped. In other words, the triangles pointing to the upper left stand for hcp sites on graphene/Ru(0001), whereas they represent fcc sites on graphene/Co/Ru(0001).

Based on the above observations, we conclude that each Co atom occupies the hcp hollow sites, with an 'ABA' stacking on the Ru substrate, as shown in Fig. 29(a), which is a schematic drawing of half covered pseudomorphic single layer of Co on two layer Ru(0001) substrate. Fig. 29(b) and Fig. 29(c) demonstrate one overlayer of graphene on Ru(0001) and Co/Ru(0001) respectively, using one graphene layer of (12 × 12) unit cells over (11 × 11) substrate unit cells. It is worth mentioning that the positions of hcp and fcc sites are also swapped in these two models, which agrees with STM images. Fig. 29(d) shows a large scale atomic model of the boundary covered with graphene, mimicking the STM image of Fig. 28(d). The same label scheme is applied to both STM image and atomic model to make comparison easier, showing that the model perfectly reflects the misalignment of atop sites, as well as the exchange of fcc and hcp sites across the border between graphene/Ru(0001) and graphene/Co/Ru(0001).

Graphene/Pd/Ru(0001)

The preparation of graphene/Pd/Ru(0001) follows the same procedure as

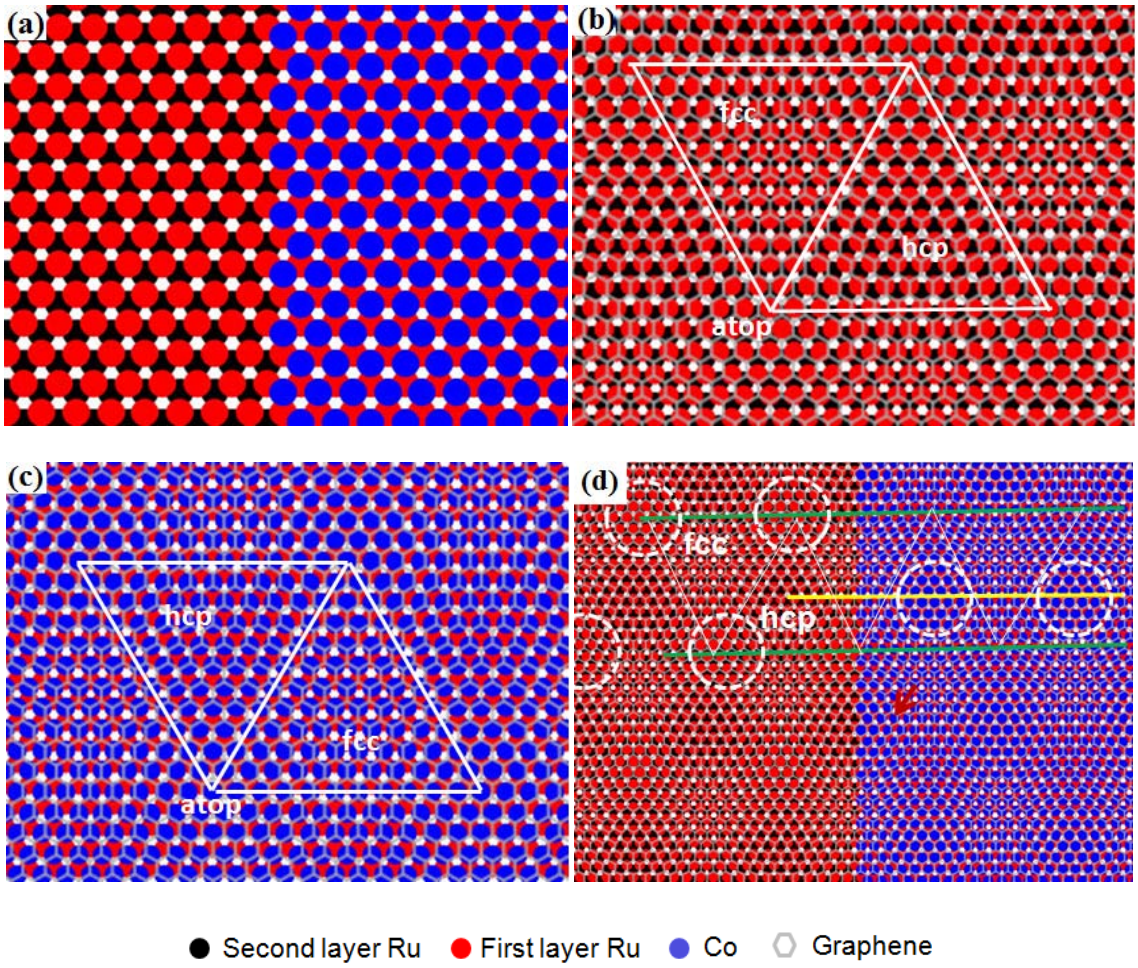

Fig. 29 Structural models of (a) two layer of Ru(0001) half covered with Co atoms. (b) graphene/Ru(0001). The highlighted unit cell is shown, where atop, fcc and hcp sites are marked. (c) graphene/Co/Ru(0001). The highlighted unit cell is shown, where atop, fcc and hcp sites are marked. (d) A large area of (a) with graphene adsorbed on top. The label scheme used in Fig. 28(c) is also applied here to make comparison simple. Dashed circles are used to highlight atop sites.

discussed above. An epitaxial Pd film is first prepared on Ru(0001), where Pd monolayer grows as dendrite islands with each Pd atom occupying hcp hollow site of the Ru substrate, and subsequent Pd layers follow the conventional fcc packing [208,213]. Our STM data (not shown) are in perfect agreement with the above results. The LEED pattern of 1.0 ML Pd/Ru(0001) is identical to Fig. 26(b). In spite of a ~4% mismatch, no evidence of Pd relaxing to its bulking spacing has been observed. The thermal stability of Pd on Ru(0001) was also studied by AES, as shown in Fig. 30(a) and (b), which are taken from 1.0 ML Pd/Ru(0001) before and after annealing to 1100 K. The ratio of the Pd peak at 330 eV to the Ru peak at 231 eV retains the same value of 1.1, which corresponds to the break point of 1.0 ML Pd on Ru(0001), indicating Pd maintains the same morphology and does not desorb from Ru(0001) surface upon annealing to 1100 K.

With an overlayer of adsorbed graphene, results obtained are similar to what we acquired from graphene/Co/Ru(0001) system. Fig. 31(a) depicts an STM image acquired on graphene/1.0 ML Pd/Ru(0001) and the inset shows the line profile of moiré pattern of graphene/Pd/Ru(0001). The lattice constant of the moiré pattern is measured to be ~3.0 nm, identical to graphene/Ru(0001), resulting from the superposition of 12 graphene unit cells on 11 unit cells of Pd/Ru(0001). Corrugation is 0.09 nm, which is slightly smaller than graphene/Ru(0001). Fig. 31(b) shows a typical LEED pattern of graphene/1.0 ML Pd/Ru(0001), where the satellite points surrounding the (1 × 1) spots of the substrate demonstrate the formation of a graphene overlayer [132,214]. Likewise, the moiré periodicity is calculated from the ratio of *a'* to *b'* and is found to be 11.3 times the substrate lattice constant. Both STM and LEED suggest that Pd atoms still maintain the

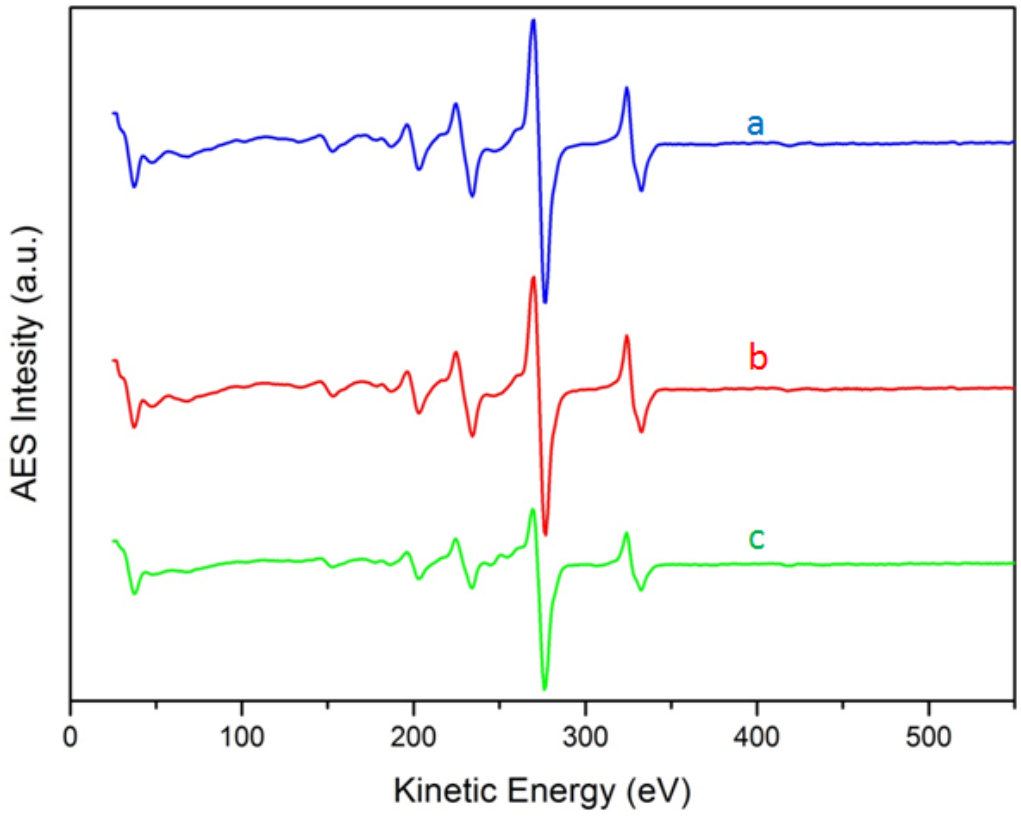

Fig. 30 AES of (a) 1.0 ML Pd on Ru(0001), (b) 1.0 ML Pd on Ru(0001) after annealing to 1100 K for 10 min and (c) graphene/1.0 ML Pd/Ru(0001).

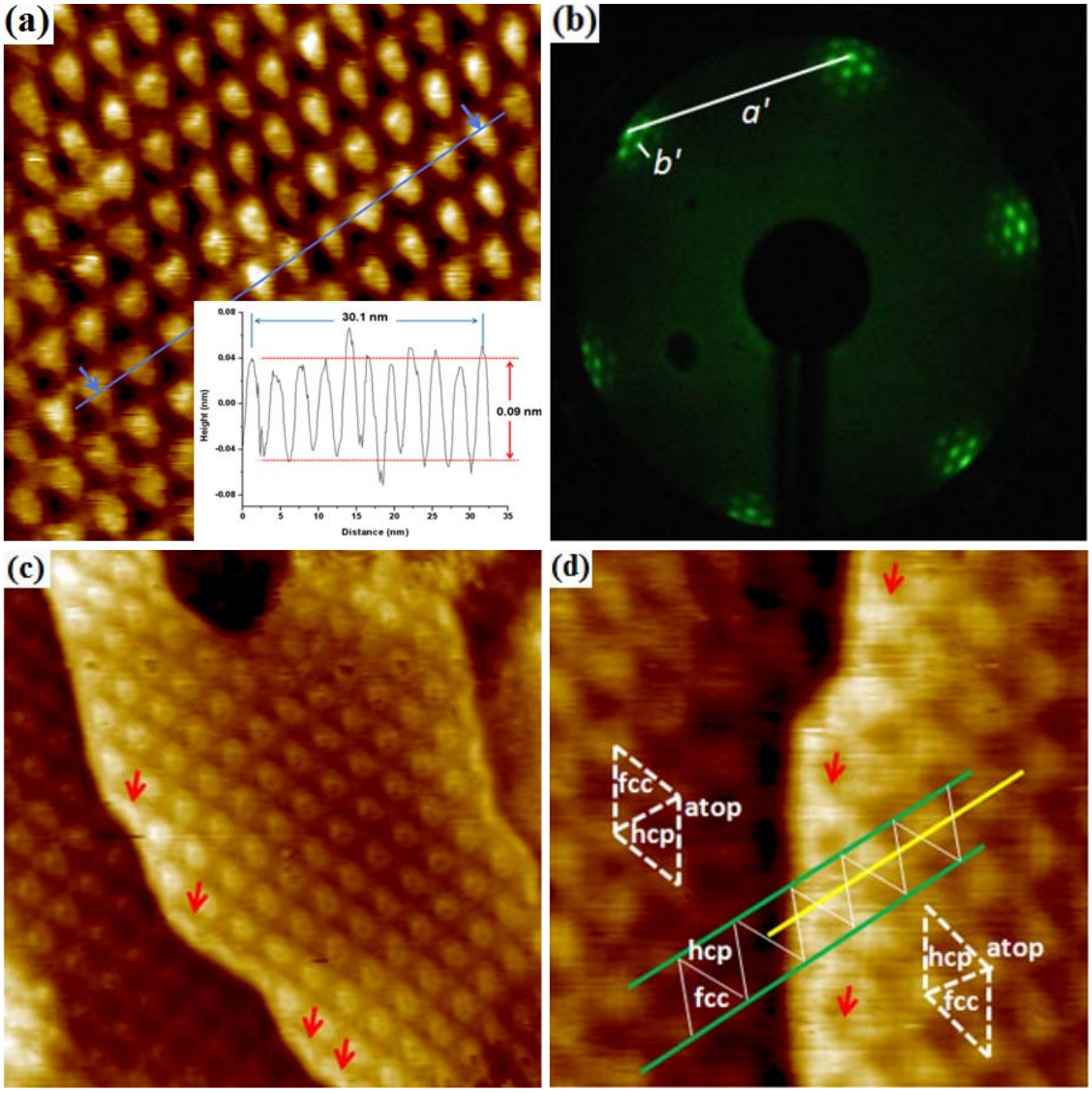

Fig. 31 (a) Room temperature STM image (35 nm × 35 nm, V_b = 1.0 V, I_t = 0.1 nA) of graphene/1.0 ML Pd/Ru(0001). The inset shows the line profile of the moiré pattern. (b) LEED pattern of graphene/1.0 ML Pd/Ru(0001) taken at 70 eV. *a'* and *b'* denote the distance between neighboring Ru(0001) substrate spots and graphene satellites spots, respectively. (c) STM image (40 nm × 40 nm, V_b = 1.0 V, I_t = 0.1 nA) of graphene grown on 0.50 ML Pd/Ru(0001). The higher terrace is graphene/Pd/Ru(0001) and lower area is graphene/Ru(0001). Incomplete atop sites at boundary are marked by red arrows. (d) Zoomed-in STM image (22 nm × 22 nm, V_b = 0.5 V, I_t = 0.3 nA) of the border between graphene/Ru(0001) (left side) and graphene/Pd/Ru(0001) (right side), which is labeled as Fig. 28(d).

Ru(0001) lattice even with an adsorbed graphene overlayer. AES data, as Ru(0001) lattice even with an adsorbed graphene overlayer. AES data, as shown in Fig. 30(c), reveal that the ratio of Pd to Ru still keeps the same value of 1.1 and that the ratio of upper to lower portions of the 271 eV peak is equal to 0.46. Therefore, Pd atoms still reside on the surface upon growing graphene and the surface is almost fully covered with graphene.

To explore the detailed structure of graphene/Pd/Ru(0001), graphene grown on 0.50 ML Pd/Ru(0001) was studied by STM. Fig. 31(c) shows a Pd island with an irregular shape covered by graphene. The different appearance of the moiré pattern is due to a change in tip shape and scanning conditions. A closer examination reveals a new feature near the boundary, i.e. the incomplete atop sites as marked by red arrows, which are absent in the case of graphene/Co/Ru(0001). Fig. 31(d) is a close up STM image focusing on the border between graphene/Ru(0001) and graphene/Pd/Ru(0001). The label scheme used here is the same as Fig. 28(c). Comparison with Fig. 28(c) suggests that the orientation of the unit cell has changed; or more exactly, the triangles pointing to the upper left are fcc sites of graphene/Ru(0001) in Fig. 31(d), whereas they become hcp sites in Fig. 28(c). Such a difference can be explained in terms of a hcp structure of Ru(0001) with an ‘ABAB’ stacking. Clearly, the unit cell of graphene grown on the ‘A’ layer would have the opposite orientation to the unit cell of graphene on the ‘B’ layer.

Similar to graphene/Co/Ru(0001), both the misalignment of atop sites and the exchange of fcc and hcp sites across the border are observed, indicating that the atomic

model proposed in Fig. 29 is also applicable to this case with replacement of Co with Pd. The model is also supported by the experimental observation that submonolayer Pd islands follow hcp stacking on Ru(0001) [208,213]. Moreover, the new feature of incomplete atop sites near the boundary can be perfectly described in the model, as marked by the red arrow in Fig. 29(d). This reflects that the graphene sheet is intact across the boundary, which is consistent with the proposed growth mechanism of graphene on many TMs [140,142,147,148]. It is worth mentioning that such partial atop sites do not appear in Fig. 28(c). A closer examination reveals that, unlike the almost straight border in Fig. 31(d), the boundary in Fig. 28(c) is of S-shape, thus allowing it to bypass the atop sites. Note, not all boundaries of islands are S-shaped on graphene/Co/Ru(0001).

Deposition of Au at Room Temperature

Because the special catalytic performance of Au nanoparticles critically depends on the particle morphology, i.e. size, shape, thickness, and support effects as well, it is particularly interesting to investigate the morphology of Au supported on different graphene systems. Fig. 32 shows STM images acquired at 0.20 ML Au deposited on graphene/Co/Ru(0001) and graphene/Pd/Ru(0001). In spite of similar moiré pattern, Au exhibits different morphologies. As reported in previous studies [201,204], Au forms large 2-D islands that extend over several graphene moiré unit cells and conform to the corrugation of the underlying moiré on graphene/Ru(0001). However, the morphology of Au noticeably changes with a pseudomorphic layer of metal introduced to the

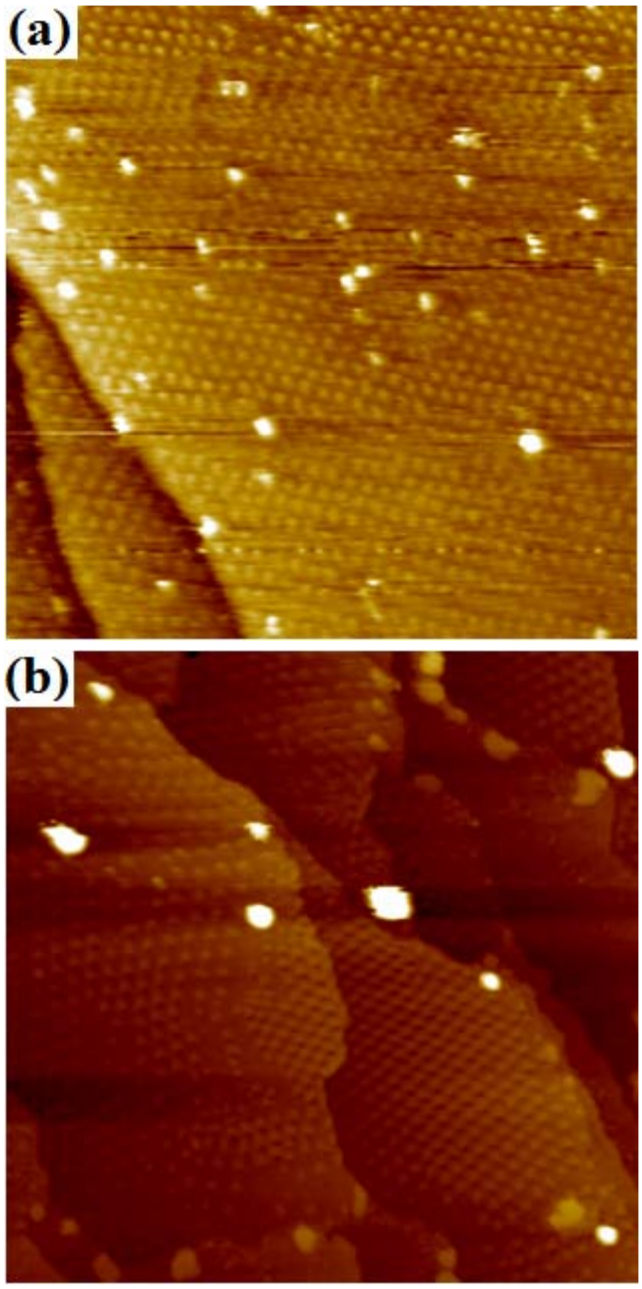

Fig. 32 Room temperature 120 nm × 120 nm STM images of (a) 0.20 ML Au on graphene/1.0 ML Co/Ru(0001) (V_b = 1.0 V, I_t = 0.1 nA) and (b) graphene/1.0 ML Pd/ Ru(0001) (V_b = 1.5 V, I_t = 0.1 nA).

interface. On graphene/Co/Ru(0001), clusters with diameters from 1 nm to 3 nm are highly dispersed. Clusters with height from one to three layers coexist and most of the clusters grow in 3-D mode, as shown in Fig. 32(a). Note that, these clusters were not stabile and sometimes were dragged or picked up by the STM tip, causing the change in resolution during scanning. In contrast, Au forms large 3-D clusters on graphene/Pd/ Ru(0001), as shown in Fig. 32(b). Some of the clusters are nucleated on the step edge, indicating that Au atoms have a large diffusion length on this surface. The size of the cluster ranges from 4 nm to 10 nm and the height is more than 1.5 nm.

The above difference can be attributed to different interactions between Au and graphene systems. Au has the strongest interaction with graphene/Co/Ru(0001), leading to a smaller diffusion coefficient, which in turn facilitates better dispersion of the 3-D Au clusters. On the other hand, Au weakly interacts with graphene/Pd/Ru(0001), thus forming large 3-D clusters with high mobility on the surface. The origin of such different interactions is due to different corrugations of graphene surface, despite all of three systems exhibiting almost the same periodicity. The corrugation of graphene follows the order: Graphene/Co/Ru > Graphene/Ru > Graphene/Pd/Ru, which explains why Au atoms have the largest diffusion length on Graphene/Pd/Ru but the smallest diffusion length on Graphene/Co/Ru. Clearly, with an interlayer of TMs, the coupling between graphene and Ru(0001) can be greatly modified, resulting in different morphologies of supported Au clusters, which might also change the catalytic properties of Au clusters. Therefore, such tuning of graphene systems is not only of significant importance in studying graphene system itself, but also offers great opportunities for investigating the

morphology effect on catalytic activities.

Graphene/Ni/Ru(0001) and Graphene/Au/Ru(0001)

To demonstrate the preparation method is versatile, two other systems, i.e. graphene/Ni/Ru(0001) and graphene/Au/Ru(0001), were also studied by LEED and AES. LEED patterns, as shown in Fig. 33(a) and Fig. 33(b), reveal that graphene sheets of high quality are grown over macroscopic areas on Ni/Ru(0001) and Au/Ru(0001). AES data (not shown) also confirm that Au and Ni pseudomorphic single layer is thermally stable when preparing graphene. In both cases, the periodicity of the graphene moiré has been determined to be ~11 times the substrate lattice constant. Note, for graphene grown on Ni(111), no moiré pattern could be observed becasuse graphene forms an atomically flat overlayer due to negligible lattice mismatch between graphene and Ni(111) [151]. Therefore, the satellite pattern in Fig. 33(a) must result from an expansion of the Ni lattice to Ru(0001) with an overlayer of graphene adsorbed on top. In the second case, it is of great interest in introducing Au into the interface between graphene and Ru(0001) since it is expected that Au interface layer might recover the intriguing electronic properties of freestanding graphene due to saturation of Ru 4d bonds by Au atoms, which is similar to intercalation of Au atoms into the graphene/Ni(111) system [205,215]. More importantly, in spite of a much larger mismatch of ~8% and the inertness of Au, graphene can still be successfully prepared, demonstrating our method is quite general as long as two conditions are satisfied: first, the metal deposited is thermally stable upon annealing to 1100 K; and second, C_2H_4 or C_3H_6 can be dissociated on the surface.

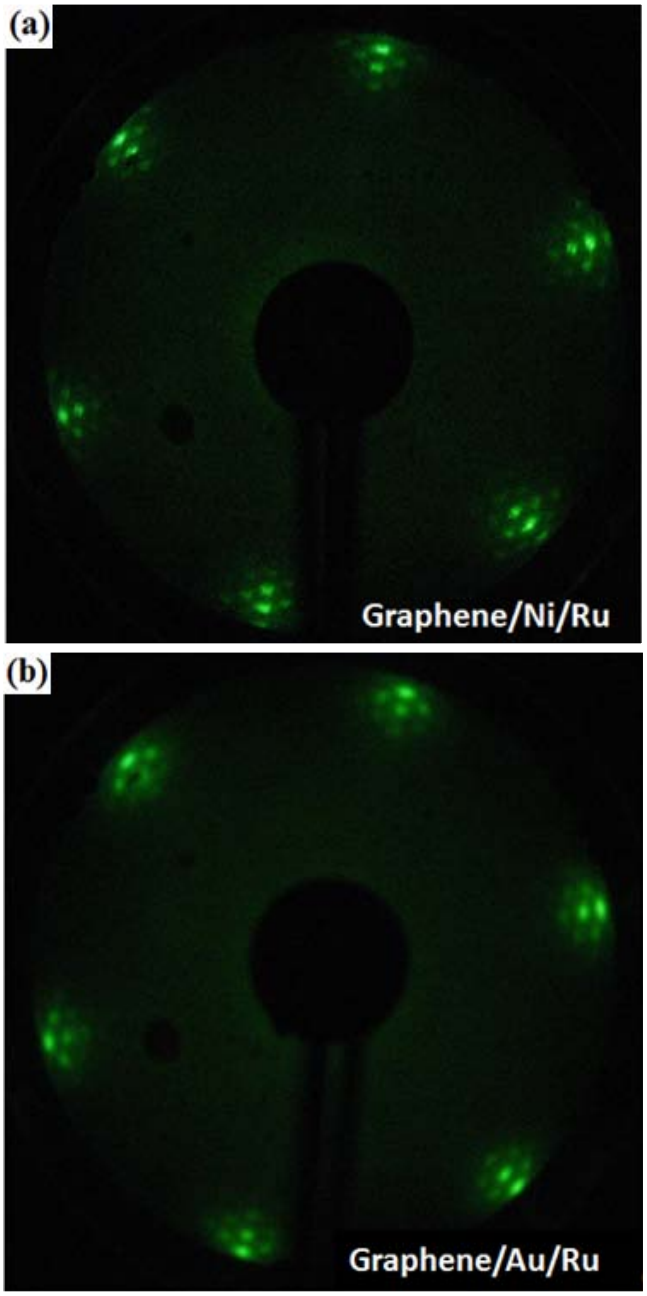

Fig. 33 LEED patterns of (a) graphene/Ni/Ru(0001) and (b) graphene/Au/Ru(0001) taken at 70 eV.

Although Ru(0001) is used as a substrate in this study, it seems that there exists no strict restriction on the substrate so far, implying this method may also apply to many other graphene systems, such as graphene/Ir(111), graphene/Ni(111), graphene/Pt(111), etc.

4.2 Graphene/O/ Ru(0001)

Structure of Graphene/O/ Ru(0001)

Oxidation of graphene/Ru(0001) was performed by annealing the sample to 800 K in 1×10^{-7} Torr O_2 for a few minutes, as mentioned in the experimental section. The oxidation of the graphene/Ru(0001) surface takes place via intercalation of oxygen atoms between the graphene and the Ru(0001) substrate surface [209,210]. Fig. 34 shows STM images and the LEED pattern of graphene/O/Ru(0001). Compared to graphene /Ru(0001), the periodic moiré pattern is the same; however, the corrugation has been measured to be 0.03 nm, much smaller than the typical value of 0.08 ~ 0.11 nm [146] for graphene/Ru(0001), indicating that the interaction between graphene and Ru become weaker with a layer of intercalated oxygen atoms. Close examination reveals some small black spots in Fig. 34(a) and (b), which might be due to adsorbed oxygen on top of the graphene. From the LEED pattern, the (2 × 1) spots could be clearly observed besides the moiré pattern. Note weaker satellite spots relative to the LEED pattern of graphene/Ru(0001) is due to the fact that some graphene area disappears because of oxidation.

In order to further study the structure of graphene/O/Ru(0001), a high resolution STM image was taken, as shown in Fig. 34 (d). The hexagonal structures can be

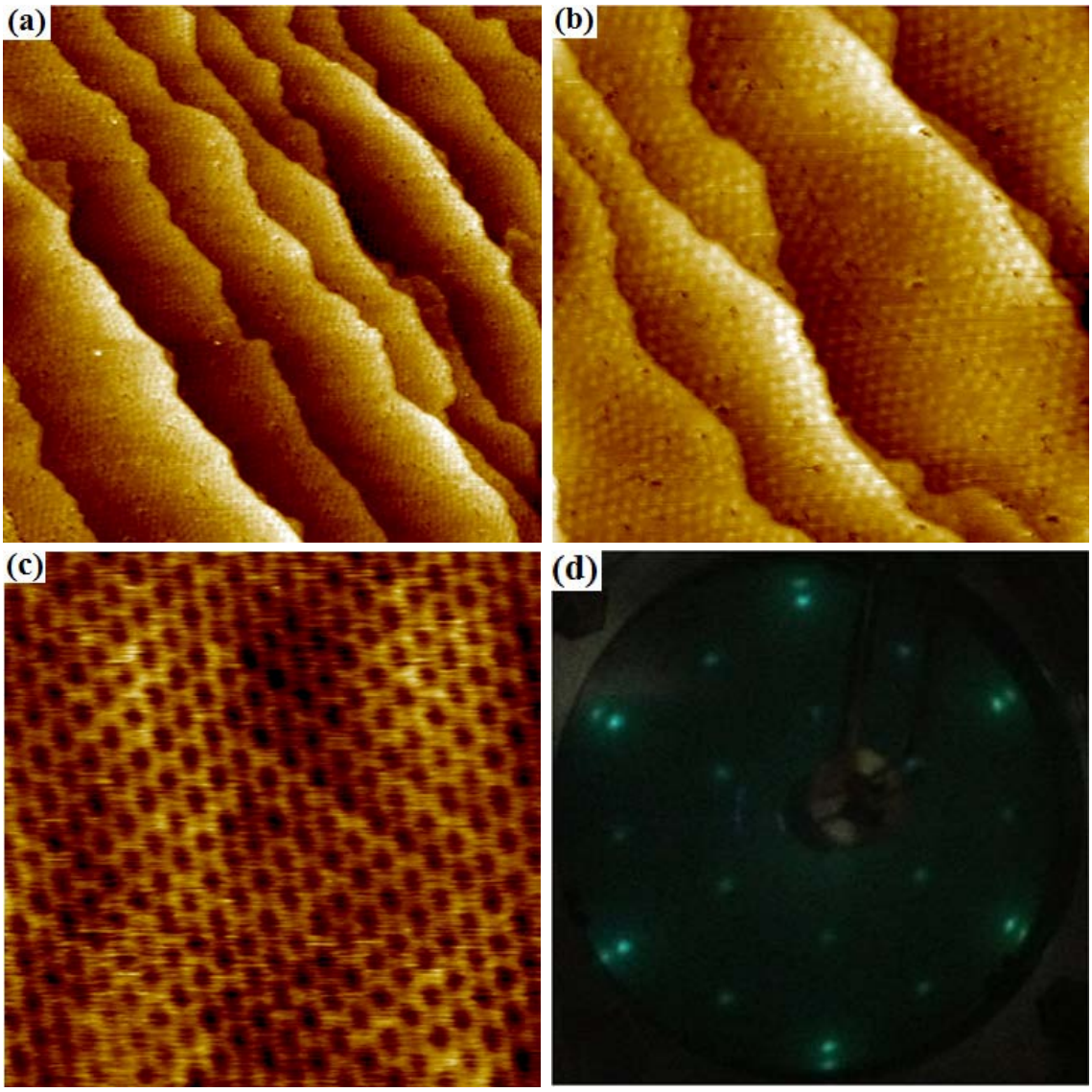

Fig. 34 Room temperature STM images and LEED pattern of graphene/O/Ru(0001). (a) 200 nm × 200 nm STM image (V_b = 1.0 V, I_t = 0.1 nA), (b) 100 nm × 100 nm STM image (V_b = 1.0 V, I_t = 0.1 nA), (c) 4 nm × 4 nm zoomed-in STM image (V_b = 0.3 V, I_t = 0.3 nA), and (d) LEED pattern taken at 65 eV.

observed in the image, which are assigned to the six-carbon rings. A slight corrugation can also be seen due to the mismatch between graphene and Ru(0001) substrate. The difference in the surface structure is noticeable between graphene/Ru and graphene/O/Ru systems. In the former system, only every other C atom can be resolved by STM due to the strong interaction between the graphene and the Ru substrate. However, in the later system, every C atom can be observed because the oxygen layer decouples the graphene from the substrate. The electronic structure is also distinguishable between the two systems. Before oxidation, graphene strongly interacts with Ru(0001) substrate, making graphene negatively charged, about 0.05 e^- per carbon atom [216-219]. In contrast, after oxidation, the Ru substrate is not fully metallic but covered by oxygen that is highly electronegative. Because oxygen interacts more strongly with Ru(0001) than graphene, the graphene becomes electron deficient. Therefore, with intercalation of oxygen between the graphene and the Ru substrate, both the geometric structure and the electronic structure of the graphene have been modified.

The graphene/Ru(0001) can be further oxidized by extending oxidization time to 30 min. STM images show that the graphene/O/Ru and the oxidized Ru coexist on the surface, as shown in Fig. 35(a). The relatively smooth areas are graphene/O/Ru and the rough areas are the oxidized Ru surface. The small holes on the smooth area indicate that the oxidation cannot only occur at the edges of graphene but also happen at defects. The height of the graphene surface was measured to be 0.16 nm, as shown in the line profile in Fig. 35 (b), further proving that the graphene as prepared via our recipe is a single layer. The oxidation process is reversible. As the oxidized graphene was annealed in

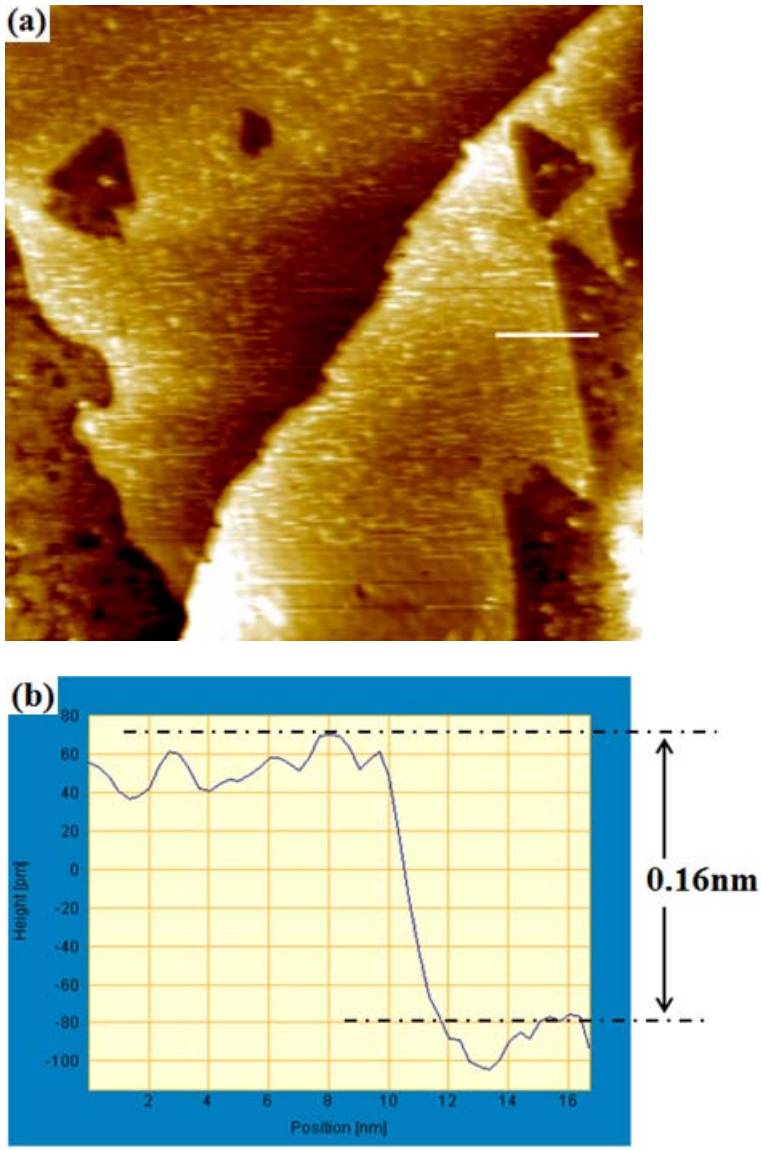

Fig. 35 (a) Room temperature 90 nm × 90 nm STM image (V_b = 1.0 V, I_t = 0.1 nA) of over oxidized graphene/O/Ru(0001). The area with relatively smooth surface is graphene/O/Ru and rough areas are oxidized Ru surface. (b) The line profile across boundary between graphene/O/Ru and oxidized Ru surface corresponding to the white line in (a).

vacuum to 1100 K for a few minutes, the STM images show the graphene moiré pattern with relatively large corrugations; in the meanwhile, the (2 × 1) LEED spots also disappears, which is consistent with previous studies [184].

Deposition of Au on Graphene/O/Ru(0001)

Because both geometric and electronic structures have been modified by the intercalated oxygen, it is intriguing to study the morphologies of metal clusters deposited on such surfaces. The morphology of Au clusters supported on graphene/O/Ru(0001) was studied by STM, as shown in Fig. 36. Unlike large 2-D Au islands on graphene/Ru(0001), coexistence of small 2-D clusters and 3-D clusters were observed. At the onset of deposition of Au, small 2-D and 3-D clusters were highly dispersed on the surface and the inter-cluster distance is smaller than 10 nm, indicating stronger interactions between Au and modified graphene surface. Note that the 2-D clusters are dominated on the surface, which could be clearly observed at higher dosages. As the Au dosage was increased to 0.40 ML and 0.60 ML, the size of the 2-D islands also increased, extending to cover a few of moiré units, which is similar to Au on graphene/Ru(0001). It is interesting to find that some of the 2-D Au islands can even cross the terrace boundary at the coverage of 0.60 ML, as shown in Fig. 36(d). A possible scenario for Au growth on graphene/O/Ru(0001) is that some defects created during oxidation process on the surface cause the formation of 3-D clusters, whereas the small 2-D Au islands were formed on the intact graphene/O/Ru(0001) terrace. The STM data suggest that 2-D Au islands are stable on the oxidized graphene surface at room temperature.

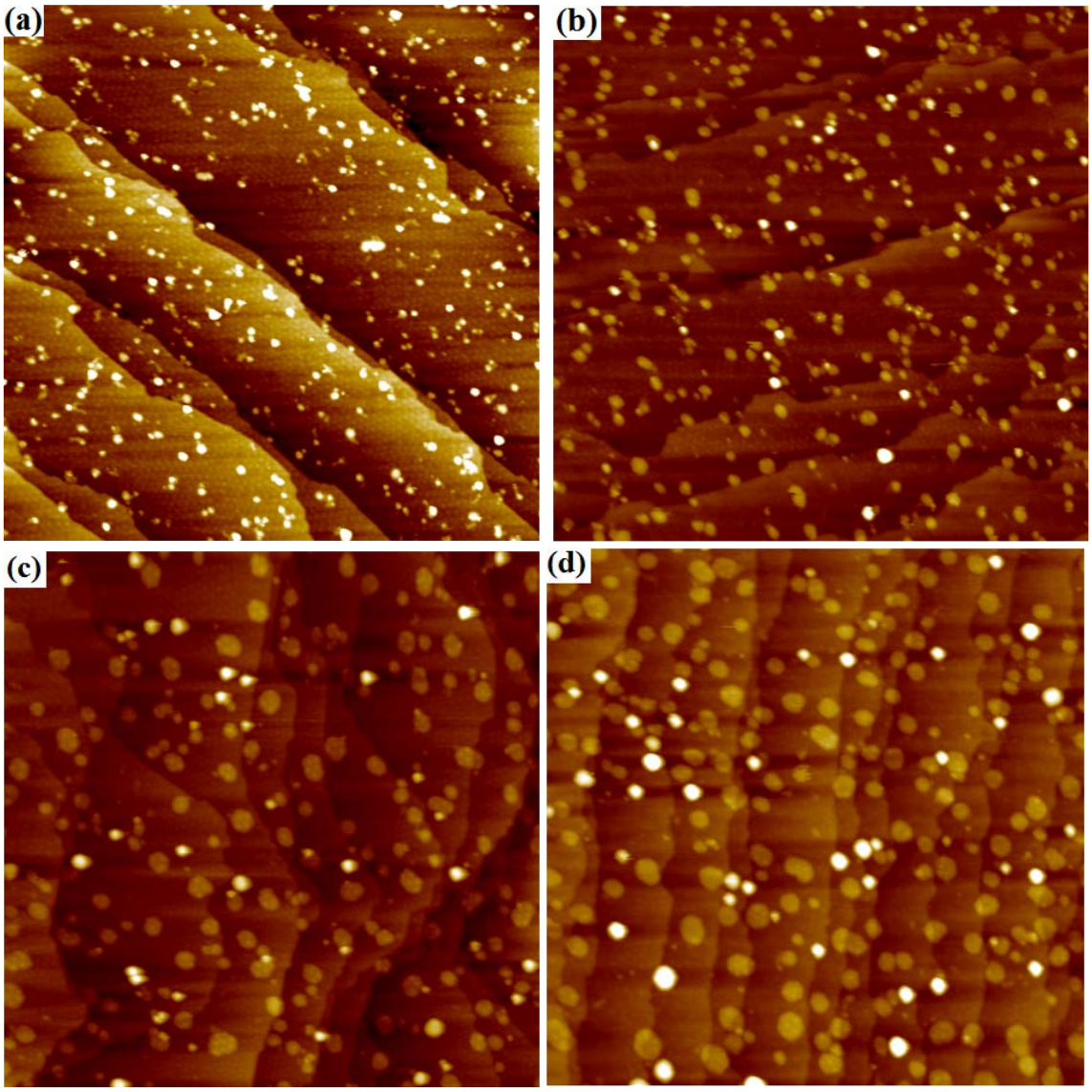

Fig. 36 Room temperature 200 nm × 200 nm STM images (V_b = 1.0 V, I_t = 0.1 nA) of Au supported on graphene/O/Ru(0001) at various dosages. (a) 0.10 ML, (b) 0.20 ML. (c) 0.40 ML, and (d) 0.60 ML.

4.3 Carbon-rich Graphene/Ru(0001)

Characterization of Carbon-rich Graphene/Ru(0001)

Carbon-rich graphene/Ru(0001) can be prepared by exposing graphene/Ru(0001) to atmosphere followed by slightly annealing the sample to 500 K in vacuum to remove any adsorbates, as described in the experimental section. Although graphene appears to be inert and should be stable upon exposure to air; however, we found evidence that this is not completely true. Fig. 37(a) and (b) are STM image and AES of graphene/Ru(0001) after exposure to air. Although STM image illustrates that the topography of the graphene almost remains the same except for some bright spots assigned to adsorbates from air such as H_2O, AES shows that the amount of carbon is increased dramatically. As mentioned in the previous chapter, the graphene coverage on Ru(0001) substrate can be monitored using the ratio of the positive to negative portions of the 272 eV Auger feature. For an essentially fully covered graphene surface, this ratio is 0.46, as shown in Fig. 9(a) (red line). After exposure to air, the ratio is decreased to approximately 0.25, indicating that lots of carbon is accumulated on the surface. Fig. 37(c) and (d) show the STM and AES results after slightly annealing the surface to 500 K for 30 min. No change was observed in AES but less bright spots were seen by STM, which could be due to removal of some adsorbates. Note that the moiré pattern in Fig. 37(c) appears to be a nanomesh structure, which is different from Fig. 37(a) because of a change in tip conditions instead of an alteration of the graphene structure. LEED was also taken before air exposure, after air exposure and after annealing. No change was observed, confirming that the graphene topography was not modified. One possible mechanism for

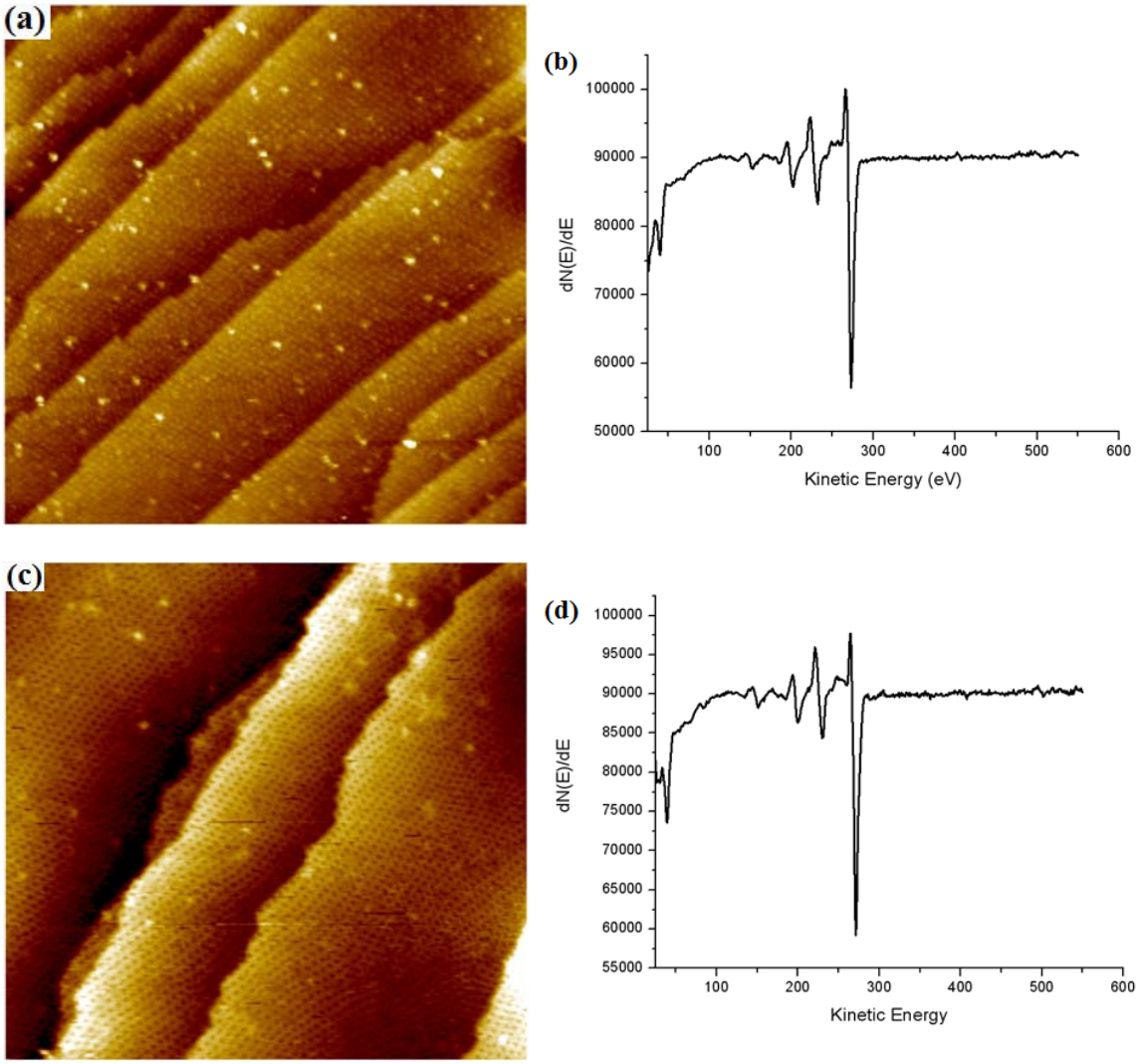

Fig. 37 Room temperature STM images and AES of carbon-rich graphene/Ru(0001) before and after annealing to 500 K for 30 min. (a) 200 nm × 200 nm STM image (V_b = 1.0 V, I_t = 0.1 nA) before annealing, (b) AES before annealing, (c) 200 nm × 200 nm STM image (V_b = 1.0 V, I_t = 0.1 nA) after annealing, and (d) AES after annealing.

the accumulation of carbon without any changes in graphene structure may be that as exposing to air, bare Ru surfaces that are not covered by graphene and other defects dissociate CO_2 in the air and the resutling carbon atoms then diffuse beneath the graphene and form a layer of amorphous carbon between the graphene and Ru substrate.

Deposition of Au on Carbon-rich Graphene/Ru(0001)

More interestingly, when Au atoms were deposited on carbon-rich graphene/ Ru(0001), highly dispersed 2-D clusters were observed on the surface by STM. Fig. 38(a) and (b) shows the STM images of 0.50 ML Au supported on the carbon-rich graphene. Except for a few large clusters nucleated on the step edge, all others appear to be small 2-D clusters with the same height. From the expanded STM image in Fig. 38(c), we can see the elongated round clusters as well as the moiré pattern underneath, confirming that these clusters indeed grow on the graphene surface. The line profile of the cluster illustrates that each cluster has a height of 0.55 nm, which is the same as the 2-D Au islands grown on graphene/Ru(0001). However, the size of the Au clusters are much smaller, only about 3 ~ 4 nm in diameter. As demonstrated by means of simple kinetic models for Au on oxide support, Au atoms prefer to form 3-D clusters because they are more stable thermodynamically. The reason why Au atoms form dispersed 2-D clusters is likely that graphene with amorphous carbon underneath may interact strongly with Au atoms. Note that the morphology is quite similar to that of Au deposited on W surface carbides W(110)/C-R(15 × 3), where two layers high Au clusters are self-assembled due to the mediation of the potential profile of the substrate [220]. The different diffusion

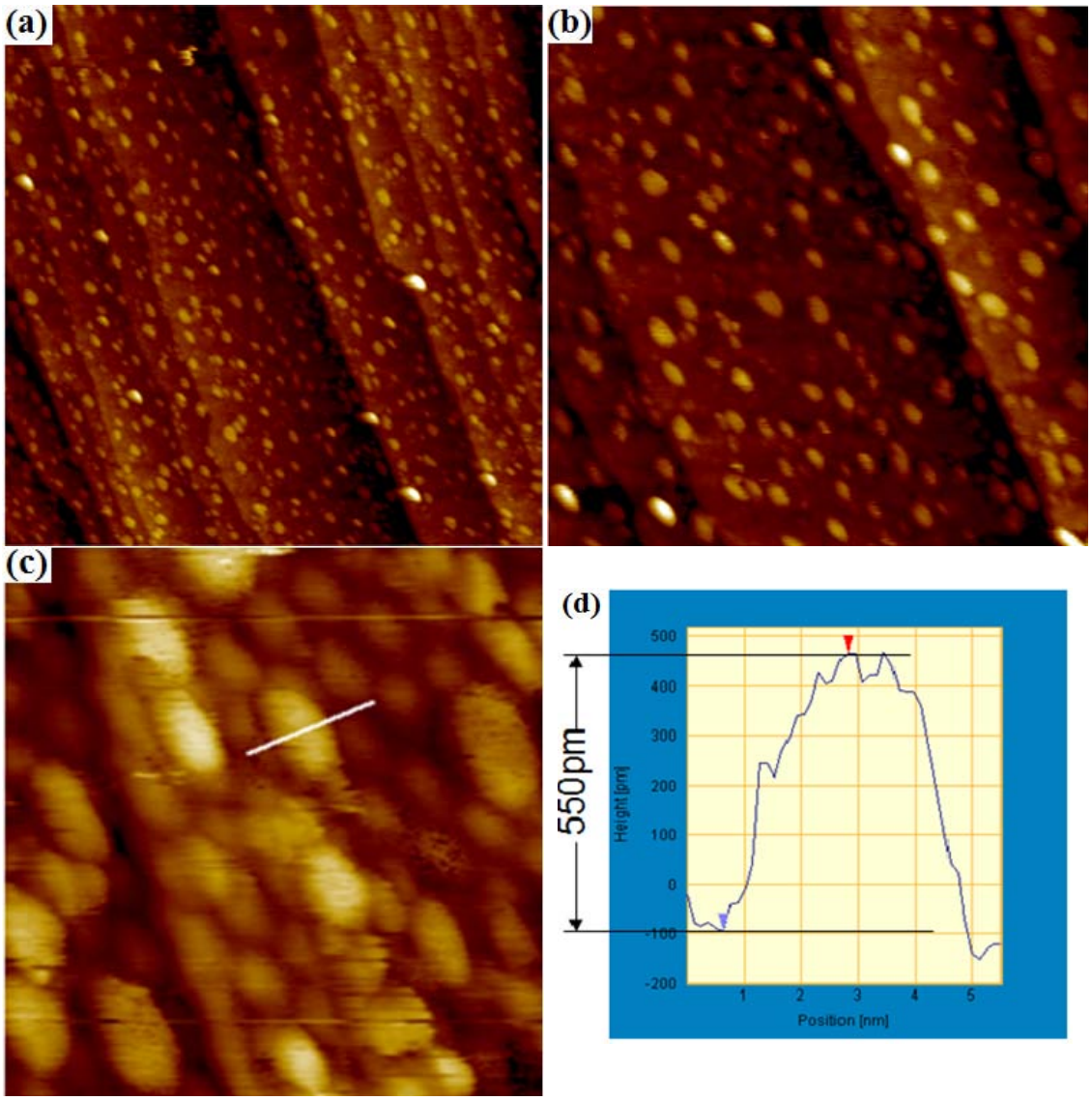

Fig. 38 Room temperature STM images of 0.50 ML Au supported on carbon-rich graphene/Ru(0001) and height profile (a) 200 nm × 200 nm, V_b = 1.0 V, I_t = 0.1 nA, (b) 100 nm × 100 nm, V_b = 1.0 V, I_t = 0.1 nA, (c) 20 nm × 20 nm, V_b = 1.0 V, I_t = 0.1 nA, and (d) line profile of an Au cluster marked by the white line in (c).

path lengths on different surfaces explain the difference in the cluster size on regular graphene and carbon-rich graphene. Obviously, the mobility of Au atoms adsorbed on carbon-rich graphene is much lower than Au atoms on graphene/Ru(0001). It is highly possible that both defects observed by STM as small bright spots and amorphous carbon underneath graphene play important roles in interacting with Au atoms.

The formation of highly dispersed 2-D Au clusters on the carbon-rich graphene is quite important in understanding the catalytic activity of Au clusters. As reported before [177], 2-D Au islands that are two layers high on oxide substrate exhibit an enhanced catalytic activity. Currently, two competing theories intend to explain such phenomena. One involves the quantum size effect of 2-D Au clusters, while the other emphasizes on the creation of an $Au^{\delta+}$ state due to electron transfer from Au to the oxide substrate. Since the carbon-rich graphene template for the two layer high 2-D Au clusters does not contain any oxygen, an investigation of catalytic activity on this system can help solve this important issue. The thermal stability and catalytic activity of this system is the subject of the ongoing studies.

4.4 h-BN Nanomesh

The Structure of h-BN Nanomesh on Ru(0001)

Hexagonal boron nitride (h-BN) is isoelectronic to graphene system because pairs of boron and nitrogen atoms have equal number of electrons as pairs of carbon atoms. Thus, h-BN shows a structure similar to that of graphene. Resembling graphene, h-BN could be prepared by chemical vapor deposition (CVD) method on many TMs,

including Ru(0001), Rh(111), Pt(111), Pd(111), Ni(111), Cu(111), etc [221-225]. Due to the different interactions between h-BN and the TM substrate, h-BN exhibits different topographies [225]. Strong interactions between the h-BN film and substrates like Ru(0001) and Rh(111) lead to a nanomesh structure. However, for substrates like Pt(111) and Pd(111), which have very weak interactions with the h-BN film, moiré pattern structures similar to graphene/Ru(0001) are formed. Whereas, h-BN forms an atomically flat overlayer on Ni(111) and Cu(111) due to negligible lattice mismatch between h-BN and the substrates. Among these structures, the nanomesh structure has received the most extensive attention because they can be a promising oxygen-free nanotemplate for both molecules and metal clusters. Some STM studies have shown that organometallic molecules such as $C_{32}H_{16}CuN_8$ [226] and metals like Co [227] and Au [228] can be successfully trapped in the pores of the h-BN nanomesh. Therefore, a h-BN nanomesh can potentially serve as a template to fabricate uniform array of molecules and nanoclusters. Furthermore, studying the metal growth on h-BN film can help understand the mechanism of metal growth on graphene systems.

h-BN/Ru(0001) was prepared following the recipe in the experimental section. Fig. 39 shows a typical STM image and LEED pattern of h-BN/Ru(0001). The STM image reveals that the connected wires and round pores compose the nanomesh structure, where the strongly bounded regions are assigned to the pores, whereas the weakly bounded regions are assigned to wire areas. Note that only N atoms could be resolved in the STM image. Consequently pores result from strong N-substrate interactions and wires are from areas where the N atoms have weak interaction with the substrate [223].

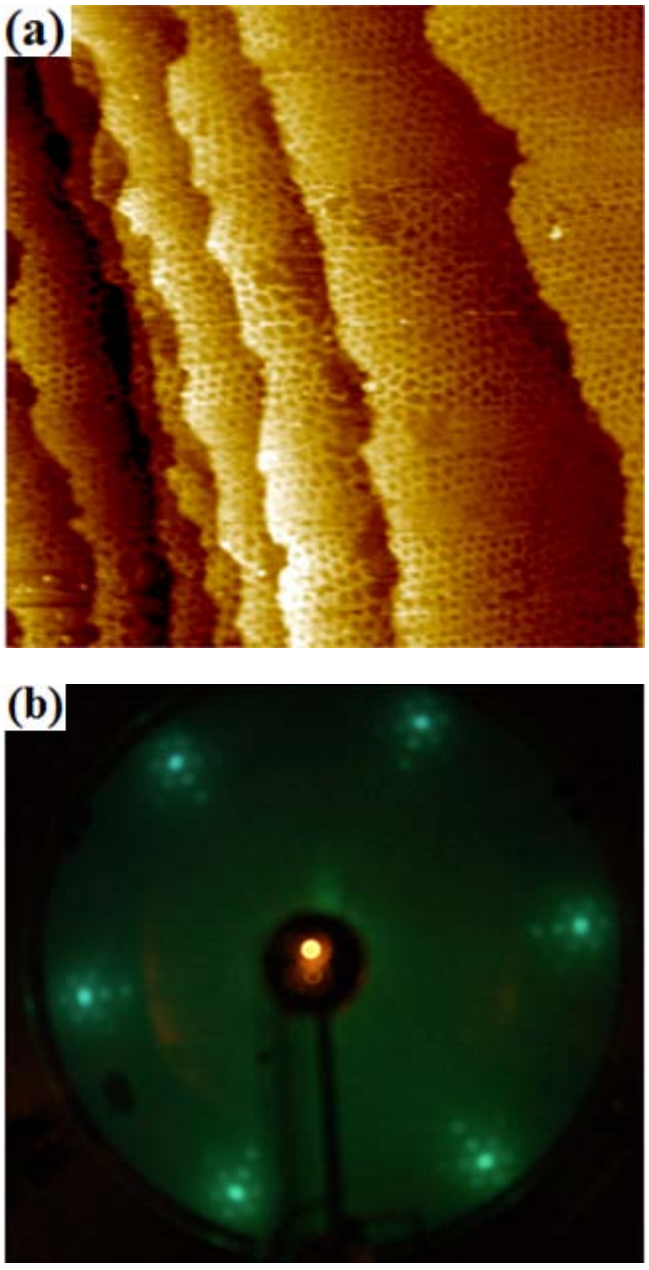

Fig. 39 (a) Room temperature 150 nm × 150 nm STM image (V_b = 1.0 V, I_t = 0.1 nA) of h-BN/Ru(0001). (b) LEED pattern of h-BN/Ru(0001).

The size of each unit cell has been measured to be 3.2 nm on average, which consists of (13 × 13) h-BN units on (12 × 12) Ru atoms, and the diameter and depth of the pore have been measured to be around 2 nm and 0.1 nm, respectively, which is consistent with previous studies [224]. In addition, defects and irregular pores can be observed, which is typical for h-BN film prepared on Ru(0001). The reason is that Ru(0001) has the strongest interactions with a h-BN film among all TM substrates studied so far [225]. As borazine reacts with a Ru substrate, a high density of nucleation sites arises and the growth of small pieces of h-BN film from these nucleation sites leads to irregular defects on the boundaries between neighboring pieces. The LEED pattern was similar to that of graphene/Ru(0001), which is consistent with (12 × 12) coincidence lattice. AES was also taken (data not shown), in which both the N peak at 380 eV and the B peak at 179 eV can be observed. The h-BN coverage on the Ru(0001) substrate can be monitored using the ratio of the 379 eV Auger peak to 272 eV peak. For an essentially fully covered h-BN surface, this ratio is 0.20, which is confirmed by STM measurements.

Deposition of Au on h-BN/Ru(0001)

Apparently, the regular hexagonal structure of 2 nm wide pores on h-BN film can be viewed as an array of trapping sites at which deposited metal atoms may preferentially nucleate, thereby allowing an array of metal nanoparticles to form with a size determined by the pore size. In addition, the corrugation of the h-BN nanomesh may hinder the sintering of the metal particles. For these reasons, the deposition of Au clusters on h-BN film was investigated. Fig. 40 shows STM images of 0.05 ML Au

deposited on h-BN/Ru(0001). Highly dispersed round 2-D and 3-D clusters with diameter from 2 nm to 3 nm were observed on the surface. The enlarged STM image, as shown in Fig. 40(b) displays that most of the small clusters are trapped in the pores, as expected, indicating that Au clusters preferentially nucleate at the pores.

As the Au dosage was increased, both the density and size of Au clusters were increased proportionally, as shown in Fig. 41, where 0.10 ML, 0.30 ML and 0.60 ML Au were deposited on the h-BN/Ru(0001). 2-D clusters with two layers coexist with 3-D clusters which are higher than 1.0 nm. At a coverage of 0.10 ML, it is clearly observed that almost all of the small clusters centered at namomesh apertures, whereas, the big 3-D nanoparticles with diameters greater than 3 nm are substantially larger than a single pore, as shown in Fig. 41(b). At coverages of 0.30 ML and 0.60 ML, the nanomesh structure of the substrate could not be resolved by STM due to a relatively high density of both 2-D and 3-D Au clusters.

The thermal stability of Au clusters supported on h-BN nanomesh was also investigated. Fig. 42 shows STM images of 0.60 ML Au deposited on h-BN film before and after annealing to different temperatures for 10 min. At 550 K, the morphology of the Au does not change significantly. Similar to STM images taken before annealing, both 2-D and 3-D clusters coexist with the original size and density. As the annealing temperature was increased to 750 K, sintering occurs as seen by the decrease in the density of clusters and an increase in the cluster size, as shown in Fig. 42(c). Even though large 3-D clusters dominated the surface, some small 2-D clusters could still be observed. Further annealing to 900 K for 10 min leads to the formation of large 3-D

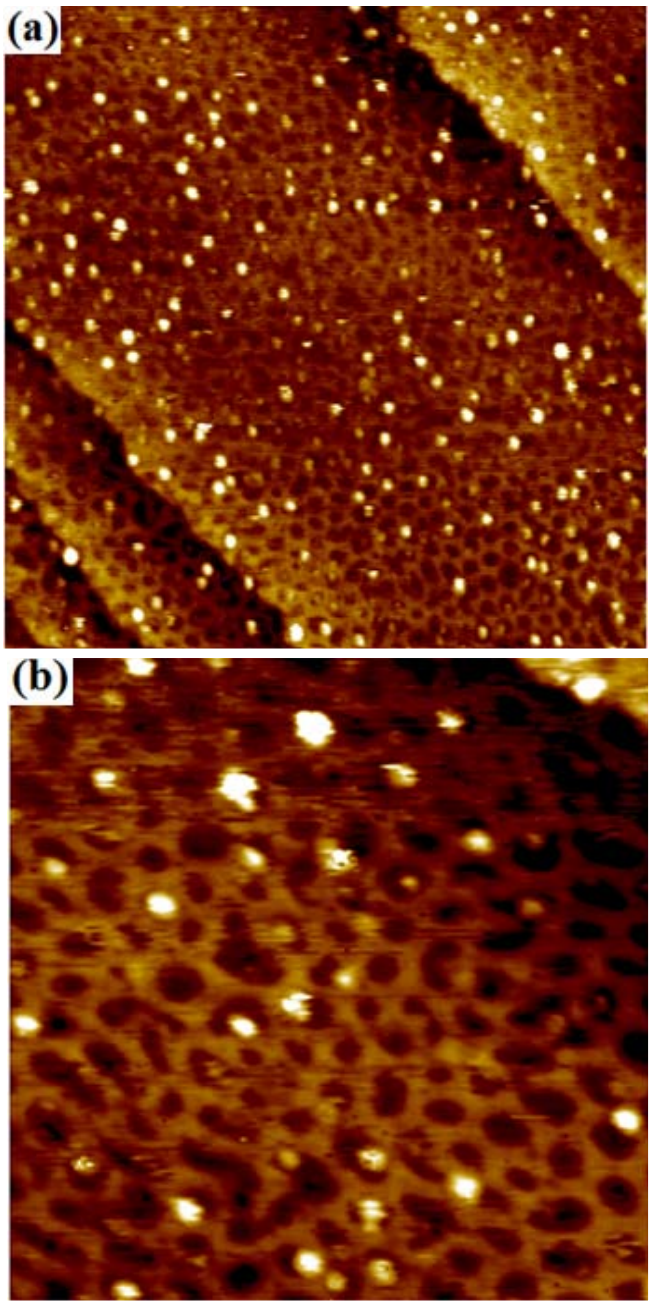

Fig. 40 Room temperature STM images of 0.05 ML Au deposited on h-BN/Ru(0001). (a) 100 nm × 100 nm, V_b = 1.0 V, I_t = 0.1 nA, and (b) 40 nm × 40 nm, V_b = 1.0 V, I_t = 0.1 nA.

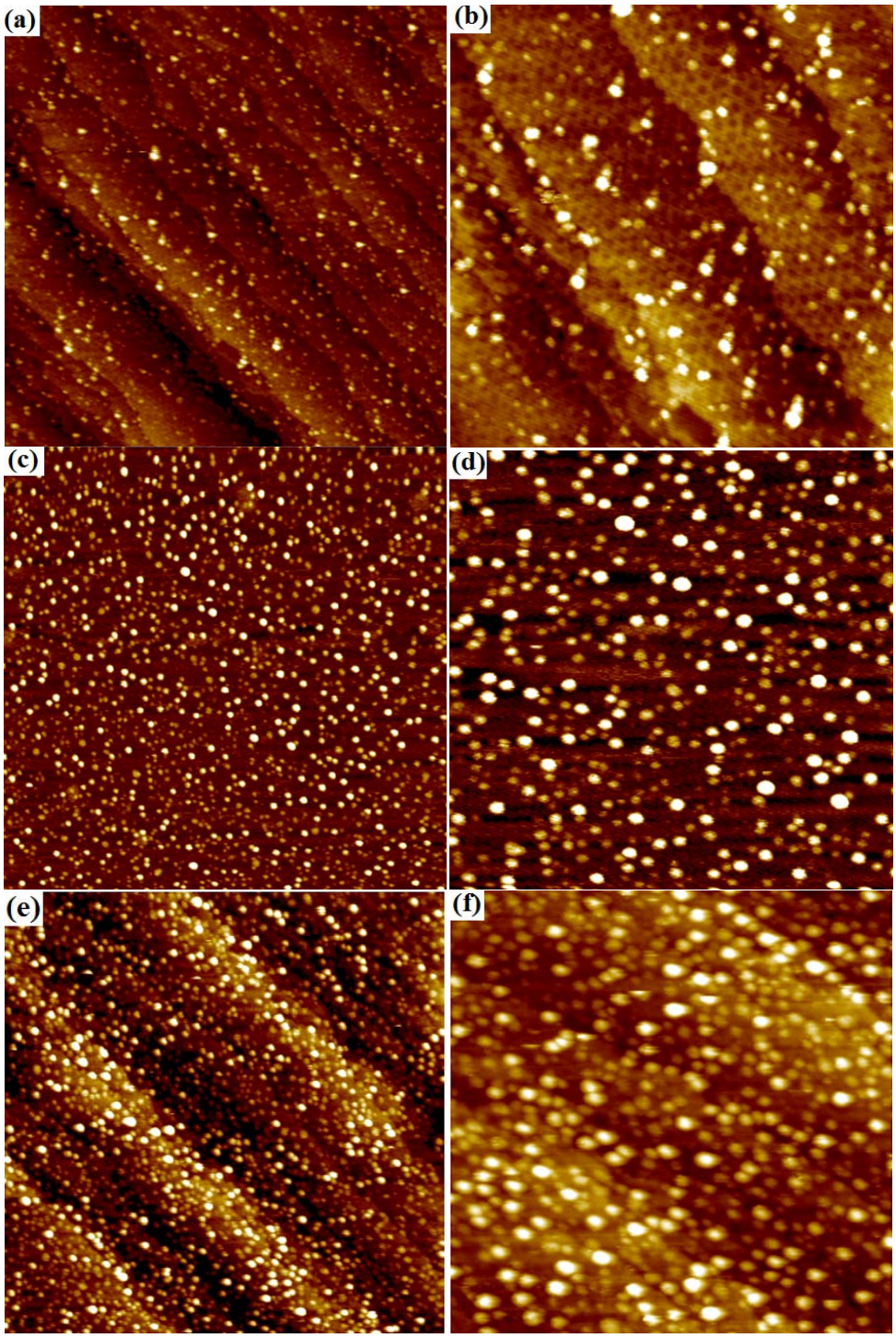

Fig. 41 STM images (V_b = 1.0 V, I_t = 0.1 nA) of various Au dosage deposited on h-BN/Ru(0001) (a) 0.10 ML Au, 200 nm × 200 nm, (b) 0.10 ML Au, 100 nm × 100 nm, (c) 0.30 ML Au, 200 nm × 200 nm, (d) 0.30 ML Au, 100 nm × 100 nm, (e) 0.60 ML Au, 200 nm × 200 nm, (f) 0.60 ML Au, 100 nm × 100 nm.

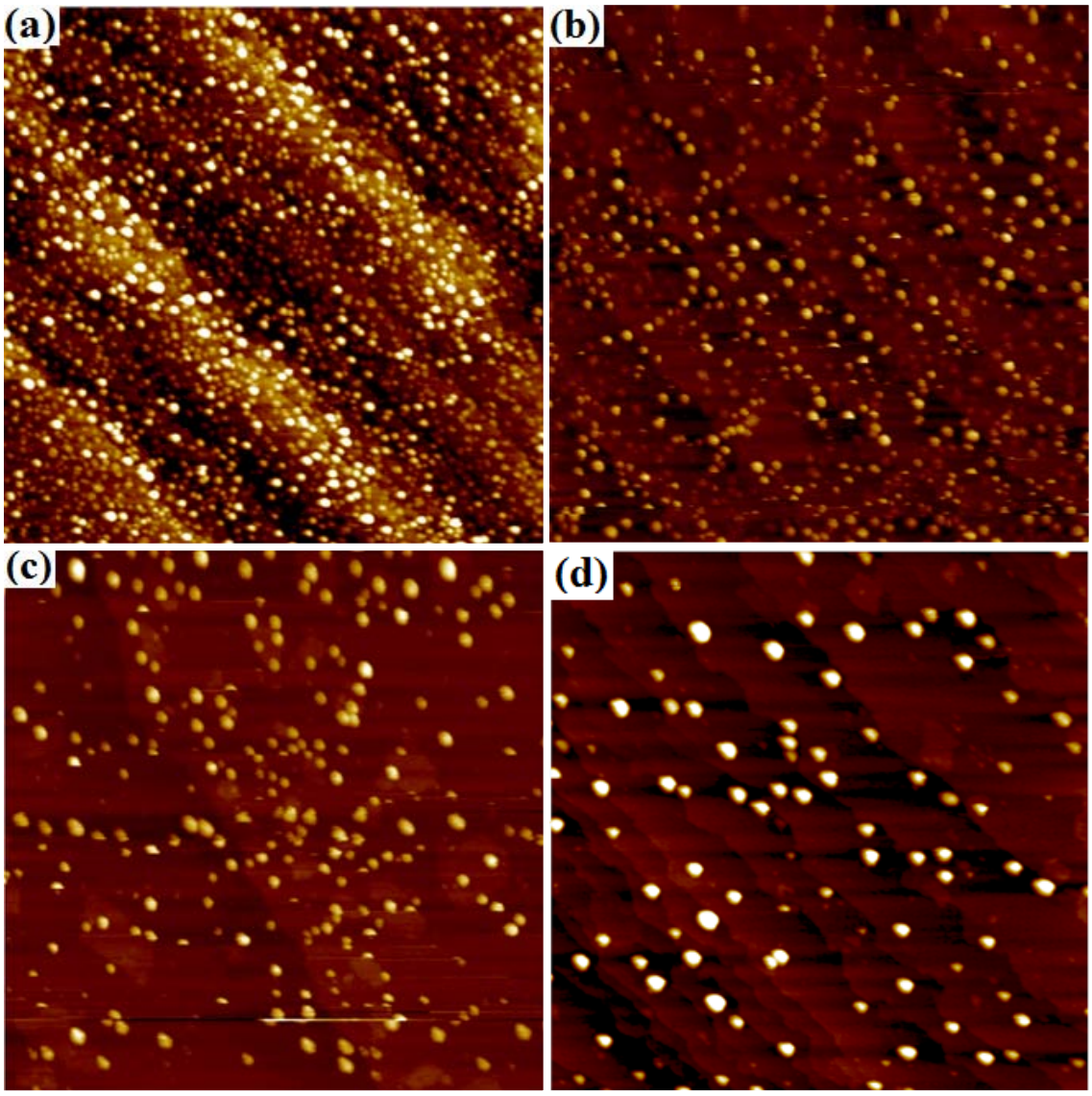

Fig. 42 STM images (200nm × 200 nm, V_b = 1.0 V, I_t = 0.1 nA) of 0.60 ML Au deposited on h-BN/Ru(0001) before and after annealing to different temperatures. (a) Room temperature, (b) 550 K, (c) 750 K, and (d) 900 K. All images are acquired after the sample has been cooled to room temperature after a 10 min annealing.

clusters with sizes larger than 5 nm as well as a remarkable decrease in cluster density. Close examination reveals that all 2-D clusters disappear after 900 K annealing. The nanomesh structure could still be resolved by STM on the areas not covered by clusters, suggesting that the h-BN nanomesh is stable upon annealing to 900K, which is consistent with the thermal stability of h-BN film without deposition of Au clusters. Note that these large round clusters are randomly distributed on the terrace instead of nucleating only at step edges, which means that the pores on the h-BN nanomesh are capable of trapping Au clusters. As expected, the h-BN nanomesh can hinder the sintering process of Au nanoparticles because the corrugation of the h-BN nanomesh can effectively lower the mobility of Au atoms even at an annealing temperature of 500 K.

Besides the thermal stability, the stability under reaction conditions is also of great importance for catalysts. In our study, we also studied the morphology of Au clusters supported on h-BN/Ru(0001) after exposure to reactant gases at room temperature. Fig. 43 (a) and (b) show the STM images of 0.60 ML Au deposited on h-BN after exposure to 1 atm O_2 at room temperature for 5 min and Fig. 43 (c) and (d) display the STM images of 0.60 ML Au after exposure to 1 atm CO at room temperature for 5 min. From the images we can see that both 2-D and 3-D clusters coexist on the surfaces and no noticeable change could be observed after exposure to the gases, indicating that Au clusters supported on h-BN nanomesh are stable upon exposure to CO or O_2 at room temperature. Thus h-BN nanomesh can be an excellent template to fabricate nanoparticles which are both thermally and chemically stable.

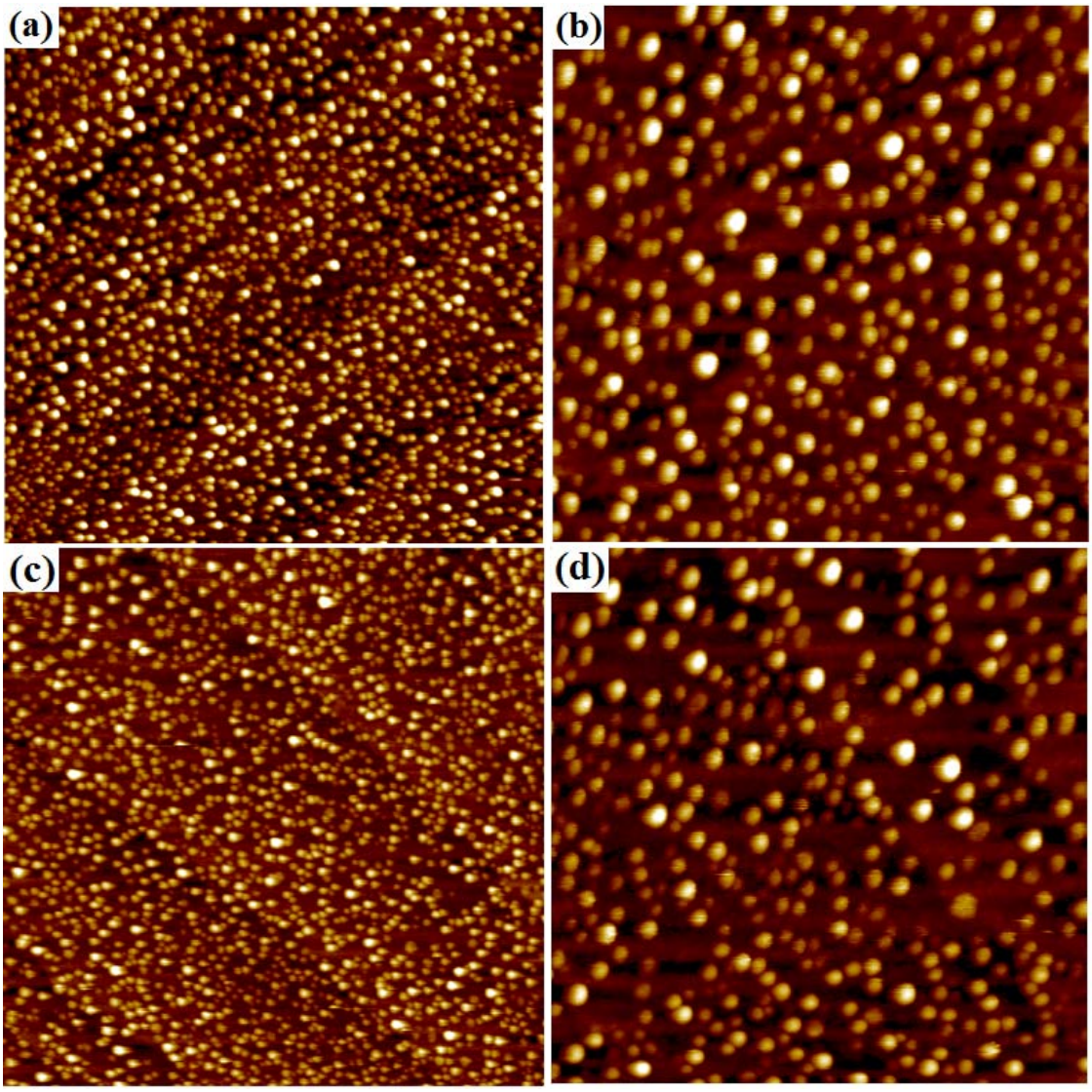

Fig. 43 (a) 200 nm × 200 nm and (b) 100 nm × 100 nm STM images of 0.60 ML Au deposited on h-BN/Ru(0001) after exposure to 1 atm O_2 at room temperature for 5 min. (c) 200 nm × 200 nm and (d) 100 nm × 100nm STM images of 0.60 ML Au deposited on h-BN/Ru(0001) after exposure to 1 atm CO at room temperature for 5 min. The images were taken in vacuum after pumping down the gases and scanning conditions are: V_b = 1.0 V and I_t = 0.1 nA.

Comparisons between h-BN and Graphene

Although h-BN nanomesh and graphene/Ru(0001) are isoelectronic systems, they exhibit different structures and also show different properties when interacting with metal clusters. Graphene/Ru(0001) exhibits typical moiré pattern which could extend to a few μm^2 on Ru terraces, while h-BN/Ru(0001) shows nanomesh structure with pores and wires with many defects. Both of them have the potential to fabricate metal clusters by nucleating at specific sites on the surface, e.g. fcc or hcp sites for graphene, and pores for h-BN; however, the natural properties of the interaction are quite different. When it comes to deposition of Au on both surfaces, we found that Au forms large 2-D islands on graphene/Ru(0001), whereas coexistence of 2-D and 3-D round clusters that are highly dispersed on h-BN/Ru(0001) was observed. Apparently, the shorter diffusion lengths of Au atoms on the h-BN/Ru(0001) nanomesh indicate that h-BN nanomesh has a stronger interaction with Au due to to its special geometric structures. The pores on the surface could effectively trap the Au atoms and the wires could successfully reduce the mobility of Au atoms.

5. DEPOSITION OF METALS ON ULTRA-THIN SILICA FILM

Thin oxide films grown on refractory single crystals have received extensive attention in the last two decades because such prepared thin films are free of the charging problem that most surface science techniques encountered when studying bulk oxides. Since silica is one of the most important oxide supports in catalysts, ultra-thin silica film supported on single crystals is an excellent substitute for bulk oxide in model catalysts studies. In the early 1990's, Goodman and coworkers successfully prepared amorphous silica thin film on Mo single crystals [229,230]. And later, well-ordered ultra-thin silica films supported on Mo(112) was synthesized by Schroeder and coworkers [231]. Since then, both experimental and theoretical efforts have been devoted to understanding the structure of the silica thin film and applying it to model catalyst studies as a support [232]. In our studies, we studied the structure of the ultra-thin silica film supported on Mo(112) and investigated the morphologies, growth mechanism, and thermal stability of three diffferent catalytically important metals, e.g. Rh, Pt, and Pd, supported on silica thin film.

5.1 The Structure of Ultra-thin Silica Film on Mo(112)

Although it has been a decade since first fabrication of well-ordered silica thin film on Mo(112), the structure of the film is still controversial. Two reasonable models have been proposed for the film. One is the 2-D network model, as shown in Fig. 44(a), suggested by Weissenrieder *et al.* [233] based on STM images and DFT calculations.

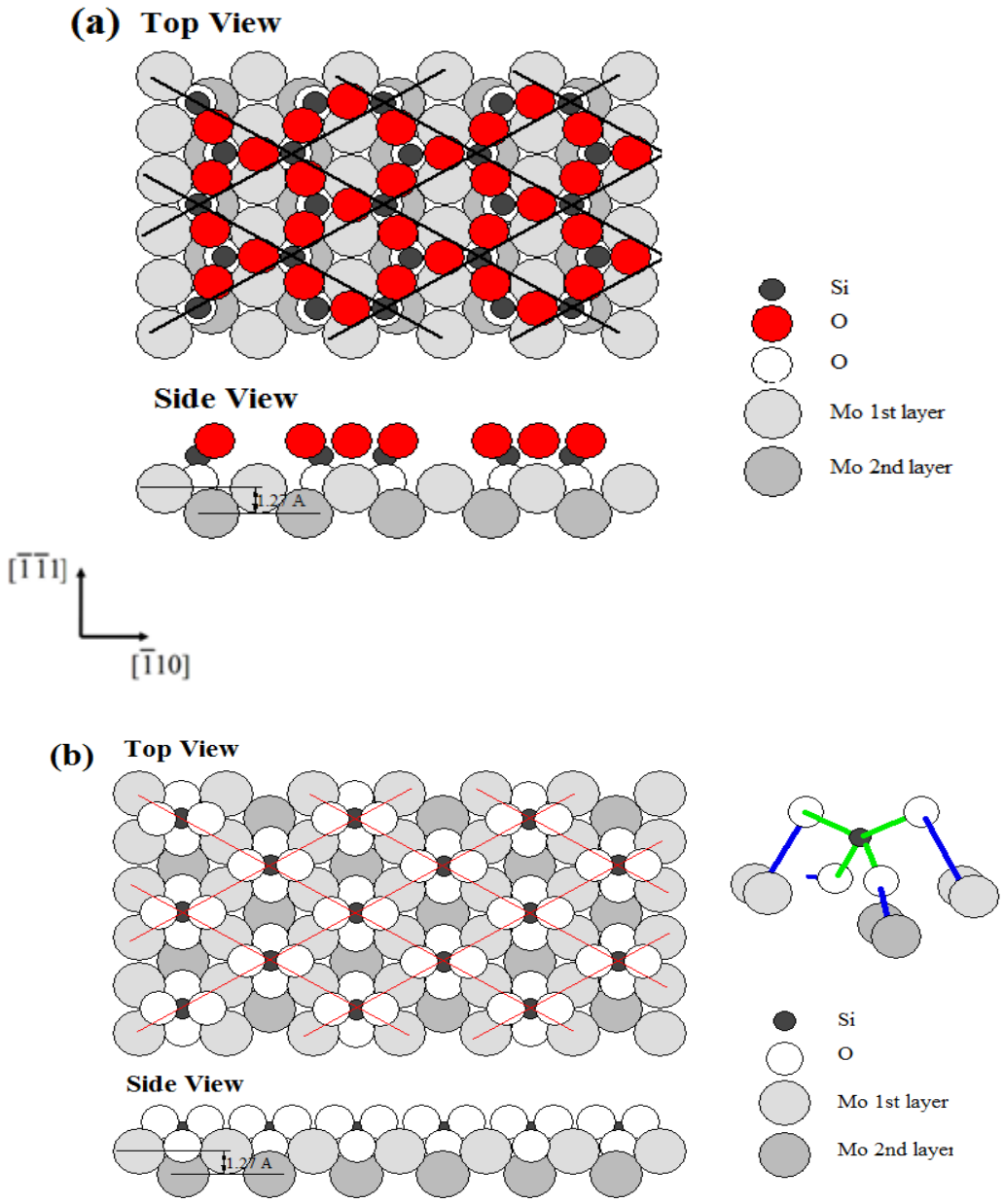

Fig. 44 (a) 2-D network model for silica thin film on Mo(112). (b) Cluster model for silica thin film on Mo(112).

The other model is the so-called cluster model, which is proposed by Chen *et al.* [234] based on STM and HREELS data. In this model, the [SiO_4] tetrahedral is isolated on the Mo(112) substrate, as shown in Fig. 44(b). As a matter of fact, there is no need to claim that one model is correct and the other is wrong, in that there may be two different types of silica films due to different preparation procedures, as pointed out by Kaya *et al.* [232]. In Weissenreider group, the multi-layer silica film was desorbed by annealing the sample in UHV [233] while Chen and coworkers removed the multi-layer silica by annealing in the presence of O_2 (10^{-8} ~ 10^{-7} Torr) [234,235]. Thus, the silica film annealed in O_2 environment, the so called O-rich silica film, may have extra oxygen atoms adsorbed on the Mo(112) sample, which is different from the O-poor silica film annealed in UHV.

In our studies, we fabricated the silica film on Mo(112) following Chen's recipe, as described in the experimental section. Fig. 45 shows high resolution STM images at different scanning voltages of ultra-thin silica film grown on Mo(112). Fig. 45(a) exhibits one bright spot in a c(2 × 2) unit cell. Fig. 45(b) shows a structure of pairs of bright spots, in which the pairs in the $[\bar{1}10]$ direction are much brighter than the other spots outside the row. In Fig. 45(c), the bright spot in each unit cell could be resolved and a line structure was also observed. Fig. 45(d) shows a structure similar to a nanomesh, where triangular protrusions consist of the "wire" area, whereas darker areas are pores. Closer examination reveals that there is one bright spot on each triangular protrusion. When the bias was reversed during scanning the surface, there was no contrast reversal. In addition the position of these bright protrusions did not change

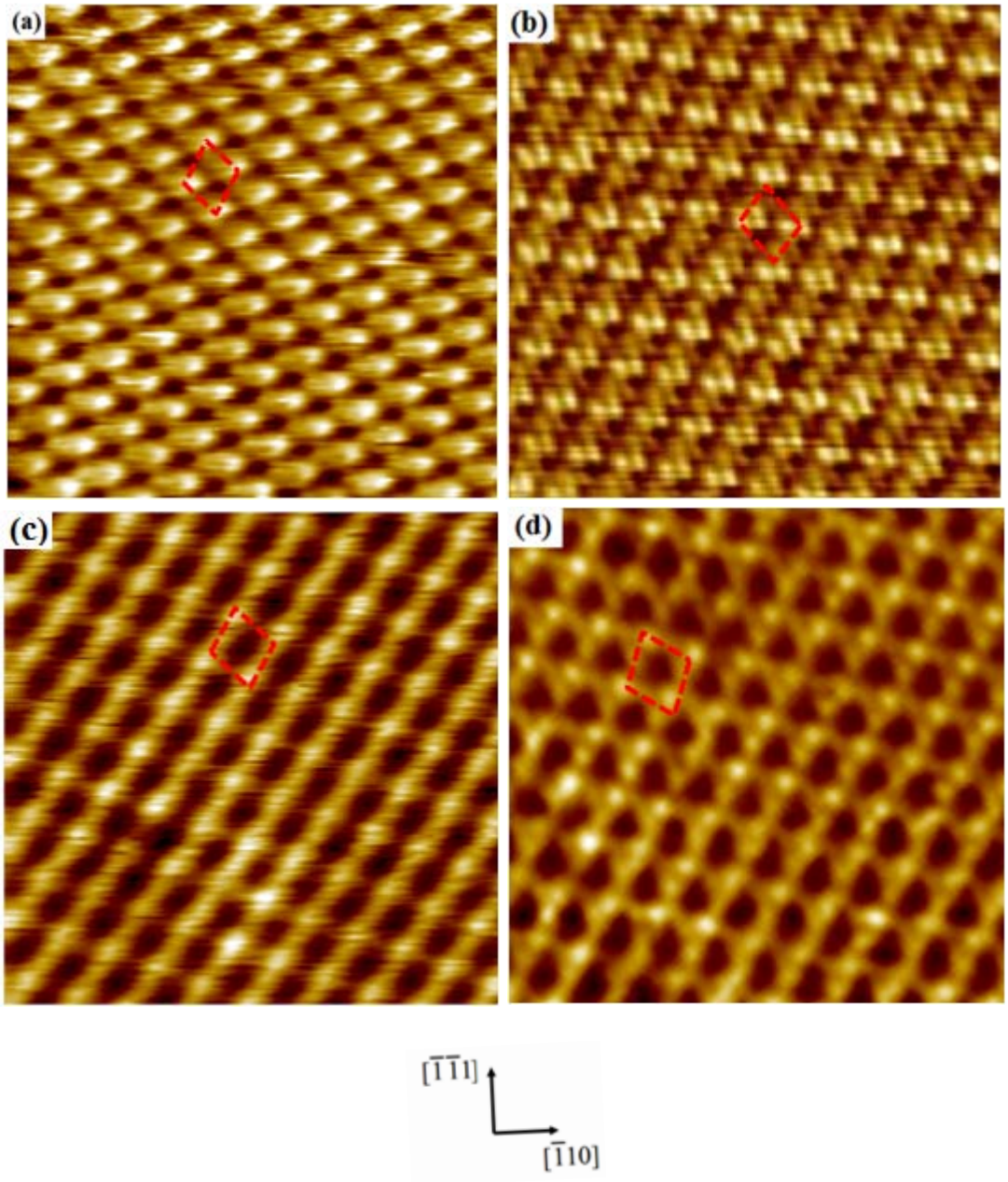

Fig. 45 Room temperature 5 nm × 5 nm STM images of ultra-thin silica film supported on Mo(112) at various sample bias voltages. Tunneling parameters are (a) V_b = 2 V, I_t = 1 nA, (b) V_b = 0.4 V, I_t = 1 nA, (c) V_b = -0.4 V, I_t = 1 nA, and (d) V_b = -0.8 V, I_t = 1 nA. The unit cell has been marked by dashed red lines in each image.

when we reversed the bias but only the pattern changed, consistent with previous studies [234]. Therefore, the bright protrusions in these figures correspond to the same surface features on the silica film. The change in pattern that we observed might be only due to a different tip-sample separation.

Our STM images agree well with the cluster model proposed by Chen *et al*. The bright protrusions in Fig. 45 could be assigned to the appropriate atoms in the cluster model based on different scanning conditions, as shown in Fig. 46, where the tunneling areas that correspond to the bright features in each STM images have been marked. In principle, an STM measures the DOS contributed by the Mo 5d electrons combined with the hybridized electron orbitals of [SiO_4] tetrahedral on the surface, as pointed out by calculations of electronic structures of the ultra-thin silica film [236]. The contrast and pattern of STM images highly depend on the extent of the overlap between the tip state and the surface state. At large scanning voltages, the tip-surface separation is so large that STM tip only overlaps with the outmost surface states of the surface. Thus, in Fig. 45(a) only single bright spots representing [SiO_4] tetrahedral clusters could be observed by STM. As the tunneling current was reduced, the tip-surface separation was also decreased, which leads to a better overlap between the tip state and the surface state. Therefore, the fine structure of the surface could be resolved by STM, as shown in Fig. 45(b). With a positive bias applied on the sample, the tunneling current flows from the tip to the topmost oxygen atoms, whose state is deficient in electrons and thereby accepts the tunneling electrons. Consequently, two bright protrusions or double-spot unit are assigned to the two topmost oxygen atoms. When changing the bias to the negative

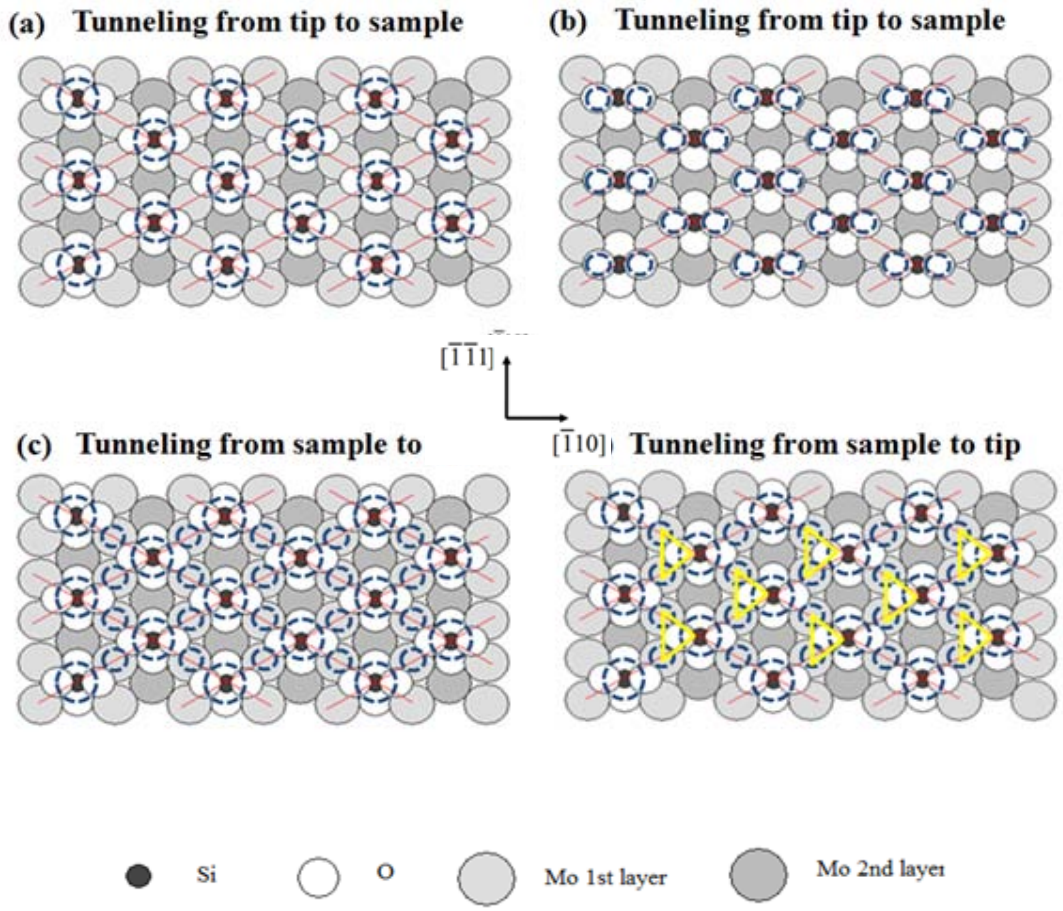

Fig. 46 Cluster models of silica thin film with tunneling areas marked by dashed circles and yellow triangles. Models (a), (b), (c), and (d) correspond to the STM images shown in Fig. 45.

values, the tunneling flows from the sample to the tip. Now the Mo substrate which has sufficient electrons also contributes to the tunneling current. Therefore, the network structure was observed in Fig. 45(c) and (d) due to the tunneling from both the (1 × 1) Mo(112) substrate and the c(2 × 2) units of silica. Note that Fig. 45(d) shows triangular protrusions, which are assigned to the combination of the [SiO_4] tetrahedrals and first layer Mo atoms, as marked by yellow triangles. The STM images obtained above are consistent with the results reported by Chen *et al*. [234]. In the following sections, we will adopt the cluster model when investigating the adsorption sites of metal clusters on the ultra-thin silica film.

5.2 Rh Clusters Supported on Ultra-thin Silica Film

Morphologies of Rh Clusters

The nucleation of Rh atoms on ultra-thin silica film/Mo(112) was studied by STM. Fig. 47 displays STM images of 0.01 ML Rh supported on the silica thin film. In Fig. 47(a), in addition to the small Rh clusters, some protrusions with a structure like bright wires (marked by red circle) or rings (marked by green circle) were observed. Closer examination, as shown in Fig. 47(b), reveals that the bright wires are located in the middle of two neighboring rows of the substrate. In addition, bright spots located right on top of the rows were observed in both Fig. 47(a) and (b), as marked by blue circles. More interestingly, the height of these bright features has been measured to be 0.06 nm, which is much lower than the size of a single Rh atom.

The bright rows in Fig. 47(a) and (b) are assigned to lines of [SiO_4] clusters, as

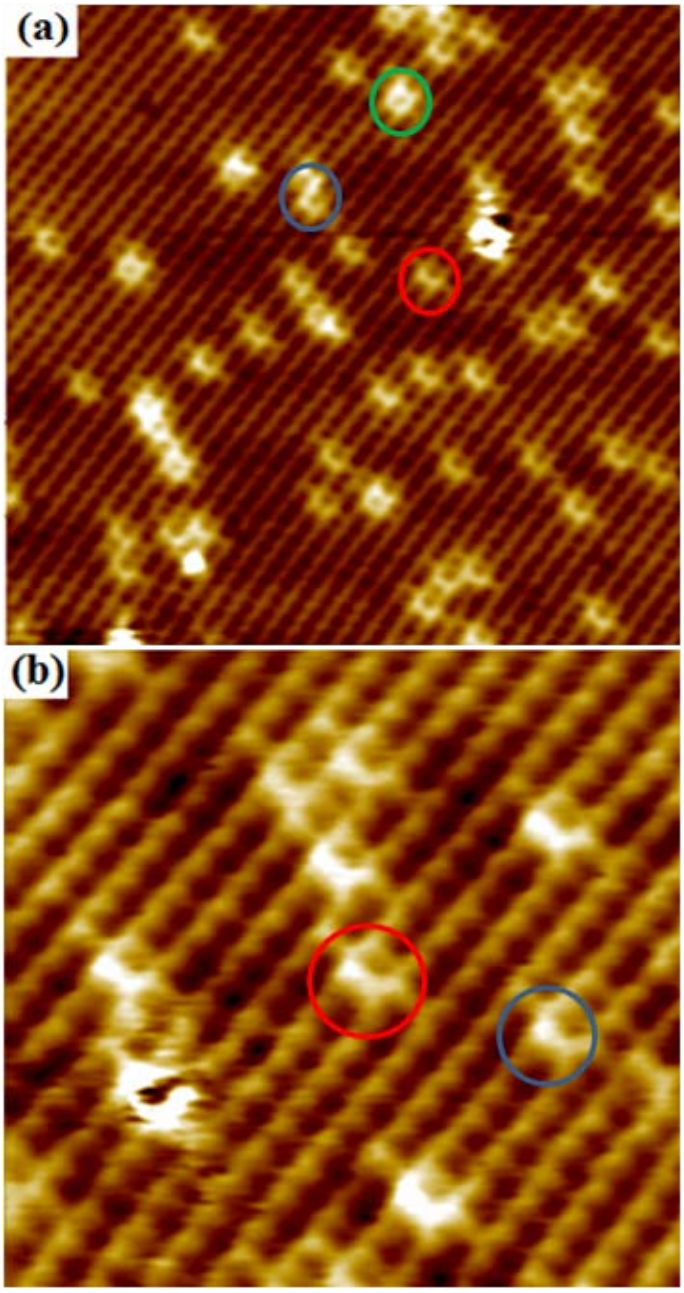

Fig. 47 Room temperature STM images of 0.01 ML Rh clusters supported on ultra-thin silica film/Mo(112) at various scanning conditions. (a) 15 nm × 15 nm, V_b = 0.6 V, I_t = 0.5 nA, and (b) 7 nm × 7 nm, V_b = -0.5 V, I_t = 0.5 nA. Some features are marked by circles with different colors. See text for details.

discussed in the previous section. Based on the height, shape and locations of these bright protrusions, the nucleation site of Rh atoms is on top of the first layer Mo atoms, surrounding by two [SiO_4] units. Fig. 48(a) is the atomic model showing the adsorption sites of Rh atoms on silica film, where the yellow lines stand for the bright lines in STM images in Fig. 47. The bright wire connecting neighboring rows is assigned to a single Rh atom sitting between two [SiO_4] units on different yellow lines, as marked by the red circle. Bright spots located on top of the bright lines are Rh atoms nucleated between two [SiO_4] units on the same yellow line, as marked by the blue circle. The ring structure is assigned to four Rh atoms nucleated on four neighboring first layer Mo atoms, as shown by the green circle. Note that the ring structure is attributed to the combination of the electronic structure of Rh atoms and [SiO_4] units. The distance between the neighboring Si atoms is 0.522 nm in the cluster model and the empirical diameter of oxygen atom is only about 0.12 nm so that the room between two [SiO_4] units is sufficient to fit a single Rh atom. Note that the distance among the neighboring Rh clusters or single Rh atoms is quite small, which is always less than 5 nm, suggesting that Rh atoms adsorb on the ultra-thin silica film so strong that the diffusion length of Rh atoms on silica thin film should be less than 5 nm.

The morphologies of the Rh clusters at higher dosages were also studied, as shown in Fig. 49 and Fig. 50, which show that STM images acquired at various Rh coverages from 1.0 to 4.0 ML, as well as the size histograms based on the randomly chosen 100 nm × 100 nm images at indicated coverage. At 1.0 ML, in addition to a few of large clusters, the sizes of most Rh clusters are between 2 nm and 3 nm. And most

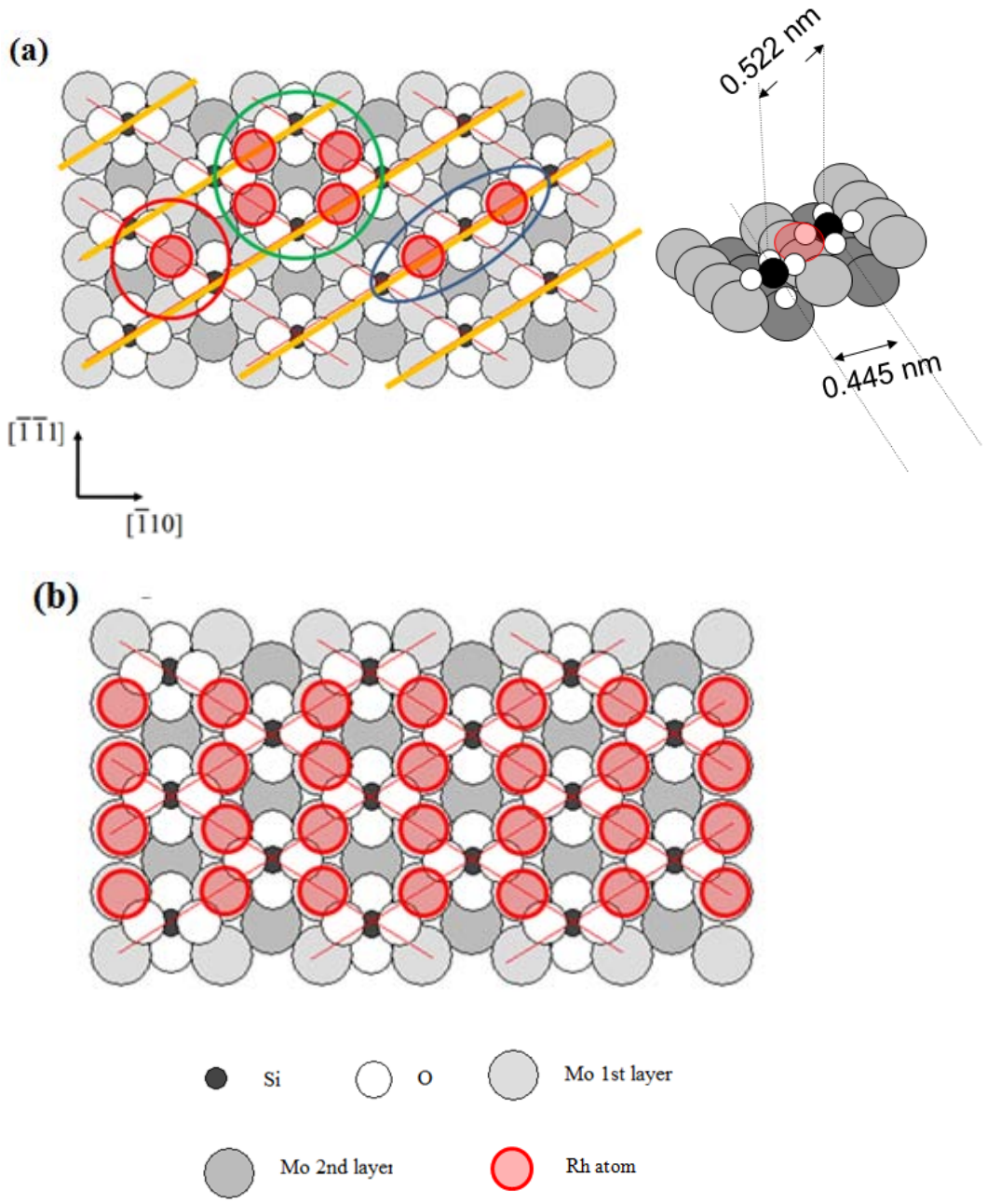

Fig. 48 The atomic models of Rh atoms nucleated on the silica thin film. (a) Room temperature. (b) After annealing to 500 K and 600 K.

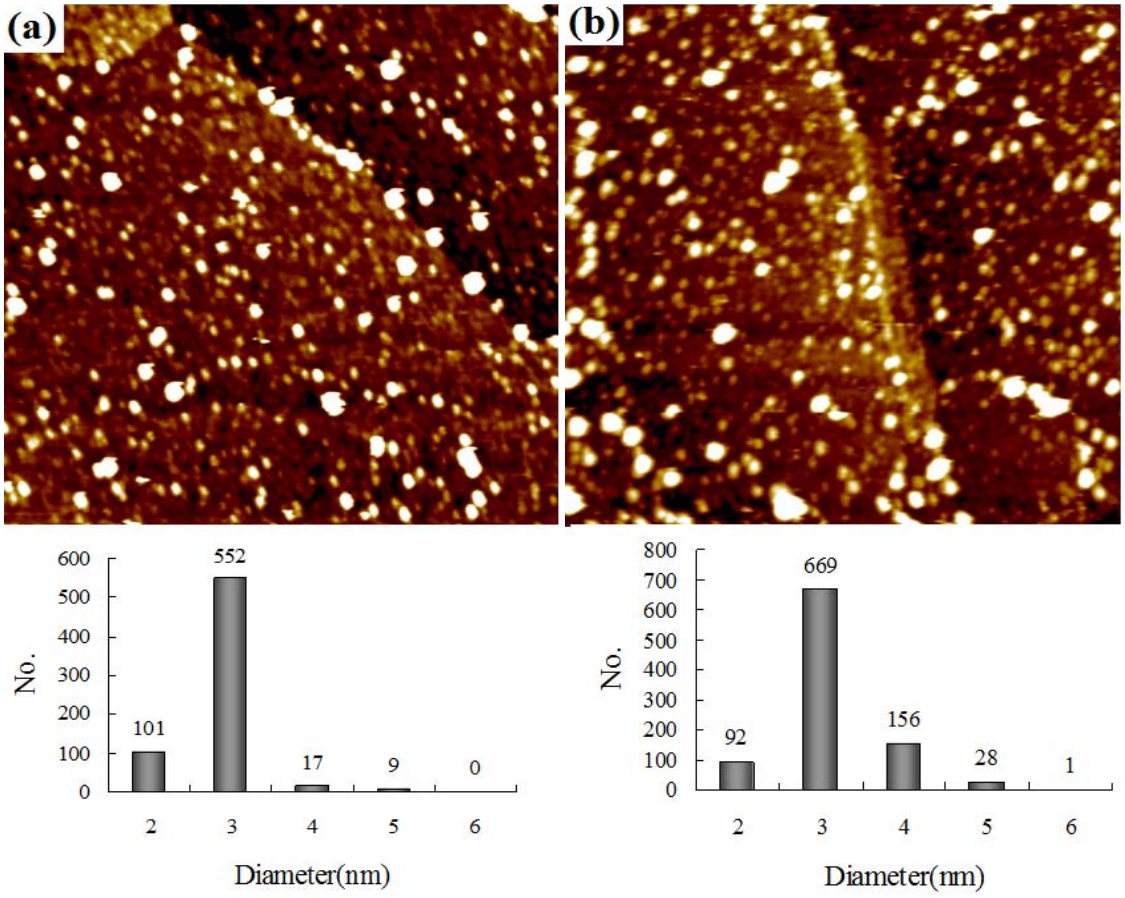

Fig. 49 Room temperature 100 nm × 100 nm STM images and cluster size distributions of Rh clusters on ultra-thin silica film at various coverages. (a) 1.0 ML Rh, V_b = 1.0 V, I_t = 0.1 nA, and (b) 1.5 ML Rh, V_b = 1.0 V, I_t = 0.1 nA.

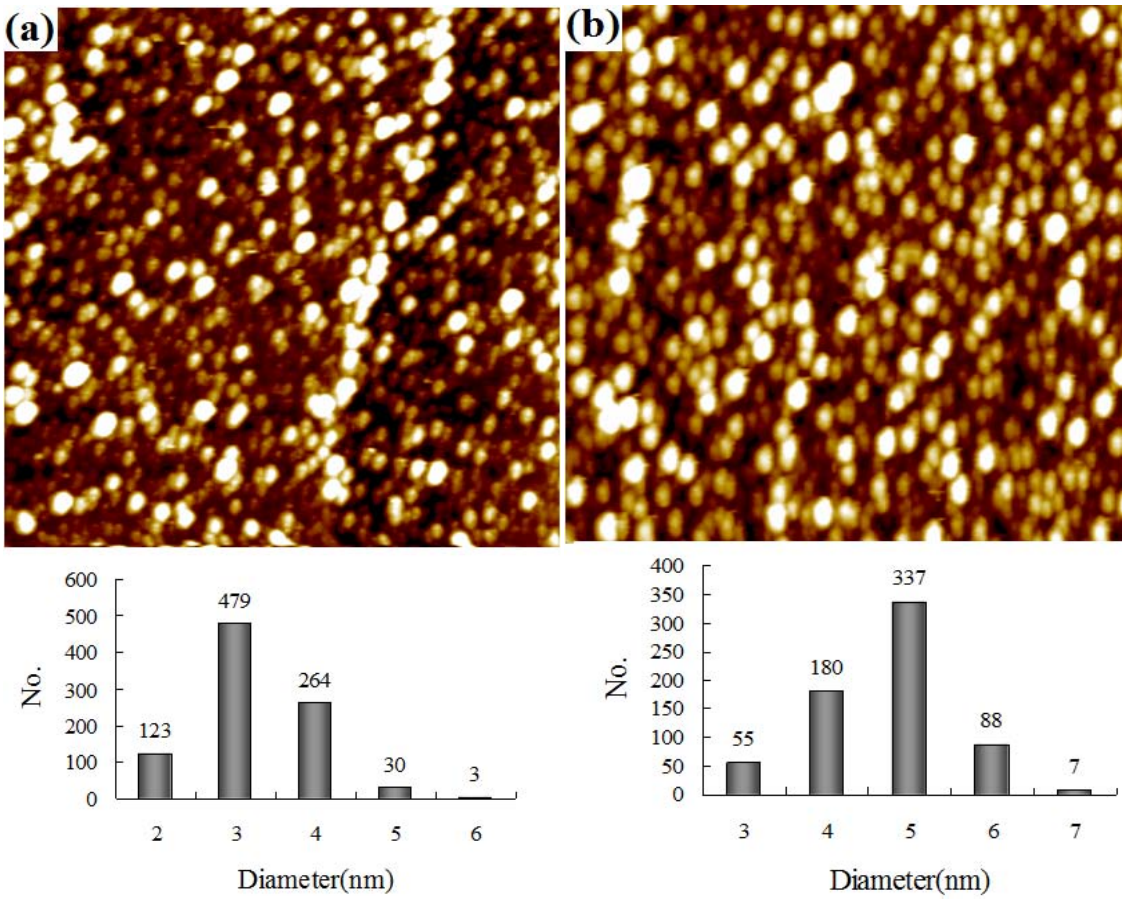

Fig. 50 Room temperature 100 nm × 100 nm STM images and cluster size distributions of Rh clusters on ultra-thin silica film at various coverages. (a) 2.0 ML Rh, V_b = 1.0 V, I_t = 0.1 nA, and (b) 4.0 ML Rh, V_b = 1.0 V, I_t = 0.1 nA.

small clusters are highly dispersed on the terrace, whereas a few large clusters are nucleated on the step edges. As the Rh coverage was increased, both the density and size of the cluster were increased accordingly. The surface was almost covered by Rh clusters when the coverage reached to 2.0 ML. The formation of highly dispersed small Rh clusters indicates a strong interaction between the Rh clusters and ultra-thin silica film.

Based on the STM images and histogram data, the averaged Rh cluster size, height, as well as the cluster shape can be estimated. To accurately determine the cluster size, we should consider the tip convolution effect, which leads to apparent particle enlargement and particle hiding. In order to remove the influence of tip apex in our size measurement, the measured particle diameter was calibrated based on two assumptions: (1) the sticking probability of Rh on the ultra-thin silica film is 1 and (2) all Rh particles are exaggerated by the same factor χ caused by the tip radius. The factor χ can be obtained by solving the following equation based on the idea that the total calculated volume of Pd particles should theoretically equal to the total deposition volume of Pd:

$$\sum_{i=1}^{n} \frac{\pi h_i [3(r_i \chi)^2 + {h_i}^2]}{6} = V_{deposit}$$

where n is the total number of clusters, h_i and r_i are the height and radius of the i^{th} cluster, and $V_{deposit}$ is the actual deposition amount of the Rh based on AES data. The volume of the i^{th} Rh cluster is calculated by $\frac{\pi h_i [3(r_i \chi)^2 + {h_i}^2]}{6}$, assuming each cluster has a shape like a spherical cap on the thin film. The calibrations have been performed on each coverage, 1.0 ML, 1.5 ML, 2.0 ML and 4.0 ML. Fig. 51(a) shows the calibrated average

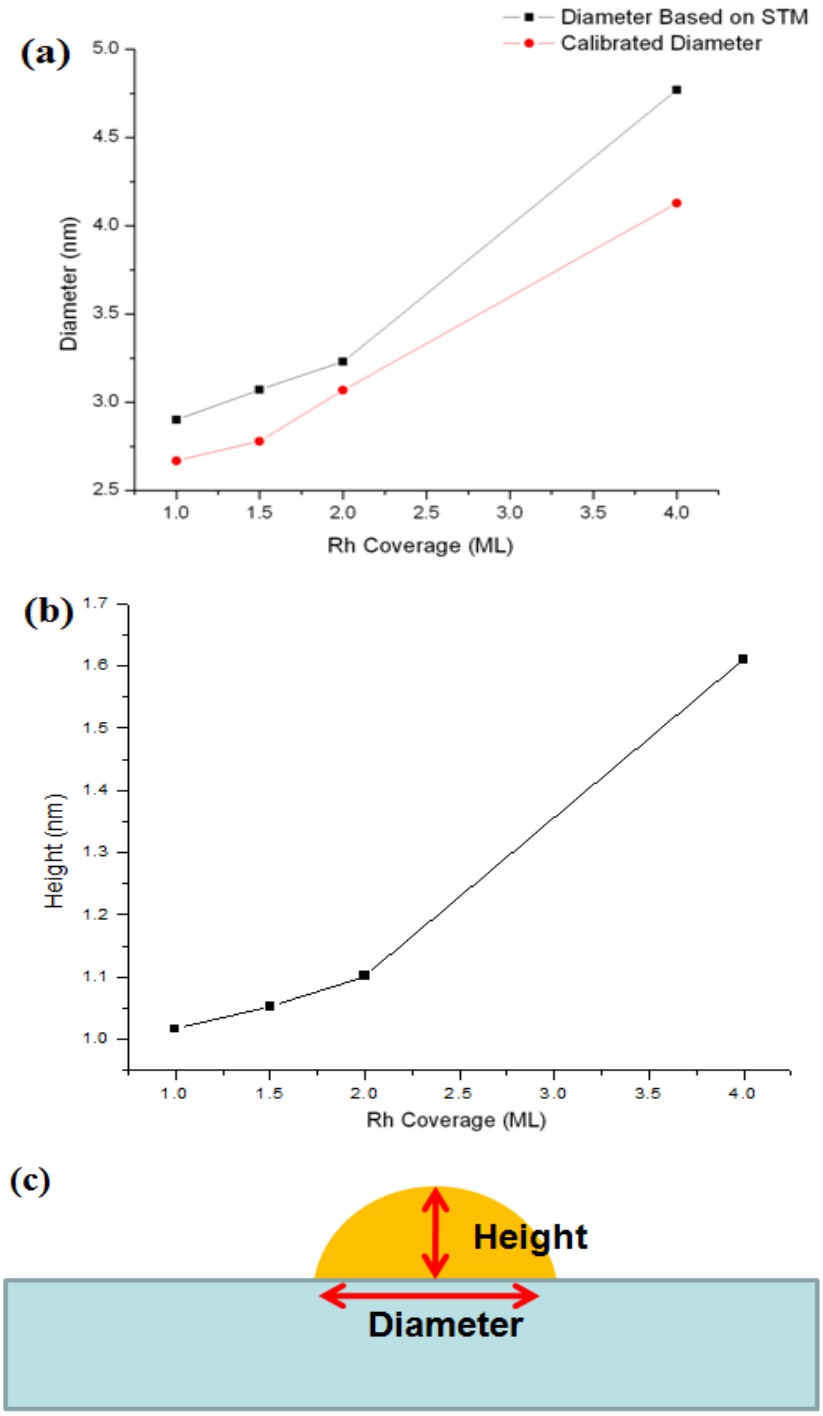

Fig. 51 (a) The plot of calibrated average cluster diameter (red line) and STM measured average diameter (black line) as a function of Rh coverage, (b) the plot of Rh cluster height as a function of Pd coverage, and (c) a schematic drawing of a Rh cluster supported on the silica film.

cluster diameter (red line) and STM measured average diameter (black line) as a function of the Rh coverage. The calibrated size is reduced by approximately 0.5 nm compared to the measured diameter. Since the height measured by STM is usually very accurate, no calibration was conducted. Fig. 51(b) shows the averaged cluster height as a function of Rh coverage. The height and size are increased almost linearly as the coverage is increased up to 2.0 ML. The slightly steep increase in the cluster height from 2.0 ML to 4.0 ML was probably due to the fact that almost all silica substrate was covered at 2.0 ML and further deposition of Rh mostly nucleated on the pre-existing clusters, leading to a sharp increase in the cluster height. Based on the information in Fig. 51(a) and (b), the shape of the clusters can be determined by calculating the averaged ratio of the height to diameter for various Rh coverages, which is about 0.4, as shown in Fig. 51(c).

The above studies can provide valuable information regarding the catalytic activities of Rh clusters supported on silica film because the number of active Rh sites per cm^2 as a function of Rh coverage can be estimated using a few simplifying geometric arguments. Fig. 52 shows the calculated Rh surface sites as a function of Rh coverage based on the calibrated particle height and diameter. The geometric estimate of the total surface sites of the UHV prepared sample can be calculated by the following equation:

$$A = 2\pi rhd$$

where r and h are the averaged radius and height of the cluster at certain Rh coverage; $2\pi rh$ is used to calculate the surface area of the spherical cap, and d is the atom density, which is assumed to be the same as Rh(111) surface atom density, 1.6×10^{15} atoms/cm^2.

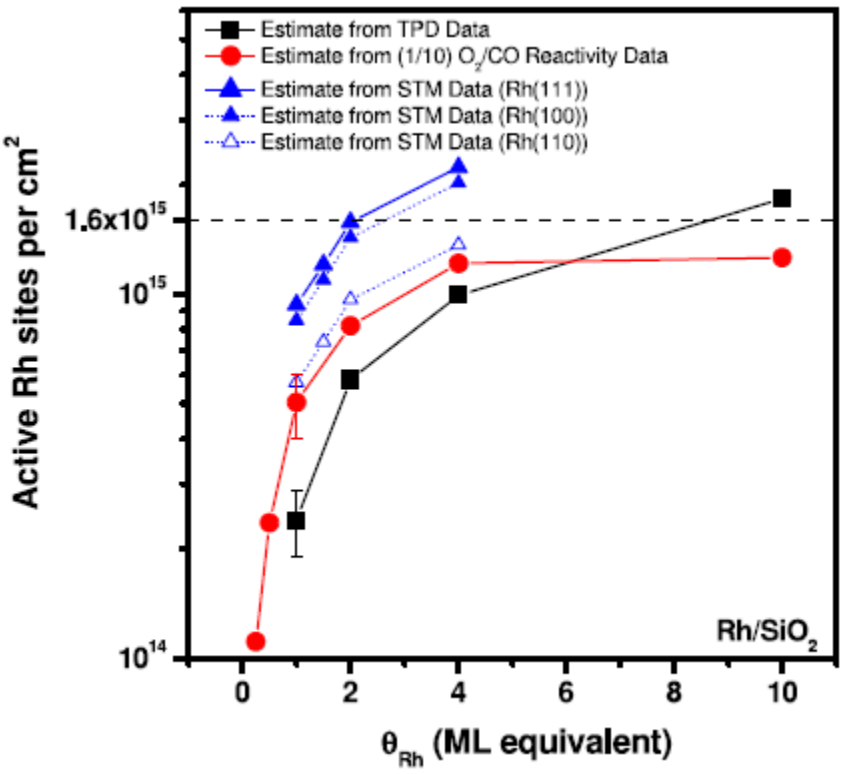

Fig. 52 Estimates of active Rh sites per cm^2 based on STM, CO TPD, and elevated pressure reaction characterization techniques as a function of Rh coverage.

Note: This figure is reprinted with permission from "Characterization of active sites on Rh/SiO_2 model catalysts" by S. M. McClure, M. Lundwall, F. Yang, Z. Zhou and D. W. Goodman, J. Phys.: Condens. Matter 21 (2009) 474223.

This assumption may provide an overestimate of the number of active Rh sites as the particles approach smaller due to more corrugated surface facets in smaller particles. As such, we have also calculated the active site density assuming less densely packed facets for the Rh particles ($d_{Rh(100)}$ = 1.45 ×10^{15} atoms/cm^2 and $d_{Rh(110)}$ = 9.8 × 10^{14} atoms/cm^2), as shown in Fig. 52. The results are compared with another two site estimation methods: CO TPD and CO reactivity measurements, both of which are conducted on various Rh clusters supported on multi-layer silica film. Experimental details regarding the latter two methods can be found in [237].

From Fig. 52, we can see general agreement is achieved among the three characterization methods. The trivial discrepancy may arise from the simplifying geometric assumptions in the STM estimation. As expected, estimation from STM using Rh(111) and Rh(100) surface atom density slightly overestimate the number of active sites present on the Rh clusters supported on the silica thin film, whereas the estimates employing Rh(110) surface atom densities agree well with the reactivity and TPD data. This is mainly because facets are more characteristic of smaller particles. Note that STM and CO TPD measurements were taken at a pressure of 10^{-10} Torr, while oxidation reactivity measurements were performed at a pressure of 8 Torr. The agreement among three estimation methods is not only surprising but also quite important because it suggests that, under the conditions of our study, STM measurements are capable of providing a reasonable estimate for the particle sizes even under elevated pressure conditions. Therefore, the above technique may offer us a practical method to accurately relate selectivity and reactivity with particle size when studying structure sensitive

reactions on model catalyst surfaces at elevated pressures.

Thermal Stability of Rh Clusters

The annealing effect of Rh clusters supported on the ultra-thin silica film/Mo(112) was also studied by STM. Fig. 53 shows STM images of 0.25 ML Rh supported on silica film annealed to 500 K and 600 K for 10 min. The three images (a), (b), and (c) on the left side were taken after 500 K annealing, from which we can see at 500 K no dramatic change occurs compared to the images without annealing. The enlarged image reveals that, in addition to some round clusters on top of the silica film, the network pattern was seen, which is different from the substrate, as shown in Fig. 53(c). The height of the wire in the 2-D network has been measured to be only 0.05 nm, which is consistent with the height of sigle Rh atoms deposited at room temperature. The network structure should be attributed to the connection of the neighboring rings that were observed in Fig. 47(a) as marked by the green circle. Thus, Rh atoms are still located on top of the first layer Mo atoms, surrounding between two [SiO_4] tetrahedral units. Fig. 48(b) shows the atomic model of the network structure consisting of Rh atoms and [SiO_4] tetrahedral units. In the model, the "wire" area of the network is Rh atoms and [SiO_4] units, whereas the "pore" area is the second layer Mo atoms not covered by [SiO_4] units.

As the annealing temperature was increased to 600 K, the network structure appears to be much better ordered, which is due to migration of the Rh atoms to form a larger network at 600 K. Closer examination of Fig. 53(e) and (f) reveals that on the 2-D bright protrusions, the network of [SiO_4] units can still be observed, which is similar to

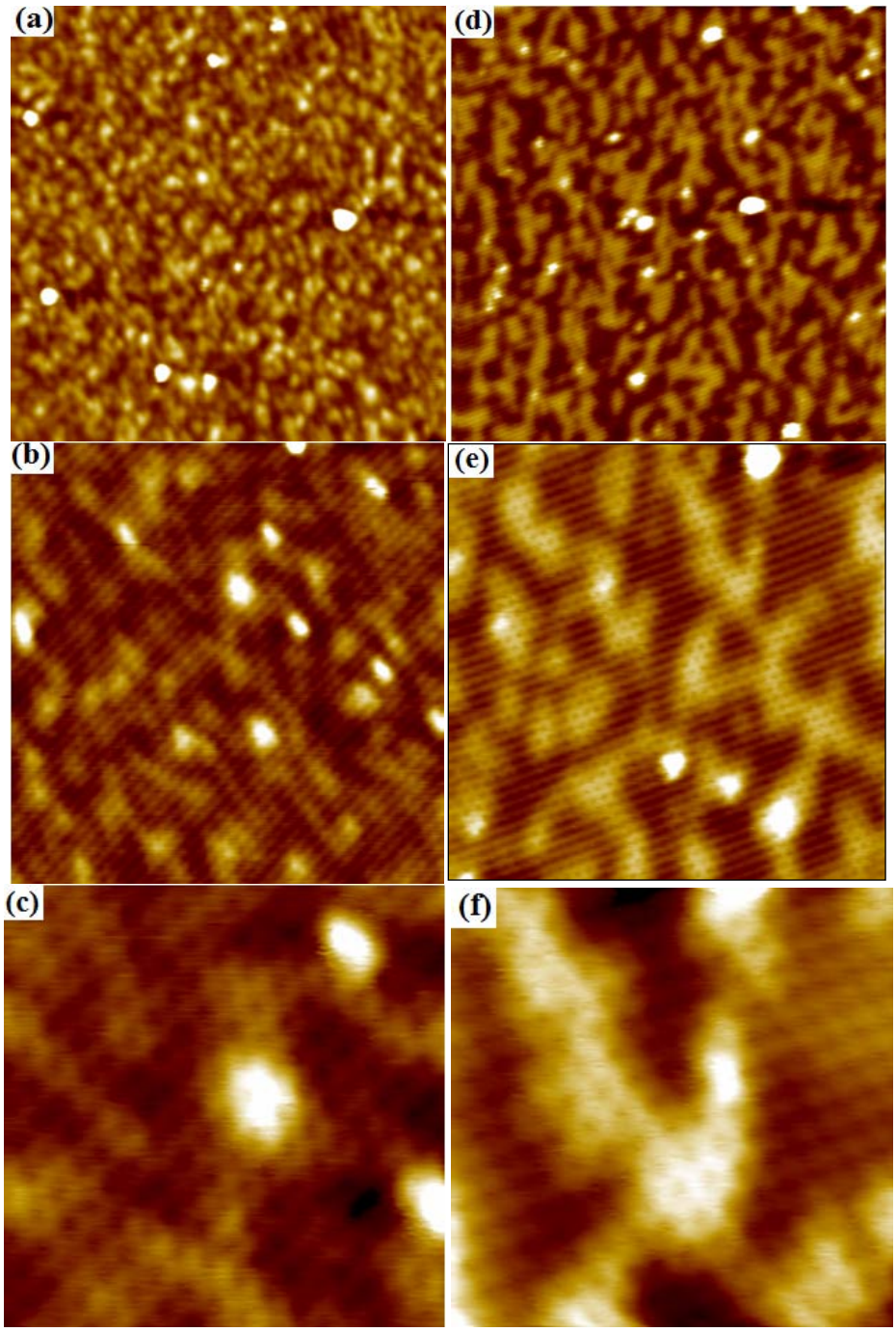

Fig. 53 STM of 0.25 ML Rh supported on ultra-thin silica film/Mo(112) annealed to 500 K and 600 K. (a) 500 K, 50 nm × 50 nm, V_b = 1.0 V, I_t = 0.1 nA, (b) 500 K, 20 nm × 20 nm, V_b = 1.0 V, I_t = 0.1 nA, (c) 500 K, 7 nm × 7 nm, V_b = 0.3 V, I_t = 0.5 nA, (d) 600 K, 50 nm × 50 nm, V_b = 1.0 V, I_t = 0.1 nA, (e) 600 K, 20 nm × 20 nm, V_b = 1.0 V, I_t = 0.1 nA, (f) 600 K, 7 nm × 7 nm, V_b = 0.3 V, I_t = 0.5 nA. All images are acquired after the sample has been cooled to room temperature after a 10 min annealing.

the substrate but with brighter color, further confirming the correctness of our model, where the adsorption site of Rh atoms is on top of the first layer Mo atoms.

As the annealing temperature was increased to 700 K, the morphologies evolved to elongated 2-D islands, as shown in Fig. 54(a). Fig. 54(b) is a high resolution STM image on one 2-D island, in which the stripe pattern on both the 2-D island and substrate can be observed. Fig. 54(c) displays a 3-D topographic STM image of the island marked by dashed green rectangular in (a). Note that some bright protrusions are found on the edge of the islands as shown in Fig. 54(b) and (c), which are assigned to Rh clusters left on the surface. Fig. 54(d) is the line profile marked in Fig. 54(a), showing the height of the 2-D islands is about 0.32 nm. Based on the fact that these 2-D islands show the same pattern as the silica substrate, the silica film should cover the 2-D islands due to SMSI effect. A reasonable mechanism for the formation of the 2-D islands is that at 700K, Rh atoms diffuse beneath the silica film to form a pseudomorphous layer on the Mo(112) surface and $[SiO_4]$ units rearrange themselves to form a new layer of silica thin film on top of the Rh layer. The intercalated Rh layer between the silica film and Mo(112) should be only a single layer based on the height of the 2-D islands.

The above scenario is further proved by scanning tunneling spectroscopy (STS) studies, where the electronic structures of silica substrate, the 2-D islands, and the boundary of the 2-D islands were investigated, as shown in Fig. 55. The STS curves taken on silica substrate (blue line) and 2-D islands (green line) are almost the same, exhibiting a very low tunneling current at voltages from -1.5 V to 1.0 V. The band gap of 2.5 eV is much smaller than the bulk silica band gap of 8.9 eV [238], which is

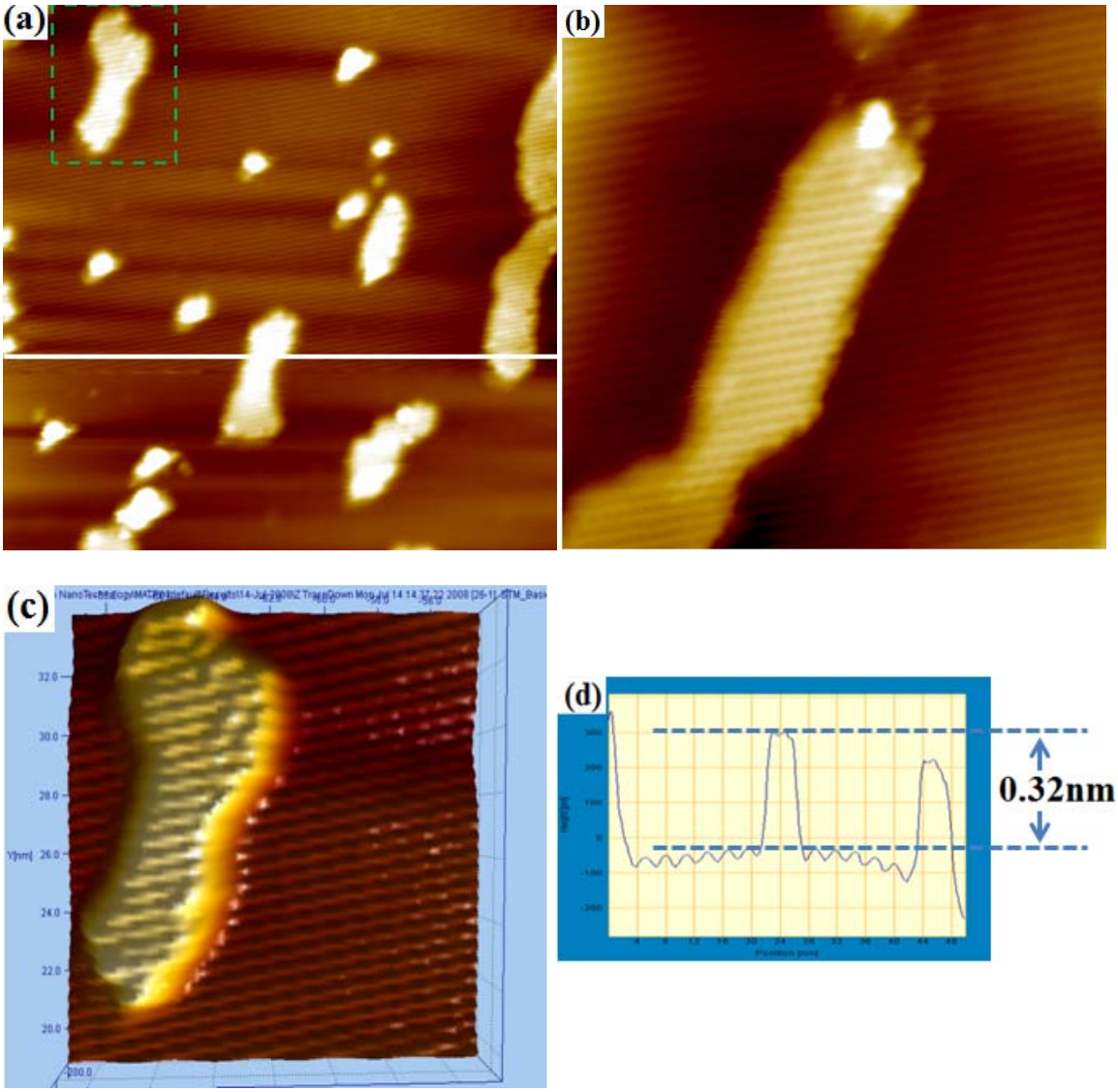

Fig. 54 STM of 0.25 ML Rh supported on ultra-thin silica film/Mo(112) annealed to 700 K. (a) 50 nm × 50 nm, V_b = 1.0 V, I_t = 0.1 nA, (b) 20 nm × 20 nm, V_b = 1.0 V, I_t = 0.1 nA, (c) 3-D image of the island marked by dashed green rectangular in (a), and (d) height profile corresponds to the white line in (a). All images are acquired after the sample has been cooled to room temperature after a 10 min annealing.

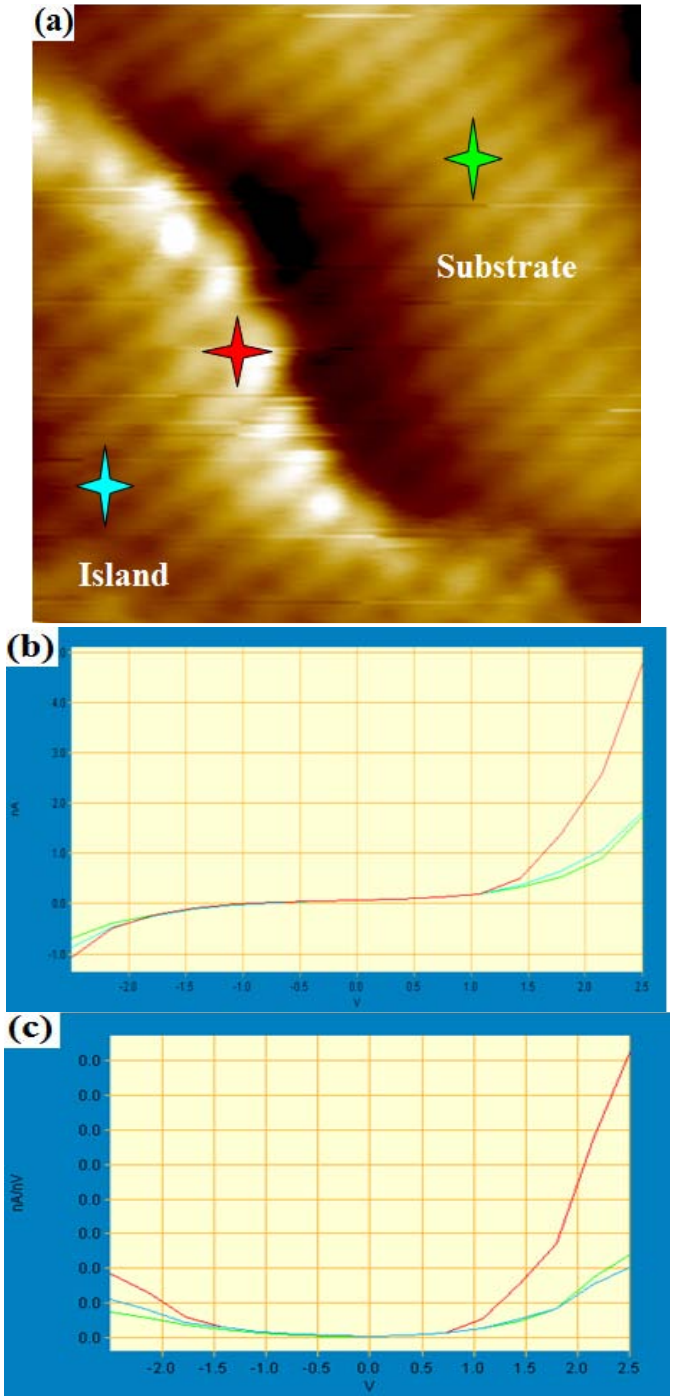

Fig. 55 (a) 5 nm × 5 nm STM image (V_b = 1.0 V, I_t = 0.1 nA) of 0.25 ML Rh supported on ultra-thin silica film/Mo(112) annealed to 700 K. The zoomed-in image shows the boundary between the island and silica substrate. (b) Room temperature STS I-V curves taken on three different areas marked by blue, red and green stars in (a), and (c) derivative curve dI/dV-V of (b)

partially attributed to the fact that thin silica film is supported on the metal substrate, thus allowing the tunneling to occur at a relatively low bias. The electronic structure of the 2-D island is similar to the substrate, indicating that the 2-D islands are covered by the silica film instead of Rh metals. In contrast, the STS curve taken on the boundary of the 2-D island shows a relatively smaller band gap, which arises from the combination of the electronic structure from both silica film and Rh atoms left on the surface. This agrees well with STM observations.

Another interesting point worth mentioning is that the coverage of 2-D islands changes from 600 K to 700 K. As shown in Fig. 56, the coverage of the bright protrusions has been analyzed by the STM imaging software, which shows that 46% of the surface was covered by the 2-D structures at 600 K, whereas only 20% was covered at 700 K. Note that only 0.25 ML Rh was deposited on the surface. As a matter of fact, such apparent discrepancy agrees well with the above model we proposed. At 600 K, the Rh atoms were intercalated into silica film and were located on top of the first layer Mo atoms. Therefore, on the brighter protrusions, every other Mo atom on the surface was covered by one Rh atom, which means for a dosage of 0.25 ML Rh, the coverage should be 50%, which is close to our experimental measurement 46%. As the temperature was increased to 700 K, the theoretical coverage should be 25% for a 0.25 ML dosage, in that a pseudomorphous single layer of Rh was formed between silica and Mo(112). Our experimental observation is 20%, also consistent with the theoretical value within acceptable error. Therefore, the coverage measurements also prove the correctness of the model we proposed for thermal evolution of Rh atoms on the silica thin film.

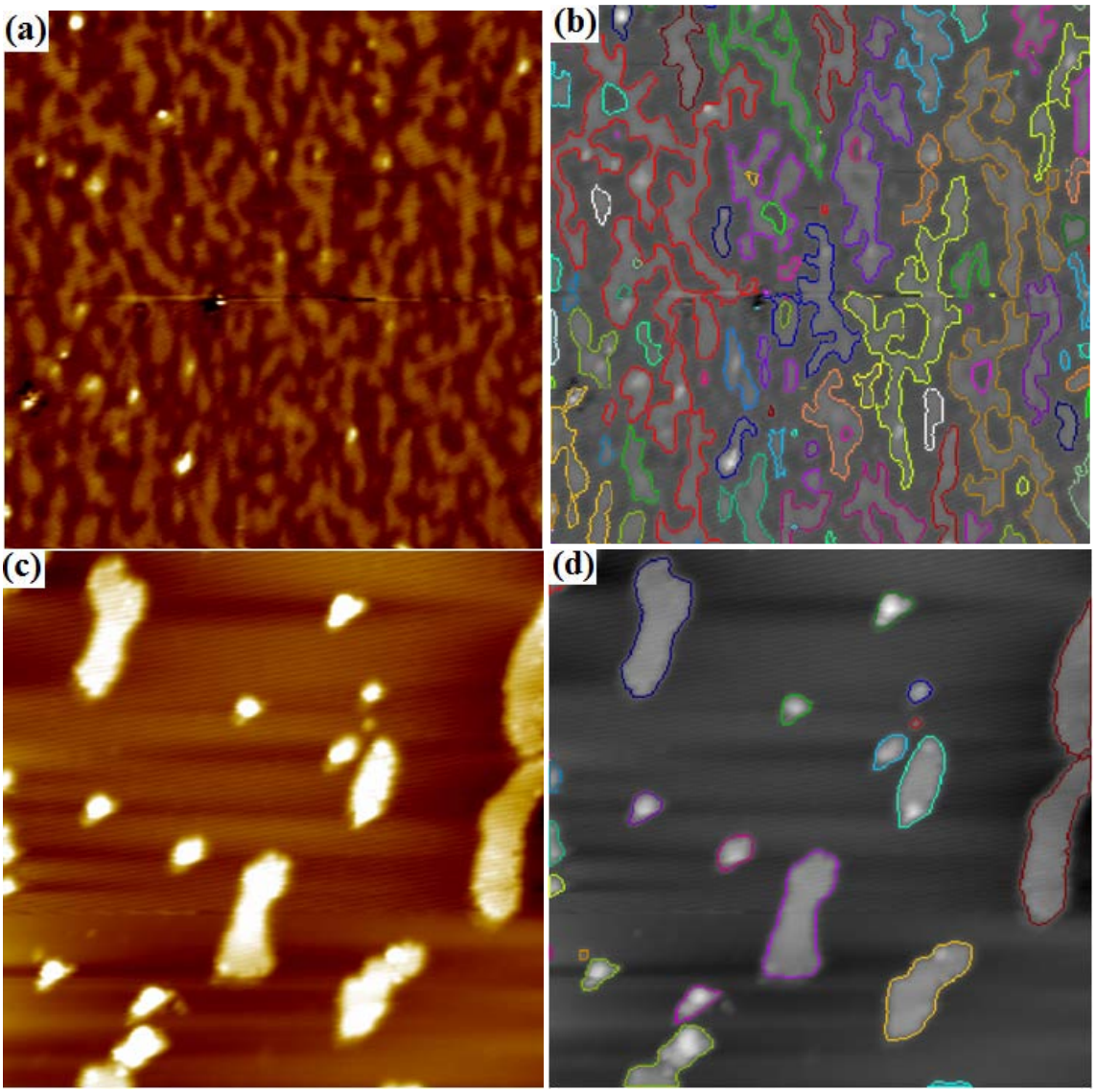

Fig. 56 STM images of 0.25 ML Rh supported on ultra-thin silica film/Mo(112) annealed to 600 K and 700 K. (a) 600 K, 50 nm × 50 nm, V_b = 1.0 V, I_t = 0.1 nA, (b) white and grey image of (a) with the coverage of all brighter areas being counted. The coverage is around 46%. (c) 700 K, 50 nm × 50 nm, V_b = 1.0 V, I_t = 0.1 nA, and (d) white and grey image of (c) with the coverage of all islands being counted. The coverage is around 20%.

5.3 Pt Clusters Supported on Ultra-thin Silica Film

Morphologies of Pt Clusters

The adsorption of Pt atoms on the ultra-thin silica film/Mo(112) at room temperature were investigated by deposition of 0.10 ML Pt on the silica thin film, as shown in Fig. 57. In Fig. 57(a), in addition to bright round clusters, some amorphous 2-D protrusions wetting the surface with the height of approximately 0.05 nm were observed. The close up image, as shown in Fig. 57(b), reveals that amorphous 2-D protrusions consist of small bright spots which appear to sit either on top of rows of the substrate (marked by blue circle) or between two rows (marked by the red circle). Some of the small bright spots are connected to form a chain which is almost vertical to the substrate rows whereas some of them construct a network structure. From the STM images, the formation of these bright small spots with such small height may arise from the adsorption of Pt atoms to the top of the first layer Mo atoms, surrounding by two [SiO_4] tetrahedral units, which is similar to nucleation site of Rh atoms on silica thin film. Fig. 58 shows the atomic model of both bright spots on top of the rows and spots between rows, which are corresponding to the areas marked by the blue and red circles in Fig. 57(b). The yellow lines represent the bright lines in STM images. As mentioned before, the space between two neighboring [SiO_4] tetrahedral units is large enough to hold a Pt atom. Since Pt atoms are only located on the every other Mo atoms, the coverage of Pt appears to be higher than 0.10 ML in Fig. 57(a). The formation of Pt-Si and Pt-O bond might be the key factor for such arrangement so that each Pt atom could contact with two Si atoms and four oxygen atoms, which will be carefully discussed in

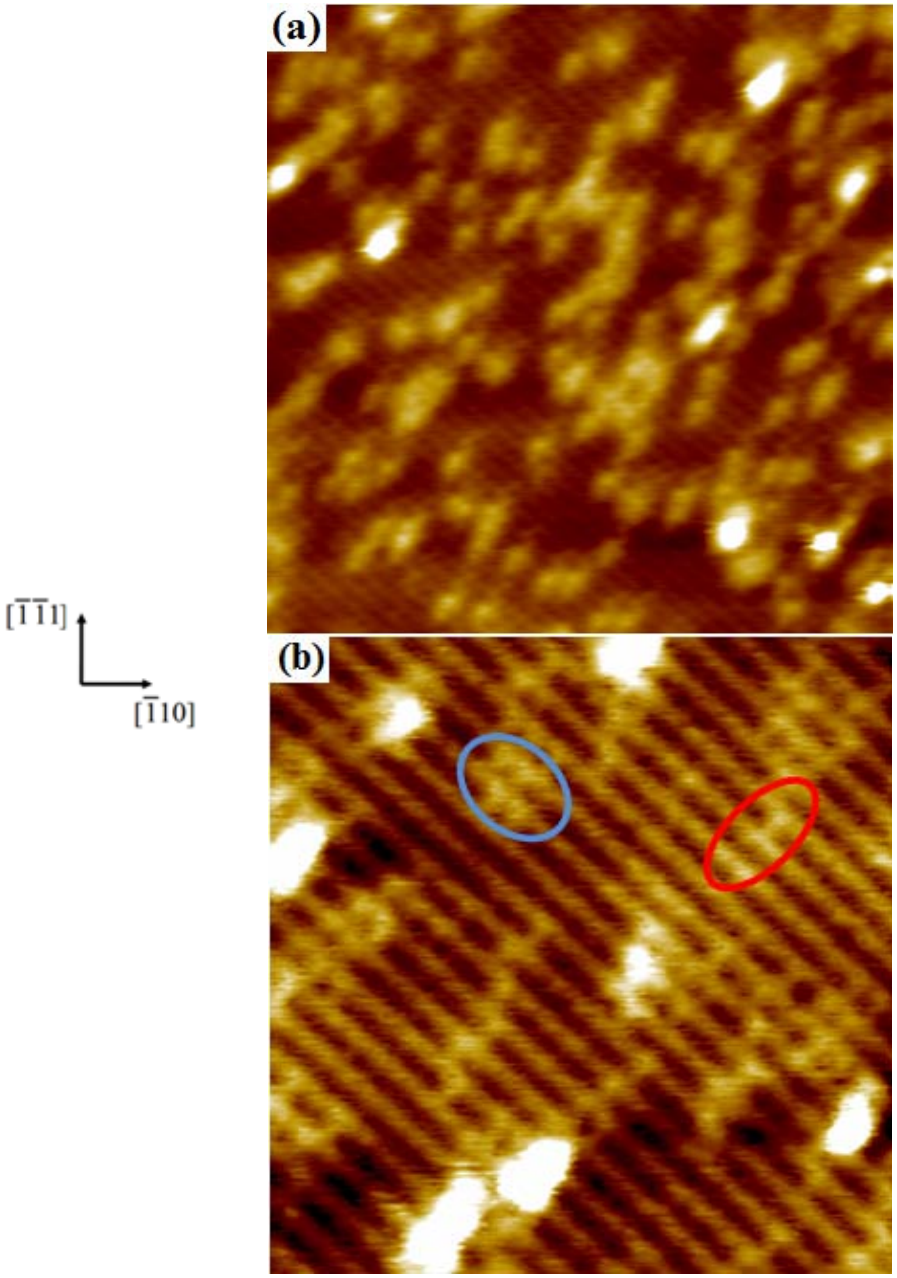

Fig. 57 Room temperature STM images of 0.10 ML Pt clusters supported on ultra-thin silica film/Mo(112) at various scanning conditions. (a) 20 nm × 20 nm, V_b = 1.0 V, I_t = 0.1 nA, and (b) V_b = -0.1 V, I_t = 0.5 nA.

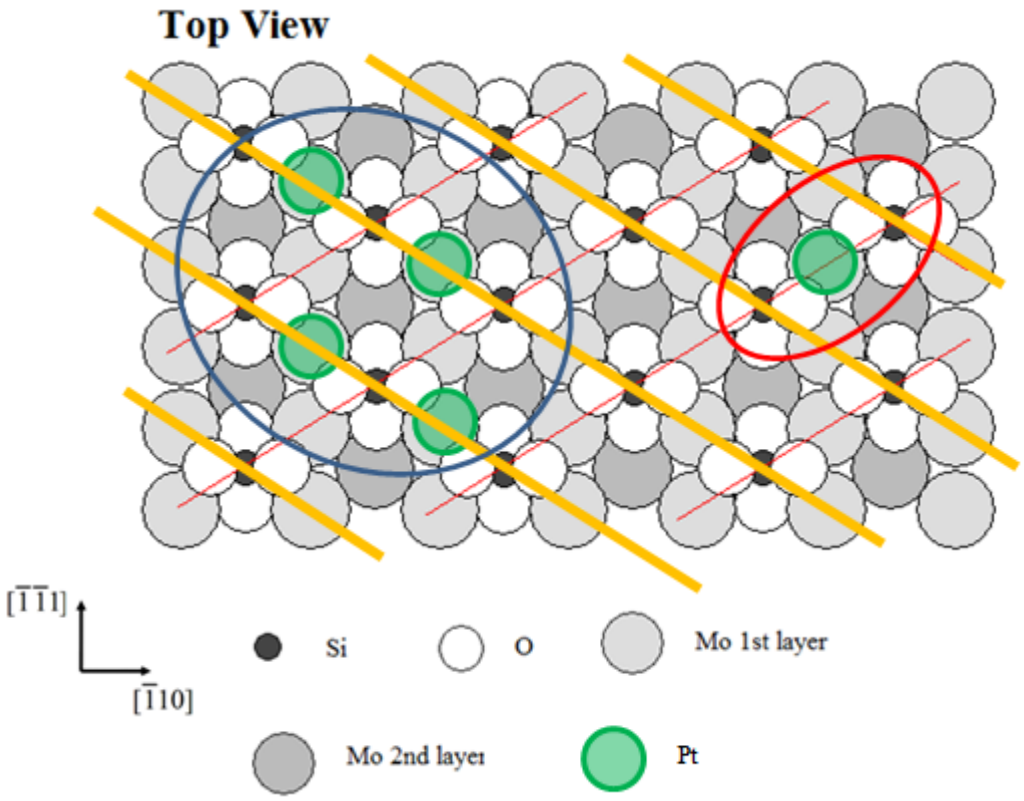

Fig. 58 The atomic model of Pt nucleation sites on the ultra-thin silica film.

the following section. Continuing with deposition of Pt atoms, the extra atoms also prefer to nucleate on the pre-existing Pt atoms because large clusters extending two or three rows were observed in Fig. 57(b).

The morphologies of Pt clusters supported on the silica thin film at higher coverages were also studied by STM, as shown in Fig. 59 and Fig. 60. At a coverage of 0.50 ML, small clusters with diameters from 2 to 3 nm were highly dispersed on the surface. No intense decoration of clusters at the step edges was observed, indicating that Pt atoms have a relatively short diffusion path on the silica film due to a strong interaction with silica film. As the coverage was increased to 1.0 ML, the size distribution of the cluster is still centered at 2 ~ 3 nm, while the density of the clusters almost doubles. It appears that Pt atoms would rather nucleate on the empty silica film rather than adsorb on the pre-existing Pt clusters at this stage, also suggesting a strong interaction between the Pt atoms and the silica film. At higher coverages, as the silica film was completely covered by Pt clusters, the size of the clusters grows proportional to the dosage, as shown in Fig. 60. The averaged cluster size is over 3 nm at 3.0 ML and it grows over 4 nm at 4.0 ML.

To avoid the enlargement effect by the tip apex, the cluster sizes at various coverages were calibrated with the same method applied to Rh clusters on the silica thin film as discussed in the previous section. Fig. 61(a) shows the averaged sizes of clusters before (black line) and after calibration (red line). The calibrated diameter is reduced by approximately 0.5 nm. Based on the averaged height measured by STM and calibrated size, the shape of the cluster can be determined by the ratio of the height to diameter,

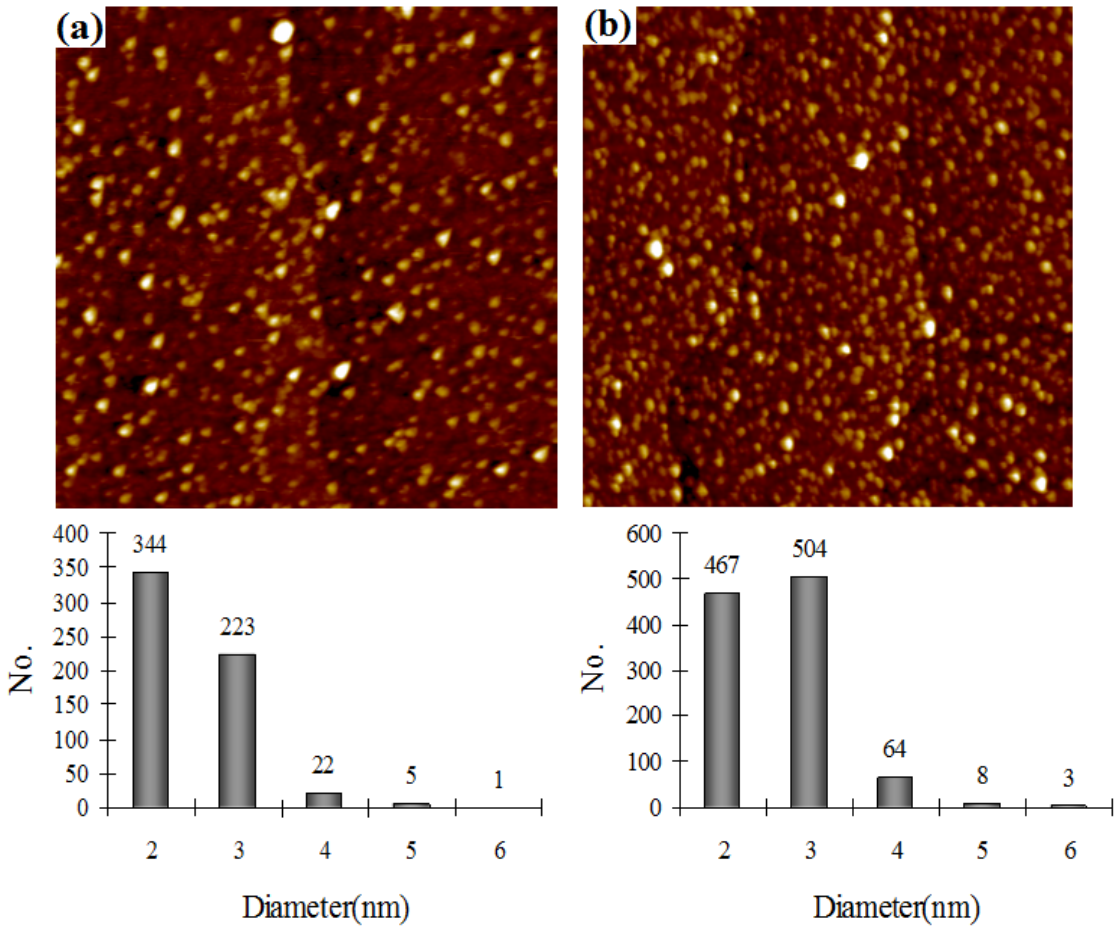

Fig. 59 Room temperature 100 nm × 100 nm STM images and cluster size distributions of Pt clusters on the ultra-thin silica film at various coverages. (a) 0.50 ML Pt, V_b = 1.0 V, I_t = 0.1 nA, and (b) 1.0 ML Pt, V_b = 1.0 V, I_t = 0.1 nA.

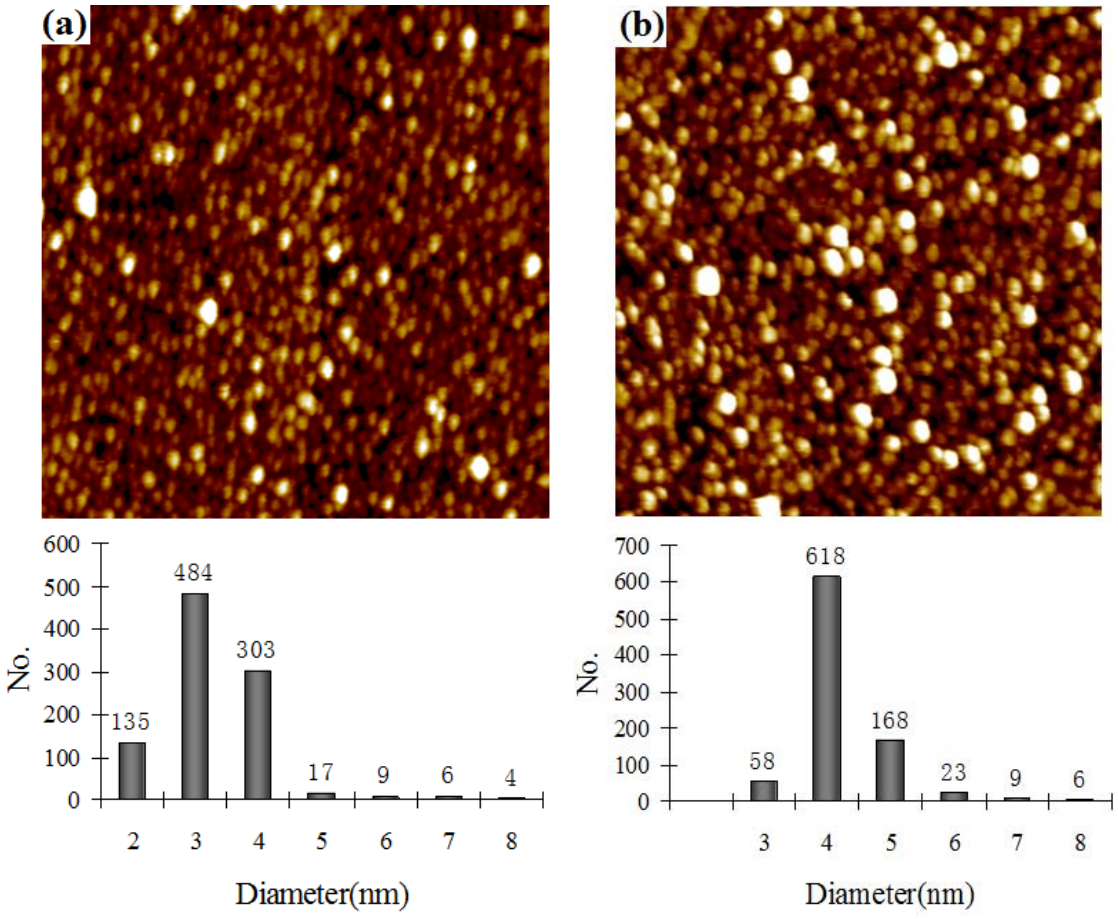

Fig. 60 Room temperature 100 nm × 100 nm STM images and cluster size distributions of Pt clusters on the ultra-thin silica film at various coverages. (a) 2.0 ML Pt, V_b = 1.0 V, I_t = 0.1 nA, and (b) 4.0 ML Pt, V_b = 1.0 V, I_t = 0.1 nA.

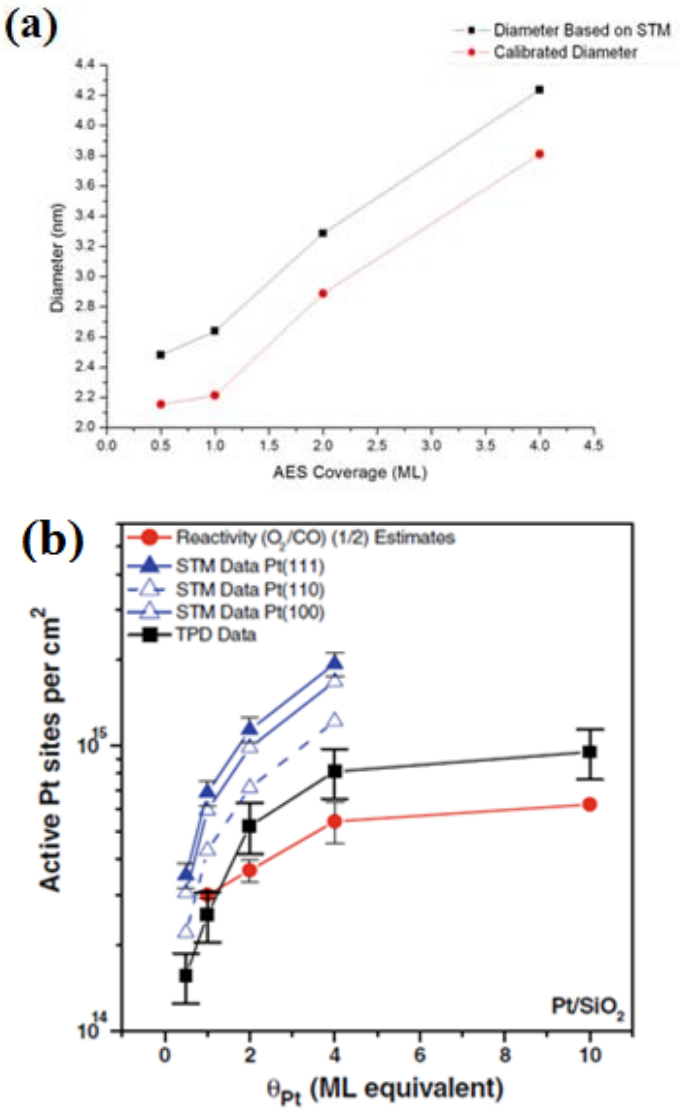

Fig. 61 (a) The plot of calibrated average Pt cluster diameter (red line) and STM measured average diameter (black line) as a function of Pt coverage. (b) Estimates of active Pt sites per cm^2 based on STM, CO TPD, and elevated pressure reaction characterization techniques as a function of Pt coverage.

Note: Fig. 61(b) is reprinted with permission from "Characterization of Pt/SiO_2 Model Catalysts at UHV and Near Atmospheric Pressures" by S. M. McClure, M. Lundwall, Z. Zhou, F. Yang and D. W. Goodman, Catal. Lett. (2009) 133:298–306. Copyright Springer Science + Business Media, LLC 2009.

which is only 0.25, suggesting that clusters tend to wet the surface.

The number of the active Pt sites per cm^2 as a function of Pt coverage was also estimated with the same method as applied to the Rh clusters on the silica thin film, as shown in Fig. 61(b). Three different facets were considered, Pt(111) facet with 1.5×10^{15} atoms/cm^2, Pt(110) with 9.2×10^{14} atoms/cm^2, and Pt(100) with 1.3×10^{15} atoms/cm^2. The results are compared with another two site estimation methods: CO TPD conducted at a pressure of 10^{-10} Torr and CO reactivity measurements taken at 8 Torr, both of which are conducted on various coverages of Pt clusters supported on the multi-layer silica film. Experimental details could be found in [239].

From Fig. 61(b) we can see the general agreement is achieved among the three characterization methods. However, STM data appears to overestimate the number of sites compared to the reaction and TPD measurements. As stated in the previous section, we hypothesize that this is because of simplifying assumptions made in estimating active sites via our geometric method. Due to the fact that facets are more characteristic of smaller particles, site estimates using Pt(110) surface atom densities provide better quantitative agreement with the reactivity and TPD data. The agreement among three estimation methods is similar to the case of Rh supported on the ultra-thin silica film, which again shows that STM measurements are capable of providing a reasonable estimate for the particle sizes even under elevated pressure conditions.

Thermal Stability of Pt Clusters

Similar to Rh clusters, Pt atoms can intercalate into the silica film to maximize its

contact with the surrounding silicon and oxygen atoms at room temperature. It is very interesting to study the thermal stability of Pt clusters. The thermal evolution of the 0.60 ML Pt clusters supported on the ultra-thin silica film/Mo(112) is shown in Fig. 62. Prior to imaging, the sample was first annealed to the target temperature and maintained for 10 min before cooling down to the room temperature. No detectable change is observed at temperatures up to 700 K. Sintering initiates at ~800 K as indicated by the decreased cluster density and increased dimensions.

At 900 K, in addition to large clusters, 2-D islands were also observed. The formation of 2-D islands is more noticeable after annealing the sample to 1000 K. Fig. 63(b) shows the enlarged image of 2-D islands, on which the same pattern as the substrate was observed, indicating that 2-D islands is covered by silica thin film. The height of the 2-D islands has been measured to be approximately 0.3 nm. Based on the height and pattern of the 2-D islands, it is highly possible that the silica film grows on a pseudomorphous layer of Pt that follows the lattice of Mo(112) facet. Furthermore, the coverage of 2-D islands is about 60%, which also favors the above scenario because it is consistent with the real dosage of Pt. It is worth mentioning that this phenomenon is similar to the annealing effect of Rh clusters supported on the silica thin film at 700 K.

When the annealing temperature was increased to 1200 K, STM image, as shown in Fig. 63(c), reveals that the size of 2-D islands grows while the island density decreases. The line profile of the 2-D islands shows that the height of the islands is increased from 0.3 nm to 0.55 nm. It is interesting to find that the higher 2-D islands also exhibit the similar pattern as the silica thin film, as shown in Fig. 63(d). Both the

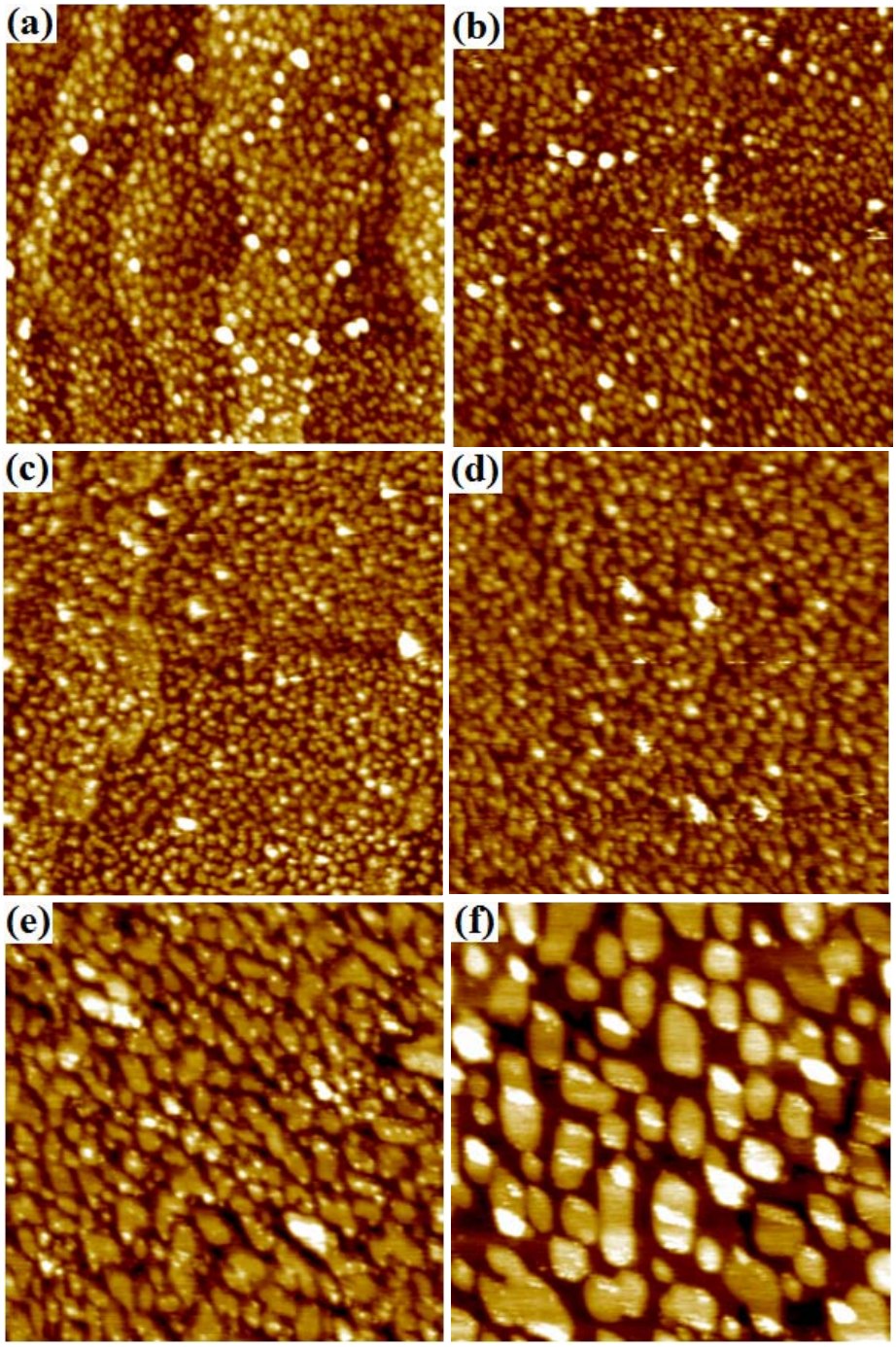

Fig. 62 STM images (100 nm × 100 nm, V_b = 1.0 V, I_t = 0.1 nA) of 0.60 ML Pt on ultra-thin silica film/Mo(112) annealed to (a) 500 K, (b) 600 K, (c) 700 K, (d) 800 K, (e) 900 K and (f) 1000 K. All images are acquired after the sample has been cooled to room temperature after a 10 min annealing.

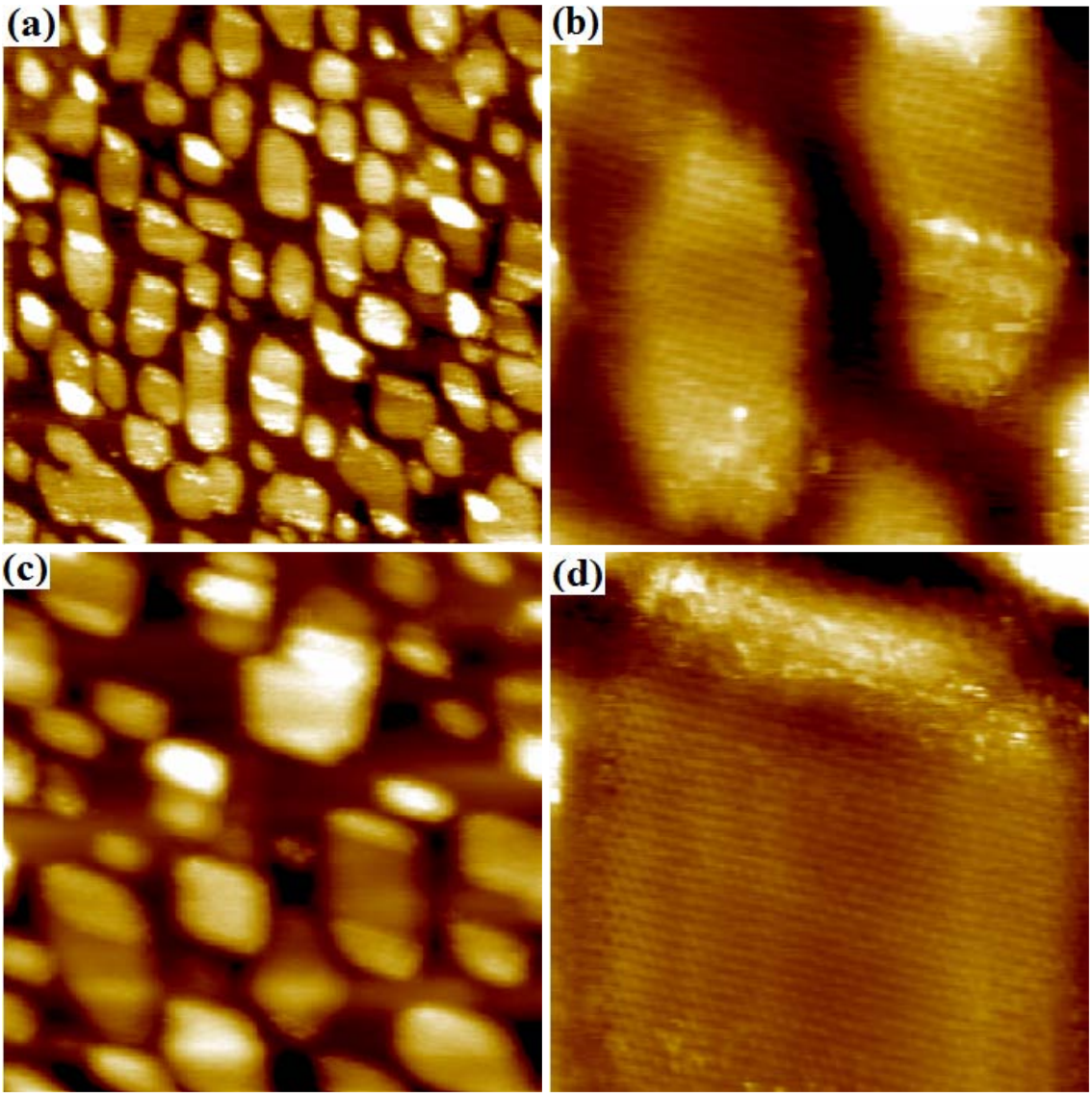

Fig. 63 STM images (V_b = 1.0 V, I_t = 0.1 nA) of 0.60 ML Pt on ultra-thin silica film/Mo(112) annealed to 1000 K and 1200 K. (a) 100 nm × 100 nm, 1000 K, (b) 20 nm × 20 nm, 1000 K, (c) 100 nm × 100 nm, 1200 K, (d) 20 nm × 20 nm, 1200 K. All images are acquired after the sample has been cooled to room temperature after a 10 min annealing.

decrease in coverage almost by half and increase in height to 0.55 nm indicate the double layers of Pt atoms are formed at the interface between silica film and Mo(112) substrate at 1200 K. The transformation from single Pt layer to double layers at 1200 K may be due to the fact that double Pt layers are more stable thermodynamically. It should be noted that these annealing temperatures are not high enough for Pt to desorb from the surface. Also, no surface alloy occurs between Mo and Pt at this temperature.

The AES measurements were also conducted during the above annealing procedures (data not shown), which is consistent with our STM data. The relative AES intensity ratio of Pt to Mo was monitored at various annealing temperatures, which shows that the ratio remains the same at 0.44 when the annealing temperatures are lower than 700 K. The ratio starts to decrease at 800 K and it was further reduced to 0.32 as the annealing temperature was increased to 1000 K, suggesting that Pt atoms diffuse beneath the silica film. The ratio keeps decreasing when the annealing temperature was raised to 1200 K, which results from the formation of double Pt layers beneath the silica film.

5.4 Pd Clusters Supported on Ultra-thin Silica Film

Morphologies of Pd Clusters

Nucleation and growth of Pd clusters on the ultra-thin silica film/Mo(112) were studied by STM. Fig. 64 shows STM images of 0.01 ML Pd deposited on the silica film. Both Pd clusters and Pd atoms were observed on the surface. In Fig. 64(a), the two neighboring Pd atoms have been marked by a green circle and Fig. 64(b) is a high resolution STM image showing one Pd atom adsorbed on the surface. The contrast and

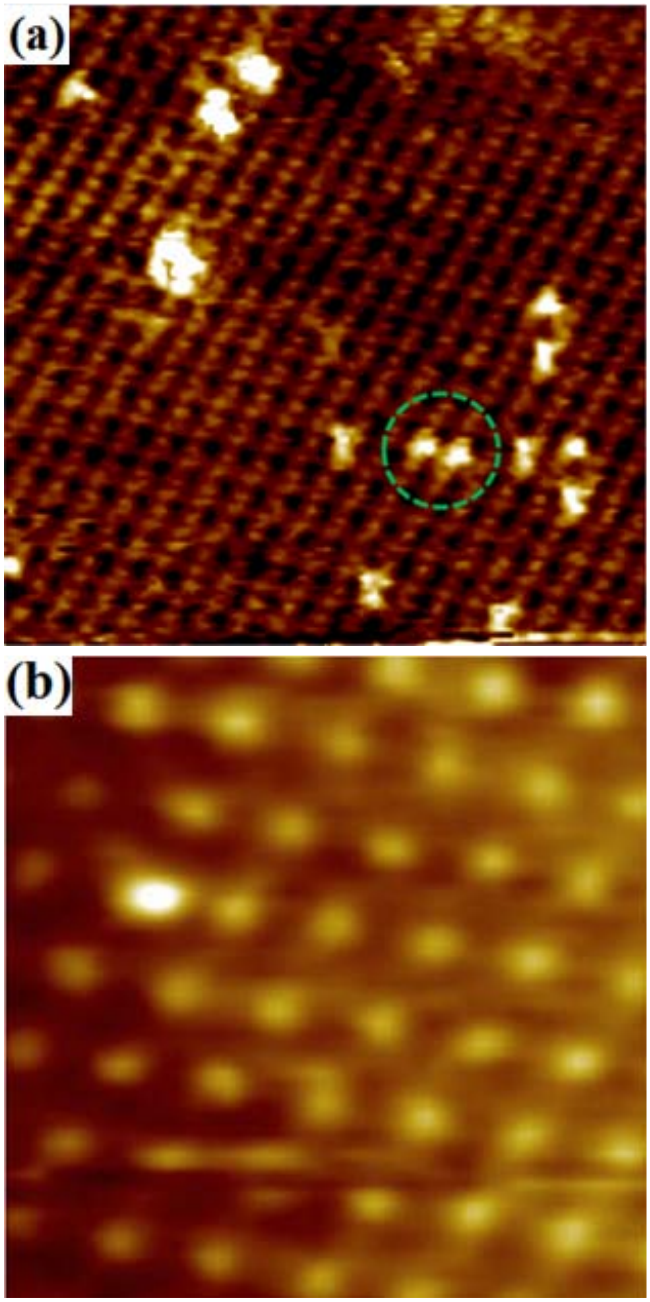

Fig. 64 STM images of 0.01 ML Pd supported on ultra-thin silica film. (a) 10 nm × 10 nm, V_b = -0.4 V, I_t = 1 nA, (b) 3 nm × 3 nm, V_b = 1.0 V, I_t = 0.5 nA.

pattern of the silica film with Pd clusters deposited are consistent with silica film as shown in Fig. 45 under similar scanning conditions, e.g. single bright protrusions obtained at a large positive bias and network structure observed at a relatively small negative bias. The bright protrusions in both images are assigned to the [SiO_4] tetrahedral clusters, as pointed out before. Thereby the adsorption sites of Pd atoms can be assigned by relating the position of Pd atoms with the bright protrusions of the substrate. A closer scrutinize of the images reveals that the Pd atoms always nucleate on top of the bright protrusions, indicating that Pd atoms prefer to adsorb on top of [SiO_4] clusters, while it may be slightly leaning toward neighbor oxygen atoms, as shown in Fig. 64(b).

The atomic model of Pd nucleation on the silica film was drawn, as shown in Fig. 65, where two Pd atoms nucleate on two neighboring [SiO_4] clusters, corresponding to the area marked by the green dashed circle in Fig. 64(a). Note that the preferential adsorption site for Pd on the silica film is different from that on the 2-D network silica film. Giordano *et al.* [236] suggested that the center of the honeycomb is the strongest binding site for Pd atoms. Such difference may also prove that two different structures of silica thin film exist, which is caused by different preparation methods.

Fig. 66 and Fig. 67 depict STM images acquired at various Pd coverages from 0.50 to 4.0 ML, and the size histograms are also shown below each image based on the randomly chosen 100 nm ×100 nm STM images at the indicated coverage. At a coverage of 0.50 ML, in addition to small clusters with diameter of 2 nm that are randomly distributed on the terrace, large clusters with sizes larger than 5 nm are mostly nucleated

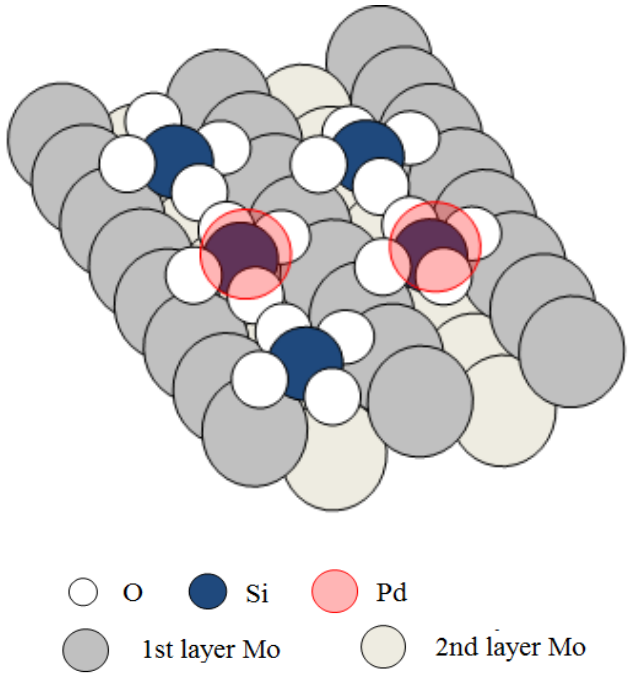

Fig. 65 Atomic model of Pd nucleation sites on the ultra-thin silica film. The model corresponds to the area marked by the green dashed circle in Fig. 64(a).

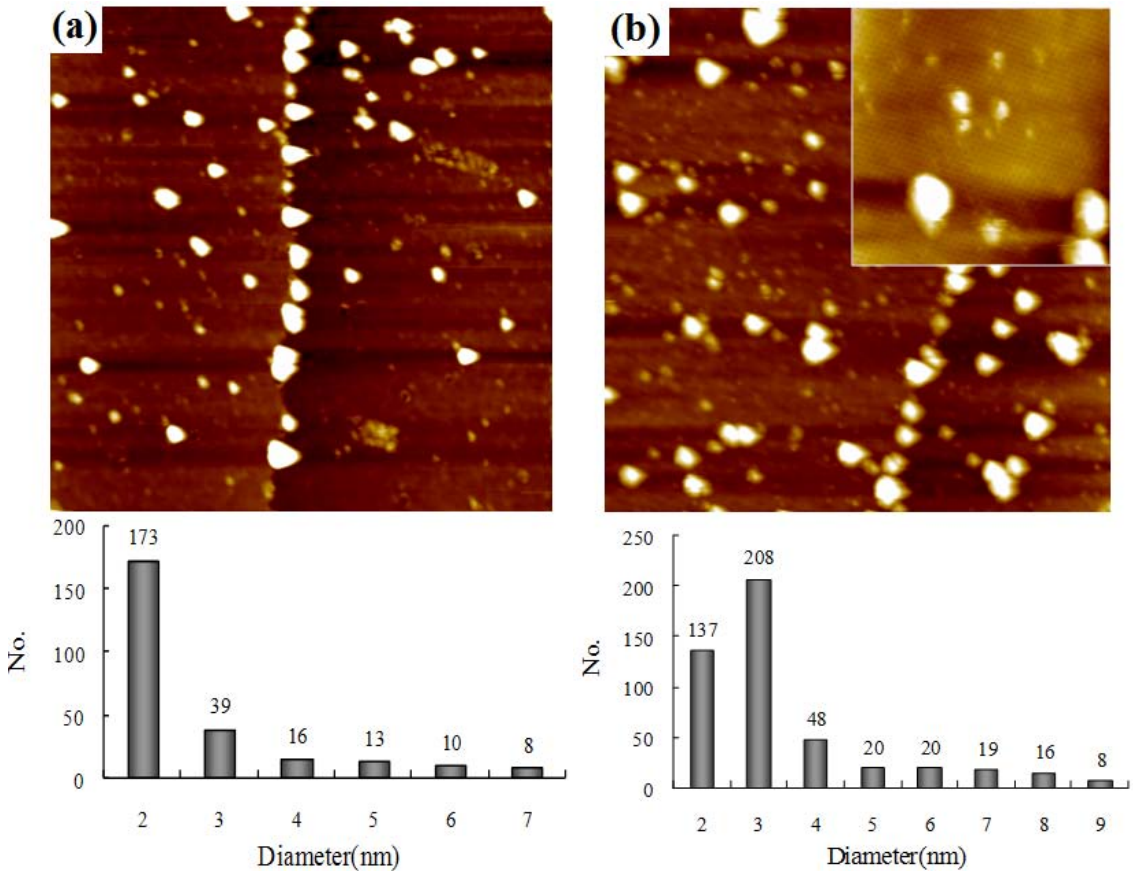

Fig. 66 Room temperature 100 nm × 100 nm STM images and cluster size distributions of Pd clusters on the ultra-thin silica film at various coverages. (a) 0.50 ML Pd, V_b = 1.0 V, I_t = 0.2 nA, and (b) 1.0 ML Pd, V_b = 1.0 V, I_t = 0.2 nA. The inset is a zoomed-in 20 nm × 20 nm STM image (V_b = 1.0 V, I_t = 0.1 nA).

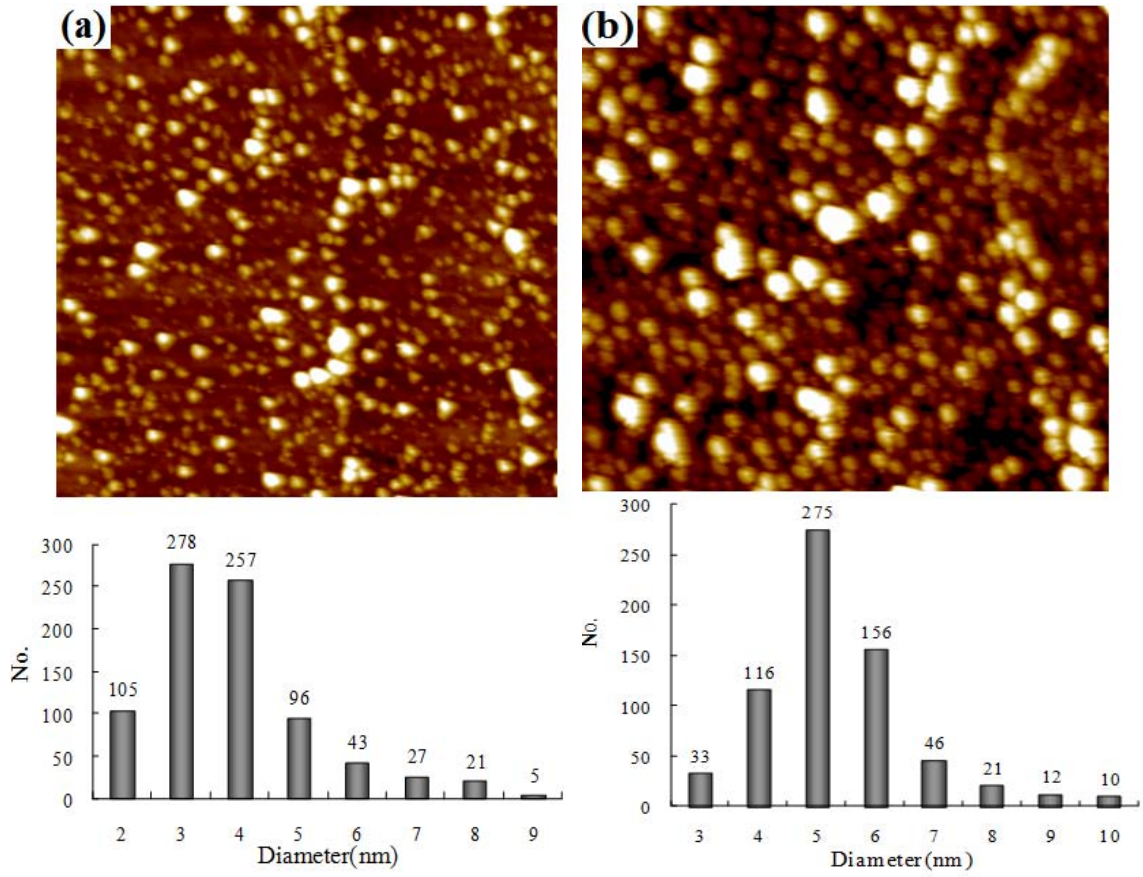

Fig. 67 Room temperature 100 nm × 100 nm STM images and cluster size distributions of Pd clusters on the ultra-thin silica film at various coverages. (a) 2.0 ML Pd, V_b = 1.0 V, I_t = 0.2 nA, and (b) 4.0 ML Pd, V_b = 1.0 V, I_t = 0.2 nA.

on the step edges, indicating that Pd atoms have a large diffusion path on the ultra-thin silica film/Mo(112). High distribution of small clusters might be due to a number of defect sites on the surface. As the Pd coverage was increased to 1.0 ML, both the density and size of the cluster increase accordingly. The inset of Fig. 66(b) shows that even at the coverage of 1.0 ML, most areas of the silica substrate were still not covered by Pd clusters, also indicating a large diffusion length of Pd atoms on silica film. The surface was completely covered by Pd clusters when the coverage reached to 4.0 ML.

Based on the STM images and histogram data, Pd cluster size can be calibrated with the same method as applied to Rh and Pt clusters supported on the silica thin film in previous sections. The calibrations have been performed on each coverage, 0.50 ML, 1.0 ML, 2.0 ML and 4.0 ML and the results are shown as the black line in Fig. 68(a). Since the height measured by STM is usually relatively accurate, no calibration was conducted and the red line in Fig. 68(a) shows the averaged cluster height as a function of Pd coverage. The height and size increase almost linearly as the coverage increases except for the range from 1.0 ML to 2.0 ML, where a slightly slow increase in cluster height was compensated by the steep increase in the cluster size. The scenario is probably that as Pd atoms nucleate on the pre-existing Pd clusters, they prefer to landing on the circumference of the clusters instead of the top of the clusters. Based on the information in Fig. 68(a), the shape of the cluster can also be determined by calculating the average ratio of height to diameter, as shown in Fig. 68(b). The averaged ratio is about 0.2, suggesting that the cluster is relatively flat. The active sites of Pd per cm^2 were also estimated based on Pd(111) facet with the same method discussed in previous sections,

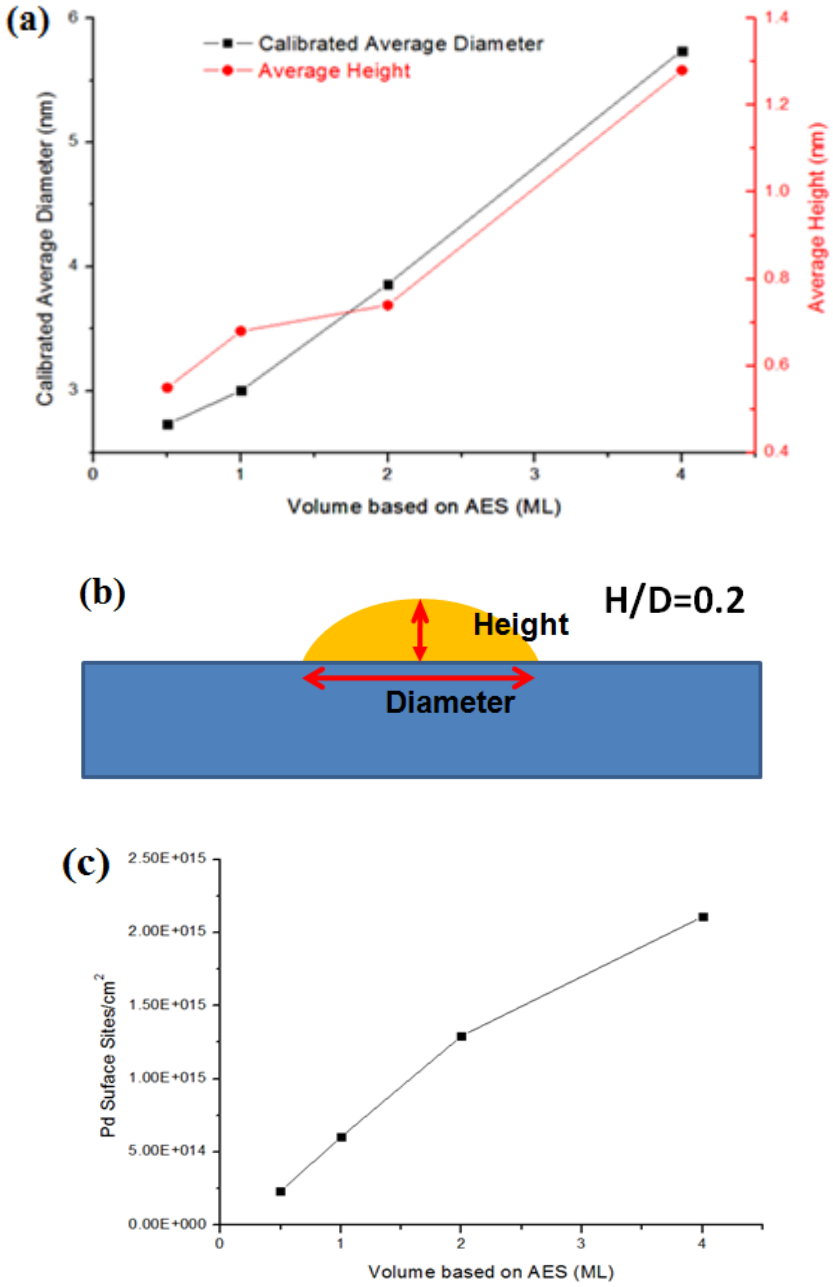

Fig. 68 (a) The plot of calibrated average cluster diameter and height as a function of Pd coverage, (b) A schematic drawing of a Pd cluster supported on the silica film, and (c) The plot of calculated Pd surface sites as a function of Pd coverage.

as shown in Fig. 68(c). As mentioned earlier, such estimates can provide valuable information to accurately relate selectivity and reactivity of Pd clusters with their particle sizes when studying structure sensitive reactions at the elevated pressures.

Thermal Stability of Pd Clusters

The thermal stability of Pd clusters supported on silica thin film was also studied by STM. Numerous literature reports have observed the formation of Pd silicide for Pd supported on SiO_2 upon annealing to higher temperatures [240-245]. It is important and interesting to understand Pd silicide since it may affect catalytic activity and selectivity of Pd catalysts supported on silica [246]. The thermal evolution of 4.0 ML Pd clusters supported on silica film is shown in Fig. 69. Prior to imaging, the sample was first annealed to the target temperature and maintained for 10 min before cooling down to room temperature. No obvious change was observed at annealing temperatures lower than 800 K. Sintering initiates at ~900 K as indicated by the formation of larger clusters. Some flat islands were also observed. The inset image in Fig. 69(d) shows an enlarged view of the islands on which no pattern was observed. Therefore, it is difficult to determine if the islands are Pd metals on top of silica film or Pd atoms diffused beneath the silica film. The silica substrate that is not covered by Pd clusters or islands can still be resolved by STM, indicating that silica film itself is still stable upon annealing to 900 K.

More interestingly, as the annealing temperature was increased to 1000 K, the line structure on the large terrace as well as some amorphous features in the upper right corner was observed, as shown in Fig. 70(a). Fig. 70(b) is a close up image showing the

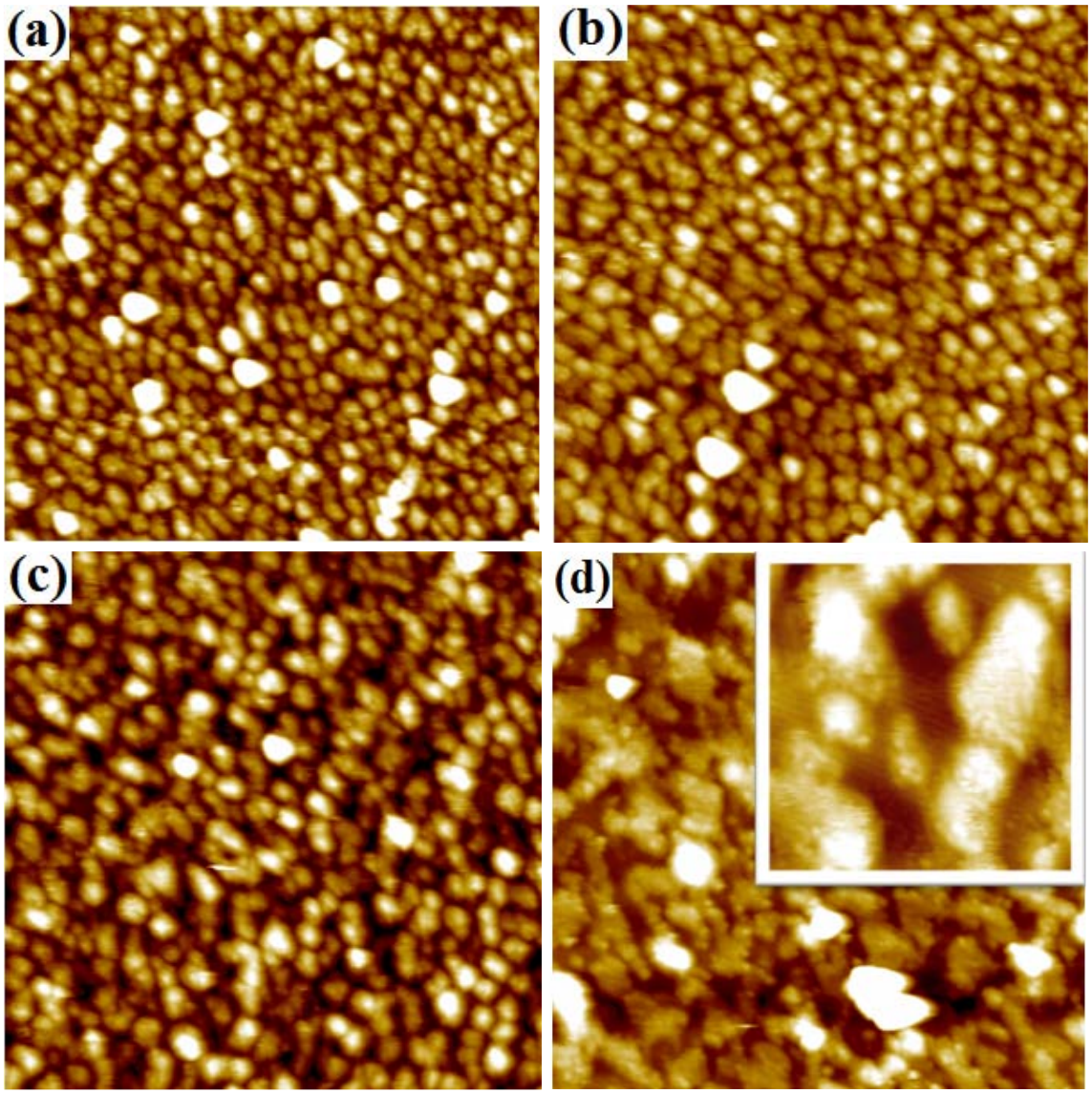

Fig. 69 STM images (100 nm × 100 nm, V_b = 1.0 V, I_t = 0.1 nA) of 4.0 ML Pd supported on ultra-thin silica film/Mo(112) annealed to (a) 600 K, (b) 700 K, (c) 800 K, (d) 900 K, the inset is a close up 20 nm × 20 nm STM image showing both the cluster and silica substrate. All images are acquired after the sample has been cooled down to room temperature after a 10 min annealing.

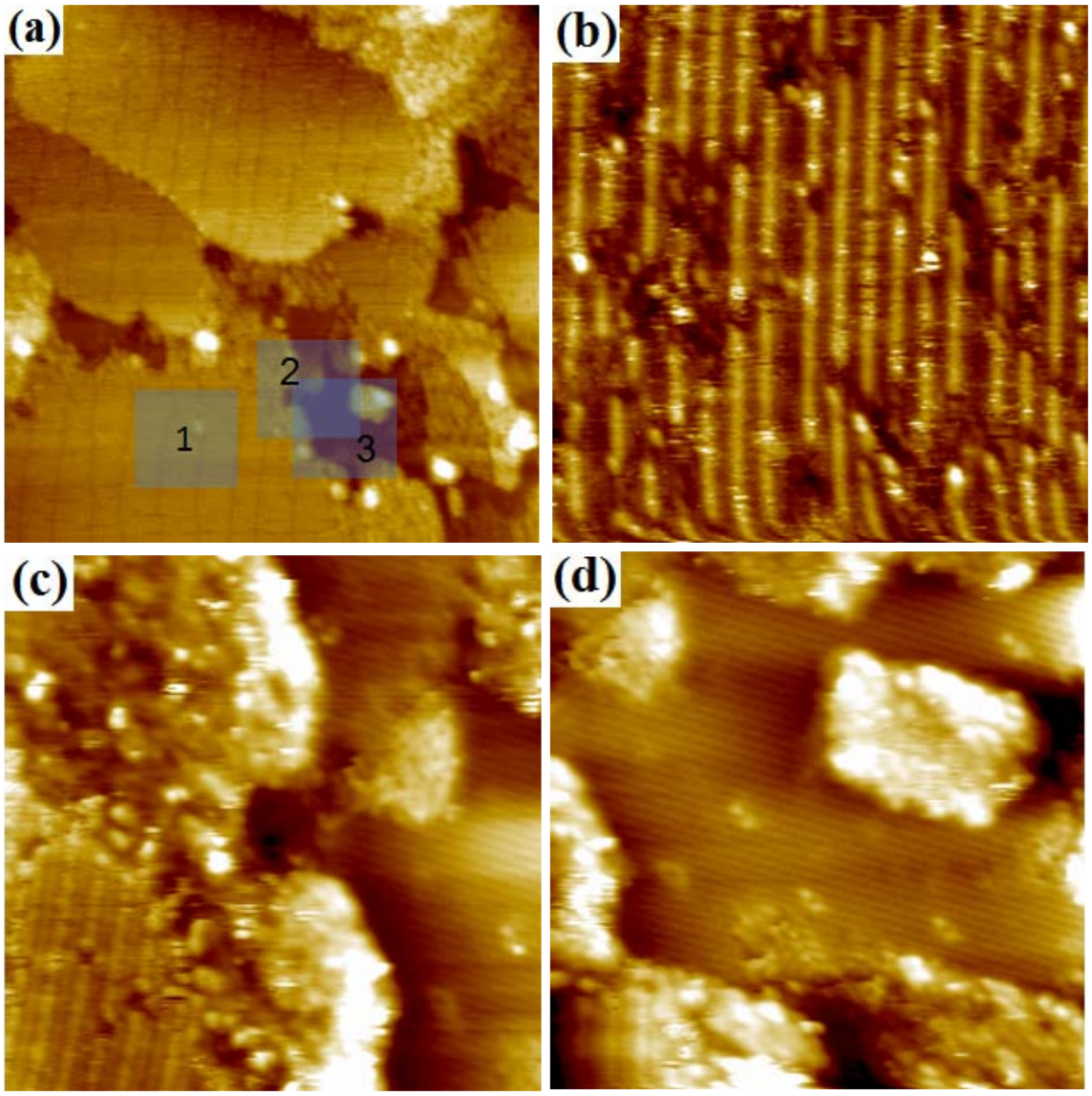

Fig. 70 STM images of 4.0 ML Pd supported on ultra-thin silica film/Mo(112) annealed to 1000 K. (a) 100 nm × 100 nm, V_b = 1.0 V, I_t = 0.1 nA. (b), (c), (d) are 20 nm × 20 nm close up STM images (V_b = 1.0 V, I_t = 0.1 nA) of areas 1, 2, and 3 marked by the blue squares in (a). All images are acquired after the sample has been cooled down to room temperature after a 10 min annealing.

area marked by the square 1 in Fig. 70(a). The line structure can be clearly resolved but not very well ordered. No further detailed structure can be resolved by STM. Fig. 70(c) is an enlarged image of the boundary between the silica substrate and the terrace with the line structure, as marked by square 2 in Fig. 70(a). The typical stripe pattern of the ultra-thin silica film can still be resolved on the area that is not reacted with Pd, indicating the silica film substrate itself is thermally stable under such annealing conditions. Fig. 70(d) shows an enlarged image of the area marked by square 3, where the flat islands are similar to the features observed after 900 K annealing.

The AES measurements were also conducted during the above annealing procedures (data not shown), which is consistent with our STM data. The relative AES intensity ratios of Pd to Mo and O to Mo were monitored at various annealing temperatures, which shows that no change in both ratios when the annealing temperatures are lower than 800 K, while the ratio of Pd to Mo starts to decrease at 900 K and the ratio of O to Mo decreases at 1000 K. It should be noted that these annealing temperatures are not high enough for Pd to desorb from the silica surface. Based on previous temperature programmed desorption (TPD) studies, the desorption temperature of Pd on silica film was determined to be 1050 K [247]. Another important AES feature worth mentioning is that after annealing to 1000 K, the high resolution AES spectrum also shows that the Si LVV peak at 92 eV was split into two peaks at 90 and 94 eV.

Based on both STM and AES data, it is believed that palladium silicide has been formed at the annealing temperature of 1000 K. In particular, the splitting of Si LVV peak is the strong evidence since the detailed AES study regarding Pd supported on

silica by Yamada and co-workers have demonstrated such feature is caused by a palladium rich silicide [242]. This also agrees with STM images, as shown in Fig. 69(d), in which total amount of 4.0 ML Pd was deposited on the surface, while only single layer of Pd silicide film was observed, indicating that more than one Pd atoms are combined with each Si atom. The exact number of Pd atoms that are attached to each Si atom is unknown since there are still amorphous features and Pd islands. Another evidence for the formation of Pd silicide is that AES shows significant loss of oxygen after annealing to 1000 K for 10 min, which is apparently due to the decomposition of SiO_2. The above observations and conclusions are consistent with previous studies of Pd clusters supported on the silica thin film [248].

5.5 Key Factor That Controls the Nucleation Sites

Rh, Pt and Pd behave differently when deposited on the ultra-thin silica film/Mo(112), e.g. Rh and Pt adsorb between two neighboring [SiO_4] units, while Pd atoms nucleate on top of the [SiO_4] units. The annealing effects of three metals supported on the silica thin film are also different. As annealed to higher temperatures, Rh and Pt atoms diffuse beneath the silica to form 2-D islands covered with a silica film, whereas the formation of Pd silicide was observed upon annealing to 1000 K. It is interesting to understand what the key factors that control the growth, nucleation, and thermal stability of different metals are.

The adsorption sites of metal clusters on the surface are usually attributed to the strong interaction between the metal atom and the adsorption site. For example, Rh

clusters prefer to adsorb on the fcc sites of graphene/Ru(0001) because the $sp^2 \rightarrow sp^3$ rehybridization of carbon atoms at the fcc sites on the graphene layer leads to the formation of Rh-C bond. If the metal atoms do not have a strong interaction with any specific sites on the surface, then the metal clusters are usually randomly distributed on the surface. In the case of silica thin film, Rh and Pt prefer to nucleate between two neighboring [SiO_4] units, while Pd atoms favor for the top of the [SiO_4] units. Apparently, at either adsorption site, the metal atom can interact with four oxygen atoms, which means the metal-oxygen bond should not be an important factor in determining the nucleation sites. As a matter of fact, metal-oxygen bonds strengths are similar for the above three metals, e.g. the bond enthalpies for metal-O diatomic species are as follows [249]: Pd-O is 380.7 ± 83.7 kJ/mol; Pt-O is 391.6 ± 41.8 kJ/mol; and Rh-O is 405.0 ± 41.8 kJ/mol. However, the metal atom has the different interactions with the Si atoms at different adsorption sites. The metal atoms nucleated on top of [SiO_4] units only interact with one Si atom, whereas the metal atoms located between neighboring [SiO_4] units interact with two Si atoms. Therefore, it is highly possible that the strength of metal-Si bond plays an important role in determining the adsorption sites. The bond strengths of the metal-silicon diatomic species support the above observations. The bond enthalpies for metal-Si are as follows [249]: Pt-Si is 501.2 ± 18.0 kJ/mol; Rh-Si is 395.0 ± 18.0 kJ/mol; and Pd-Si is only 261 ± 12 kJ/mol. Therefore, in order to maximize the contact with Si atoms, both Pt and Rh atoms prefer to nucleate between neighboring [SiO_4] units. On the contrary, Pd atoms which have a weak interaction with the Si atoms only adsorb on top of the [SiO_4] units.

The size of the metal atoms, which is often critical for the nucleation sites, was also considered. However, we exclude the possibility that Pd atom is too large to fit into the room between two neighboring [SiO_4] units. The diameters of Pd, Rh and Pt are 275.1 pm, 269.0 pm, and 277.5 pm, respectively. As discussed ealier, the space between neighboring Si atoms is large enough to hold any single atom of above three metals. Apparently, the atom size should not be the reason for the different nucleation sites.

Another adsorption site which appears to be appealing for metal atoms is the top of second layer Mo atoms that are not covered by [SiO_4] units. However, in our studies, we did not observe any metal atoms nucleated at this site. Although it seems that the metals at this site might be able to interact with four [SiO_4] units, two in the $[\bar{1}\bar{1}1]$ direction, and the other two in the $[\bar{1}10]$ direction, closer examination reveals that the distance between the two neighboring [SiO_4] units in the $[\bar{1}10]$ direction is so large, i.e. 0.89 nm, that a single Rh or Pt atom nucleated on top of second layer Mo atoms is not able to contact with both of them. In the meanwhile, the metal atom on this site loses two neighboring oxygen atoms compared to the other two sites discussed above. It explains why no metal atom was found to nucleate on this site in our experiments.

Based on the bond enthalpies, it is expected that Pt and Rh have very strong metal-support interactions, whereas Pd has a weak interaction with silica film, which agrees well with our experimental observations. Both Pt and Rh tend to wet the silica thin film, on which they form highly dispersed small clusters. On the other hand, the large Pd clusters decorated at the step edge were observed, suggesting that Pd atoms have a long diffusion path on the silica thin film at room temperature.

The annealing effect studies show that the metal atoms nucleated at the sites between two neighboring [SiO_4] units are relatively thermally stable. In the case of Rh, after annealing to 600 K, the resolved 2-D network structure indicates Rh atoms are still located at the sites between two neighboring [SiO_4] units. At 700 K, the 2-D network transforms to the 2-D islands due to the formation of a pseudomorphous layer of Rh on Mo(112) and migration of [SiO_4] clusters on top of the Rh layer. Pt exhibits similar annealing effects but requires for a little higher annealing temperature. And double layers of Pt atoms were formed underneath silica film upon annealing to 1200 K. Pd exhibits totally different annealing effects. The formation of Pd silicide was observed when annealing to 1000 K.

6. SUMMARY AND CONCLUSIONS

In this dissertation, STM was primarily employed to study two supported model catalyst systems: metals supported on the graphene and metals supported on the ultra-thin silica film. The structures of graphene substrate and silica thin film were thoroughly investigated and modifications were performed on the graphene system in order to adjust both geometric and electronic structures of the graphene surface. In addition, the nucleation sites, morphologies and annealing effects of deposited metals were carefully studied on the two supports.

6.1 Deposition of Metals on Graphene/Ru(0001)

In the studies of deposition of metal clusters on the single-layer graphene/Ru(0001), the key factors that govern cluster growth were investigated. Our experimental findings show that Pt and Rh form finely dispersed small clusters on graphene/Ru(0001), whereas Pd and Co form large clusters at similar coverages. These results, coupled with previous finding that Ir forms the best finely dispersed clusters, suggest that both M-C bond strength and metal cohesive energies play significant roles. The final structures of various clusters then are a competitive effect between these two factors. At coverages lower than the critical point, where the M-C bond dissociation energy is higher than the cohesive energy, 2-D cluster seeds form. At coverages higher than the critical point, the effect of cohesive energy exceeds the interaction between metals and graphene, leading to the formation of 3-D clusters. With this understanding

of cluster growth of these metals on graphene, it is possible to predict the morphology of other transition metals that have not been explored. The M-C bond dissociation energy is the most important factor that affects the morphology of clusters at the initial stages of growth. This suggests that higher M-C dissociation energies should lead to more finely dispersed clusters. The thermal stability of metal clusters supported on graphene is quite impressive. This is very important for studies in heterogeneous catalysis since many metal catalyzed reactions require high reaction temperatures. Our results show that metals with strong M-C interaction tend to have high thermal stabilities and are resistant to sintering even under harsh reaction conditions, which makes them potential candidates as realistic heterogeneous catalysts. .

On the other hand, Au behaves quite differently on graphene. Our experimental findings show that Au form 2-D islands that span several moiré unit cells with the height of 0.55 nm. They conform to the corrugation of the graphene and display commensurate moiré patterns as well, suggesting that other factors such as the effect of the substrate metal and match of the lattice should also be considered. Four Au overlayer models on graphene/Ru(0001) were proposed based on the STM images and have been examined by DFT calculations. The results show that the close-packed Au monolayer and bilayer are energetically more stable but interact weakly with graphene surface. And their heights are not consistent with the observed height of the Au islands measured by STM. On the contrary, (12×12)-Au monolayer and stacked Au trilayer structures are anchored by the formation of Au-C bonds in the mound regions of the graphene, and the height of Au trilayer structure agrees well with our STM measurements. Note that all of the four

models are meta-stable with respect to the bulk Au metal. The experiments were also conducted to test the activity of the 2-D Au islands, which shows that CO molecules adsorb on 2-D Au islands with a binding energy of 30 – 40 kJ/mol and display a C-O stretching frequency of 2095 cm^{-1}, notably red-shifted from that on the neutral Au. This red shift in the CO stretching mode suggests that the 2-D Au islands are electron rich, presumably due to electron transfer from the graphene support to Au. Preliminary data suggest that this adsorbed CO is reactive toward molecular oxygen.

6.2 Graphene/Ru(0001) Modifications and h-BN/Ru(0001)

For the purpose of adjusting the geometric and electronic structures of graphene, three modified graphene/Ru(0001) systems were investigated, including graphene/TM/ Ru(0001), graphene/O/Ru(0001), and carbon-rich graphene/Ru(0001). In the graphene /TM/Ru(0001) system, a pseudomorphic single layer of TM, such as Pd and Co was introduced at interface between graphene and substrate. Our STM and LEED results show that macroscopic self-organized graphene overlayer with high quality can be prepared on Co/Ru(0001) and Pd/Ru(0001). Similar to graphene/Ru(0001), the moiré superstructure lattice constants of both systems have shown to be ~3.0 nm, resulting from superposition of 12 graphene unit cells and 11 unit cells of Co/Ru(0001) or Pd/Ru(0001). Closer inspection of STM image acquired at graphene grown on half covered Ru substrate reveals that the detailed structure of the modified graphene systems, where Co or Pd atoms occupy the hcp hollow sites of Ru(0001) with an intact graphene sheet adsorbed on top. The corrugation of the graphene systems follows the order:

graphene/Co/Ru(0001) > graphene/Ru(0001) > graphene/Pd/Ru(0001). The modification of graphene system was verified by deposition of Au on different graphene systems. Au forms tiny 3-D clusters on graphene/Co/Ru(0001), while large 3-D clusters are observed on graphene/Pd/Ru(0001). These results, coupled with previous findings that large 2-D Au islands grown on graphene/Ru(0001), suggest that an interlayer of TMs may significantly modify the coupling between graphene and Ru(0001). Such tuning of interaction between graphene and its substrate is not only of great importance in studying graphene system itself, but also offers wider opportunities for exploring the morphology effect on model catalysts. In addition, this method has been successfully applied to graphene/Ni/Ru(0001) and graphene/Au/Ru(0001) systems, demonstrating a versatile route to adjust the coupling of graphene to a substrate. It appears that only two conditions are sufficient: first, the metal deposited forms an ultrathin film, which is thermally stable upon annealing to 1100 K; and second, such surface is capable of dissociating the carbon-containing molecules. Thus, various TMs might be used to tune different graphene systems such as graphene/Ir(111), graphene/Ni(111), etc.

In the graphene/O/Ru(0001) system, the intercalation of oxygen leads to change in both corrugation and electronic structure of graphene. The corrugation is about 0.03 nm, which is relatively smaller than 0.12 nm of graphene/Ru(0001) surface. The graphene also becomes electron deficient due to the insertion of oxygen atoms with strong electronnegativity. The deposition of Au on graphene/O/Ru(0001) shows the coexistence of both the 3-D clusters and small 2-D clusters, which are highly dispersed on the surface, suggesting that the interaction between graphene/O/Ru(0001) and Au

clusters is stronger and diffusion length of Au atoms is smaller than that on graphene/Ru(0001).

In the carbon-rich graphene system, our experimental findings show that the exposure of graphene/Ru(0001) to air leads to the formation of amorphous carbon between the graphene and Ru(0001). Although STM images exhibit the same moiré pattern as regular graphene/Ru(0001), the properties of this graphene system is believed to be different because the morphology of Au deposited is quite different from that on graphene/Ru(0001). Similar to Au deposited on graphene/O/Ru(0001), small 2-D clusters highly dispersed on the surface were observed, indicating that graphene with amorphous carbon underneath might interact strongly with the Au. And the diffusion length of Au atoms on carbon-rich graphene is also relatively small.

h-BN/Ru(0001) nanomesh, the isoelectronic system to graphene/Ru(0001), was also investigated and compared with graphene system. Instead of moiré pattern, the nanomesh structure was observed on h-BN/Ru(0001), which consists of the connected wires and round pores. At the onset of deposition of Au atoms, coexistence of small 2-D clusters centered at namomesh apertures and 3-D nanoparticles with diameters greater than the pores were observed. Apparently, the regular hexagonal structure of 2 nm wide pores on the h-BN film can be viewed as trapping sites for these smaller clusters. The annealing effect studies show that the Au clusters are stable upon annealing to 550 K, suggesting that the corrugation of the h-BN nanomesh may hinder the sintering process of metal particles. Furthermore, the studies of stability under reaction conditions show that the morphology of Au clusters supported on h-BN/Ru(0001) keeps the same after

exposure to 1 atm CO or 1 atm O_2 at room temperature. Such stability is gained through a stronger interaction between Au and h-BN, which is probably due to the special geometric structures of h-BN nanomesh. Therefore, h-BN nanomesh might be an excellent template to fabricate nanoparticles that are stable under reaction conditions.

6.3 Deposition of Metals on Ultra-thin Silica Film

In the studies of deposition of metals on the ultra-thin silica film/Mo(112), the structure of silica thin film was carefully investigated, and nucleation and the growth of three catalytically important metals, namely, Rh, Pt and Pd on the film were studied. The high-resolution STM images of silica thin film agree well with the cluster mode proposed by Chen *et al*. The nucleation and adsorption studies show that Rh and Pt nucleate between two neighboring [SiO_4] units, while Pd atoms adsorb on top of the [SiO_4] units. Such distinction is attributed to different interactions of metal atoms with Si atoms. Both Pt and Rh atoms bond strongly to Si atoms and thus they prefer to nucleate between neighboring [SiO_4] units in order to maximize the contact with Si atoms. On the other hand, Pd atoms bond weakly with Si and only adsorb on top of [SiO_4] cluster. The above difference also explains why Rh and Pt interact strongly with the film, whereas Pd atoms have a relatively weak interaction. The annealing effects of three metals supported on silica thin film also exhibit different behaviors. As annealed to higher temperatures, Rh and Pt atoms diffuse beneath the silica to form the 2-D islands covered with the silica film. It is interesting to observe that the 2-D islands are also covered with the silica thin film with the same structure as the substrate, suggesting that Rh and Pt atoms form

pseudomorphous layers on Mo(112). On the contrary, formation of Pd silicide was observed upon annealing to 1000 K.

In addition, based on the STM images and histogram data of metal clusters on silica thin film, the active sites per cm^2 as a function of coverage can be estimated using a few simplifying geometric arguments, which can provide valuable information regarding the catalytic activities of metal clusters supported on silica film. To testify the correctness of STM estimates, CO TPD and oxidation reactivity measurements were also employed to characterize active sites in this system and we found that general agreement was achieved among three characterization methods. The trivial inconsistency may be due to the simplifying geometric assumptions in the STM estimation because facets are more characteristic of smaller particles. Note that STM and CO TPD measurements were taken under UHV conditions (10^{-10} Torr), whereas oxidation reactivity measurements was performed at high pressures (8 Torr). The agreement among three estimation methods suggests that STM measurements are capable of providing a reasonable estimate of the particle sizes even under elevated pressure conditions. Therefore, in some cases, we can practically relate selectivity and reactivity with the particle size measured by STM when studying structure sensitive reactions on model catalyst surfaces at elevated pressures.

REFERENCES

[1] J.H. Sinfelt, Surf. Sci. 500 (2002) 923.

[2] X. Su, P.S. Cremer, Y.R. Shen, G.A. Somorjai, Phys. Rev. Lett. 77 (1996) 3858.

[3] G. Rupprechter, H. Unterhalt, M. Morkel, P. Galletto, L.J. Hu, H.J. Freund, Surf. Sci. 502 (2002) 109.

[4] T. Dellwig, G. Rupprechter, H. Unterhalt, H.J. Freund, Phys. Rev. Lett. 85 (2000) 776.

[5] E. Ozensoy, C. Hess, D.W. Goodman, J. Am. Chem. Soc. 124 (2002) 8524.

[6] E. Ozensoy, D.W. Goodman, PCCP 6 (2004) 3765.

[7] G. Rupprechter, T. Dellwig, H. Unterhalt, H.J. Freund, J. Phys. Chem. B 105 (2001) 3797.

[8] E. Ozensoy, C. Hess, D. Loffreda, P. Sautet, D.W. Goodman, J. Phys. Chem. B 109 (2005) 5414.

[9] D.W. Goodman, Surf. Rev. Lett. 2 (1995) 9.

[10] J.A. Rodriguez, D.W. Goodman, Surf. Sci. Rep. 14 (1991) 1.

[11] G.A. Somorjai, Surf. Sci. 299 (1994) 849.

[12] X.P. Xu, D.W. Goodman, J. Phys. Chem. 97 (1993) 683.

[13] G.A. Somorjai, Y. Li, Introduction to Surface Chemistry and Catalysis, Wiley, New York, 2010.

[14] A.G. Sault, D.W. Goodman, Adv. Chem. Phys. 76 (1989) 153.

[15] M. Che, C.O. Bennett, Adv. Catal. 36 (1989) 55.

[16] D.A. King, D.P. Woodruff, Growth and Properties of Ultrathin Epitaxial Layers, Elsevier, Amsterdam, 1997.

[17] H.J. Freund, M. Baumer, H. Kuhlenbeck, Adv. Catal. 45 (2000) 333.

[18] C.R. Henry, Surf. Sci. Rep. 31 (1998) 235.

[19] S.A. Chambers, Surf. Sci. Rep. 39 (2000) 105.

[20] R. Franchy, Surf. Sci. Rep. 38 (2000) 199.

[21] D.R. Rainer, D.W. Goodman, J. Mol. Catal. A: Chem. 131 (1998) 259.

[22] D.W. Goodman, J. Phys. Chem. 100 (1996) 13090.

[23] A.K. Santra, D.W. Goodman, J. Phys.: Condens. Matter 15 (2003) R31.

[24] C.T. Campbell, Surf. Sci. Rep. 27 (1997) 1.

[25] V.P. Zhdanov, B. Kasemo, Surf. Sci. Rep. 39 (2000) 29.

[26] W.W. Crew, R.J. Madix, Surf. Sci. 319 (1994) L34.

[27] R.J. Koestner, M.A. Vanhove, G.A. Somorjai, Surf. Sci. 121 (1982) 321.

[28] M.A. Vanhove, R.J. Koestner, P.C. Stair, J.P. Biberian, L.L. Kesmodel, I. Bartos, G.A. Somorjai, Surf. Sci. 103 (1981) 189.

[29] M.A. Vanhove, R.J. Koestner, P.C. Stair, J.P. Biberian, L.L. Kesmodel, I. Bartos, G.A. Somorjai, Surf. Sci. 103 (1981) 218.

[30] M. Eiswirth, G. Ertl, Surf. Sci. 177 (1986) 90.

[31] G. Ertl, Ber. Bunsen. Phys. Chem. 90 (1986) 284.

[32] P. Moller, K. Wetzl, M. Eiswirth, G. Ertl, J. Chem. Phys. 85 (1986) 5328.

[33] D.W. Goodman, R.D. Kelley, T.E. Madey, J.T. Yates, J. Catal. 63 (1980) 226.

[34] C.T. Campbell, M.T. Paffett, Surf. Sci. 139 (1984) 396.

[35] R.A. Campbell, D.W. Goodman, Rev. Sci. Instrum. 63 (1992) 172.

[36] B.J. Mcintyre, M.B. Salmeron, G.A. Somorjai, Catal. Lett. 14 (1992) 263.

[37] B.J. Mcintyre, M. Salmeron, G.A. Somorjai, J. Vac. Sci. Technol. A 11 (1993) 1964.

[38] B.J. Mcintyre, M. Salmeron, G.A. Somorjai, Rev. Sci. Instrum. 64 (1993) 687.

[39] B.J. Mcintyre, M. Salmeron, G.A. Somorjai, Science 265 (1994) 1415.

[40] B.J. Mcintyre, M. Salmeron, G.A. Somorjai, Surf. Sci. 323 (1995) 189.

[41] B.J. McIntyre, M. Salmeron, G.A. Somorjai, J. Catal. 164 (1996) 184.

[42] B.J. McIntyre, M. Salmeron, G.A. Somorjai, Catal. Lett. 39 (1996) 5.

[43] B.J. Mcintyre, P. Sautet, J.C. Dunphy, M. Salmeron, G.A. Somorjai, J. Vac. Sci. Technol. B 12 (1994) 1751.

[44] J.A. Jensen, K.B. Rider, M. Salmeron, G.A. Somorjai, Phys. Rev. Lett. 80 (1998) 1228.

[45] P.B. Rasmussen, B.L.M. Hendriksen, H. Zeijlemaker, H.G. Ficke, J.W.M. Frenken, Rev. Sci. Instrum. 69 (1998) 3879.

[46] J.A. Jensen, K.B. Rider, Y. Chen, M. Salmeron, G.A. Somorjai, J. Vac. Sci. Technol. B 17 (1999) 1080.

[47] A. Kolmakov, D.W. Goodman, Catal. Lett. 70 (2000) 93.

[48] T. Kobiela, R. Dus, Vacuum 63 (2001) 267.

[49] A. Kolmakov, D.W. Goodman, Surf. Sci. 490 (2001) L597.

[50] K.B. Rider, K.S. Hwang, M. Salmeron, G.A. Somorjai, Phys. Rev. Lett. 86 (2001) 4330.

[51] E. Laegsgaard, L. Osterlund, P. Thostrup, P.B. Rasmussen, I. Stensgaard, F. Besenbacher, Rev. Sci. Instrum. 72 (2001) 3537.

[52] B.L.M. Hendriksen, J.W.M. Frenken, Phys. Rev. Lett. 89 (2002).

[53] K.B. Rider, K.S. Hwang, M. Salmeron, G.A. Somorjai, J. Am. Chem. Soc. 124 (2002) 5588.

[54] E.K. Vestergaard, P. Thostrup, T. An, E. Laegsgaard, I. Stensgaard, B. Hammer, F. Besenbacher, Phys. Rev. Lett. 88 (2002).

[55] B.L.M. Hendriksen, S.C. Bobaru, J.W.M. Frenken, Surf. Sci. 552 (2004) 229.

[56] S.H. Kim, J. Mendez, J. Wintterlin, G. Ertl, Phys. Rev. B 72 (2005).

[57] M. Rossler, P. Geng, J. Wintterlin, Rev. Sci. Instrum. 76 (2005).

[58] B.L.M. Hendriksen, S.C. Bobaru, J.W.M. Frenken, Catal. Today 105 (2005) 234.

[59] M. Montano, K. Bratlie, M. Salmeron, G.A. Somorjai, J. Am. Chem. Soc. 128 (2006) 13229.

[60] M. Montano, M. Salmeron, G.A. Somorjai, Surf. Sci. 600 (2006) 1809.

[61] R. Reichelt, S. Gunther, M. Rossler, J. Wintterlin, B. Kubias, B. Jakobi, R. Schlogl, PCCP 9 (2007) 3590.

[62] M. Rossler, S. Gunther, J. Wintterlin, J. Phys. Chem. C 111 (2007) 2242.

[63] W.P.A. Jansen, A.W.D. van der Gon, G.M. Wijers, Y.G.M. Rikers, H.H. Brongersma, P.W. van der Hoogen, J.A.M. de Laat, T.M. Maas, E.C.A. Dekkers, P. Brinkgreve, Rev. Sci. Instrum. 73 (2002) 354.

[64] D.F. Ogletree, H. Bluhm, G. Lebedev, C.S. Fadley, Z. Hussain, M. Salmeron, Rev. Sci. Instrum. 73 (2002) 3872.

[65] K. Siegbahn, ESCA Applied to Free Molecules, Amsterdam, North-Holland Pub. Co.,, 1969.

[66] B. Lindberg, L. Asplund, H. Fellnerfeldegg, P. Kelfve, H. Siegbahn, K. Siegbahn, Chem. Phys. Lett. 39 (1976) 8.

[67] H. Siegbahn, L. Asplund, P. Kelfve, K. Hamrin, L. Karlsson, K. Siegbahn, J. Electron. Spectrosc. Relat. Phenom. 5 (1974) 1059.

[68] H. Siegbahn, L. Asplund, P. Kelfve, K. Siegbahn, J. Electron. Spectrosc. Relat. Phenom. 7 (1975) 411.

[69] H. Fellnerfeldegg, H. Siegbahn, L. Asplund, P. Kelfve, K. Siegbahn, J. Electron. Spectrosc. Relat. Phenom. 7 (1975) 421.

[70] H. Poppa, Cat. Rev. - Sci. Eng. 35 (1993) 359.

[71] R.J. Lad, Surf. Rev. Lett. 2 (1995) 109.

[72] A. Zangwill, Physics at Surfaces, Cambridge University Press, New York, 1988.

[73] S.H. Overbury, P.A. Bertrand, G.A. Somorjai, Chem. Rev. 75 (1975) 547.

[74] H.P. Steinruck, F. Pesty, L. Zhang, T.E. Madey, Phys. Rev. B 51 (1995) 2427.

[75] L. Zhang, R. Persaud, T.E. Madey, Phys. Rev. B 56 (1997) 10549.

[76] A. Berko, G. Menesi, F. Solymosi, Surf. Sci. 372 (1997) 202.

[77] A. Berko, F. Solymosi, Surf. Sci. 400 (1998) 281.

[78] A. Berko, G. Menesi, F. Solymosi, J. Phys. Chem. 100 (1996) 17732.

[79] G.E. Poirier, B.K. Hance, J.M. White, J. Phys. Chem. 97 (1993) 6500.

[80] G.E. Poirier, B.K. Hance, J.M. White, J. Phys. Chem. 97 (1993) 5965.

[81] C. Xu, W.S. Oh, G. Liu, D.Y. Kim, D.W. Goodman, J. Vac. Sci. Technol. A 15 (1997) 1261.

[82] C. Xu, D.W. Goodman, Chem. Phys. Lett. 263 (1996) 13.

[83] U. Diebold, J.M. Pan, T.E. Madey, Phys. Rev. B 47 (1993) 3868.

[84] J.M. Pan, U. Diebold, L.Z. Zhang, T.E. Madey, Surf. Sci. 295 (1993) 411.

[85] C. Xu, X. Lai, G.W. Zajac, D.W. Goodman, Phys. Rev. B 56 (1997) 13464.

[86] R.D. Moorhead, H. Poppa, Thin Solid Films 58 (1979) 169.

[87] Chakrave.Bk, J. Phys. Chem. Solids 28 (1967) 2401.

[88] C.H. Bartholomew, Catalyst Deactivation 1997 111 (1997) 585.

[89] H.R. Sadeghi, V.E. Henrich, Appl. Surf. Sci. 19 (1984) 330.

[90] H.R. Sadeghi, V.E. Henrich, J. Catal. 109 (1988) 1.

[91] F. Pesty, H.P. Steinruck, T.E. Madey, Surf. Sci. 339 (1995) 83.

[92] Y. Gao, Y. Liang, S.A. Chambers, Surf. Sci. 365 (1996) 638.

[93] A. Berko, I. Ulrych, K.C. Prince, J. Phys. Chem. B 102 (1998) 3379.

[94] R.A. Bennett, C.L. Pang, N. Perkins, R.D. Smith, P. Morrall, R.I. Kvon, M. Bowker, J. Phys. Chem. B 106 (2002) 4688.

[95] Q. Fu, T. Wagner, S. Olliges, H.D. Carstanjen, J. Phys. Chem. B 109 (2005) 944.

[96] S. Labich, E. Taglauer, H. Knozinger, Top. Catal. 14 (2001) 153.

[97] G. Ertl, Handbook of heterogeneous catalysis, Wiley-VCH, Weinheim, 2008.

[98] G. Ertl, J. Küppers, Low Energy Electrons and Surface Chemistry, VCH, Weinheim, Germany, 1985.

[99] N.S. Harris, Modern vacuum practice, McGraw-Hill, London, 1989.

[100] F. Besenbacher, Rep. Prog. Phys. 59 (1996) 1737.

[101] R.J. Hamers, Annu. Rev. Phys. Chem. 40 (1989) 531.

[102] C. Bai, Scanning Tunneling Microscopy and Its Application, Springer, Shanghai, 1995.

[103] P. Auger, J. Phys.-Paris 6 (1925) 205.

[104] J.J. Lander, Phys. Rev. 91 (1953) 1382.

[105] L.B. Leder, J.A. Simpson, Rev. Sci. Instrum. 29 (1958) 571.

[106] P.W. Palmberg, G.K. Bohn, J.C. Tracy, Appl. Phys. Lett. 15 (1969) 254.

[107] L. de Broglie, Philos. Mag. 47 (1924) 446.

[108] C. Davisson, L.H. Germer, Phys. Rev. 30 (1927) 705.

[109] M.C. Wu, Q. Xu, D.W. Goodman, J. Phys. Chem. 98 (1994) 5104.

[110] J. Mendez, M. Luna, A.M. Baro, Surf. Sci. 266 (1992) 294.

[111] R. Zhang, D.G. Ivey, J. Vac. Sci. Technol. B 14 (1996) 1.

[112] A.I. Oliva, A. Romero, J.L. Pena, E. Anguiano, M. Aguilar, Rev. Sci. Instrum. 67 (1996) 1917.

[113] V. Weinstein, M. Slutzky, A. Arenshtam, E. Benjacob, Rev. Sci. Instrum. 66 (1995) 3075.

[114] A.G. Guell, I. Diez-Perez, P. Gorostiza, F. Sanz, Anal. Chem. 76 (2004) 5218.

[115] R. Fainchtein, P.R. Zarriello, Ultramicroscopy 42 (1992) 1533.

[116] M.C. Baykul, Mater. Sci. Eng., B 74 (2000) 229.

[117] B. Ren, G. Picardi, B. Pettinger, Rev. Sci. Instrum. 75 (2004) 837.

[118] G.A. Fried, X.D. Wang, K.W. Hipps, Rev. Sci. Instrum. 64 (1993) 1495.

[119] M. Iwami, Y. Uehara, S. Ushioda, Rev. Sci. Instrum. 69 (1998) 4010.

[120] A.J. Melmed, J. Vac. Sci. Technol. B 9 (1991) 601.

[121] J.A. Kubby, J.J. Boland, Surf. Sci. Rep. 26 (1996) 61.

[122] A.K. Geim, K.S. Novoselov, Nat. Mater. 6 (2007) 183.

[123] M. Jacoby, Chem. Eng. News 87 (2009) 14.

[124] S. Hagstrom, H.B. Lyon, G.A. Somorjai, Phys. Rev. Lett. 15 (1965) 491.

[125] H.B. Lyon, G.A. Somorjai, J. Chem. Phys. 46 (1967) 2539.

[126] A.E. Morgan, G.A. Somorjai, Surf. Sci. 12 (1968) 405.

[127] J.W. May, Surf. Sci. 17 (1969) 267.

[128] J.T. Grant, T.W. Haas, Surf. Sci. 21 (1970) 76.

[129] K.S. Novoselov, A.K. Geim, S.V. Morozov, D. Jiang, Y. Zhang, S.V. Dubonos, I.V. Grigorieva, A.A. Firsov, Science 306 (2004) 666.

[130] I. Forbeaux, J.M. Themlin, V. Langlais, L.M. Yu, H. Belkhir, J.M. Debever, Surf. Rev. Lett. 5 (1998) 193.

[131] C. Berger, Z.M. Song, T.B. Li, X.B. Li, A.Y. Ogbazghi, R. Feng, Z.T. Dai, A.N. Marchenkov, E.H. Conrad, P.N. First, W.A. de Heer, J. Phys. Chem. B 108 (2004) 19912.

[132] T. Ohta, A. Bostwick, T. Seyller, K. Horn, E. Rotenberg, Science 313 (2006) 951.

[133] N.A. Kholin, E.V. Rutkov, A.Y. Tontegode, Surf. Sci. 139 (1984) 155.

[134] E.V. Rutkov, A.Y. Tontegode, Surf. Sci. 161 (1985) 373.

[135] A.T. N'Diaye, J. Coraux, T.N. Plasa, C. Busse, T. Michely, New J. Phys. 10 (2008) 043033.

[136] E. Loginova, S. Nie, K. Thürmer, N. Bartelt, K. McCarty, Phys. Rev. B 80 (2009) 085430.

[137] T.A. Land, T. Michely, R.J. Behm, J.C. Hemminger, G. Comsa, Surf. Sci. 264 (1992) 261.

[138] H. Ueta, Surf. Sci. 560 (2004) 183.

[139] T. Fujita, W. Kobayashi, C. Oshima, Surf. Interface Anal. 37 (2005) 120.

[140] P. Sutter, J.T. Sadowski, E. Sutter, Phys. Rev. B 80 (2009) 245411.

[141] D.G. Castner, B.A. Sexton, G.A. Somorjai, Surf. Sci. 71 (1978) 519.

[142] F. Müller, H. Sachdev, S. Hüfner, A.J. Pollard, E.W. Perkins, J.C. Russell, P.H. Beton, S. Gsell, M. Fischer, M. Schreck, B. Stritzker, Small 5 (2009) 2291.

[143] M. Sicot, S. Bouvron, O. Zander, U. Rüdiger, Y.S. Dedkov, M. Fonin, Appl. Phys. Lett. 96 (2010) 093115.

[144] F.J. Himpsel, K. Christmann, P. Heimann, D.E. Eastman, P.J. Feibelman, Surf. Sci. 115 (1982) L159.

[145] M.C. Wu, Q. Xu, D.W. Goodman, J. Phys. Chem. 98 (1994) 5104.

[146] S. Marchini, S. Günther, J. Wintterlin, Phys. Rev. B 76 (2007) 075429.

[147] P.W. Sutter, J.-I. Flege, E.A. Sutter, Nat. Mater. 7 (2008) 406.

[148] E. Loginova, N.C. Bartelt, P.J. Feibelman, K.F. McCarty, New J. Phys. 10 (2008) 093026.

[149] D. Martoccia, P. Willmott, T. Brugger, M. Björck, S. Günther, C. Schlepütz, A. Cervellino, S. Pauli, B. Patterson, S. Marchini, J. Wintterlin, W. Moritz, T. Greber, Phys. Rev. Lett. 101 (2008) 126102.

[150] Y. Gamo, A. Nagashima, M. Wakabayashi, M. Terai, C. Oshima, Surf. Sci. 374 (1997) 61.

[151] Y.S. Dedkov, M. Fonin, C. Laubschat, Appl. Phys. Lett. 92 (2008) 052506.

[152] Y.S. Dedkov, M. Fonin, U. Rudiger, C. Laubschat, Phys. Rev. Lett. 100 (2008) 107602.

[153] A.T. N'Diaye, S. Bleikamp, P.J. Feibelman, T. Michely, Phys. Rev. Lett. 97 (2006).

[154] Y. Pan, M. Gao, L. Huang, F. Liu, H.J. Gao, Appl. Phys. Lett. 95 (2009).

[155] H. Zhang, Q. Fu, Y. Cui, D.L. Tan, X.H. Bao, Chin. Sci. Bull. 54 (2009) 2446.

[156] P.J. Feibelman, Phys. Rev. B 77 (2008).

[157] P.J. Feibelman, Phys. Rev. B 80 (2009).

[158] A.T. N'Diaye, T. Gerber, C. Busse, J. Myslivecek, J. Coraux, T. Michely, New J. Phys. 11 (2009).

[159] D.W. Goodman, J.M. White, Surf. Sci. 90 (1979) 201.

[160] S. Marchini, S. Gunther, J. Wintterlin, Phys. Rev. B 76 (2007).

[161] J. Wintterlin, M.L. Bocquet, Surf. Sci. 603 (2009) 1841.

[162] D. Martoccia, P.R. Willmott, T. Brugger, M. Bjorck, S. Gunther, C.M. Schleputz, A. Cervellino, S.A. Pauli, B.D. Patterson, S. Marchini, J. Wintterlin, W. Moritz, T. Greber, Phys. Rev. Lett. 101 (2008).

[163] S.R. Wang, Y. Zhang, N. Abidi, L. Cabrales, Langmuir 25 (2009) 11078.

[164] L.Z. Mezey, J. Giber, Jpn. J. Appl. Phys., Part 1 21 (1982) 1569.

[165] P. Feibelman, Phys. Rev. B 80 (2009) 085412.

[166] J.A.M. Simoes, J.L. Beauchamp, Chem. Rev. 90 (1990) 629.

[167] D. Tzeli, A. Mavridis, J. Phys. Chem. A 110 (2006) 8952.

[168] H.K. Kim, S.H. Huh, J.W. Park, J.W. Jeong, G.H. Lee, Chem. Phys. Lett. 354 (2002) 165.

[169] K.K. Nanda, S.N. Sahu, S.N. Behera, Phys. Rev. A 66 (2002).

[170] W.H. Qi, M.P. Wang, M. Zhou, W.Y. Hu, J. Phys. D: Appl. Phys. 38 (2005) 1429.

[171] M.A. Turchanin, P.G. Agraval, Powder Metall. Met. Ceram. 47 (2008) 26.

[172] M. Haruta, N. Yamada, T. Kobayashi, S. Iijima, J. Catal. 115 (1989) 301.

[173] M. Valden, X. Lai, D.W. Goodman, Science 281 (1998) 1647.

[174] G.C. Bond, D.T. Thompson, Cat. Rev. - Sci. Eng. 41 (1999) 319.

[175] A.T. Bell, Science 299 (2003) 1688.

[176] D.R. Rolison, Science 299 (2003) 1698.

[177] M.S. Chen, D.W. Goodman, Science 306 (2004) 252.

[178] A. Haruta, Chem. Rec. 3 (2003) 75.

[179] R. Meyer, C. Lemire, S.K. Shaikhutdinov, H. Freund, Gold Bull. 37 (2004) 72.

[180] M.C. Daniel, D. Astruc, Chem. Rev. 104 (2004) 293.

[181] G.J. Hutchings, Catal. Today 100 (2005) 55.

[182] M. Haruta, Catal. Today 36 (1997) 153.

[183] B. Borca, F. Calleja, J.J. Hinarejos, A.L.V. de Parga, R. Miranda, J. Phys.: Condens. Matter 21 (2009).

[184] H. Zhang, Q. Fu, Y. Cui, D.L. Tan, X.H. Bao, J. Phys. Chem. C 113 (2009) 8296.

[185] Z.H. Zhou, F. Gao, D.W. Goodman, Surf. Sci. 604 (2010) 1071.

[186] Y. Xu, L. Semidey-Flecha, L. Liu, Z.H. Zhou, D.W. Goodman, Faraday Discuss. 152 (2011) 267.

[187] B. Wang, S. Gunther, J. Wintterlin, M.L. Bocquet, New J. Phys. 12 (2010).

[188] N. Lopez, J.K. Norskov, Surf. Sci. 515 (2002) 175.

[189] Y. Zhang, L. Giordano, G. Pacchioni, J. Phys. Chem. C 112 (2008) 191.

[190] H. Pfnur, D. Menzel, F.M. Hoffmann, A. Ortega, A.M. Bradshaw, Surf. Sci. 93 (1980) 431.

[191] P.A. Redhead, Cc./Eng. Tech. Appl. Sci. (1980) 16.

[192] M. Chen, Y. Cai, Z. Yan, D.W. Goodman, J. Am. Chem. Soc. 128 (2006) 6341.

[193] D.C. Meier, V. Bukhtiyarov, A.W. Goodman, J. Phys. Chem. B 107 (2003) 12668.

[194] M.S. Chen, D.W. Goodman, Acc. Chem. Res. 39 (2006) 739.

[195] G. Giovannetti, P.A. Khomyakov, G. Brocks, V.M. Karpan, J. van den Brink, P.J. Kelly, Phys. Rev. Lett. 101 (2008).

[196] P.A. Khomyakov, G. Giovannetti, P.C. Rusu, G. Brocks, J. van den Brink, P.J. Kelly, Phys. Rev. B 79 (2009).

[197] B. Yoon, H. Hakkinen, U. Landman, J. Phys. Chem. A 107 (2003) 4066.

[198] A. Preobrajenski, M. Ng, A. Vinogradov, N. Mårtensson, Phys. Rev. B 78 (2008) 073401.

[199] A. N'Diaye, S. Bleikamp, P. Feibelman, T. Michely, Phys. Rev. Lett. 97 (2006) 215501.

[200] A.T. N'Diaye, T. Gerber, C. Busse, J. Mysliveček, J. Coraux, T. Michely, New J. Phys. 11 (2009) 103045.

[201] Z.H. Zhou, F. Gao, D.W. Goodman, Surf. Sci. 604 (2010) 1071.

[202] K. Donner, P. Jakob, J. Chem. Phys. 131 (2009) 164701.

[203] Y. Pan, M. Gao, L. Huang, F. Liu, H.J. Gao, Appl. Phys. Lett. 95 (2009).

[204] L. Liu, Z.H. Zhou, Q.L. Guo, Z. Yan, Y.X. Yao, D.W. Goodman, Surf. Sci. 605 (2011) L47.

[205] A. Varykhalov, J. Sánchez-Barriga, A. Shikin, C. Biswas, E. Vescovo, A. Rybkin, D. Marchenko, O. Rader, Phys. Rev. Lett. 101 (2008) 157601.

[206] A. Nagashima, N. Tejima, C. Oshima, Phys. Rev. B 50 (1994) 17487.

[207] C. Liu, S.D. Bader, J. Magn. Magn. Mater. 119 (1993) 81.

[208] A. de Siervo, E. De Biasi, F. Garcia, R. Landers, M. Martins, W. Macedo, Phys. Rev. B 76 (2007) 075432.

[209] H. Zhang, Q. Fu, Y. Cui, D. Tan, X. Bao, J. Phys. Chem. C 113 (2009) 8296.

[210] P. Sutter, J.T. Sadowski, E.A. Sutter, J. Am. Chem. Soc. 132 (2010) 8175.

[211] H.J. Zhang, Y.F. Xu, X.S. Wang, H.F. Wu, H.Y. Li, S.N. Bao, P. He, Piers 2009 Beijing: Progess in Electromagnetics Research Symposium, Proceedings I and II (2009) 1097.

[212] J. Wintterlin, M.L. Bocquet, Surf. Sci. 603 (2009) 1841.

[213] H. Hoster, E. Filonenko, B. Richter, R. Behm, Phys. Rev. B 73 (2006) 165413.

[214] C. Berger, Z.M. Song, T.B. Li, X.B. Li, A.Y. Ogbazghi, R. Feng, Z.T. Dai, A.N. Marchenkov, E.H. Conrad, P.N. First, W.A. de Heer, J. Phys. Chem. B 108 (2004) 19912.

[215] A.M. Shikin, G.V. Prudnikova, V.K. Adamchuk, F. Moresco, K.H. Rieder, Phys. Rev. B 62 (2000) 13202.

[216] E. Sutter, D.P. Acharya, J.T. Sadowski, P. Sutter, Appl. Phys. Lett. 94 (2009).

[217] T. Brugger, S. Gunther, B. Wang, J.H. Dil, M.L. Bocquet, J. Osterwalder, J. Wintterlin, T. Greber, Phys. Rev. B 79 (2009).

[218] P. Sutter, M.S. Hybertsen, J.T. Sadowski, E. Sutter, Nano Lett. 9 (2009) 2654.

[219] L.M. Kong, C. Bjelkevig, S. Gaddam, M. Zhou, Y.H. Lee, G.H. Han, H.K. Jeong, N. Wu, Z.Z. Zhang, J. Xiao, P.A. Dowben, J.A. Kelber, J. Phys. Chem. C 114 (2010) 21618.

[220] A. Varykhalov, O. Rader, W. Gudat, Phys. Rev. B 77 (2008).

[221] W. Auwarter, T.J. Kreutz, T. Greber, J. Osterwalder, Surf. Sci. 429 (1999) 229.

[222] M. Corso, W. Auwarter, M. Muntwiler, A. Tamai, T. Greber, J. Osterwalder, Science 303 (2004) 217.

[223] S. Berner, M. Corso, R. Widmer, O. Groening, R. Laskowski, P. Blaha, K. Schwarz, A. Goriachko, H. Over, S. Gsell, M. Schreck, H. Sachdev, T. Greber, J. Osterwalder, Angew. Chem. Int. Ed. 46 (2007) 5115.

[224] A. Goriachko, Y.B. He, M. Knapp, H. Over, M. Corso, T. Brugger, S. Berner, J. Osterwalder, T. Greber, Langmuir 23 (2007) 2928.

[225] A.B. Preobrajenski, A.S. Vinogradov, M.L. Ng, E. Cavar, R. Westerstrom, A. Mikkelsen, E. Lundgren, N. Martensson, Phys. Rev. B 75 (2007).

[226] H. Dil, J. Lobo-Checa, R. Laskowski, P. Blaha, S. Berner, J. Osterwalder, T. Greber, Science 319 (2008) 1824.

[227] J. Zhang, V. Sessi, C.H. Michaelis, I. Brihuega, J. Honolka, K. Kern, R. Skomski, X. Chen, G. Rojas, A. Enders, Phys. Rev. B 78 (2008).

[228] A. Goriachko, Y.B. He, H. Over, J. Phys. Chem. C 112 (2008) 8147.

[229] J.W. He, X. Xu, J.S. Corneille, D.W. Goodman, Surf. Sci. 279 (1992) 119.

[230] X.P. Xu, D.W. Goodman, Surf. Sci. 282 (1993) 323.

[231] T. Schroeder, M. Adelt, B. Richter, M. Naschitzki, M. Baumer, H.J. Freund, Surf. Rev. Lett. 7 (2000) 7.

[232] S. Kaya, M. Baron, D. Stacchiola, J. Weissenrieder, S. Shaikhutdinov, T.K. Todorova, M. Sierka, J. Sauer, H.J. Freund, Surf. Sci. 601 (2007) 4849.

[233] J. Weissenrieder, S. Kaya, J.L. Lu, H.J. Gao, S. Shaikhutdinov, H.J. Freund, M. Sierka, T.K. Todorova, J. Sauer, Phys. Rev. Lett. 95 (2005).

[234] M.S. Chen, D.W. Goodman, Surf. Sci. 600 (2006) L255.

[235] M.S. Chen, A.K. Santra, D.W. Goodman, Phys. Rev. B 69 (2004).

[236] L. Giordano, A. Del Vitto, G. Pacchioni, J. Chem. Phys. 124 (2006).

[237] S.M. McClure, M. Lundwall, F. Yang, Z. Zhou, D.W. Goodman, J. Phys. Chem. C 113 (2009) 9688.

[238] R.B. Laughlin, Phys. Rev. B 22 (1980) 3021.

[239] S.M. McClure, M. Lundwall, Z. Zhou, F. Yang, D.W. Goodman, Catal. Lett. 133 (2009) 298.

[240] B. Schleich, D. Schmeisser, W. Gopel, Surf. Sci. 191 (1987) 367.

[241] N. Walchli, E. Kampshoff, A. Menck, K. Kern, Surf. Sci. 382 (1997) L705.

[242] K. Tanaka, K. Furui, M. Yamada, J. Phys. Soc. Jpn. 64 (1995) 4790.

[243] D.M. Scott, S.S. Lau, R.L. Pfeffer, R.A. Lux, J. Mikkelson, L. Wielunski, M.A. Nicolet, Thin Solid Films 104 (1983) 227.

[244] R. Anton, U. Neukirch, M. Harsdorff, Phys. Rev. B 36 (1987) 7422.

[245] H. Dallaporta, M. Liehr, J.E. Lewis, Phys. Rev. B 41 (1990) 5075.

[246] W. Juszczyk, Z. Karpinski, J. Catal. 117 (1989) 519.

[247] X.P. Xu, J. Szanyi, Q. Xu, D.W. Goodman, Catal. Today 21 (1994) 57.

[248] B.K. Min, A.K. Santra, D.W. Goodman, J. Vac. Sci. Technol. B 21 (2003) 2319.

[249] R.C. Weast, Handbook of Chemistry and Physics, CRC Press, Cleveland, 2004.

VITA

Name: Zihao Zhou

Address: Department of Chemistry
c/o Dr. D. Wayne Goodman
Texas A&M University
3255 TAMU
College Station, TX 77843-3255

Email Address: zihaozh@gmail.com

Education: Ph.D., Chemistry, Texas A&M University, 2012
B.S., Chemistry, University of Science&Technology of China, 2007

Selected Publications:

1. "Graphene on Ru(0001): Evidence for Two Graphene Band Structures", K. Katsiev, Y. Losovyj, Z. Zhou, E. Vescovo, L. Liu, P. Dowben and D. Wayne Goodman, *Phys. Rev. B*, in press.
2. "The 2-D Growth of Gold on Single-layer Graphene/Ru(0001): Enhancement of CO Adsorption", L. Liu, Z. Zhou, Q. L. Guo, Z. Yan, Y. X. Yao and D. W. Goodman, *Surf. Sci.*, 605, L47-L50 (2011).
3. "Exploring the Structure and Chemical Activity of 2-D Gold Islands on Graphene Moiré/Ru(0001)", Y. Xu, L. Semidey-Flecha, L. Liu, Z. Zhou and D. W. Goodman, *Faraday Diss.*, 152, 267-276 (2011).
4. "Deposition of Metal Clusters on Single-Layer Graphene/Ru(0001): Factors that Govern Cluster Growth" Z. Zhou, F. Gao and D. W. Goodman, *Surf. Sci.*, 604, L31-L38, (2010).
5. "Characterization of Pt/SiO2 Model Catalysts at UHV and Near Atmospheric Pressures", S. M. McClure, M. Lundwall, Z. Zhou**,** F. Yang and D. W. Goodman, *Catal. Lett.*, 133, 298-306 (2009).
6. "Characterization of Active Sites on Rh/SiO2 Model Catalysts", S. M. McClure, M. Lundwall, F. Yang, Z. Zhou and D. W. Goodman, *J. Phys.: Condensed Matter*, 21, 474223-1~7 (2009).
7. "CO Oxidation on Rh/SiO2/Mo(112) Model Catalysts at Elevated Pressures", S. M. McClure, M. Lundwall, F. Yang, Z. Zhou and D. W. Goodman, *J. Phys. Chem. C*, 113, 9688-9697, (2009)
8. "Catch and Release: DNA Tweezers that Can Capture, Hold, and Release an Object under Control" X. Han, Z. Zhou, F. Yang, Z. Deng, *J. Am. Chem. Soc.*,130, 14414–14415, (2008)